THERMODYNAMIC AND OPTICAL INVESTIGATION OF THE COMBUSTION MECHANISMS OF DIESEL-IGNITED DUAL-FUEL NATURAL GAS COMBUSTION

by

Jeremy Rochussen

B.A.Sc, The University of Waterloo, 2012

A THESIS SUBMITTED IN PARTIAL FULFILLMENT OF

THE REQUIREMENTS FOR THE DEGREE OF

MASTER OF APPLIED SCIENCE

in

THE FACULTY OF GRADUATE AND POSTDOCTORAL STUDIES

(Mechanical Engineering)

THE UNIVERSITY OF BRITISH COLUMBIA

(Vancouver)

December 2015

Abstract

Diesel-ignited dual-fuel (DIDF) combustion of natural gas (NG) is a promising, and immediately available strategy to improve heavy-duty compression-ignition (CI) engine performance to meet challenging and evolving emissions regulations. The DIDF concept utilizes a combination of port-injected NG and direct-injected diesel to couple the relatively low-cost and low-emissions characteristics of NG combustion with the operational and performance characteristics that have made diesel CI engines ubiquitous. This combination of fuelling strategies permits a wide range of different operating modes, which are characterized by a number of fundamental combustion mechanisms.

Combustion mechanisms specific to particular modes of DIDF operation have previously been addressed, however a comprehensive conceptual description of the combustion processes and modes of DIDF operation is lacking. A clear context for specific observed phenomena and DIDF operating modes is needed to bridge and extend the conclusions of investigations in this field. That need is addressed by this investigation through experimental analysis of thermodynamic and optical measurements of a broad range of DIDF fuelling modes.

A 2-litre single-cylinder CI research engine capable of both conventional and optically-accessible operation was commissioned and operated with port-injected methane (CH_4). Fuelling modes were characterized using the global equivalence ratio (φ_{global} =0.55—0.88) and pilot fuel ratio (R_{pilot} =0.06—0.61) and were performed with combinations of pilot injection timing and pressure. A novel set of criteria, which used the measured apparent heat release rate (AHRR),

defined sequential stages of DIDF combustion and mapped fundamental regimes of DIDF operation in the R_{pilot}-φ_{global} space. Flame propagation, and non-flame propagation DIDF operating regimes were distinguished by an apparent lean flame propagation limit observed at a CH_4 equivalence ratio (φ_{CH4}) equal to 0.4. Pilot injection parameters were observed to be critical to combustion and emissions processes across all operating modes except for a unique subset of operating points with R_{pilot}=0.06. Spatially-resolved broadband visible light and OH*-chemiluminescence measurements supported the identified operating regimes, and indicated that the conventional conceptual model of DIDF combustion is not a complete description of the DIDF combustion process for all operating modes.

Preface

I was principally responsible for generation of the research focus of this work; however essential feedback and guidance was contributed by my supervisor, Dr. Patrick Kirchen.

Commissioning of the single-cylinder research engine facility was a collaborative effort involving several people. I performed the mechanical design, installation and commissioning of the fuel systems, thermal management system, and safety control panel in addition to the initial build-up and commissioning of the stock single-cylinder engine systems. Jeff Yeo commissioned both the hardware and software associated with engine control and data acquisition systems. Mahdiar Khosravi commissioned the optical imaging systems.

I was solely responsible for the design of all thermodynamic and optical tests, with consultation from my supervisor, Dr. Patrick Kirchen. I was also solely responsible for all thermodynamic testing, while optical testing was performed by myself, Mahdiar Khosravi, and Jeff Yeo.

All data analysis presented in this thesis is my original work, with the exception of the image post-processing routines used to align and synchronize OH*- and visible-image sets, which was developed by Mahdiar Khosravi.

The thermodynamic measurements and analysis presented in chapter 4 of this thesis has been submitted for review to be included in the 2016 SAE World Congress and, at the time of writing, acceptance is pending. I was the lead author for this work and performed all written and analytical work with the assistance of Jeff Yeo and Dr. Patrick Kirchen.

Table of Contents

Abstract ..... **ii**

Preface ..... **iv**

Table of Contents ..... **v**

List of Tables ..... **viii**

List of Figures ..... **ix**

List of Symbols ..... **xiv**

List of Abbreviations ..... **xvi**

Acknowledgements ..... **xvii**

Dedication ..... **xix**

Chapter 1: Introduction **1**

1.1 Motivation & Background 1

1.2 Natural Gas as a Transportation Fuel 3

1.3 The 'Dual-Fuel' Operating Concept 4

1.4 Objectives 7

1.5 Approach 8

Chapter 2: Literature Review **9**

2.1 Conceptual Understanding & Theory of DIDF Combustion of Natural Gas 10

2.2 Background Theory & Modelling of Conventional Combustion Phenomena 16

2.2.1 Diesel Spray Combustion Theory & Modelling 16

2.2.2 Turbulent Flame Propagation Theory & Modelling 20

2.3 Experimental Investigations of DIDF Combustion 23

2.3.1 Impact of Operating Mode on DIDF Combustion 23
2.3.2 Impact of Pilot-Injection 28
2.3.3 Optical Investigations of Dual-Fuel Combustion 32
2.4 Summary & Literature Gap 36
Chapter 3: Experimental Facility 38
3.1 Facility Overview 38
3.2 Single-Cylinder Research Engine 39
3.2.1 Engine Control 42
3.2.2 Fueling 44
3.2.3 Auxiliary Systems 45
3.3 Optical Engine Configuration 46
3.4 Measurement & Instrumentation 53
3.4.1 Thermodynamic Measurement & Instrumentation 53
3.4.2 Optical Instrumentation & Measurement 59
3.4.3 Data Acquisition 63
3.5 Summary 64
Chapter 4: Thermodynamic Results & Discussion 65
4.1 Thermodynamic Measurements 65
4.2 Thermodynamic Data Analysis 70
4.3 Thermodynamic Results 78
4.3.1 Pilot Injection Pressure 78
4.3.2 Pilot Injection Timing 81
4.3.3 Pilot Ratio and Equivalence Ratios 84

4.4 Discussion 95
4.4.1 Stages of DIDF Combustion 96
4.4.2 Operating Regimes of DIDF Combustion 101
4.5 Summary of Thermodynamic DIDF Investigation 112
Chapter 5: Optical Results & Discussion 117
5.1 Optical Measurement Selection 117
5.2 Optical Measurement Background & Analysis 120
5.2.1 Visible Light Emissions 120
5.2.2 OH*-Chemiluminescence 121
5.2.3 Optical Measurement Analysis 122
5.3 Optical Measurement Results & Discussion 125
5.3.1 Pilot-Independent DIDF Combustion (Regime A) 125
5.3.2 Flame Propagation DIDF Operation Regime (B) 134
5.3.3 Non-Flame Propagation DIDF Combustion 143
5.4 Summary of Optical DIDF Investigation 149
Chapter 6: Conclusions 154
Chapter 7: Recommendations 165
References 172
Appendices 178
Appendix A : Experimental Facility P&IDs 178
Appendix B : Thermodynamic Test Point Data 182
Appendix C : Optical Heat Release Rates 193

List of Tables

Table 1: EPA and EU mandated emissions restrictions for heavy-duty on-highway vehicles [3,4]. 2

Table 2: Major specifications of single-cylinder engine in thermodynamic configuration..... 40

Table 3: Thermodynamic instrumentation details. 54

Table 4: Statistical variability of operating parameters for thermodynamic measurement repeatability point. 58

Table 5: Optical measurement equipment specifications. 60

Table 6: Signal conditioning and logging details 64

Table 7: Pilot injection parameters for thermodynamic DIDF measurements 69

Table 8: Summary of DIDF combustion regime characteristics. 116

Table 9: Optical test parameters for pilot-independent DIDF operating regime (A) measurements. 126

Table 10: Optical test parameters for flame propagation DIDF operating regime (B) measurements..... 134

Table 11: Optical test parameters for non-flame propagation DIDF operating regime (C) measurements..... 144

List of Figures

Figure 1: Three conceptual heat release mechanisms of DIDF combustion at heavy-load (left) and light-load (right). Adapted from [23] with permission of SAE. 12

Figure 2: Conceptual description of transient diesel spray combustion adapted from [30] with permission of SAE. 17

Figure 3: Schematic variations of the unconverted CH_4 and CO concentrations in the exhaust emissions with total equivalence ratio. Reprinted from [29] with permission of Elsevier. 24

Figure 4: OH*-chemiluminescence image sequences for low-load (left) and high-load (right) DIDF operation with constant pilot mass. Adapted from [28] with permission of SAE. 33

Figure 5: OH*-chemiluminescence of DIDF combustion in a RCEM. Adapted from [46] with permission from SAE. 35

Figure 6: P&ID of single-cylinder research engine facility in thermodynamic configuration. 41

Figure 7: Schematic of Bowditch piston arrangement in optical engine configuration and imaging systems arrangement. 48

Figure 8: P&ID of single-cylinder research engine facility in optical configuration. 49

Figure 9: Skip-firing and image record sequence used in all optical testing. 51

Figure 10: AHRR of first 5 consecutive fired cycles from skip-fired operation in the thermodynamic engine configuration. 52

Figure 11: Intake temperature variation during optical measurement using an intake wall temperature of 132°C. 53

Figure 12: Mean DIDF AHRR and 95% confidence interval calculated from 100 measured cycles at P_{pilot}=300, 800, 1300bar. 57

Figure 13: Flowchart of image post-processing procedure. 61

Figure 14: Optical measurement protocol flowchart. 63

Figure 15: Selected thermodynamic operating points in R_{pilot}-φ_{global} operating space. 68

Figure 16: Complete set of all measured thermodynamic operating points at all P_{pilot} and θ_{pilot}.. 70

Figure 17: Defined stages of DIDF combustion and superposition of diesel-only and DIDF AHRR data. 72

Figure 18: Comparison of P_{pilot} effect on AHRR of DIDF combustion for R_{pilot}=0.27 (left) and R_{pilot}=0.53 (right). 79

Figure 19: Effect of P_{pilot} on mean relative amount of energy released during each stage of combustion (Q_x/Q_{tot}) for optimized timing at each operating point and P_{pilot}. Vertical bars represent maximum and minimum data points in experimental set. Note that for plot clarity, data points at each injection pressure are presented with a horizontal offset. 79

Figure 20: AHRR trends for typical sweep of commanded pilot injection timing, θ_{pilot}, for θ_{pilot}=-12,-8,-4,+0°CA aTDC. 82

Figure 21: AHRR trends for sweep of commanded pilot injection timing, θ_{pilot}, for θ_{pilot}=-12,-8,-4,+0,+4°CA aTDC for an operating point exhibiting increased peak AHRR at late θ_{pilot}. 83

Figure 22: Example of trade-off between emissions performance and GIMEP used to select 'best timing' for a given operating point and P_{pilot}. 84

Figure 23: Contour plots of GIMEP across the R_{pilot}-φ_{CH4} operating space for P_{pilot}=300, 800, and 1300bar and best θ_{pilot}. 86

Figure 24: Contour plots of GISFC across the R_{pilot}-φ_{CH4} operating space for P_{pilot}=300, 800, and 1300bar and best θ_{pilot}. 87

Figure 25: Contour plots of $\eta_{thermal}$ across the R_{pilot}-φ_{CH4} operating space for P_{pilot}=300, 800, and 1300bar and best θ_{pilot}. 88

Figure 26: Contour plots of peak AHRR of stage 1 combustion, $q_{1,max}$, across R_{pilot}-φ_{CH4} operating space for P_{pilot}=300, 800, and 1300bar and best θ_{pilot}..... 90
Figure 27: Contour plots of mean AHRR of high-intensity portion of stage 2 combustion, $q_{2a,mean}$, across R_{pilot}-φ_{CH4} operating space for P_{pilot}=300, 800, and 1300bar and best θ_{pilot}. 91
Figure 28: Contour plots of fraction of total cycle energy released during low-intensity portion of stage 2 combustion, Q_{2b}/Q_{tot}, across R_{pilot}-φ_{CH4} operating space for P_{pilot}=300, 800, and 1300bar and best θ_{pilot}. 93
Figure 29: Contour plots of NO_x emissions across R_{pilot}-φ_{CH4} operating space for P_{pilot}=300, 800, and 1300bar and best θ_{pilot}..... 94
Figure 30: Contour plots of CH_4 emissions across R_{pilot}-φ_{CH4} operating space for P_{pilot}=300, 800, and 1300bar and best θ_{pilot}..... 95
Figure 31: Effect of m_{diesel} on fraction of energy released in stage 1 combustion (Q_1/Q_{tot}). 98
Figure 32: Impact of φ_{CH4} on stage 2 combustion mean AHRR ($q_{2a,mean}$). 100
Figure 33: Proposed division of DIDF operating space based on stage 2 combustion mechanisms for all pilot injection pressures. 102
Figure 34: Effect of φ_{global} and pilot injection pressure on CH_4 emissions. 103
Figure 35: Comparison of DIDF and diesel-only AHRRs for typical operating point found in the 'non flame propagation' regime..... 105
Figure 36: Correlation between the fraction of energy released in stage 1 combustion (Q_1/Q_{tot}) and emissions of NOx (g/kW-hr). Filled figures indicate points categorized as not possessing flame propagation by Figure 33. 106
Figure 37: Comparison of dual-fuel and diesel pilot AHRRs for typical operating point within the 'flame propagation' regime. 107

Figure 38: Effect of stage 2 combustion peak intensity ($q_{2a,max}$) on CH_4 emissions. Filled markers represent combustion modes indicated to possess flame propagation mechanisms in Figure 33. 108

Figure 39: Effect of stage 2 combustion intensity (q2a,mean) on NO_x emissions. 109

Figure 40: Emissions and GIMEP trends for all θ_{pilot} and P_{pilot} measurements in 'pilot-independent' operating point. 111

Figure 41: Comparison of DIDF and diesel-only AHRRs for operating point classified as pilot-independent case of flame propagation combustion regime. 112

Figure 42: DIDF operating regimes and transitionary boundaries identified for the experimental conditions of this investigation. 115

Figure 43: Selected DIDF operating points for optical investigation. 118

Figure 44: Summary of optical measurement points selected for detailed analysis. 119

Figure 45: Description of cumulative histogram time series plot formulation. 123

Figure 46: Single-cycle image sequences of pilot-independent regime (A) DIDF combustion using a pilot injection pressure of 300bar (columns 1 and 2) and 1300bar (columns 3 and 4); φ_{global}=0.74, φ_{CH4}=0.61, R_{pilot}=0.07. 127

Figure 47: Cumulative histogram time series of visible- and OH*-signal intensities and AHRR for pilot-independent regime (A) DIDF combustion with P_{pilot}=300bar, φ_{global}=0.74, φ_{CH4}=0.61, R_{pilot}=0.07. 131

Figure 48: Cumulative histogram time series of visible- and OH*-signal intensities and AHRR for pilot-independent regime (A) DIDF combustion with P_{pilot}=1300bar, φ_{global}=0.74, φ_{CH4}=0.61, R_{pilot}=0.07. 133

Figure 49: Single-cycle image sequences of flame propagation regime (B) DIDF combustion using a pilot injection pressure of 300bar (columns 1 and 2) and 1300bar (columns 3 and 4); φ_{global}=0.66, φ_{CH4}=0.48, R_{pilot}=0.17. 136

Figure 50: Cumulative histogram time series of visible- and OH*-signal intensities and AHRR for flame propagation regime (B) DIDF combustion with P_{pilot}=300bar, φ_{global}=0.66, φ_{CH4}=0.48, R_{pilot}=0.17. 140

Figure 51: Cumulative histogram time series of visible- and OH*-signal intensities and AHRR for flame propagation regime (B) DIDF combustion with P_{pilot}=1300bar, φ_{global}=0.66, φ_{CH4}=0.48, R_{pilot}=0.17. 142

Figure 52: Single-cycle image sequences of non-flame propagation regime (C) DIDF combustion with P_{pilot}=1300bar, φ_{global}=0.53, φ_{CH4}=0.25, R_{pilot}=0.47. 146

Figure 53: Cumulative histogram time series of visible- and OH*-signal intensities and AHRR for non-flame propagation regime (C) DIDF combustion with P_{pilot}=1300bar, φ_{global}=0.53, φ_{CH4}=0.25, R_{pilot}=0.47. 147

Figure 54: Definition of dual-fuel operating space based on R_{pilot}, φ_{global}, and φ_{CH4} used to design experiments in this investigation. 155

Figure 55: Correlation between cumulative histogram time series of OH*-chemiluminescence measurements and corresponding thermodynamic AHRR. 158

Figure 56: Observed boundaries of transition regions between ‘pilot independent’, ‘flame propagation’, and ‘non-flame propagation’ DIDF combustion regimes across the R_{pilot}-φ_{global} operating space. 159

List of Symbols

$\frac{A}{F}$	Air-fuel mass ratio
A_t	Wrinkled flame front area
C_2	Diatomic carbon
CA50	Crank angle corresponding to 50% heat release
CH	Carbyne
CH_4	Methane
CH_2O	Formaldehyde
CO	Carbon monoxide
CO_2	Carbon dioxide
C_v	Specific heat, constant volume
D_a	Damköhler number
$\eta_{thermal}$	Thermal efficiency
h	Planck's constant
$\dot{m}_r$	Mass flow rate of reactants
m_{pilot}	Mass of pilot injection
ν	Frequency of light
NO_x	Oxides of nitrogen
OH	Hydroxyl radical
OH*	Electronically-excited hydroxyl radical
O_2	Oxygen
φ	Equivalence ratio
φ_{CH4}	Equivalence ratio of methane
φ_{diesel}	Equivalence ratio of diesel
φ_{global}	Equivalence ratio of diesel and methane combined
$\varphi_{lean,\ flam.\ limit}$	Equivalence ratio at lean flammability limit
φ_{local}	Equivalence of local mixture
$\varphi_{rich\ flam.\ limit}$	Equivalence ratio at rich flammability limit
P_{pilot}	Pilot injection pressure
$q_{1,max}$	Peak apparent heat release rate in stage 1 combustion
$q_{2a,mean}$	Mean apparent heat release rate in stage 2a combustion
Q_x/Q_{tot}	Fraction of total energy released in stage X of combustion
R_{pilot}	Pilot ratio
$\mathcal{R}$	Universal gas constant
ρ_u	Unburned gas density
SO_x	Oxides of sulphur
s_l	Laminar flame speed
s_t	Turbulent flame speed
θ_{pilot}	Commanded start of pilot injection
θ_1	Crank angle at start of stage 1 combustion
θ_{2a}	Crank angle at start of stage 2a combustion
θ_{2b}	Crank angle at start of stage 2b combustion

θ_{port}	Commanded start of port injection
T_u	Unburned gas temperature
u'	Fluctuating component of turbulent velocity field

List of Abbreviations

AHRR	Apparent heat release rate
aTDC	After top dead centre
bTDC	Before top dead centre
CA	Crank angle
CAD	Crank angle degree
CI	Compression ignition
CMOS	Complementary metal-oxide semiconductor
COV	Coefficient of variance
CNG	Compressed natural gas
DAQ	Data acquisition
DIDF	Diesel-ignited dual-fuel
ECU	Engine control unit
EGR	Exhaust gas recirculation
ESD	Emergency shut down
EU	European Union
FPGA	Field-programmable gate array
GHG	Greenhouse gas
GISFC	Gross indicated specific fuel consumption
GUI	Graphic user interface
HC	Hydrocarbon
HCCI	Homogeneous charge compression ignition
HRR	Heat release rate
HPDI	High-pressure direct injection
ICE	Internal combustion engine
IMEP	Indicated mean effective pressure
IRO	Intensified relay optics
LHV	Lower heating value
LNG	Liquefied natural gas
NG	Natural gas
nmHC	Non-methane hydrocarbons
ON	Octane number
P&ID	Process and instrumentation diagram
PLIF	Planar laser induced fluorescence
PM	Particulate Matter
RCCI	Reactivity-controlled compression ignition
RCEM	Rapid compression/expansion machine
SI	Spark ignition
TDC	Top dead centre
tHC	Total hydrocarbons
TMS	Thermal management system
TTL	Transistor-transistor logic
UV	Ultra-violet

Acknowledgements

In retrospect this work has been a personal journey as much as an academic one. A journey I could not have completed without the host of people who have helped, encouraged, and contributed to me and this work along the way.

I will owe my supervisor, Dr. Patrick Kirchen, an eternal debt of gratitude. He has been an unwavering and dependable source of inspiration throughout the often difficult, but always rewarding trials of experimental research. He has always held me accountable to the highest standards and I am very proud of my achievements from the past 3 years because of it.

I would also like to acknowledge the sincere benefit that both this work and myself as an engineer and scientist have enjoyed due to the contributions of Dr. Steve Rogak, Dr. Gord McTaggart-Cowan, and Dr. Ning Wu over the past three years. I must also acknowledge Bob Parry, who has solved more than a few of my technical problems and has been a reliable source of stories and perspective over the years. My lab mates Jeff and Mahdiar have spent many late nights in the lab with me, and I could not have completed this without them; I hope I can contribute to them as much as they have to me.

Even when I drop off the face of the planet because of an impending deadline, my friends are always there for me, ready for a pint and a laugh. I am incredibly lucky to have these people in my life. I have to single out and thank my best friend, David, who is probably the biggest reason I decided to pursue graduate studies and also why I haven't lost my mind because of it.

Finally, I would like to thank my family, Cindy, Peter, Devin and of course granny Doreen. You have been my champions from day one and have made sacrifices on my behalf that have given me the opportunity to follow my passion. Thank you.

To Doreen,

Life isn't always tough on a kid.

Chapter 1: Introduction

The purpose of this chapter is to provide the motivation for the work described in this document by presenting some background information relevant to current applications of diesel-ignited dual-fuel (DIDF) combustion of natural gas (NG). The objectives of this work and the approach followed are subsequently presented to give the reader a roadmap for the remainder of the document.

1.1 Motivation & Background

In the past half-century, over half of the observed rise in mean surface temperature of the planet is attributed to anthropogenic increases of green-house gas (GHG) concentrations in the atmosphere [1]. The transportation sector constitutes a major contributor to global climate change; as of 2014, an estimated 14% of total GHG emissions in the US were as a direct result of transportation sources, where in excess of 90% of all energy is derived from petroleum sources such as gasoline, diesel, and NG [2].

The heavy-duty sector is one of several classes of on-highway vehicle for which legislated reductions in emissions are firmly enforced. Major markets, notably the United States and the European Union (EU), define acceptable upper limits of specific chemical species in the exhaust gases of new vehicles sold within their jurisdiction. In North America, emissions standards for heavy-duty on-highway applications are set by the Environmental Protection Agency (EPA) and the National Highway Traffic Safety Administration (NHTSA). As of 2015, the North American standards restrict emissions of CO, NO_x, non-methane hydrocarbons (nmHC), and particulate

matter (PM). The latest standards (implemented for model year 2013 vehicles) imposed by the EU restrict emissions of CO, hydrocarbons (HC), NO_x and PM. The mandated emissions standards are strict and continuously tightening, which necessitates active research and development efforts be made by heavy-duty vehicle manufacturers. Current emissions limits imposed by the EPA and EU are presented in Table 1.

Table 1: EPA and EU mandated emissions restrictions for heavy-duty on-highway vehicles [3,4].

Exhaust Species	EPA Emissions Limit [g/bhp-hr]	EU Emissions Limits [g/kW-hr]
CO	15.5	1.5
nmHC	0.14	-
HC	-	0.13
NO_x	0.02	0.4
PM	0.01	0.01

In heavy-duty on-highway applications, the compression-ignition (CI) internal combustion engine (ICE) fueled with petroleum-derived diesel is by far the most common propulsion system architecture. The potential for high thermal efficiency and reliable operation has traditionally prevented displacement of this technology, and has led to its ubiquity. As current and future legislation continues to put an emphasis on the reduction of emissions of GHGs, such as CO_2 and NO_x in addition to PM, the development of alternative fuels and combustion strategies will become essential.

1.2 Natural Gas as a Transportation Fuel

NG is a popular alternative to diesel for a number of environmental and economic reasons. NG composition varies widely by source, but primarily consists of CH_4. Typical CH_4 content of NG is 80—95% [5], however regulations often require higher concentrations be distributed to end-users to ensure consistent fuel properties. CH_4 is the simplest hydrocarbon molecule, possessing the highest hydrogen-to-carbon ratio, which is an inherent advantage for the reduction of CO_2 emissions.

Related to the simple structure of CH_4, is its very high resistance to auto-ignition, typically specified as an octane number (ON). The most important consequence of the high octane number of CH_4 (Research ON≈120) is the feasibility of combining a high compression ratio engine design with premixed fuel admission. Fuels with lower octane numbers, or higher propensities to auto-ignite, will tend to homogeneously ignite throughout the cylinder when premixed in high compression ratio cylinders, which leads to engine knock and ultimately damage to engine components. Increased cylinder compression ratios are well known to produce higher thermal efficiency, while premixed fuel oxidation tends to reduce PM formation.

From a practical point of view, NG is also a cheaper fuel on an energy basis than conventional petroleum-based fuels. Natural reserves of NG are widespread globally and accordingly, prices remain lower and less volatile than other fossil fuels. A major practical drawback, however, is that CH_4 is gaseous at standard temperature and pressure, which presents on-board storage and infrastructure challenges.

Application of NG as a transportation fuel is achieved through a number of propulsion architectures. NG may be stored on a vehicle as compressed natural gas (CNG), or cryogenically as liquefied natural gas (LNG). In either case, NG is in a gaseous state when it is delivered to the engine cylinder. The other major defining feature of the propulsion system architecture is whether it is a CI or spark-ignition (SI) system. In heavy-duty applications, CI architectures are favoured, but typically require a second fuel to enhance the control of the NG ignition. Such concepts are referred to as dual-fuel engines.

1.3 The 'Dual-Fuel' Operating Concept

The term 'dual-fuel' is used by engine researchers and manufacturers to describe a broad array of ICE combustion strategies. The major feature of dual-fuel combustion is the combination of two fuels, one of which is typically used in significantly greater quantity to provide the bulk of the energy, known as the primary fuel. The second fuel employed is selected to complement the primary fuel, often to increase the controllability of the combustion event. A wide variety of combinations of liquid and gaseous fuels can be delivered to the engine cylinder by several different methods; the precise combination of fuels and delivery methods dictates the particular set of advantages and disadvantages of the dual-fuel engine in comparison to a conventional CI engine.

A major advantage of the dual-fuel engine is the designer's freedom to select from a wide range of primary fuels. Traditional hydrocarbon fuels can be replaced with unconventional fuels possessing superior emissions characteristics, lower costs, domestic availability or any other property of importance to the particular application. Across many applications, a primary

motivation for adopting dual-fuel combustion is the reduction of NOx, PM, and CO_2. It is the goal of the dual-fuel engine designer to leverage the benefits of the selected fuels, while maintaining acceptable performance.

Generally, dual-fuel engines are modified versions of existing diesel CI engines. The principle modification to the base CI engine is the addition of a second fueling system. Regardless of the method of delivery, the primary fuel possesses a high resistance to auto-ignition (a high ON), such that the high compression ratio, and corresponding high thermal efficiency, of the base CI engine is retained. Without a second fuel, the high ON primary fuel would be subject to knocking as well as poor controllability of combustion phasing, which typically limits the application of pre-mixed CI fueling strategies, such as Homogeneous Charge Compression Ignition (HCCI) combustion [6]. Accordingly, a fuel with high reactivity (a high cetane number) is selected as the secondary fuel. The amount, distribution and timing of introduction of the high-reactivity secondary fuel dictate the phasing and rate of combustion of the primary fuel.

The family of ICE combustion strategies labelled ‘dual-fuel’ encompasses a diverse array of different technologies, many of which have substantially different characteristics from one another. The majority of current dual-fuel applications can be classified as pilot-controlled dual-fuel engines where a port-injection system is installed to deliver the primary fuel to the cylinder as a homogeneously mixed charge, while the existing direct-injection system is retained to deliver the pilot fuel which controls combustion phasing. Some pilot-controlled concepts exist where both the primary fuel and the pilot fuel are introduced via direct-injection, such as in high-pressure direct-injection (HPDI) combustion [7]. Other variants of the dual-fuel combustion

strategy exist where both fuels are introduced as premixed charge, such as in reactivity-controlled compression ignition (RCCI) engines [8]. In these concepts, the proportion of each fuel injected is modified to control combustion phasing. In addition to pilot-controlled and reactivity-controlled dual-fuel concepts, a spectrum of hybrid concepts exist where the application of multiple pre-mixed fuels and a late injection of pilot fuel are employed [9].

Possibly the most widely investigated and applied dual-fuel strategy is the diesel-ignited combustion of NG, due to the existing wealth of practical and theoretical knowledge concerning the use of both diesel and NG as ICE fuels in transportation applications and the inherent suitability of modern CI diesel engines for conversion to dual-fuel operation. Major deficiencies of this operating mode are knocking at high-load and high emissions of unburned combustion species, particularly CH_4, at low load. CH_4 has been shown to have a 21—72 times more significant GHG effect than CO_2 [10] and its reduction from exhaust emissions is therefore of critical importance to the increased commercial adoption of DIDF engines. While emissions of CH_4 are not currently restricted by the EPA, the EU limits emissions of all HC, including CH_4 to 0.13g/kW-hr (see Table 1).

As will be reviewed in the following chapter, a strong experimental knowledge base surrounds DIDF combustion of NG, however a comprehensive conceptual understanding of the combustion phenomena remains incomplete. Investigations of DIDF combustion have been largely focussed on minimal pilot injection mass operating modes, while many real-world applications are unable to operate using such strategies due to practical engine performance considerations.

Experimental investigation bridging all the different DIDF operating strategies is necessary for continued advancement of DIDF engine technologies and their increased application.

1.4 Objectives

The over-arching objective of this investigation is to characterize a broad range of DIDF operating conditions in terms of the fundamental combustion and emissions mechanisms. This objective is exploratory in nature and it is designed to provide context and motivation for future investigations of DIDF combustion. This objective also strives to connect the observations and understanding developed by previous investigations, which is necessary for a comprehensive conceptual treatment of DIDF operation. In order to characterize the fundamental combustion and emissions mechanisms of DIDF combustion, the following aspects of the problem are addressed:

- Identification of the defining engine control parameters that dictate DIDF operating characteristics.
- Identification of the fundamental combustion mechanisms present in DIDF combustion and comparison with the existing conceptual understanding of DIDF combustion.
- Development of tools appropriate for the analysis of DIDF thermodynamic and optical data across all operating modes.
- Classification of features observed to be common to all explored DIDF combustion modes.
- Classification of subsets of DIDF operating modes observed to have unique combustion and emissions mechanisms and the boundaries that distinguish the identified subsets.

1.5 Approach

The experimental approach applied to reach the stated objectives is reflected in the layout of this thesis. A survey of the current state of the theoretical and experimental knowledge base developed for DIDF combustion was performed to identify likely engine control parameters of interest and design the DIDF operating space to be explored. A summary of this survey is given in chapter 2. An experimental facility comprising a single-cylinder research engine configurable as either thermodynamic (conventional) or optically-accessible was commissioned to operate in a DIDF mode, which is described in detail in chapter 3.

The designed DIDF operating space was first explored using the thermodynamic engine configuration. A summary of the identified DIDF operating space, the analysis method and tools developed, and results of thermodynamic data collected are presented in chapter 4. A subset of operating points deemed to capture the different mechanisms of DIDF combustion observed in the thermodynamic measurement were repeated with the engine in the optical configuration to support and enrich the conclusions drawn from the thermodynamic data. Chapter 5 presents the optical measurement points, developed analysis tools and conclusions drawn from the optical measurements. In chapter 6, conclusions encompassing the observations of both the thermodynamic and optical measurements are presented.

Chapter 2: Literature Review

The DIDF combustion strategy is a promising solution to the increasingly demanding restrictions being placed on transportation technologies, but is far from being novel. DIDF combustion of NG has been utilized in real world applications for several years and has been studied for several decades. To date, the conceptual understanding of DIDF combustion remains at least partially contested, which continues to make detailed and predictive modelling of DIDF engine performance a significant challenge, despite the wealth of knowledge in the related fields of CI and SI combustion phenomena.

Rigorous connection of the well-understood base combsustion phenomena (*e.g.* turbulent flame propagation, premixed auto-ignition, diffusion combustion, *etc.*) with practical engine processes (*e.g.* compression, sprays, expansion, *etc.*) remains a goal in the field of DIDF combustion. The objective of this chapter is to:

i. Provide a brief introduction and review of the accepted fundamental understanding and theory of the combustion phenomena in DIDF engine operation.
ii. Review the state of the art in how the fundamental combustion concepts are applied to DIDF combustion.
iii. Review the knowledge base that has been built around DIDF combustion through experimental investigations.

2.1 Conceptual Understanding & Theory of DIDF Combustion of Natural Gas

Two general categories of the DIDF combustion strategy can be considered based on the relative quantity of diesel and NG employed: i) the application of a relatively small diesel pilot injection to ignite the premixed charge of air and primary fuel (NG), and ii) the addition of premixed NG to a conventional, diesel-only operating mode [11]. In general, DIDF research focus is more heavily targeted at the small-pilot injection strategies because these leverage the benefits of NG the most. In commercial practice however, there exist many applications, such as retro-fitting of dual-fuel systems to mid-life engines, where operation is more similar to a conventional diesel engine with the addition of premixed NG [12]. Because of the increased academic and research focus on the 'small-pilot' DIDF strategies, the majority of the existing knowledge and especially conceptual understanding concerns these concepts.

Although a promising operating strategy to reduce emissions of NO_x, CO_2, and PM, DIDF operation is limited to a narrower band of operating loads than comparable, conventional CI combustion strategies. At high-loads, DIDF combustion suffers from knocking limitations resulting from the compression of a premixed fuel-air mixture in a high compression ratio cylinder typical of modern CI engines, which are used as starting platforms for DIDF engine conversions. At low loads, DIDF combustion suffers from the emissions of HC, especially CH_4, which has been shown to possess 21—72 times the greenhouse warming effect of CO_2 [13], making low-load emissions reduction in DIDF engines a particularly intense field of current research.

The complexities and nuances of DIDF operation far exceed the already analytically challenging physical and chemical processes occurring in conventional CI engines. The chemistry and physical properties of the charge are subject to significant change during the compression process, subsequently the environment to which the direct injection is exposed is affected, which has implications on the pilot injection processes [14]. At the same time, changes in the pilot combustion processes have significant influence over the combustion of the premixed charge [*e.g.* 6–13]. The highly intertwined physics of the DIDF combustion processes necessitate the application of a broad set of experimental and numerical approaches to increase the conceptual and practical understanding of these systems, and ultimately to increase the commercial adoption of these technologies.

The inducted mixture properties, engine design and operating conditions and the pilot-injection parameters are all understood to variously affect the operational qualities of DIDF combustion. Important mixture properties include the inducted charge equivalence ratio, exhaust gas recirculation (EGR) concentration, and cylinder temperature and pressure; important engine parameters are expected to be speed, transient loadings, and cylinder/piston design; and the important pilot-injection parameters are injection pressure, timing, mass, and the sequence of injection events in each cycle.

The predominantly accepted conceptual understanding of DIDF combustion was originally proposed by [23], and has been regularly referenced by many other experimental and numerical investigations. The principle features of the model are a description of three generic and

overlapping heat release mechanisms, which are purported to be present in all cases of DIDF operation:

i. Rapid combustion of the premixed pilot fuel.
ii. Combustion of the gaseous fuel in the immediate vicinity of the ignition and combustion centers of the pilot.
iii. Pre-ignition reactivity and subsequent combustion via turbulent flame propagation in the premixed fuel.

A schematic representation of the heat release rate from each of the three mechanisms is presented in Figure 1.

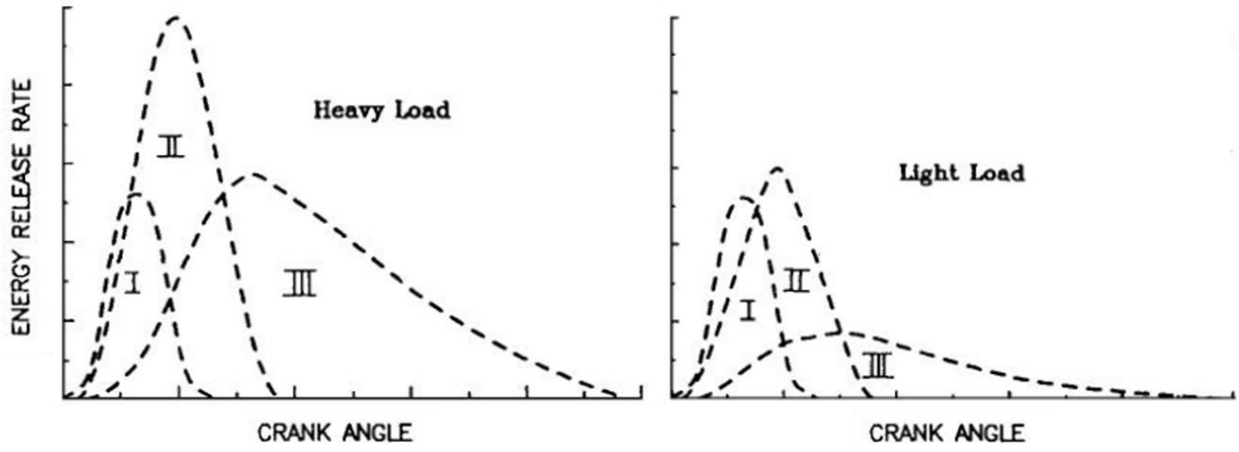

Figure 1: Three conceptual heat release mechanisms of DIDF combustion at heavy-load (left) and light-load (right). Adapted from [23] **with permission of SAE.**

Theoretically, superposition of the heat release from each of the three identified mechanisms would produce the overall DIDF heat release, which could be measured experimentally. The interactions between each of the proposed heat release mechanisms are too complex to fully

decouple and analyze individually, however they do provide a useful context for discussion of the physical mechanisms occurring throughout the DIDF process. A similar conceptual description of DIDF combustion is presented in [24] where the stages of combustion are considered to be:

i. Pilot ignition delay
ii. Pilot premixed combustion
iii. Primary fuel (NG) ignition delay
iv. Rapid combustion of primary fuel
v. Diffusion combustion stage

In both models, the diesel combustion is assumed to occur by a fully premixed mechanism and the primary CH_4 combustion mechanism is proposed to be turbulent flame propagation, although a lean limit to this mechanism is acknowledged by the author in [23]. The transition from diesel pilot combustion to premixed NG combustion is described in varying terms; the combustion of entrained CH_4 is proposed as an intermediate step by [23], while an ignition delay due to the higher auto-ignition temperature of CH_4 is cited by [24]. Finally, a late stage low-intensity 'diffusion combustion stage' is proposed in [24] where the effect of combustion diluents and an expanding cylinder volume cause combustion reactions rates to decrease.

The ignition delay of the diesel pilot is often described by Arrhenius formulations featuring an inverse exponential dependence on temperature, making the temperature of the cylinder gasses into which the pilot is injected a defining parameter for the pilot ignition process. Admission of NG with the fresh charge produces a charge-cooling effect due to the higher specific heat

capacity of NG compared to air, resulting in an increase in the pilot ignition delay period. However, even with relatively stable pure CH_4 as the premixed fuel, rising temperatures and pressures during the compression stroke increasingly cause pre-ignition reactions to take place as the piston approaches top dead centre (TDC [14]. The pre-ignition chemistry produces some heat in addition to partial oxidation products such as aldehydes, radicals and CO. Depending on the intake temperature and equivalence ratio of the premixed charge, the heat release from the pre-ignition reactions may or may not compensate for the charge cooling effect. With respect to the ignition delay of the diesel pilot, competition for certain pre-ignition radicals, such as formaldehyde, by the NG and diesel may also extend the ignition delay [25]. In addition to affecting the ignition delay of the diesel pilot, pre-ignition reactivity contributes to the combustion of the NG in the vicinity of the pilot ignition sites, and indirectly to combustion in the remaining cylinder volume [11].

Slightly before TDC, a liquid diesel jet is issued into the cylinder as in conventional diesel operation, however typically at a much lower pressures than modern common rail systems operate at. The liquid diesel jet rapidly evaporates and entrains the surrounding NG-air mixture. After the pilot ignition delay, spontaneous auto-ignition of the diesel occurs. As a result of the pilot-injection, a reactivity gradient exists in the cylinder prior to combustion; the location of the first auto-ignition sites is dependent on the local equivalence ratio and preparation of the diesel. Preparation of the diesel is often considered in terms of a residence time of an individual fuel packet, where increasing residence time permits greater heat transfer, vaporization and mixing of the fuel packet with oxidizer [*e.g.* 9]. Shortly after the first combustion kernels form, rapid premixed combustion of the diesel pilot mass and a fraction of the NG entrained by the pilot jet

is considered to occur. These processes fall within the domain of mechanisms 1 and 2 in the description provided by [23].

Entrainment and pilot fuel preparation processes are complex and strongly dependent on pilot injection parameters such as pressure, timing, and mass in addition to the physical injector design. The authors of [26] described the pilot zone as a conical reaction zone concentric to the fuel jet. This reaction zone is calculated based on the well-known spray combustion model based on conservation principles, which was proposed for conventional diesel operation by [27], and is discussed in further detail in section 2.2.1.

Following the rapid premixed combustion of the pilot fuel and entrained NG, a significantly higher cylinder temperature and pressure exists in addition to the creation of a radical pool in the immediate vicinity of the premixed reaction zone. As is commonly done in SI combustion modelling, several thermodynamic zones are now considered: the hot burned gases, the cooler unburned gases, and the current reaction zone (flame front), the mass of which is often neglected based on assumption of negligible thickness. The remainder of the combustion process is widely considered to be turbulent flame propagation throughout the remaining premixed CH_4-air mixture, provided the premixed NG concentration exceeds the practical lean flammability limit for the particular conditions.

It is important to note that, unlike SI operation, the flame propagation mechanism in DIDF combustion proceeds from a distributed reaction zone defined by the pilot combustion processes. In [28], visualization of the hydroxyl radical, OH, indicated that flame propagation commences

in the periphery of the piston bowl and proceeds centripetally regardless of CH_4 equivalence ratio, φ_{CH4}. Below critical φ_{CH4}, turbulent flame propagation is not possible and significant portions of CH_4 are not oxidized [29]. The turbulent flame propagation process occurs during the expansion stroke where dropping charge temperatures cause the turbulent flame speed to drop and give way to slower reaction rates (described as 'diffusion combustion' by [24]), where it is expected that partial oxidation reactions occur.

2.2 Background Theory & Modelling of Conventional Combustion Phenomena

The conceptual understanding of DIDF combustion is substantially based on knowledge and experience gained from previous investigations of conventional combustion modes in CI and SI applications. In the simplest terms, DIDF combustion can be considered as diesel spray combustion followed by flame propagation through premixed NG; the theory and modelling of these individual processes are mature fields of science which have been drawn upon and applied by several DIDF investigations. This section aims to lend context to discussions of DIDF phenomena by presenting an introduction to the basic theory and common modelling practices for diesel spray combustion and turbulent flame propagation.

2.2.1 Diesel Spray Combustion Theory & Modelling

It is recognized that the physics involving the pilot injection and combustion are of critical importance to the phenomena in DIDF combustion. Many theoretical and practical investigations have been performed to improve the understanding of direct-injection spray combustion processes as they pertain to conventional diesel operation. Much of the knowledge gained from the diesel investigations is of use in the context of DIDF combustion. For the purposes of this

work, diesel jet combustion descriptions are considered to fall into one of two broad categories: i) conventional, quasi-steady state descriptions where fuel injection and combustion overlap temporally, and ii) transient or 'puff' jets, where the end of injection occurs well in advance of the start of combustion.

A thorough and widely accepted conceptual description of the development and features of reacting diesel jets based on optical and thermodynamic measurements is given by [30]. This model considers the spatial and temporal formation of mixing-controlled combustion of a diesel fuel jet in the absence of wall interactions, and is presented in Figure 2.

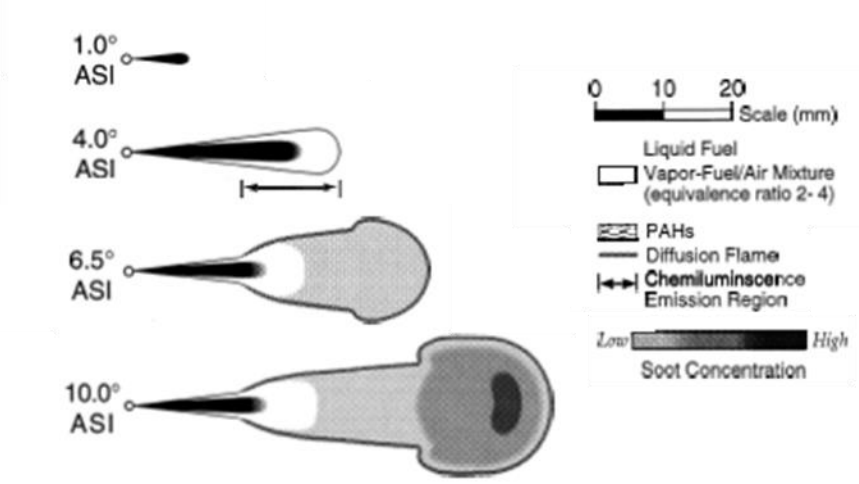

Figure 2: Conceptual description of transient diesel spray combustion adapted from [30] **with permission of SAE.**

Although it does not present mathematical expressions for specific mixture-formation and combustion phenomena, this model does provide a platform for the application of theoretical and empirical models to individual phenomena of significance to combustion performance such as liquid penetration length, ignition delay, onset of the diffusion flame, and the qualitative

distribution of fuel throughout the injection process. Figure 2 also illustrates the differences in mixture stratification that are achieved spatially and temporally with the development of a diesel spray. The authors acknowledged certain important limitations including the lack of a description of the 'burn-out' phase of combustion occurring from the end of injection to the end of combustion, no consideration of specific operating parameters such as cylinder temperature and pressure, injection parameters, or fuel properties, and also no consideration of wall- or swirl-interactions.

For the purposes of combustion modelling, simplified physics that focus on important features are often considered. The Cummins model [31] was developed before the publication of the modern model of diesel spray combustion by [30] and was based on undisturbed turbulent gas jet theory given by [32]. This model assumes the diesel jet to be uniquely composed of diesel vapour (no liquid phase) which is represented by a continuous profile of fuel vapour concentration from the rich jet core to the far-field concentration of pure air. Estimation of heat release rate (HRR) is based on calculated entrainment rate of fresh air into the jet zones where $\varphi_{\text{lean flam. limit}} < \varphi_{\text{local}} < \varphi_{\text{rich flam. limit}}$. Throughout diesel combustion literature, the entrainment mechanisms mixing oxidizer with the fuel jet are of crucial importance for combustion and emissions performance.

Another popular modelling approach for diesel spray combustion is the 'packet model', first proposed by [27], and later extended by other authors. In this approach, individual packets of liquid fuel are tracked in time and space starting from the start of injection. Based on radial location (relative to fuel jet axis), axial location, residence time, and jet parameters, the

composition of each packet is considered to be the summation of the following components; i) liquid fuel, ii) vaporized fuel, iii) air, iv) combustion products. The packet model and its extensions are some of the most popular models for diesel combustion modeling and have shown excellent ability to replicate HRR trends including the premixed and diffusion flame zones in addition to emission formation trends across many applications once specific tuning parameters are determined.

Based on the spray studies of [33] it was found that for small pre-injections, the base packet model of [27] did not adequately describe the increased air-fuel mixing rates of very short injections characteristic of diesel pre-injections (and accordingly small pilot injections in DIDF combustion). A 'time-scale' approach with special consideration for the assumed fully premixed combustion of the pilot injection is presented in [34]. The authors describe the initiation of flame propagation through the premixed diesel vapour, originating at multiple ignition sites in the premixed fuel envelop. The premixed diesel envelop is assumed to be a spherical region having a uniform fuel concentration, empirically chosen to be φ_{diesel}=1.25, and which grows based on turbulent mixing mechanisms. The addition of this pre-injection sub-model to an existing long-duration injection model allowed the authors to predict HRR and emissions of NO with a high degree of fidelity.

Although the conceptual description of a diesel pre-injection intuitively matches the pilot-injection of DIDF operation, the assumption of a fully premixed diesel combustion mode is not commonly made. In [26], a semi-empirical two-zone model originally described by [35] is applied to describe the premixed and subsequent diffusion combustion modes of the pilot fuel in

a DIDF application. The investigators applied the well-known Hiroyasu model [27] to predict the pilot jet growth and consequentially the entrainment of CH_4 into the pilot jet. The model predicted both absolute values and trends of the HRR of corresponding DIDF and diesel-only combustion measured in a single-cylinder engine with reasonable accuracy as concluded by the authors.

2.2.2 Turbulent Flame Propagation Theory & Modelling

The second primary combustion mode identified in DIDF combustion is turbulent flame propagation through premixed CH_4. A brief overview of turbulent flame propagation theory is given here to lend context to discussion later in this work.

A common assumption in studies of flame propagation in turbulent, premixed combustion, is that the flame front is wrinkled due to interactions with the eddies in the turbulent field, but can be considered laminar when observed on smaller, local scales [36]. This assumption is commonly known as the flamelet assumption and is often applied in SI combustion modelling. This flamelet assumption is valid for regions where the turbulence length scales are much larger than the chemical length scales (*i.e.* the flame front thickness). The Damköhler number, D_a, is defined as the ratio of macroscopic turbulent time scale to chemical time scale, where $D_a > 1$ indicates that the chemistry occurs faster than the turbulent mixing, which is necessary for the flamelet assumption. That is to say that the laminar flame front is stretched by the turbulent eddies, but is not torn into distributed reaction zones. In this scenario, the overall combustion rate is subject to the mixture turbulence properties [37]. A common method to practically apply the flamelet

assumption to internal combustion modelling is through the statement given by equation (1) where the flame reaction zone is treated as a static frame of reference.

$$\dot{m}_r = \rho_u A_t s_t \quad \textbf{(1)}$$

Where $\dot{m}_r$ is the mass flow rate of reactants into the reaction zone. ρ_u is the unburned gas temperature, A_t is the effective area of the wrinkled flame front, and s_t is the turbulent flame speed. Many different calculations and correlations of s_t have been proposed, but generally the statement given by equation (2) can be made.

$$s_t = f(s_l, u') \quad \textbf{(2)}$$

Where s_l is the laminar flame speed of the premixed fuel, and u' is a measure of the turbulence intensity in the flow (often the fluctuating component of the velocity field, u', is used). For a flame to propagate, radicals and energy must be transported ahead of the flame front to the pre-reaction zone; this process is a function of temperature, pressure and the chemical properties of the premixed fuel, as indicated by equation (3).

$$s_l = f(\varphi, T_u, P) \quad \textbf{(3)}$$

Where φ is the equivalence ratio of the fuel-oxidizer mixture, T_u is the unburned gas temperature, and P is the reaction pressure. In a laminar flame, the mass and energy transport rely on diffusion, while in a turbulent flame, advection of properties is predominant. The enhancing effect of turbulence on flame speed is evident when considering the general form of correlations relating s_t and s_l, given by equation (4) [37].It can be seen, therefore $s_t > s_l$.

$$\frac{s_t}{s_l} = 1 + C \cdot \frac{u'}{s_l} \quad \textbf{(4)}$$

Because of the increased flame temperatures, the peak s_l for a given fuel is achieved with near stoichiometric fuel-oxidizer mixtures. Many fundamental laboratory studies of laminar flame speeds have been performed to characterize common fuels, including CH_4. Important properties of interest include the lean and rich flammability limits of specific fuels which are theoretically predictable chemical properties of the fuel-oxidizer mixture. In practice, flammability limits are subject to reactor properties such as turbulence and heat loss, and are therefore are difficult to predict with certainty in complex systems such as ICEs. In the context of DIDF combustion, understanding the lean flammability limit is of crucial importance to engine efficiency and HC emissions.

Discussion and analysis of the premixed combustion in an ICE based on the flamelet assumption is valid for $D_a>1$ [37]. As the chemical time scales increase due to dropping temperatures or low fuel concentrations, the flamelet assumption breaks down. With increasing chemical time scales, the flame front will transition to a distributed reaction zone and eventually a well-stirred reactor where the turbulence time scales are shorter than the chemical time scales. If $D_a<1$ the flamelet assumption is no longer valid and the chemical reaction timescales will dictate overall reaction rates.

2.3 Experimental Investigations of DIDF Combustion

Because of the complex physics involved in DIDF combustion, experimental investigations are a valuable approach to advance this technology. The core tool of these investigations is the research engine facility, which is a highly instrumented ICE, which can be operated with a wide array of control parameters such that specific operating conditions can be explored as desired. In DIDF research, investigations often focus on either the operating mode phenomena, such as premixed mixture preparation properties, or on the pilot injection phenomena, such as novel injection strategies. In addition to conventional engine experiments, a suite of optical investigation techniques exist, which can provide increased information about the combustion processes than conventional, or thermodynamic measurement techniques.

2.3.1 Impact of Operating Mode on DIDF Combustion

Through the conceptual consideration of DIDF combustion, it is evident that chemical kinetics play a significant role in both the pilot combustion processes and the conversion of CH_4 following the pilot combustion. Common mixture parameters of interest include: φ_{CH4}, charge temperature, and EGR concentration. The effect of these mixture properties on overall combustion and emissions performance of DIDF engines is an active field of research addressing emissions reductions and increasing the operating range of DIDF engines.

CH_4 Equivalence Ratio

The only engine calibration parameter with direct control of the premixed CH_4 combustion mechanism is φ_{CH4}, making it one of the most important parameters for DIDF combustion. Furthermore, both the high- and low-load limitations of DIDF combustion (knock and

incomplete CH_4 combustion, respectively) are directly influenced by the CH_4 mixture conditions following the pilot combustion. Accordingly, many investigations have been directed at understanding the effects of φ_{CH4} on DIDF combustion. There has also been some investigation of intentional stratification of the premixed CH_4 in order to manipulate CH_4 heat release rates through a reactivity gradient [38].

Primarily concerned with the light-load emissions of HC and CO, [29] considered the effect of φ_{CH4} on the turbulent flame speed and lower flammability limit for the premixed mixture of a DIDF engine. Based on the measured emissions of CO and CH_4 in a naturally-aspirated single-cylinder engine, three φ_{CH4} thresholds were observed, and are presented in Figure 3.

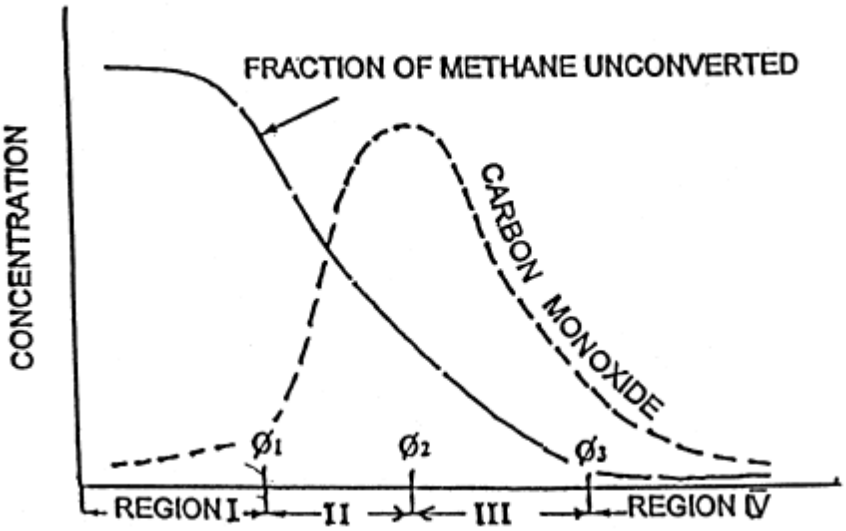

Figure 3: Schematic variations of the unconverted CH_4 and CO concentrations in the exhaust emissions with total equivalence ratio. Reprinted from [29] **with permission of Elsevier.**

Engine operation leaner than the first threshold, φ_1, was characterized by high emissions of CH_4 and low emissions of CO. Operation between the φ_1 and φ_2, was characterized by a decrease in

CH_4 and an increase in CO emissions. Operation between φ_2 and φ_3 was characterized by decreasing CH_4 and CO. φ_{CH4} richer than the 3rd limit, produced constant CH_4 emissions. The proposed explanation for these operating limits was given as follows (in order of ascending CH_4 concentration):

i. Lower limit of significant partial oxidation.
ii. Lower limit for flame initiation. Observed to occur at $\varphi_{CH4}\approx0.45$ for the investigated conditions.
iii. Lower limit for flame propagation. Observed to occur at $\varphi_{CH4}\approx0.7$ for the investigated conditions.

In [28], the overall cylinder equivalence ratio considering both fuels, φ_{global} was varied from 0.05 (diesel only)—0.94 with a constant pilot mass in a single-cylinder light duty research engine. Through qualitative analysis of the HRR shape, a transition was observed around $\varphi_{CH4}\approx0.6$; operation with richer mixtures exhibited a 'bell-shape' similar to SI operation, which the authors interpreted as flame propagation, while leaner mixtures exhibited an extended tail and were deemed to be below the effective flame propagation limit. It was also noted that while the trailing edge of HRR varied significantly across the range of tested φ_{CH4}, the slope of the leading edge remained relatively unchanged, consistent with the conceptual description of the first stage of DIDF combustion being dominated by the pilot combustion proposed by [23].

A complex relationship between φ_{CH4} and the ignition delay was observed in [14], arising from several competing mechanisms (with increasing CH_4 admission): reduction of O_2 partial pressure, increasing heat release due to pre-ignition reactions, competition for pre-ignition

radicals and increasing specific heat ratio. With increasing φ_{CH4}, increasing ignition delays were observed up to a maximum at $\varphi_{CH4}\approx0.4$. Richer than $\varphi_{CH4}\approx0.4$, the ignition delay decreased to a minimum value at $\varphi_{CH4}\approx0.8$, before increasing monotonically for all $\varphi_{CH4}>0.8$. Increased ignition delays retard the overall combustion phasing and enable increased premixing of the diesel pilot with air and CH_4.

Exhaust Gas Recirculation

Application of EGR in diesel engines is a common practice to reduce emissions of NO_x, and to reduce pumping losses in SI engines. For the same reasons, EGR is an important parameter for DIDF engines. Practically, many components in the base CI engines from which DIDF engines are typically modified, are not rated for the exhaust temperatures associated with the near stoichiometric combustion achieved with DIDF strategies [39]. Application of un-cooled EGR has been suggested as a method to improve lean DIDF performance by virtue of increased charge temperatures [40]. Application of EGR has also been predicted as a method to reduce emissions of HC by recirculating emissions of unburned species into the combustion chamber for multiple cycles [41].

For EGR mass fractions up to 5% [40] noted a slight increase in thermal efficiency attributed to the thermal enhancement of turbulent flame propagation, while larger EGR mass fractions decreased the thermal efficiency across a range of operating speeds in an indirect injection, pre-chamber engine. In a single-cylinder heavy duty engine, [39] observed a 75% reduction of NO_x emissions with application of 20% EGR, with only a minor increase in hydrocarbon emissions.

Further increase of the EGR rate to 40% resulted in significant combustion instability and necessitated an increase of pilot injection mass.

Intake Temperature

Although not typically a direct control parameter in existing CI engines, the intake temperature plays significant roles in DIDF combustion. Increasing intake temperatures are evidently linked to increased NO_x emissions. In [39], an increase of intake temperature from 30—60°C extended the lean operating limit for acceptable emissions from φ=0.55 to φ=0.42. The authors attributed the reduced emissions to enhancing conditions for flame propagation, in addition to a bulk-ignition of fresh charge in the crevice volume, which was indicated by a late stage peak in the AHRR. The increase of intake temperature increased the knocking tendency of the engine and accordingly reduced the peak load achievable.

In a turbocharged DIDF engine, where 60% of the energy was supplied from premixed CNG, the authors of [42] noted reduced ignition delays, advancing combustion and higher peak cylinder pressures when increasing the post-intercooler temperature from 59°C—86°C. In addition to the expected increase in NO_x emissions, increasing intake temperature also increased emissions of PM, which the authors attributed to the decreased ignition delays; with less time to mix before combustion, larger fuel-rich zones were exposed to high-temperatures, conditions which are known to be PM precursors.

2.3.2 Impact of Pilot-Injection

The significant advantage of DIDF strategies over other dual-fuel concepts such as RCCI combustion is the enhanced engine control afforded by the application of the diesel pilot. Because modern common rail direct-injection systems are used for the pilot injection, all the same control and calibration parameters exist for the control of the DIDF pilot: pilot injection mass (m_{pilot}), pilot injection timing (θ_{pilot}), pilot injection pressure (P_{pilot}), and split injection strategies such as pre- and post-injections. There is a vast collective knowledge base surrounding diesel spray combustion, which is useful for explaining the physics of DIDF pilot injections (briefly discussed in § 2.2.1), however the complex interactions between the diesel and NG combustion necessitate dedicated discussion.

Pilot Injection Mass

Many of the investigations examined in the previous section acknowledged the limitation of exploring mixture effects for one single pilot injection mass, or performed their experiments for a range of pilot injection masses to reinforce their findings; highlighting the recognized importance of this parameter. The conceptual description of DIDF combustion proposed by [23] notes the expected increase in influence of the pilot combustion event on overall engine performance as engine loads are reduced. The characteristics of the pilot combustion event have a strong influence on emissions of various species (*i.e.* CO, NO_x, HC, PM), combustion stability and harshness, and efficiency. It is an over-arching goal in DIDF research to minimize the amount of diesel required to maintain satisfactory engine control and emissions since many of the advantages of DIDF combustion relate to the substitution of NG in place of diesel.

For many instances of DIDF operation, the major trend with increasing diesel pilot mass is a reduction of HC emissions at the expense of increased NO_x and PM emissions depending on the particular operating mode. For sufficiently small diesel injections below a critical mass, there is no dependence of PM emissions on pilot mass, this critical injection mass was found to be a function of engine load and speed by the authors of [16]. It was suggested that this critical pilot mass was related to the threshold of where the diesel mixture became completely homogeneous at the time of pilot combustion as in RCCI operation, and therefore PM would not form. Above the critical pilot mass, increased PM emissions with increasing pilot diesel mass were attributed to increased formation of locally fuel-rich zones in the cylinder.

In the same investigation, an optimum m_{pilot} for reduced NO_x emissions was observed for a given engine load and speed. For high m_{pilot}, an apparent diesel diffusion combustion mode was interpreted to promote NO_x formation, while at very low m_{pilot} the increasing NO_x was observed and attributed to higher combustion temperatures in the conversion of the CH_4 which was enriched to maintain engine load. In most cases, the optimum pilot mass for NO_x emissions was found to be similar to the threshold mass observed for soot formation. In other studies, it has been observed that the smallest amount of diesel will always result in lower emissions of NO_x as the volume of the high temperature reaction zone due to the pilot combustion scales with m_{pilot} [23].

For operation leaner than $\varphi_{global} \approx 0.6$, increasing m_{pilot} was observed to reduce emissions of CH_4 in [23]. In [29], a similar limit was observed, and was attributed to the enhancement of the turbulent flame propagation mechanism in the premixed CH_4. Below the flame propagation limit,

it is understood that increasing m_{pilot} entrains increasing amounts of CH_4, which may then be converted in the pilot combustion event. In [43], peak cylinder pressure and HRR was observed to increase with increasing pilot mass, however this effect was observed with simultaneously decreasing φ_{CH4} in order to maintain engine load, which affected ignition delays.

Pilot Injection Pressure

As in conventional diesel operation, the direct injection pressure plays a significant role on combustion performance through its complex influences on the diesel mixture preparation. In [18], bio-diesel and diesel pilot performance was compared in a DIDF engine. Increasing P_{pilot}, for a constant θ_{pilot} was observed to have a number of significant effects on overall engine performance for both pilot fuels:

- Increasing indicated mean effective pressure (IMEP).
- Increasing peak cylinder pressure.
- Decreasing coefficient of variance (COV) of IMEP to a minimum value for P_{pilot} > 60MPa.
- Decreasing ignition delay.
- Increasing NO_x emissions.
- Decreasing PM and CH_4 emissions.

Much of the noted effects can be attributed to the enhanced mixing of the diesel pilot fuel, leading to higher premixed fractions and more rapid pilot combustion. Additionally, improvements to the CH_4 emissions can be attributed to increased entrainment of CH_4 by the pilot jet. The authors of [17] observed similar trends in combustion performance with P_{pilot} for

standard (near TDC) timings in a high compression ratio (17.8:1) medium-duty single-cylinder engine, however as θ_{pilot} was advanced to 20°CA bTDC and beyond, trends with P_{pilot} were inconsistent with the observed trends at later timings.

Pilot Timing

As in conventional diesel operation, the timing of the pilot injection, θ_{pilot}, has been shown to play a significant role in DIDF combustion performance. Often an optimal timing for a given operating point exists as a compromise of thermal efficiency, $\eta_{thermal}$, and emissions. In [18], the effect of θ_{pilot} from 35—0°CA before TDC (bTDC) across 3 values of m_{pilot} was explored. Emissions of CO and HC exhibited similar trends to one another; lowest emissions occurring for $\theta_{pilot} \approx$15—10°CA bTDC, and increasing trends for later and earlier timings. The inverse trend was observed for NO_x emissions (peak emissions at $\theta_{pilot} \approx$15°CA bTDC), with larger m_{pilot} cases tending to have peak NO_x emissions at earlier timings. θ_{pilot} =20—5° CA bTDC produced peak $\eta_{thermal}$.

With increasingly advanced θ_{pilot}, an increase in the 2nd peak of HRR was observed in [18], which was interpreted as increasing turbulent flame speed. The authors concluded that the apparent increase in turbulent flame speed for early θ_{pilot}, was due to the increased effective φ resulting from enhanced mixing of diesel vapour with the premixed CH_4, given the longer ignition delays at early injection timings.

2.3.3 Optical Investigations of Dual-Fuel Combustion

Optically-accessible engines and rapid compression/expansion machines (RCEM) are able to add valuable spatial information to the traditional DIDF analyses performed on the basis of calculated AHRR and engine-out emissions. Significant modifications to the combustion environment (quartz/sapphire piston crown, modified piston rings / top-land height, *etc*.) and engine operating mode (skip-firing, synthetic EGR, low-load) are necessarily made such that optical data can be recorded, a thorough overview of these considerations is given by [44]. It is necessary to interpret optical engine and RCEM data with the caveat of the fundamental differences between these combustion environments and that of a conventional engine considered. Despite the necessary modifications to the combustion chamber, the data collected in these investigations has deepened the understanding of DIDF phenomena, and is valuable for the validation of computational and numerical models.

In [28], the authors were concerned with understanding whether DIDF combustion was characterized by auto-ignition, sequential auto-ignition, flame propagation, diffusion or a combination of these combustion modes. Through measurement of visible light, OH*-chemiluminescence, and OH-Planar Laser Induced Fluorescence (OH-PLIF), a number of DIDF combustion mechanisms were explored in an optically-accessible 0.5L single-cylinder DIDF engine. Visible and OH*-chemiluminescent emissions revealed that for φ_{global}=0.33—0.94 (with a constant m_{pilot}), ignition occurred in the periphery of the piston bowl. The OH* signal was interpreted as an indicator of high temperature reactions characteristic of the reaction zones in a flame front. Following ignition, increasing OH* signal was observed to progress radially-inward, which was interpreted as the flame front propagation. For φ_{global}=0.94, the reaction zones

indicated by the OH* signal propagated from the bowl wall to the centre of the bowl; peak signal intensity was observed uniformly across the bowl. With φ_{global}=0.56, the OH* signal began at the bowl periphery, but did not propagate completely to the bowl centre, where a significant region indicated zero signal intensity. The qualitative differences in combustion progress for the high- and low-φ cases can be observed in Figure 4.

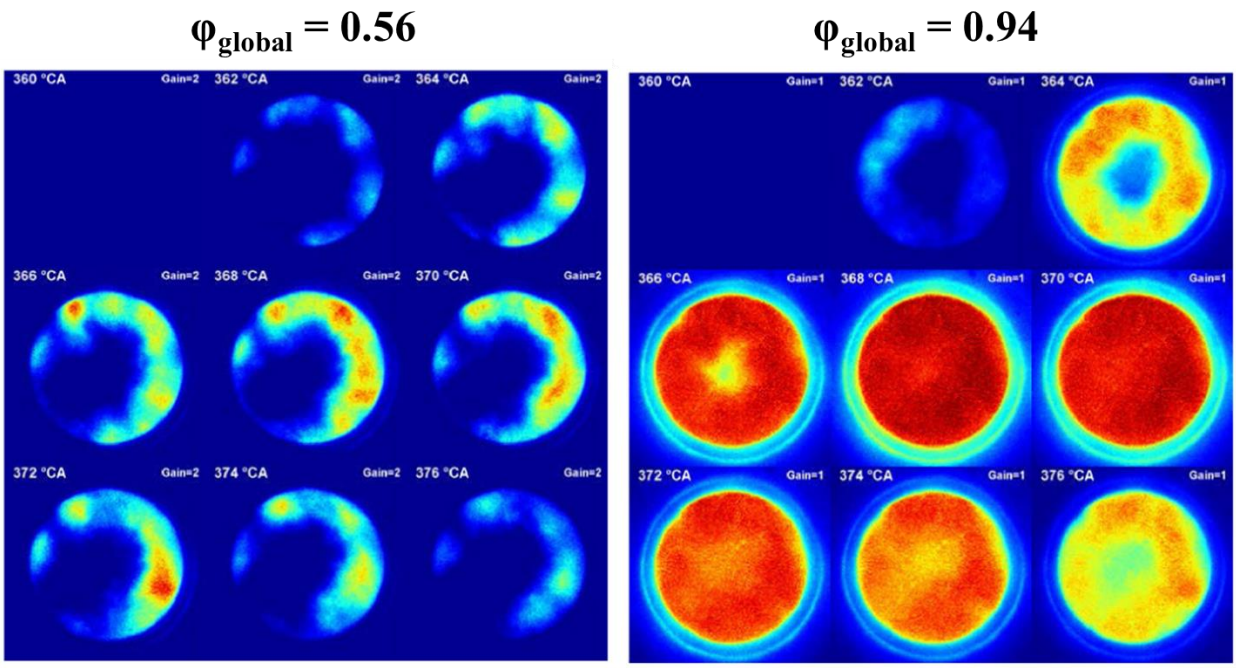

Figure 4: OH*-chemiluminescence image sequences for low-load (left) and high-load (right) DIDF operation with constant pilot mass. Adapted from [28] **with permission of SAE.**

In the low φ_{global} case, it was concluded that a significant proportion of the emissions of HC were a result of the reaction zone being unable to propagate from the ignition sites through the lean mixture. This conclusion supported observed apparent HRR (AHRR) trends discussed in §2.3.1. With the application of a higher-reactivity premixed fuel (iso-octane), a bulk-ignition of the

premixed fuel was observed for high φ_{global}, indicating that the flame propagation or quenching mechanisms are among a larger set of possible combustion mechanisms.

In [45], the distribution of fuel reactivity (as indicated by φ) in a heavy-duty RCCI engine fueled with premixed iso-octane and pilot injections of n-heptane at different timings was explored using OH*-chemiluminescence of the entire piston bowl region and fuel tracer fluorescence on one of the n-heptane jets. The latest pilot injection timing presented was at -15°CA aTDC, which made the observed phenomena similar to DIDF operation where the pilot injections are typically in the range of -20—0°CA aTDC. At -5°CA aTDC, a peak of φ=2 was measured in the centre of the head of pilot jet near the bowl wall, where ignition sites were observed to occur, consistent with [28]. In imaging of natural luminosity, the highest intensities measured were coincident with the richest regions measured in the pilot jet; it was concluded that significant PM production in the rich jet core produced an incandescing signal in these regions.

The authors of [46] investigated the effect of φ_{CH4}=0—0.65 and the number of pilot jets (3 or 6) on the auto-ignition and combustion behaviour in a RCEM through measurement of OH*- and CH*-chemiluminescence. In all cases, P_{pilot}= 400bar, and pilot timing was held constant at 4.1ms before TDC. In high and low φ_{CH4} cases, the reaction zones identified by OH* signal were highly stratified with peak intensities along the pilot jet axes as shown in Figure 5.

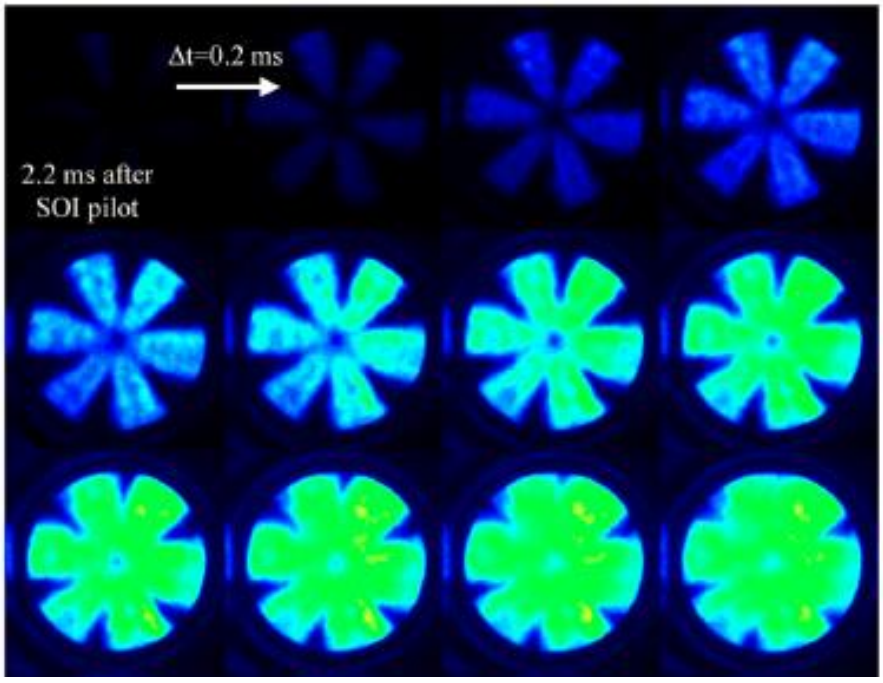

Figure 5: OH*-chemiluminescence of DIDF combustion in a RCEM. Adapted from [46] **with permission from SAE.**

Unlike the observations of [28] and [45], the flame propagation combustion mode appears to initiate uniformly around a conical zone concentric with the pilot jets, which is conceptually similar to the model proposed in [26,47]. In accordance with other investigations [28], operation with low φ_{CH4} resulted in significant regions of the cylinder to not be reached by the reaction zone. In this investigation, the last regions in the cylinder to undergo combustion are located in the interstitial spaces of the fuel jet structures; in [28] a single central-bowl region was identified as the last region for combustion to occur (if thorough flame propagation was possible). The cause for the differences between the two flame propagation modes is unclear as both investigations used the same injection pressure and similar injected masses.

2.4 Summary & Literature Gap

It is currently understood that in DIDF combustion, auto-ignition of premixed diesel vapour with entrained CH_4 initiates flame propagation through the remainder of the premixed charge, provided the premixed charge equivalence ratio, φ_{CH4}, exceeds the lean flammability limit for the particular cylinder conditions. Decreasing φ_{CH4} below the lean flammability limit results in unacceptable emissions of CH_4, which is the primary factor limiting low-load operation of DIDF engines. High emissions of CH_4 may be addressed through enhancement of the flame propagation (*i.e.* by increasing equivalence ratio, temperature, or charge turbulence) or by modification of pilot injections settings, such as increasing the pilot injection pressure or mass; these parameters also tend to increase emissions of NOx and/or PM under certain conditions. It is desirable to employ a minimum mass of diesel per cycle to maximize the benefits gained from substitution of diesel by NG, and for a given load and speed an optimal diesel mass which minimizes PM and NO_x emissions exists. Unlike in conventional SI operation, flame propagation commences from distributed reaction sites, which has been observed to follow the perimeter of the piston bowl or the shape of the pilot jet structure and progress towards fuel-leaner regions of the cylinder.

Experimental investigation of DIDF operating conditions and pilot injection strategies have built a strong understanding of the influence of many engine operating parameters on combustion and emissions performance. The scope of these investigations is typically limited to the individual consideration of a few related parameters within specific operating mode ranges, while all other conditions are kept constant; the vast number of engine control parameters for DIDF combustion makes full factorial experiment campaigns intractable. Increased consideration of where the

boundaries of experimentally observed combustion phenomena are valid requires investigation of a wide range of DIDF operating modes and pilot injection parameters simultaneously. The boundaries defining where conceptual descriptions and detailed models of DIDF combustion are valid also need to be studied further. Interpretation of emissions and pressure data alone has not been enough to unambiguously define the combustion mechanisms present in DIDF combustion; the increased application of optical techniques to conventional measurements is necessary. The next chapter will discuss the design and operation of the experimental facility commissioned in this work to address the gaps in experimental and conceptual understanding of DIDF combustion.

Chapter 3: Experimental Facility

The purpose of this chapter is to provide the reader a clear description of the experimental facility employed in this investigation, so that both the measurement capabilities and limitations are evident. Dimensions and specifications are provided as necessary for the interpretation of the results discussed later in this document.

3.1 Facility Overview

The experimental facility employed in this work is focused around a single-cylinder research engine developed from a standard Ricardo 'Proteus'. The term 'facility' refers to both the engine systems in the engine test-cell and the control systems and measurement equipment located in the adjacent operator's control room. The key feature of the facility is the ability to configure the engine to operate in one of two configurations:

i) Thermodynamic Configuration: All metal components are used as in a conventional ICE application.

ii) Optical Configuration: An engine block extension and Bowditch piston arrangement providing optical access to the piston bowl during engine operation are fitted to the thermodynamic engine block.

This work constitutes the first major research investigation performed using this facility; several people made significant contributions to the construction and commissioning of the facility over 2.5 years. Engine commissioning was primarily focused on the installation of modern fueling

and data acquisition systems, and baseline performance testing of the facility to permit investigations of advanced NG-based CI engine combustion strategies. The following sections present the facility in its state for the measurements reported in this work. Development and enhancement of the facility is on-going, and it is expected that the facility will be used for a wide range of applications in the future.

3.2 Single-Cylinder Research Engine

The Ricardo 'Proteus' design is based upon the Volvo TD120-family of engines: turbocharged, 12-litre, in-inline 6-cylinder heavy-duty CI engines first produced by Volvo for on-highway applications beginning in 1970, and later used in different configurations for off-highway and marine applications. The Ricardo Proteus is composed of a single head, cylinder, piston, and valve train assembly from the stock Volvo engine. Ricardo supplied a custom designed and fabricated engine block, unit-injection fuel system, and drivetrain to produce a 2-litre, single-cylinder research engine platform. Also designed by Ricardo are the optical engine configuration components, which are detailed in §3.3. Major specifications for the engine in thermodynamic configuration are presented in Table 2.

Table 2: Major specifications of single-cylinder engine in thermodynamic configuration

Configuration	4-stroke, compression ignition
Displaced volume	1998 cc
Stroke	152 mm
Bore	130 mm
Connecting rod length	275 mm
Compression ratio	14.25:1
Number of valves	2
Bowl shape	Eccentric torroid
Exhaust valve open	145° aTDC @ 1.0 mm lift
Exhaust valve close	-330° aTDC @ 1.0 mm lift
Inlet valve open	-390° aTDC @ 0.6 mm lift
Inlet valve close	-150° aTDC @ 0.6 mm lift
Maximum speed	2100 rpm
Maximum cylinder pressure	170 bar
Direct injector included angle	142°
Direct injector nozzle orifices	5 x 0.205mm diameter
Direct injector angle relative to firedeck	70°
Min/max fuel spray angle relative to firedeck	-1° / 39°

Through this work, the following systems were added to the baseline engine:

i. Instrumented intake & exhaust systems.

ii. Modern common-rail diesel direct-injection fuel system.

iii. Custom port-injection system.

iv. Integrated engine control and data acquisition (DAQ) systems.

v. Thermal regulation system (coolant temperature heating/cooling).

vi. Safety monitoring panel and automated emergency shut-down system.

A high-level process and instrumentation diagram (P&ID) of the facility is presented in Figure 6. Locations of important sensors are highlighted in blue. Detailed P&IDs of individual systems can be found in Appendix A

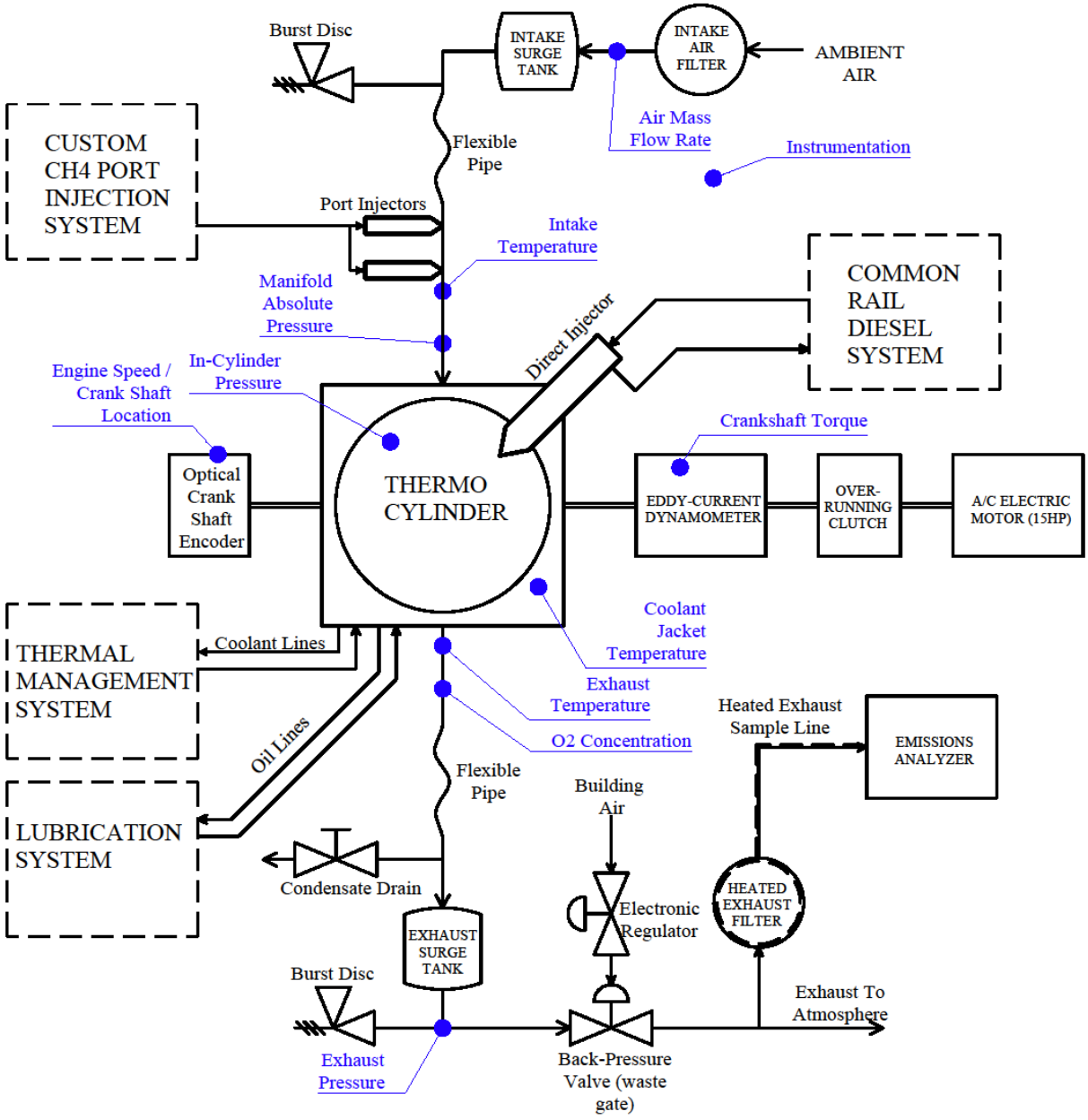

Figure 6: P&ID of single-cylinder research engine facility in thermodynamic configuration.

3.2.1 Engine Control

Control of the engine facility and data acquisition is performed via several processing systems:

i. Operating PC

ii. Real-time control module

iii. Safety control panel

Operating PC: The main control of the engine facility is performed via a custom LabVIEW program running on the operating PC. The software provides a graphic user interface (GUI) through which the operator can view and configure all data acquisition signals from the test-cell and control engine operating parameters on the real-time control module. In addition to the DAQ and real-time controller, the operating PC runs standalone software to control the engine dynamometer, and receives digital signals from the emissions analyzer and diesel fuel scale. The LabVIEW software logs of measurements from the DAQ, emissions analyzer, and diesel fuel scale.

Real-time control module: The real-time control module consists of a National Instruments CompactRIO field-programmable gate array (FPGA) chassis, and generally serves the function of the engine control unit (ECU). In this work, the chassis was equipped with I/O modules designed to perform the following functions: direct and port injector drivers, engine synchronous transistor-transistor logic (TTL) signal output ,wideband O_2 sensor conditioning, general solenoid drivers, and conventional 0-10V analog signal input. A high-degree of configuration and customization flexibility of the ECU functions was available through the LabVIEW software interface on the operating PC. In particular, a customized direct-injector solenoid waveform

could be prescribed in addition to any physically-possible combination of up to 5 injection pulses per combustion cycle.

An important feature of the ECU is the ability to perform discrete, high-speed operations, such as a fuel injection event, in synchronization with the engine crank position. Engine position tracking was performed with fly-wheel and cam-shaft mounted hall-effect sensors providing crank and cam position phasing, respectively.

Safety control panel: The purpose of the safety control panel is to provide a robust monitoring system for critical process values related to the safety of the engine and the operator, which is independent of software systems. If the safety control panel detects any critical process values to cross pre-set thresholds, it automatically engages an emergency shut down (ESD) of the facility, which de-energizing all facility systems. The safety control panel operates on a 24VDC circuit, with process monitors controlling relays arranged in series; if any process value reaches an unsafe value, the circuit is tripped and all power is cut from the facility.

The safety control panel also permits the operator to control several test-cell systems from the operator's control room, including: Exhaust back-pressure, coolant heater and pump, high-pressure fuel pump speed, exhaust sampling line temperature, oil temperature and pump, safety shut-offs and vents for diesel and CH_4 supply systems.

3.2.2 Fueling

To perform DIDF combustion experiments, the engine facility was equipped with two separate fueling systems; i) a diesel direct injection system, ii) a port-injection system equipped with CH_4.

Diesel Direct-Injection System: The diesel direct injection system was designed and built based on components from a medium-duty Bosch common rail application. Approximately 7kg of pump-grade diesel is stored in a fuel pail supported by a gravimetric scale, which determines the time-averaged diesel flow rate. A pre-supply pump and fuel filter condition the diesel before it is delivered to the high-pressure fuel pump (Bosch CP3). The high-pressure pump is operated by an independent 5hp AC motor running at 1500rpm, and pressurizes two common rails which possess redundant pressure relief valves, a pressure transducer used for common rail pressure feedback, a solenoid needle valve used to control rail pressure, and an injector supply line. The injector is a Bosch CRIN2 having a 5-hole nozzle with a 142° included angle and nozzle orifice diameters of 0.205mm and is mounted at an angle of 70° relative to the firedeck. The non-vertical mounting of the injector may affect the performance of the research engine if the liquid fuel sprays impinge on the firedeck or piston bowl in a manner not intended in the original engine design.A detailed P&ID of the diesel common rail system is provided in Appendix A .

CH_4 Port-Injection System: The CH_4 port-injection system was a custom-designed and fabricated system fed by a single cylinder of pure CH_4 with a maximum pressure of 2400psi. The cylinder pressure was reduced downstream by an initial regulator to 400psi. A coriolis flowmeter, capable of reading flowrates down to 0.4kg/hr, was used to measure the CH_4 mass flowrate upstream of a 0.5L accumulating volume, which damped pulsations resulting from the injection events. A

second, heated regulator further reduced the CH_4 pressure to 150psig, which was delivered to two port injectors (Bosch NGI2), each capable of delivering up to 4.5kg/hr of CH_4. The injectors were located at ~400mm and ~1000mm upstream of the intake port, respectively. Only the injector located at ~400mm was used in this investigation as the engine loading requirements were sufficiently low. For all testing, the port-injection pulse was delivered at -330°CA aTDC, and the pulse duration was varied until the desired flowrate was achieved. A detailed P&ID of the CH_4 port-injection system is provided in Appendix A .

3.2.3 Auxiliary Systems

Dynamometer: An air-cooled, eddy-current dynamometer was used to control engine speed and measure engine crankshaft torque. A 15hp AC motor was connected to the driveshaft by means of an over-riding clutch, which allowed motored operation of the engine for thermodynamic start-up and optical skip-fired operation. Control of the dynamometer was performed via stand-alone software provided by Mustang Dyne, operating on the control PC

Thermal Management System (TMS): The purpose of the TMS was to maintain engine temperature to a specified range during operation by conditioning the coolant temperature. The primary components of the TMS are: a heat exchanger connected to cold building water, a 3kW domestic hot water heater and a 3-way mixing valve were used to heat the engine up prior to operation and keep engine temperature controlled to a maximum value during continuous, thermodynamic operation. A mixture of 50% water, 50% ethylene glycol (and anti-corrosion additives) was circulated through the engine block and engine head (see Figure 7), depending on the desired engine temperature, the mixing valve automatically diverted appropriate proportions

of the recirculated coolant mixture through the heat exchanger or heater. Without engine combustion, the maximum engine temperature that could be achieved was 65°C, which was used for all optical testing. All thermodynamic testing was performed between 72—78°C.

Lubrication system: The lubrication system used an external electric pump to circulate 10W-40 engine oil throughout the engine, and was always enabled before the engine was started in order to protect the bearing surfaces. In the oil sump, two 1kW resistance heaters were used to pre-heat the circulated oil. In all testing, the oil temperature was set to 80°C. In the thermodynamic engine configuration, a piston oil-jet was used to distribute oil to the piston skirt to provide lubrication and cooling; the jet nozzle was removed for optical operation.

3.3 Optical Engine Configuration

Several important differences between the optical and thermodynamic engine configurations exist, which must be considered during data interpretation and analysis. Figure 7 presents a schematic of the optical block, piston, and optical measurement arrangement used in this work. The non-vertical and non-centred mounting location of the direct injector should be noted in Figure 7, as this is expected to produce significant asymmetry in the spatially-resolved optical measurements. In Figure 8, the P&ID of the research engine facility configured for optical measurements is presented; equipment specific to the optical engine configuration is highlighted in red. The most significant performance differences between the two engine configurations arise from the design of the Bowditch piston:

i. The Bowditch piston produces a lower compression ratio than the thermodynamic piston; 13.25:1 compared to 14.25:1.
ii. The quartz piston window necessitates a cylindrical bowl, compared to the thermodynamic bowl, which is toroidal.
iii. The thermal conductivity of quartz is much lower than the aluminum of thermodynamic piston, which may promote the formation of hot spots.
iv. The optical liner used with the Bowditch piston has a greater clearance than the stock thermodynamic liner, which results in greater piston ring blow-by.
v. The Bowditch piston used two of the three stock (thermodynamic) piston rings, which necessitate manual lubrication of the liner and piston rings at very frequent intervals during testing.

The conversion of the engine from thermodynamic to optical configuration consists primarily of the following changes and/or additions to the existing engine facility:

i. Swapping the thermodynamic piston assembly with the 'dummy'-piston assembly.
ii. Mounting the optical block on top of the thermodynamic block.
iii. Bolting the optical piston to the crown of the 'dummy' piston.
iv. Re-installation of the thermodynamic head and valve train onto optical block.
v. Re-configuration of the intake for heating.

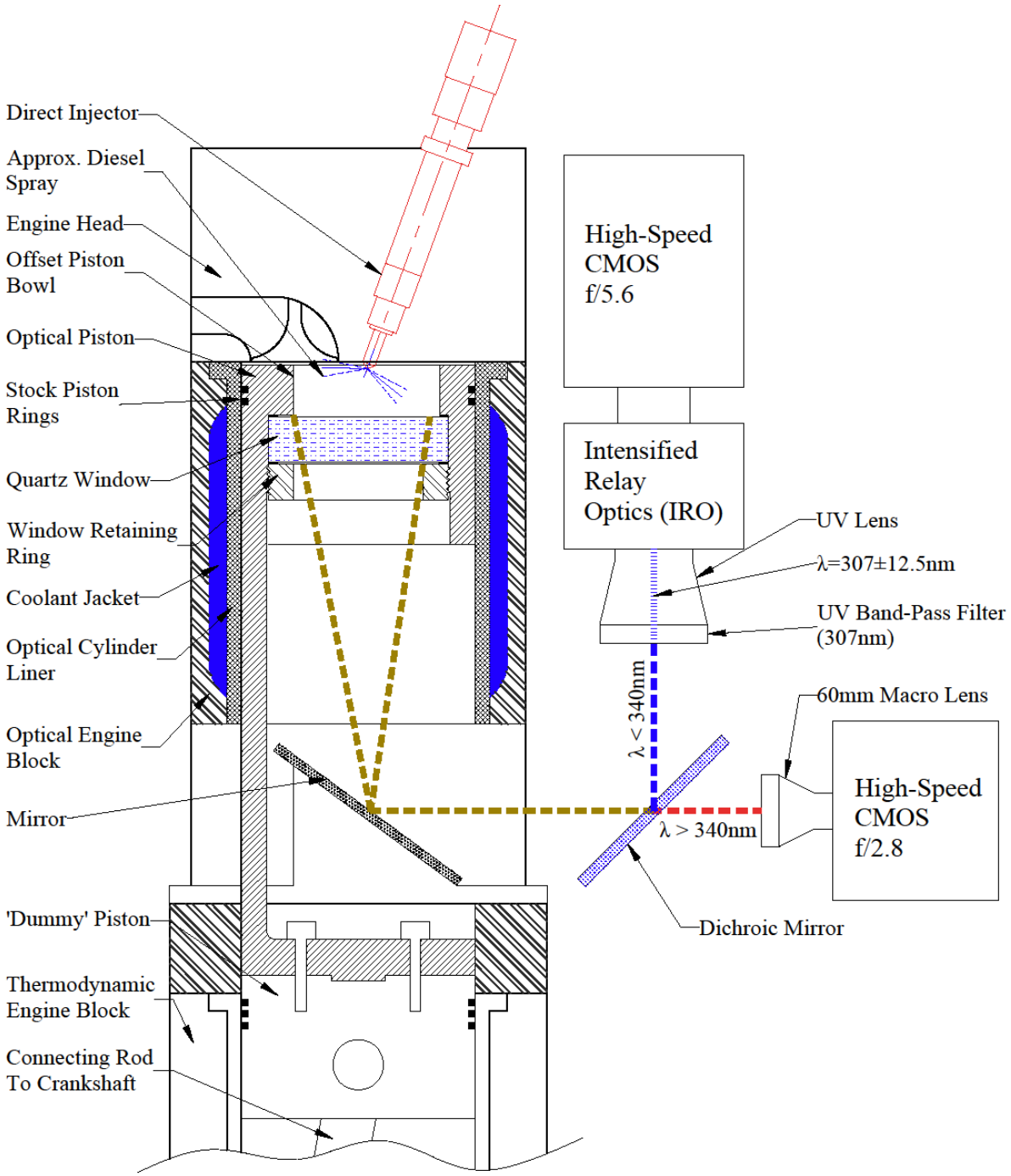

Figure 7: Schematic of Bowditch piston arrangement in optical engine configuration and imaging systems arrangement.

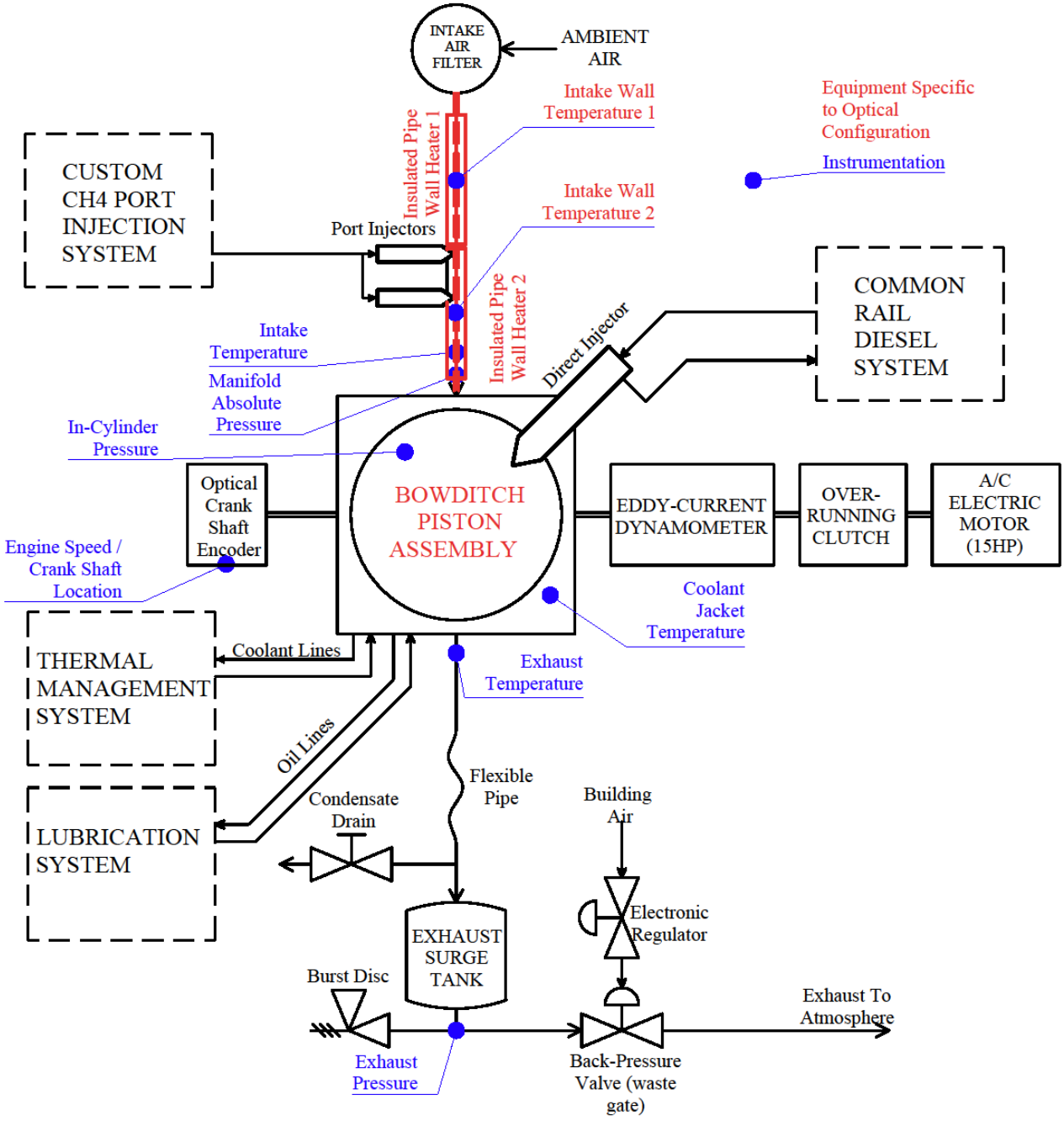

Figure 8: P&ID of single-cylinder research engine facility in optical configuration.

Because of the numerous differences between the optical and thermodynamic engine configurations, a different operating protocol is required when performing optical engine measurements.

To keep the quartz window from over-heating, the engine must be operated in a skip-fired mode, where a small number of consecutive fired cycles are followed by a larger number of motored cycles to allow the window to cool. To offset the lower TDC temperatures produced by the lower optical piston compression ratio and increased blow-by, intake heating is applied.

Skip-Firing: DIDF AHRR measurements were performed using the thermodynamic engine configuration to assess the transient behaviour of the combustion with respect to skip-firing. The goal of this testing was to determine the ideal skip-firing sequence to be used; a compromise of approximating steady-state operation and maintaining sufficient cooling of the quartz window. The selected sequence was 3 consecutive fired cycles followed by 9 motored cycles. Images were only recorded on the 3rd cycle of each fired sequence. The skip-firing and image recording sequence is illustrated schematically in Figure 9. The buffer of the visible imaging system limited the number of firing sequences to 15 for each optical measurement run.

The decision to only record images on the third fired cycle of each skip-firing sequence was made based on thermodynamic skip-firing measurements of AHRR. In Figure 10, the average AHRR of the first 5 consecutively-fired cycles after steady-state motoring is presented. The AHRR of the first two cycles always had a lower peak value and total integrated energy release than all following cycles because the port-injected CH_4 and residual gases required some time to

reach steady-state concentrations in the cylinder. The third cycle was observed to be a good compromise of an AHRR similar to steady-state operation and a low number of fired cycles (to protect the window). It was assumed that the optical engine configuration exhibited the same development period in skip-fired operation.

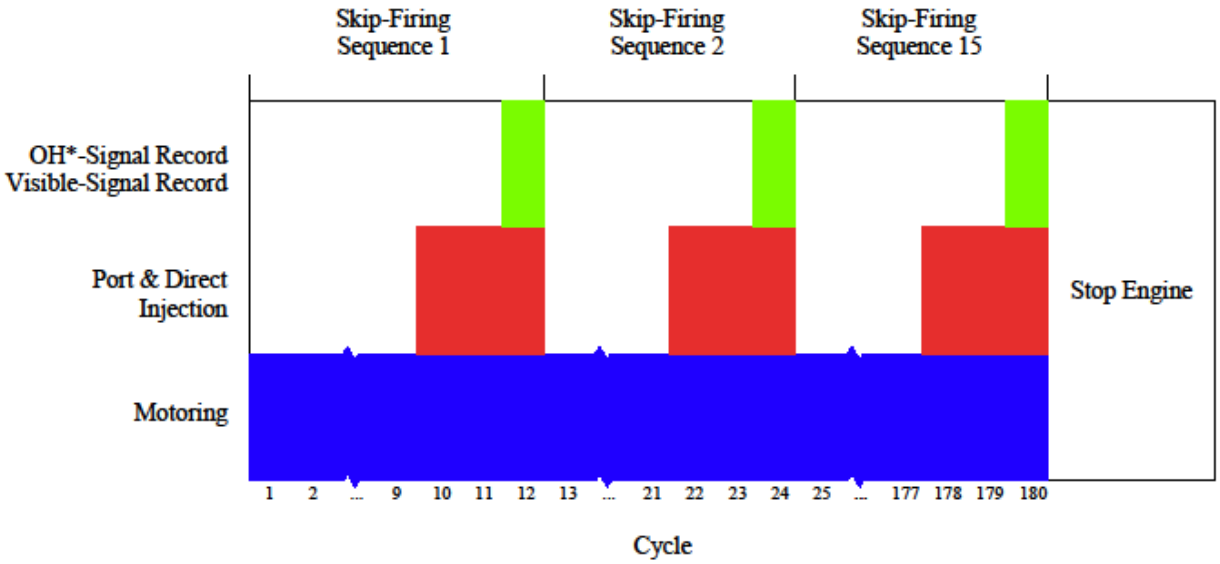

Figure 9: Skip-firing and image record sequence used in all optical testing.

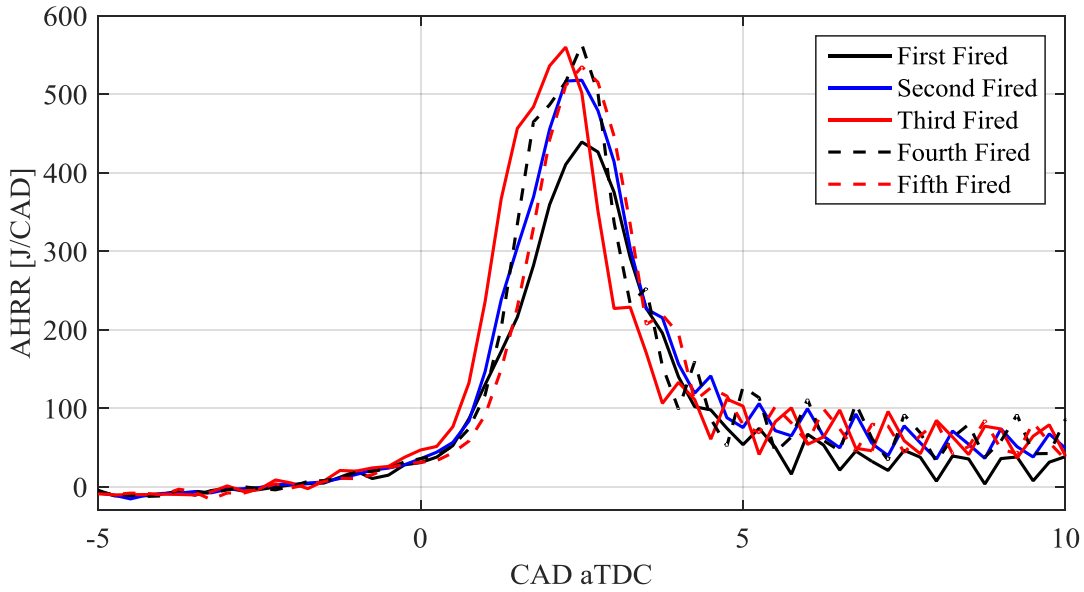

Figure 10: AHRR of first 5 consecutive fired cycles from skip-fired operation in the thermodynamic engine configuration.

Intake heating: It is known from the literature that DIDF combustion is particularly sensitive to temperature [39,48,49]. A 2-stage intake heating system was employed for all optical measurements, which is presented within the modified engine facility P&ID for the optical configuration in Figure 8. The intake heaters were used to heat soak ~2m of intake pipe wall to an operator-prescribed set temperature. The intake wall temperature required to produce the desired average intake temperature during the set of 15 skip-firing sequences was heuristically established. For all measurements in this investigation, a wall temperature of 130—132°C was used to achieve an average intake temperature of ~77°C during the optical measurements. The desired average intake temperature was selected to match the timing of 50% total heat release (CA50) of the optical AHRR to the corresponding thermodynamic measurement, for similar pilot

injection timings. Figure 11 presents the measured intake air temperature during the measurement period of an optical test where intake wall heating was used.

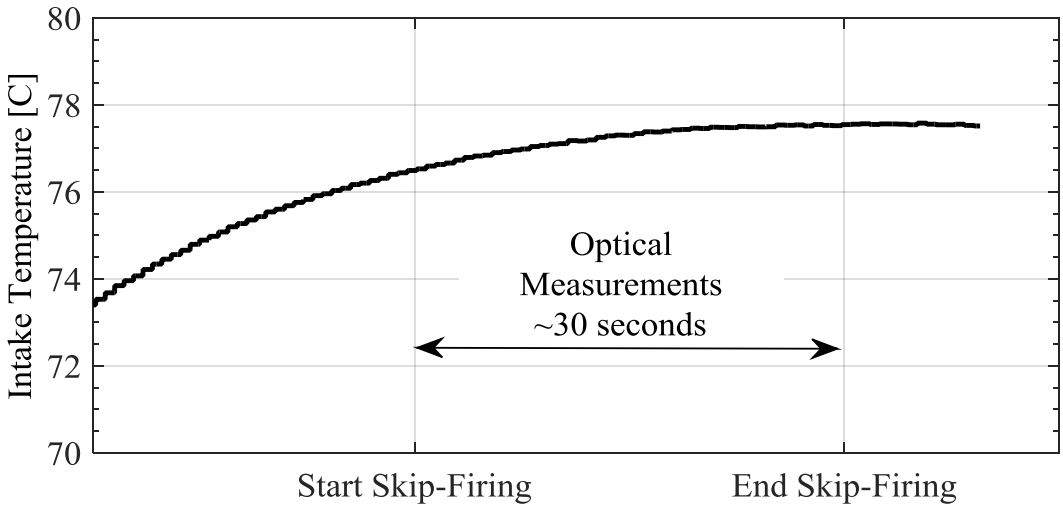

Figure 11: Intake temperature variation during optical measurement using an intake wall temperature of 132°C.

3.4 Measurement & Instrumentation

This section gives specific descriptions of the instrumentation, equipment and measurement protocols used for measurement of important process parameters in both thermodynamic and optical configurations.

3.4.1 Thermodynamic Measurement & Instrumentation

The following categories of thermodynamic measurements were employed:

i. Process temperatures and pressures from the engine and auxiliary systems.

ii. High-speed, crank- synchronous intake manifold and cylinder pressure measurement.

iii. Flow rates of air, diesel, and CH_4.

iv. Rotational speed and position of the crank and camshaft.

v. Exhaust species concentrations.

The specific instrumentation used for thermodynamic measurements is given in Table 3.

Table 3: Thermodynamic instrumentation details.

Measurement	Instrumentation
i) Process pressures & temperatures	General temperature: Omega K-type thermocouples General pressure: Omega PX319-050A5V CH_4 supply pressure: Ashcroft 0-7500psia transducer
ii) Synchronous pressures	Manifold absolute pressure: Kistler 4005B piezo-resistive + Kistler 4618A amplifier In-cylinder pressure: Kistler 6125C piezo-electric + Kistler 5010B charge amplifier
iii) Flow rates	Air: Bosch OEM hot film sensor (sourced from VW 2.0 TDI) CH_4: Endress + Hauser Promass 80A coriolis meter Diesel: Mettler Toledo Viper Ex MB SM12 gravimetric scale
iv) Engine speed and rotational position	Synchronous measurement position: BEH H25 incremental optical encoder (1440 pulses/rev), crank mounted ECU position: Hamlin 55505 hall-effect gear tooth sensor, flywheel mounted (100pulse/rev -1 pulse)
iv) Exhaust species concentration	AVL CEB NA2 emissions analysis bench CH_4: Flame ionization detector NO_x: Chemiluminescence detector O_2: Paramagnetic detector CO +CO_2: Non-dispersive infrared absorption

Measurement Protocol- Diesel-Only Testing

An initial round of diesel-only measurements was carried out for all the points in the thermodynamic measurement set. The primary purpose of these measurements was to determine the required commanded pilot injection pulse-widths required to achieve the desired m_{pilot} for

each diesel injection pressure. Measurement of diesel mass flow rate was performed by a gravimetric scale having a 12kg measurement range; which provided a maximum useable range of ~7kg of diesel consumption, sampled at 2Hz and averaged over 180s. During diesel-only testing, all pilot injections at P_{pilot}=300, 800, and 1300bar were performed at θ_{pilot}=-8°,-6°, and -2°, respectively. For each operating point and pilot injection pressure, the commanded injection durations were adjusted to the nearest 0.01ms until the desired diesel flow rate was observed for a 180 second averaging period. In the case of the smaller injection masses, the energy released by the diesel was insufficient to maintain engine speed; in these cases the dynamometer motor was manually adjusted to maintain the engine speed to 600 ±2rpm.

In addition to the determination of pilot injection control parameters, the diesel-only measurements also provided AHRR data to compare to corresponding DIDF operating points. Because all the DIDF measurement points were performed at θ_{pilot} values of -16°, -12°, -8°, -4°, 0°, +4°CA, and the diesel-only measurements for P_{pilot}=300, 800, and 1300bar were performed at θ_{pilot}=-8°,-6°, and -2°CA, respectively, only the P_{pilot}=300bar diesel-only and DIDF data directly overlap.

Measurement Protocol and Uncertainty- DIDF Testing

Once the engine control parameters had been determined for all operating points in the diesel-only testing, the DIDF points were then measured. The direct-injection parameters determined in the diesel-only testing were applied and the injection duration of the port-injectors was progressively increased in increments of 0.1ms until the desired mass flow rate of CH_4 was achieved. For all testing, the commanded start of port injection, θ_{port}, was -330°CA aTDC. The

selected port injection timing was intended to reduce the build-up of CH_4 in the intake manifold, while permitting sufficient mixing time for the injected CH_4 and intake air. No investigation of other port injection timings was performed. The engine facility was equipped with two port-injectors mounted at ~400mm and ~800mm upstream of the intake port, respectively. All presented measurements were performed using the 400mm location injector. A single repeat test using the 800mm location injector was performed and no measurable difference in performance was observed. Therefore, complete, homogeneous mixing of CH_4 was assumed for all subsequent testing.

At all measurement points, emissions of NO, NO_x, CO, O_2, CH_4, total hydrocarbons (tHC) and CO_2 were recorded over a span of 180 seconds. For each new measurement point, the stabilization of all emissions species signals to within ±50ppm for 1 minute was used as the steady-state criteria before measurement recording was started. Diesel, CH_4, and air mass flow rates were averaged over the same 180 second period in addition to all engine operating temperatures and pressures.

In-cylinder and intake manifold absolute pressure data from 100 consecutive cycles was recorded by the high-speed DAQ system while non-synchronous measurements were being recorded. The in-cylinder pressure was ‘pegged’ to the average intake manifold pressure at -175°— -165° aTDC for every cycle. All presented data is based on the ensemble averaging of the pressure data (*i.e.* the average was calculated before any heat release calculations were performed). Figure 12 presents the 95% confidence interval (based on 100 measured cycles) for the AHRR calculated,

without filtering, for a typical DIDF operating point at P_{pilot}=300, 800, and 1300bar to characterize cyclic variability.

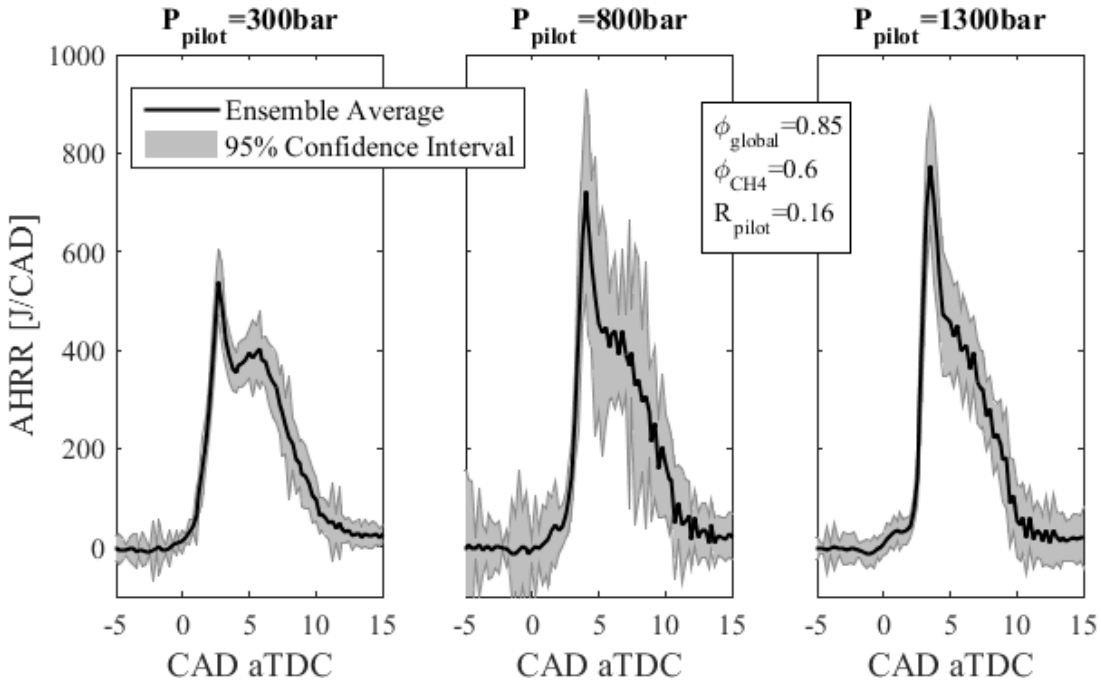

Figure 12: Mean DIDF AHRR and 95% confidence interval calculated from 100 measured cycles at P_{pilot}=300, 800, 1300bar.

It was noted that for a subset of the measurements performed with P_{pilot}=800bar, the cyclic variability was substantially greater than for the rest of the measurements, as seen in Figure 12. The measurements exhibiting this high cyclic variability were all performed on the same day of testing, while P_{pilot}=800bar measurements on no other testing days exhibited the same variability. It is therefore likely that the observed variability was due to an instrumentation issue related to measurement of in-cylinder pressure.

Due to limited CH_4 supply, only a single set of measurements for every operating point was taken. To assess the repeatability and uncertainty of the experiment, a set of measurements for a

single repeatability point were taken on 5 of the 7 measurement days. The mean, standard deviation (σ) and coefficient of variance (COV) of several key operating parameters is presented in Table 4. The repeatability point was performed with P_{pilot}=800bar, θ_{pilot}=4°CA aTDC, pilot pulse width of 1.36ms, and a port injection pulse width of 15.0ms. Particularly high variability in the measurement of NO_x emissions was noted. Although otherwise consistent, a step change of approximately 5g/kW-hr was noted mid-way through the measurement campaign; further investigation of the emissions bench NO_x sensor for future investigations is necessary. Conclusions in this work based on emissions of NO_x must be considered with the caveat of potentially high variability. All other values measured at the repeatability point were deemed to exhibit acceptable repeatability given the qualitative analyses being performed.

Table 4: Statistical variability of operating parameters for thermodynamic measurement repeatability point.

Parameter	Units	Mean	σ	COV
GIMEP	[bar]	8.921	0.090	0.010
CH_4 Emissions	[g/kW-hr]	2.592	0.128	0.049
NOx Emissions	[g/kW-hr]	7.571	3.552	0.469
CA50	[CAD aTDC]	8.799	0.860	0.098
Peak AHRR	[J/CAD]	304.801	7.066	0.023
φ_{global}	[-]	0.834	0.050	0.060
φ_{CH4}	[-]	0.369	0.014	0.038
φ_{diesel}	[-]	0.411	0.037	0.089
R_{pilot}	[-]	0.496	0.015	0.031
GISFC	[g/kW-hr]	232.951	6.055	0.026
Air Flowrate	[kg/hr]	37.713	1.499	0.040
CH_4 Flowrate	[kg/hr]	0.925	0.013	0.014
Diesel Flowrate	[kg/hr]	1.030	0.053	0.052

3.4.2 Optical Instrumentation & Measurement

Simultaneous measurement of broadband visible light emissions and natural emissions of light having a wavelength of 307nm was performed to measure total combustion and OH*-chemiluminescent light intensity, respectively. To perform these measurements, an optical measurement system consisting of two high-speed complementary metal-oxide semiconductor (CMOS) devices was used; a schematic of the measurement system layout is presented in Figure 7. The major specifications of the optical measurement devices as configured for testing in this investigation are given in Table 5. Commissioning and operation of the optical measurement systems was performed by Mahdiar Khosravi.

Table 5: Optical measurement equipment specifications.

Measurement Device	Details
Visible light high-speed CMOS	• Vision Research Inc. Phantom V7.1 • 12-bit CMOS (13.2mm x 17.6mm) • 320 x 240 pixels • ~14400 fps (crank-synchronous, 0.25°CA @ 600rpm)
307nm filtered high-speed CMOS	• LaVision HighSpeedStar 6 • 12-bit CMOS (20.48mm x 20.48mm) • 640 x 640 pixel • 12000fps
Intensified relay optics (IRO)	• 10000ns gating • Phosphor screen decay time <300ns • Photocathode efficiency ~12% (UV)
UV bandpass filter	• 307nm ±12.5nm
Dichroic mirror	• Transmit > 340nm (>95% @ 700-800nm) • Reflect < 340nm (>98% @ 307nm)

Triggering of the visible light imaging system shutter was synchronized with 0.25°CA pulses received from the optical crank encoder. Triggering of the intensifier gate for the 307nm imaging system shutter was performed at a nominal rate of 14000fps to approximately match the 0.25°CA frame rate of the visible imaging system. The image sets were synchronized through a post-processing routine written by Mahdiar Khosravi and performed in MATLAB, described in Figure 13.

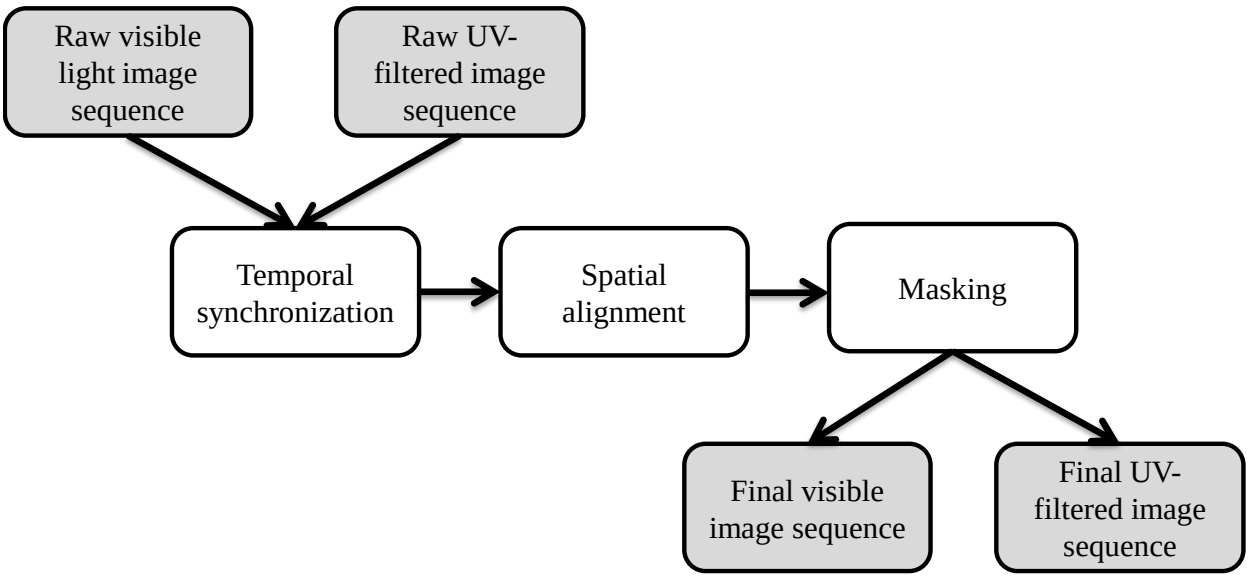

Figure 13: Flowchart of image post-processing procedure.

Temporal synchronization: Using timestamps from crank synchronous data, ultra-violet (UV) filtered images were matched to nearest visible images, which triggered at a variable rate determined by instantaneous rotational velocity of the crankshaft for every 0.25°CA. The instantaneous rotational velocity of the shaft exceeded 600rpm during power strokes, resulting in the need to duplicate successive UV-filtered images to match every visible-signal image. The effect of this procedure can be seen in chapter 6, where OH*-signal profiles have a saw-tooth feature at locations where the UV-filtered image was duplicated. For all frames, the maximum position error is 0.25°CA.

Spatial Alignment: The goal of spatial alignment was to produce two sets of images that could be directly overlaid. No analysis of overlaid image was performed in this investigation; and will not be discussed further.

Masking: The final image processing step was application of a binary mask to remove all signals resulting from reflections and sensor noise outside of the bowl area. The bowl dimensions and location used to produce the mask were determined by the Hough transform used to perform the spatial alignment step.

Optical Measurement Protocol

Because of the numerous mechanical and instrument-related limitations, a specific optical testing protocol was followed to maximize the number of optical measurements, which could be carried out, while ensuring the health of the optical engine components. The optical measurement protocol is presented in Figure 14.

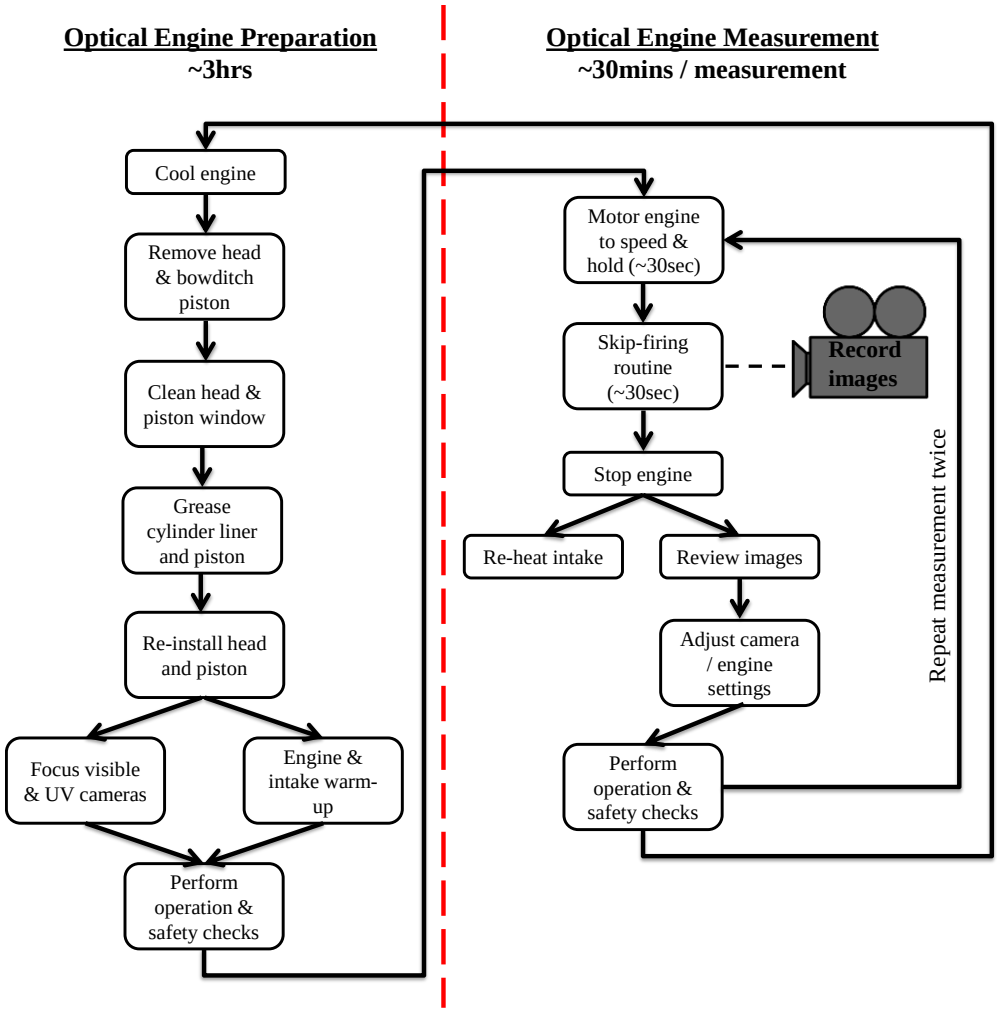

Figure 14: Optical measurement protocol flowchart.

3.4.3 Data Acquisition

The DAQ system was used to collect signals from all test-cell sensors and relay the signal values to the operating PC for logging. The commissioning of the DAQ system was performed by Jeff Yeo. The DAQ module was a National Instruments CompactDAQ 8-card chassis, which can be equipped with a wide variety of I/O modules. The DAQ configuration used during this work included modules tailored to the following functions: logging the crank-mounted quadrature encoder, thermocouple signals, conventional 0-10V analog inputs, and high-speed crank

synchronous signals, such as in-cylinder pressure, that are logged against the encoder signal. Details of how specific measurement signals were handled are presented in Table 6.

Table 6: Signal conditioning and logging details

Sensors	Signal Conditioning	Logging Details
General temperature/ pressure, air flowrate, CH_4 flow rate	Averaged over measurement duration.	Sampled for 100 consecutive cycles.
Crank-synchronous pressures	In-cylinder pressure: 'Pegged' to average manifold pressure from -175°—-165°CA aTDC for every cycle. Ensemble averaged. Manifold absolute pressure: Ensemble averaged.	Recorded for 100 consecutive cycles.
Emissions, diesel flowrate	Averaged over measurement duration.	Recorded for 180s at 2Hz.

During optical measurements, the signals from the high-speed CMOS devices is stored in a local device buffer and then transferred via Ethernet cable to a dedicated PC after the test has terminated.

3.5 Summary

This chapter has described the single-cylinder research engine facility commissioned and used for thermodynamic and optical measurement of DIDF combustion. Many efforts were made to ensure the combustion conditions in the optical engine configuration matched the thermodynamic configuration, however it is expected that significant discrepancies exist, which must be considered when comparing data from the thermodynamic and optical measurement sets to one another. Thermodynamic and optical measurement sets are presented and discussed in detail in chapters 4 and 5, respectively.

Chapter 4: Thermodynamic Results & Discussion

The objective of this chapter is to summarize and discuss the effects that the major operating parameters selected for thermodynamic investigation have on the characteristics of the fundamental combustion mechanisms present in DIDF operation. The methodology for defining the measurement campaign will be discussed, as will the tools and approaches for the data analysis. Following this, a summary and explanation of the selected measurement points is presented in §4.1. The analytical tools developed for this investigation are described in §4.2. The observed effects that variations of P_{pilot}, θ_{pilot}, pilot energy ratio, φ_{CH4}, and global equivalence ratio have on DIDF operation are presented in §4.3. To characterize the fundamental combustion mechanisms present across the explored ranges of DIDF operation, the effects of operating parameters on identified stages of DIDF combustion are explored in detail in §4.4. In §4.5, a summary of the observations made based on thermodynamic analysis is presented along with a conceptual map of the different operating regimes observed for DIDF combustion for the experimental conditions considered in this work.

4.1 Thermodynamic Measurements

The thermodynamic measurements in this work were performed on the all-metal configuration of the research engine facility described in the previous chapter (see Figure 6). Unlike the optical engine configuration, the all-metal configuration permits continuous operation of the engine with cylinder temperatures and pressures representative of real-world DIDF applications. There are several major objectives for the thermodynamic measurements:

i) Determine the engine control settings required to produce the desired diesel and CH_4 fueling rates.

ii) Characterize the combustion process based on the heat release rate, engine-out emissions and brake torque for a range of DIDF fuelling modes.

iii) Identify operating points to be further investigated with the optically-accessible engine configuration, with the ultimate objective of better characterizing DIDF combustion.

Thermodynamic Measurement Points

It is the goal of this work to bridge gaps in the knowledge of DIDF operation across the wide spectrum of possible fuelling strategies. In order to address this goal, a range of operating modes possible with DIDF strategies was selected. The global equivalence ratio, φ_{global} (given by equation (5)), φ_{CH4} and the pilot energy ratio, R_{pilot} (given by equation (6)) were selected as the metrics to characterize the fuel-air mixture, while pilot injection pressure and θ_{pilot} were selected as pilot-injection control parameters of interest. In equation (5), $\frac{A}{F}$ is the air-fuel ratio and in equation (6), LHV is the lower heating value.

$$\varphi_{global} = \frac{\dot{m}_{diesel,meas.} \cdot \frac{A}{F}_{diesel,stoich} + \dot{m}_{CH4,meas.} \cdot \frac{A}{F}_{CH4,stoich}}{\dot{m}_{air,meas.}} \quad \textbf{(5)}$$

$$R_{pilot} = \frac{\dot{m}_{diesel,meas.} \cdot LHV_{diesel}}{\dot{m}_{diesel,meas.} \cdot LHV_{diesel} + \dot{m}_{CH4,meas.} \cdot LHV_{CH4}} \quad \textbf{(6)}$$

φ_{global} and φ_{CH4} are known to be important parameters to conceptually describe DIDF combustion [23]. These parameters have been observed to significantly impact the characteristics of the flame propagation mechanisms observed in optical investigations of DIDF combustion [28,46]. Emissions of CH_4 have also been shown to be strongly dependent on φ_{global} and φ_{CH4} in addition to R_{pilot} [23,29]. Pilot injection pressure and timing have also been shown to significantly affect DIDF combustion and emissions [17,20,50]. The effects of pilot injection parameters, however, are not as well characterized as φ_{global} and φ_{CH4}; varying effects on emissions and performance have been observed for different engine operating conditions [18]. These observations in the literature motivated the selection of φ_{global}, φ_{CH4}, R_{pilot}, P_{pilot}, and θ_{pilot} as the key parameters to experimentally investigate in this work.

Figure 15 illustrates the operating space investigated, with specific desired measurement points indicated by circles. In Figure 15, the measurement locations were selected at the intersection of lines of constant φ_{global} and lines of constant φ_{CH4}, to facilitate comparison of effects across these parameters.

φ_{CH4} was varied from approximately φ_{CH4}=0.25—0.62 such that operational variation related to the apparent flame propagation transition point noted by [28] at $\varphi_{CH4}\approx$0.6 could be further explored. The minimum R_{pilot} that could be achieved was limited by the minimum injection duration of the direct-injector at the highest injection pressure investigated. The lower bound of φ_{global} was set at φ_{global}=0.6 based on previous experience with the lower limit of stable DIDF combustion in the experimental facility. The upper bound of φ_{global} was set to φ_{global}=0.9 to avoid knock at high φ_{CH4} points and to avoid excessive soot emissions at high R_{pilot} operating points.

Because the research engine employed in this work was naturally aspirated, the engine load across the DIDF space is not constant; load was observed to be approximately proportional to φ_{global}.

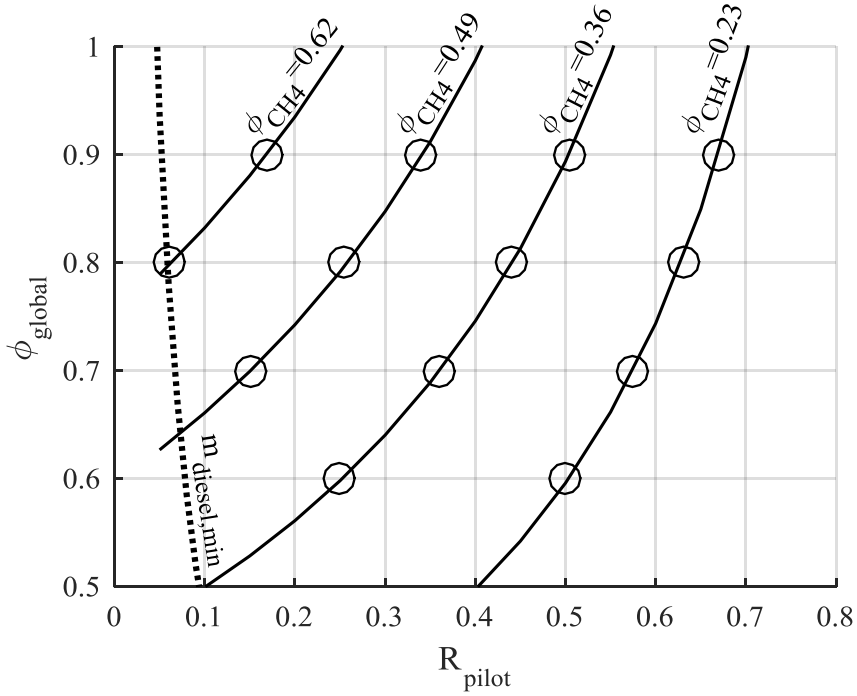

Figure 15: Selected thermodynamic operating points in R_{pilot}-φ_{global} operating space.

To simplify the design of the experiment, a constant mass airflow rate was used to calculate fuelling parameters for all operating conditions. The mass airflow rate used to calculate the desired diesel and CH_4 fueling rates was 39kg/hr, which was measured for the same operating speed in previous experiments performed on the same research engine facility. The displacement of inducted air by port-injected CH_4 and a lack of an intake air-conditioning system caused some variability of actual airflow rates measured during the testing of this investigation. Actual airflow rates ranged from 36.8kg/hr—40.2kg/hr depending on the operating point and testing day. All

reported equivalence ratios and fueling statistics are given based on the measurements from the particular test, not the assumed values used for experiment design purposes.

At each selected R_{pilot}-φ_{global} operating point, a sweep of pilot injection pressures and timings was performed with a single-pulse diesel injection. Although multiple-pulse pilot injections have been shown to significantly improve DIDF engine performance [17,50] and are often used, single-pulse injections were considered here to simplify comparison of pilot injection effects across different operating points. A summary of the performed pilot injection settings is presented in Table 7.

Table 7: Pilot injection parameters for thermodynamic DIDF measurements

Injection Pressure [bar]	Commanded Injection Timing [°CA aTDC]
300	-16, -12, -8, -4, 0
800	-12, -8, -4, 0, +4
1300	-12, -8, -4, 0, +4

At certain operating points, not all pilot injection pressures and timings were possible. In some cases, the latest timings were observed to result in unstable combustion and were excluded from the investigation. The largest pilot injection masses (R_{pilot} > 0.5) could not be achieved with 300bar pilot injections due to the excessive injection durations required and were also excluded from the investigation. Finally, due to limited CH_4 quantities, the set of measurements for φ_{CH4}=0.36 and P_{pilot}=800bar were not completed; it is a recommendation of this work to complete these measurements. Appendix B lists the details of the specific operating points measured and highlights regions of the experimental space where measurements were planned,

but not carried out. Figure 16 presents the complete set of measurement points for all P_{pilot} and θ_{pilot}. Including diesel-only measurements, 173 unique operating points were measured.

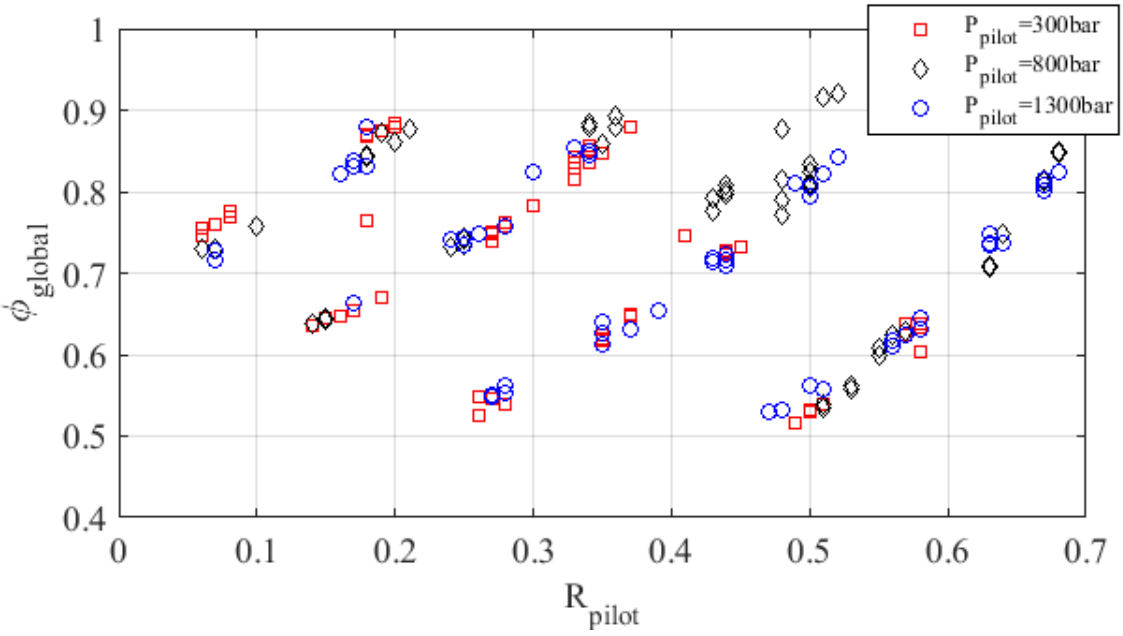

Figure 16: Complete set of all measured thermodynamic operating points at all P_{pilot} and θ_{pilot}.

4.2 Thermodynamic Data Analysis

Calculations of the AHRR were performed using the ensemble-averaged cylinder pressure data from the 100 recorded cycles with no additional filtering using equation (7) [51]. Constant gas properties (C_v,$\mathcal{R}$) corresponding to air at 800K were used. All calculations of cycle work used to normalize fuel consumption and emissions were based on the gross, indicated measurements.

$$AHRR = \left(\frac{c_v}{\mathcal{R}}\right) \cdot V \cdot dp + \left(\frac{c_v}{\mathcal{R}} + 1\right) \cdot p \cdot dV \qquad (7)$$

The DIDF combustion process is characterized by the combination of multiple combustion mechanisms, which overlap and influence one another. The presence of the 3 stages of combustion proposed in [23] are readily apparent in the data collected in this investigation; however they are difficult to separate from one another. The lower portion of Figure 17 presents a typical DIDF AHRR exhibiting a large peak (denoted as stage 1 combustion), followed by a broader, lower intensity peak (stage 2 combustion). The AHRR and the first derivative of the AHRR (presented in the upper portion of Figure 17) were found to be a useful metrics to define boundaries in the combustion stages and are presented in the lower and upper portions of Figure 17, respectively. Specifics of the combustion stage boundary definitions are given later in this section. The 2nd peak in the AHRR is split into high and low intensity stages (2a and 2b, respectively). These stages of combustion were found to be present across the range of operating points investigated; however, wide variability in the characteristics of each stage was observed as different operating parameters were changed. These observations suggest wide ranges of performance and possibly changes of the fundamental combustion mechanism (*i.e.* pre-mixed auto-ignition vs. flame propagation) can be achieved in a given stage of combustion as operating parameters are modified.

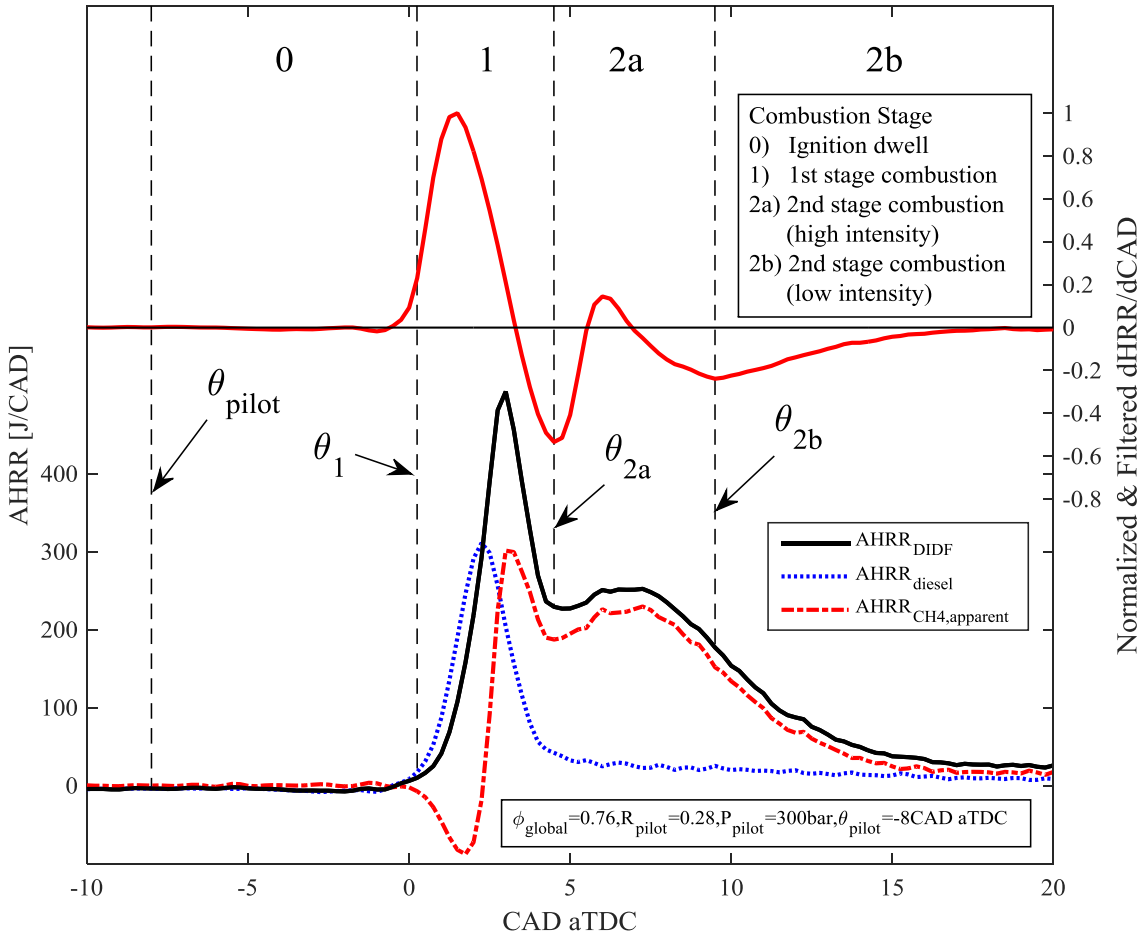

Figure 17: Defined stages of DIDF combustion and superposition of diesel-only and DIDF AHRR data.

Also presented in the lower portion of Figure 17, are the diesel-only and apparent CH_4-only AHRRs ($AHRR_{diesel}$ and $AHRR_{CH4,apparent}$, respectively). The diesel-only AHRR is calculated from measurements taken during diesel pilot operation in the absence of CH_4, but with the same pilot injection parameters as the corresponding DIDF operating point. The apparent CH_4-only AHRR is calculated as the arithmetic difference of the dual-fuel AHRR and the diesel-only AHRR, as given by equation (8). The notation, $AHRR|_{\theta}$, refers to the value of the AHRR evaluated at θ° aTDC. While it is known that the presence of CH_4 will affect the diesel ignition

and combustion [14,25], the apparent CH_4-only AHRR provides useful qualitative information about the effects of premixed CH_4 on diesel combustion.

$$AHRR_{CH4,apparent}|_\theta = AHRR_{dual-fuel}|_\theta - AHRR_{diesel}|_\theta \quad \textbf{(8)}$$

Variations in the characteristics of each combustion stage are expected to affect the major operating performance metrics of the engine such as efficiency and pollutant emissions. In order to isolate the relationships between global metrics and particular combustion mechanisms, a simple algorithm was applied to the AHRR data for each investigated test point to systematically identify the boundaries of each combustion stage. These stages of combustion are presented in the upper section of Figure 17 for a typical dual-fuel operating point. Transitions in the AHRR shape are expected to be the result of changes in dominant fuel conversion mechanism, the volume of the reaction zone, and heat transfer to/from the cylinder in each combustion cycle. In reality there is no clear division between the start of one stage of combustion and the end of another as these mechanisms always overlap one another. The selection logic and physical meaning of each stage is presented below:

Ignition dwell: This stage begins at the commanded start of injection (θ_{pilot}) and ends as the integrated AHRR becomes positive at θ_1 (crank angle indicating start of stage 1 combustion). This process consists of the electronic delay of the ECU hardware, mechanical delay of the injector needle, followed by evaporation and mixing of the liquid fuel before auto-ignition occurs. In some cases, a small release of energy is observed during this phase, attributed to pre-ignition reactions of well-mixed diesel vapour.

Stage 1 Combustion: This stage begins at θ_1, as the integrated AHRR becomes positive (indicating the start of high-temperature combustion) and terminates at the first local minimum of the derivative of AHRR occurring after the peak of the AHRR, denoted as θ_{2a} (crank angle indicating the start of stage 2a combustion) and given by equation (9), where q represents the AHRR.

$$\theta_{2a} = \theta|_{min\left(\frac{dq}{d\theta}\right)} \quad \textbf{(9)}$$

After a decrease in the AHRR following the peak, the subsequent minimum in the derivative of AHRR indicates where the AHRR begins to increase again. The increase in the reaction rate is interpreted as the point at which another combustion mechanism becomes dominant, similar to interpretations presented in the literature. The processes in the first stage of combustion are expected to be dominated by the ignition and rapid combustion of the pilot fuel and any pre-mixed CH_4 entrained into the pilot injection jet. Because the processes in stage 1 combustion lead to high AHRR values, a useful parameter for discussion is the maximum AHRR in stage 1 combustion, $q_{1,max}$, given by equation (10).

$$q_{1,max} = \max\left(AHRR|_{\theta_1 \rightarrow \theta_{2a}}\right) \quad \textbf{(10)}$$

Stage 2 Combustion: This stage of combustion represents all the fuel conversion processes following stage 1 combustion. The start of this combustion stage(θ_{2a}) is defined as the point where rate of change of the AHRR transitions from negative to positive following the peak of stage 1combustion. In much of the literature, the second AHRR peak in dual-fuel combustion is attributed to flame propagation through the premixed fuel. In this work, some operating modes resulted in a low-intensity tail on the AHRR which extended far into the expansion stroke while there is little or no second AHRR peak. The systematic identification of a 'high intensity' portion of the stage 2 combustion (2a) facilitated analysis of the proposed flame propagation stage without interference from the extended tail (stage 2b). The definition for the end the stage 2a combustion (θ_{2b}) was selected as the inflection point in the AHRR following the stage 2 combustion peak, given by equation (11).

$$\theta_{2b} = \theta|_{min\left(\frac{dq}{d\theta}\right)|_{\theta>\theta_{2a}}} \quad \textbf{(11)}$$

The average AHRR of the stage 2a combustion ($q_{2a,mean}$) as given by equation (12), was found to be the most relevant parameter to characterize the high-intensity portion of the stage 2 combustion (*i.e.* stage 2a).

$$q_{2a,mean} = \frac{1}{\theta_{2b} - \theta_{2a}} \cdot \int_{\theta_{2a}}^{\theta_{2b}} q d\theta \quad \textbf{(12)}$$

The low-intensity portion of the stage 2 combustion (2b) considers all remaining processes contributing to the remainder of the AHRR; there is no clear consensus on what this mode of combustion is. A descriptive parameter for this stage of combustion was expected to be the fraction of total cycle energy released in stage 2b combustion, Q_{2b}/Q_{tot}, given by equation (13).

$$Q_{2b}/Q_{tot} = \frac{\int_{\theta_{2b}}^{\theta|AHRR,max} q d\theta}{\int_{\theta_{=-180}}^{\theta|AHRR,max} q d\theta} \quad \textbf{(13)}$$

Flame Propagation Analysis

Because the CH_4 is inducted as a pre-mixed charge, it is expected that combustion of this fuel will take place by means of a turbulent flame propagation mechanism, provided bulk auto-ignition or knock does not occur. If the turbulent flame propagation mechanism is assumed to have the form of a wrinkled laminar front, as is common in SI engine operation, a turbulent flame speed (s_t) can be defined by equation (14), treating the flame as a static frame of reference [52]. Combining a simplified approximation for the AHRR produced by flame propagation through CH_4 given by equation (15), and combining with equation (14) produces a relationship between the AHRR and mixture properties (equation (16)).

$$s_t \equiv \frac{\dot{m}_r}{\bar{A} \cdot \rho_u} \quad \textbf{(14)}$$

$$AHRR \propto LHV_{mixture} \cdot \dot{m} \quad \textbf{(15)}$$

$$AHRR \propto LHV_{mixture} \cdot s_t \cdot \bar{A} \cdot \rho_u \quad \textbf{(16)}$$

Where, $\dot{m}_r$ is the mass flow rate of reactants through the flame front, $\bar{A}$ is the time-averaged flame front area, ρ_u is the unburned mixture density, and $LHV_{mixture}$ is the lower heating value of the premixed mixture (assumed to be CH_4). From turbulent flame theory, the following statements can be made using equations (2) and (3) [52]:

$$s_t = f(s_l, u') \quad \textbf{(2)}$$

$$s_l = f(\varphi, T_u, P) \quad \textbf{(3)}$$

Where s_l is the laminar flame speed (s_l of CH_4 in this case), u' is a measure of the fluctuating component of the turbulent flow field (a measure of turbulence intensity), φ is the mixture equivalence ratio (φ_{CH4} in this case), T_u is the temperature of the unburned gases, and P is the mixture pressure. Combining equations (2), (3), and (16) gives the following relation in equation (17), which will be used to discuss trends in stage 2a combustion:

$$AHRR_{Turb.\ flame\ prop.} = f(LHV, T_u, \rho_u, \bar{A}, u', P, \varphi) \quad \textbf{(17)}$$

While the preceding discusses flame propagation through a CH_4-air mixture, stage 2 combustion will be sensitive to the mass of evaporated diesel, air and CH_4 present after the stage 1

combustion has substantially ended. It is this mixture state which, ultimately, defines the laminar flame speed for stage 2 combustion. To test the hypothesis that stage 2 combustion consists of flame propagation, the sensitivity of $q_{2a,\ mean}$ (mean AHRR during stage 2a combustion) to φ_{CH4} and φ_{global} was considered. It is expected that a decrease in the relevant equivalence ratio will result in a decrease in the $q_{2a,mean}$, which is used here as an indirect measure of the flame speed.

4.3 Thermodynamic Results

This section reviews the observed effects that variations of P_{pilot}, θ_{pilot}, R_{pilot}, φ_{global}, and φ_{CH4} have on the emissions of NO_x and CH_4, and AHRR characteristics of the DIDF operating points measured. The observations in this section are used as the basis of detailed discussion and analysis in the subsequent section.

4.3.1 Pilot Injection Pressure

Pilot injection pressure is expected to have a strong impact on the mixing of the diesel pilot and entrainment of air and CH_4 into the pilot jet. Figure 18, presents a comparison of the effect of P_{pilot} on the AHRR for a given φ_{global}, with two different R_{pilot} (left and right figures). Figure 19 presents trends in the fraction of energy released during each of the identified stages of combustion, and generally indicates that P_{pilot} will influence the relative distribution of the fuel conversion in the different stages. The spread of the data points in Figure 19 reflects the wide range of operating modes being presented together (*i.e.* entire ranges of R_{pilot}=0.06—0.61 and φ_{global}=0.55—0.88 are all presented together for a given P_{pilot}). The impact of P_{pilot} on DIDF combustion was generally considered with respect to the enhanced mixing effects achieved through increased injection pressure; several trends were observed.

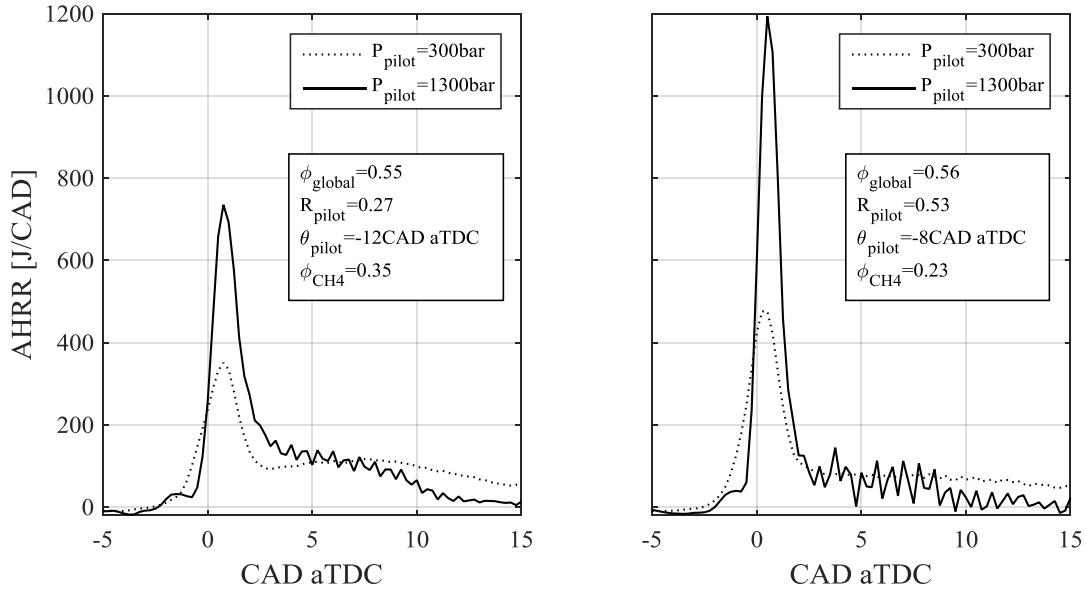

Figure 18: Comparison of P_{pilot} effect on AHRR of DIDF combustion for R_{pilot}=0.27 (left) and R_{pilot}=0.53 (right).

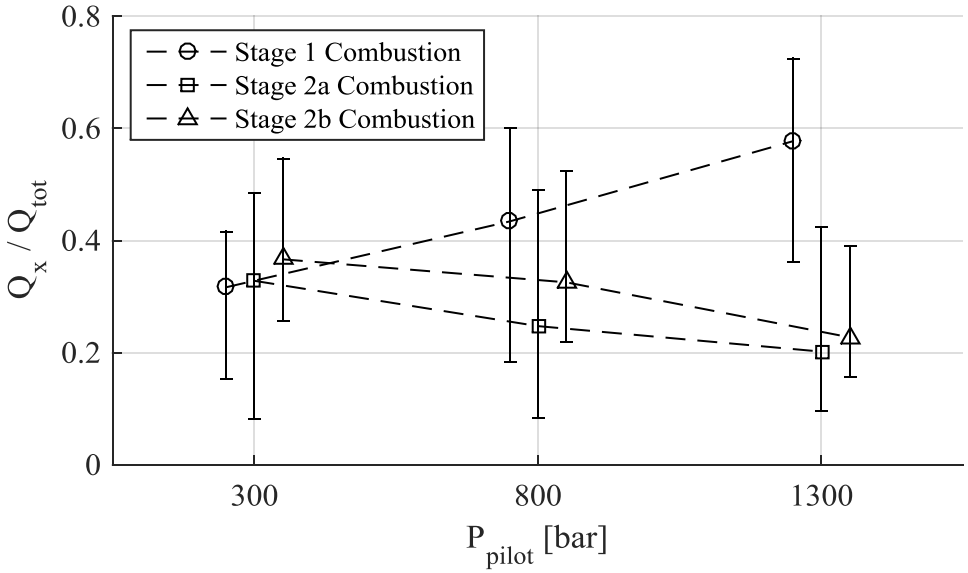

Figure 19: Effect of P_{pilot} on mean relative amount of energy released during each stage of combustion (Q_x/Q_{tot}) for optimized timing at each operating point and P_{pilot}. Vertical bars represent maximum and minimum data points in experimental set. Note that for plot clarity, data points at each injection pressure are presented with a horizontal offset.

i) The $q_{1,max}$ increases with increasing P_{pilot}. Because the duration of the stage 1 combustion remains approximately constant across large variations of P_{pilot}, the increase of $q_{1,max}$ was interpreted as an increase in one or both of the following quantities: the mass of diesel that has been adequately prepared (evaporated and mixed with oxidizer) for rapid premixed combustion, and/or the mass of CH_4 entrained by the pilot jet and reacted with the premixed fraction of the diesel pilot.

ii) The duration of stage 2a combustion and Q_{2b}/Q_{tot} decrease with increasing P_{pilot}. This effect is evident in the top plot of Figure 18. In Figure 19, increases in the fraction of energy released in stage 1 combustion (Q_1/Q_{tot}), achieved through increased pilot injection pressure, are shown to correlate with decreases in Q_{2a}/Q_{tot} and Q_{2b}/Q_{tot}. Less fuel remained following stage 1 combustion to be oxidized in subsequent stages of combustion; indicating increased entrainment of premixed CH_4 into the pilot jet with increasing P_{pilot}.

iii) Apparent heat release from pre-ignition reactions became more pronounced with increasing P_{pilot}; high pilot injection pressure cases in Figure 18 show distinct AHRR peaks before the main premixed combustion reactions, which was observed to be a consistent trend across the operating space explored. This trend may indicate that the higher pilot mixing rates produced by high injection pressures caused a greater fraction of fuel to be converted in a cool flame. Further investigation is required to confirm this mechanism, however.

4.3.2 Pilot Injection Timing

Sweeps of θ_{pilot} were carried out for all operating points and each P_{pilot} in increments of 4°CA across a range of timings assessed to be practical. The early and late bounds of the measured timing sweeps met two criteria. The CA50 of the earliest timing must occur at TDC or later, and the AHRR of the latest timing must be stable. Stability of the AHRR was qualitatively assessed at the time of the measurements by observing the live display of the AHRR shape and CA50. If, a steady state value for these two parameters was not achieved within approximately 1 minute then the timing was taken out of the measurement plan. Generally, instability of the AHRR was easily identified by misfired cycles which released only a small fraction of the energy that normally-fired cycles did. Figure 20 depicts typical variations observed in the AHRR for a given point across a sweep of θ_{pilot}.

Typically, the peak AHRR was observed to marginally decrease with later timings, attributed to lower temperatures and pressures during combustion due to increasing cylinder volumes. Lower temperatures resulting in slower chemical kinetics are attributed to the observed enhancement of pre-ignition reactions with later injection timings; in Figure 20, the delay between the onset of positive AHRR and start of stage 1 combustion increases from approximately 2° CA to 5° CA between the earliest and latest timings.

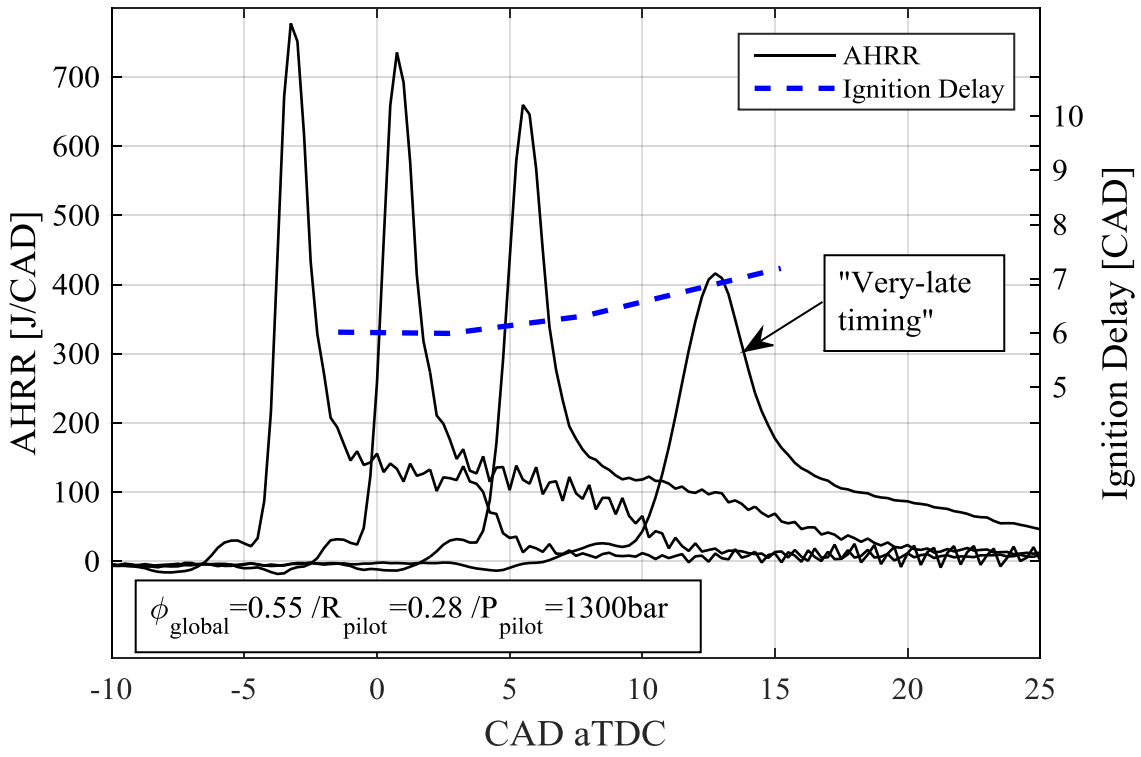

Figure 20: AHRR trends for typical sweep of commanded pilot injection timing, θ_{pilot}, for θ_{pilot}=-12,-8,-4,+0°CA aTDC.

In many cases, a 'very-late timing' case was observed in which a long ignition delay was accompanied by a single-peak AHRR (atypical of all other tested timings). The very-late timing case was observed at a number of points in the φ_{global} –R_{pilot} operating space and was often accompanied with a decrease in NO_x emissions, at the expense of combustion stability, efficiency, and HC emissions. In a few cases, the peak AHRR of the 'very-late timing' case was higher than for earlier timings despite the later combustion phasing. Figure 21 presents the AHRRs for a timing sweep at a point with an increasing peak AHRR for later timings; it was also noted that the ignition delay for these operating points is not monotonically increasing. While beyond the scope of this investigation, it is possible that the long ignition delay permits

more thorough mixing of the diesel vapour with the premixed CH_4, which results in a larger fraction of the total fuel to react by a premixed auto-ignition mechanism. The auto-ignition characteristics in these cases should be dependent on the spatial distribution of reactivity due to mixture heterogeneity such as in premixed compression ignition (PCI) and RCCI operation, such as those investigated by [9,22,45,53,54]. Further detailed investigation of this operating mode is required to support this theory.

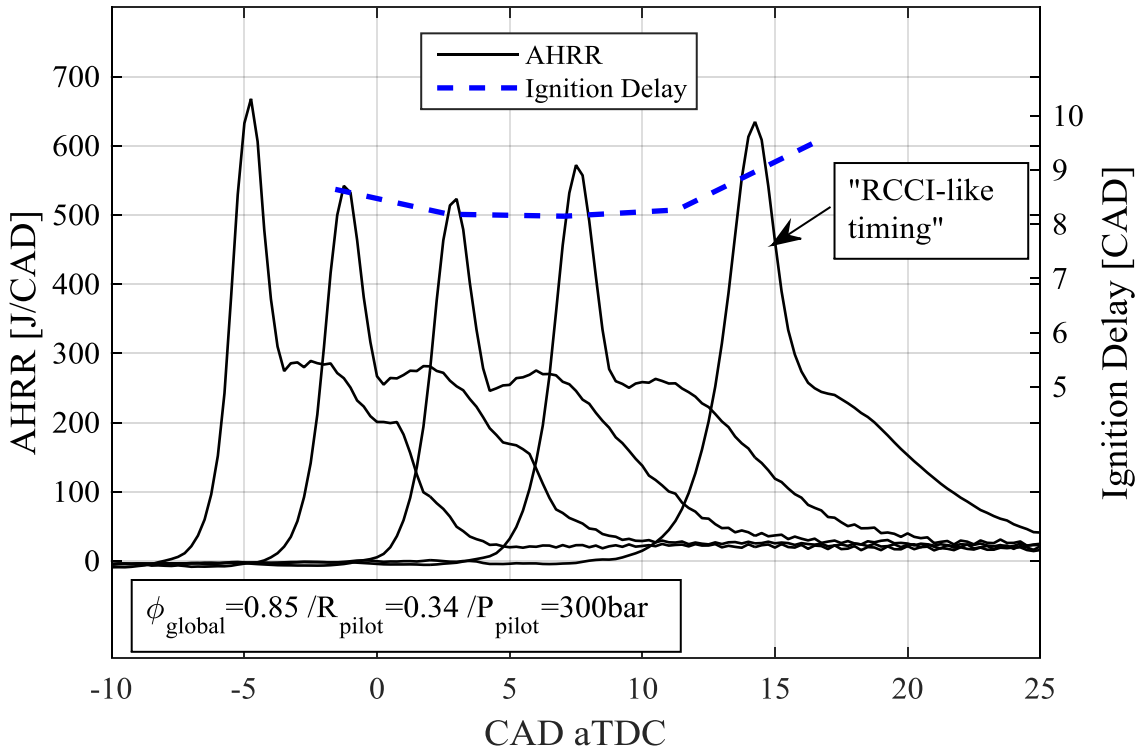

Figure 21: AHRR trends for sweep of commanded pilot injection timing, θ_{pilot}, for θ_{pilot}=-12,-8,-4,+0,+4°CA aTDC for an operating point exhibiting increased peak AHRR at late θ_{pilot}.

To increase the clarity of figures, all following data sets will present trends for a selected 'best' timing for each operating point. The 'best' timing at each operating point was manually selected based on lowest emissions of CH_4, NO_x, CO and highest gross indicated mean effective pressure,

GIMEP. These criteria were in competition with one another and, generally, a clear best compromise was evident. An example of the selection based on competing criteria is presented in Figure 22. The 'very-late timing' was not selected as a best timing for any operating point due to high emissions of CO, HC and low GIMEP. All selected 'best timing' points exhibited typical stage 1 combustion as presented in the above discussion followed by a stage 2 combustion event.

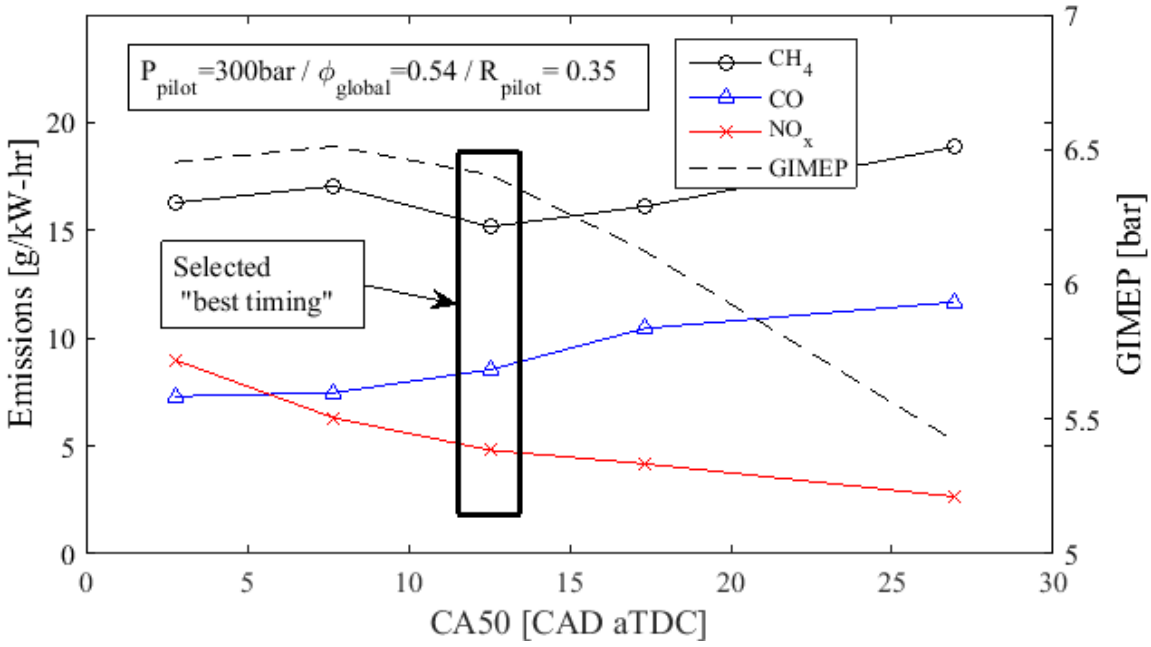

Figure 22: Example of trade-off between emissions performance and GIMEP used to select 'best timing' for a given operating point and P_{pilot}.

4.3.3 Pilot Ratio and Equivalence Ratios

Different combinations of pilot and premixed fuel (R_{pilot}) can be used to meet a given load requirement. The fueling strategy employed to satisfy the load demand has numerous implications on the relative importance and characteristics of the different stages of combustion present and as a result, the engine-out emissions. In this section, several important trends are

presented as a function of φ_{global}, R_{pilot} and the P_{pilot}, by means of 'performance maps'. To lend context to the selected operating points, trends in common engine performance metrics are presented first. Next, trends in key AHRR metrics for DIDF combustion, which are introduced in §4.2, are presented, followed by trends in the emissions of CH_4 and NO_x.

The performance maps show trends across the R_{pilot}- φ_{global} space and are consistently shaded so that trends across pilot injection pressures can also be viewed. Contours across the maps are generated by cubic interpolation between the single data points at each R_{pilot}- φ_{global} location (actual measurement points represented by black dots). Lines of constant φ_{CH4}, which roughly correspond to the tested conditions are also plotted to clarify any correlations between φ_{CH4} and the plotted metric. The presented data reflects the selected 'best timings' from each operating point.

Efficiency, Fuel Consumption, Mean Effective Pressure

The variation of common engine performance metrics across the R_{pilot}-φ_{global} operating space are presented so that comparison of the investigated operating points against other engine performance investigations can be made. The selected performance metrics are GIMEP, gross indicated specific fuel consumption (GISFC), and thermal efficiency ($\eta_{thermal}$).

Figure 23 presents the trends of GIMEP across the R_{pilot}-φ_{global} operating space at P_{pilot}=300, 800, and 1300bar. Across the majority of the investigated operating space, GIMEP appears to be linearly proportional to φ_{global}; indicated by approximately horizontal contours. This behaviour is expected because the research engine used in this investigation was naturally aspirated. It is also

observed that the GIMEP is not a strong function of P_{pilot}. It should be noted that the presented data points correspond to operating points with best compromise of emissions and GIMEP (see Figure 22). The trends observed in GIMEP and other presented metrics may be different if another set of pilot timing criteria were applied.

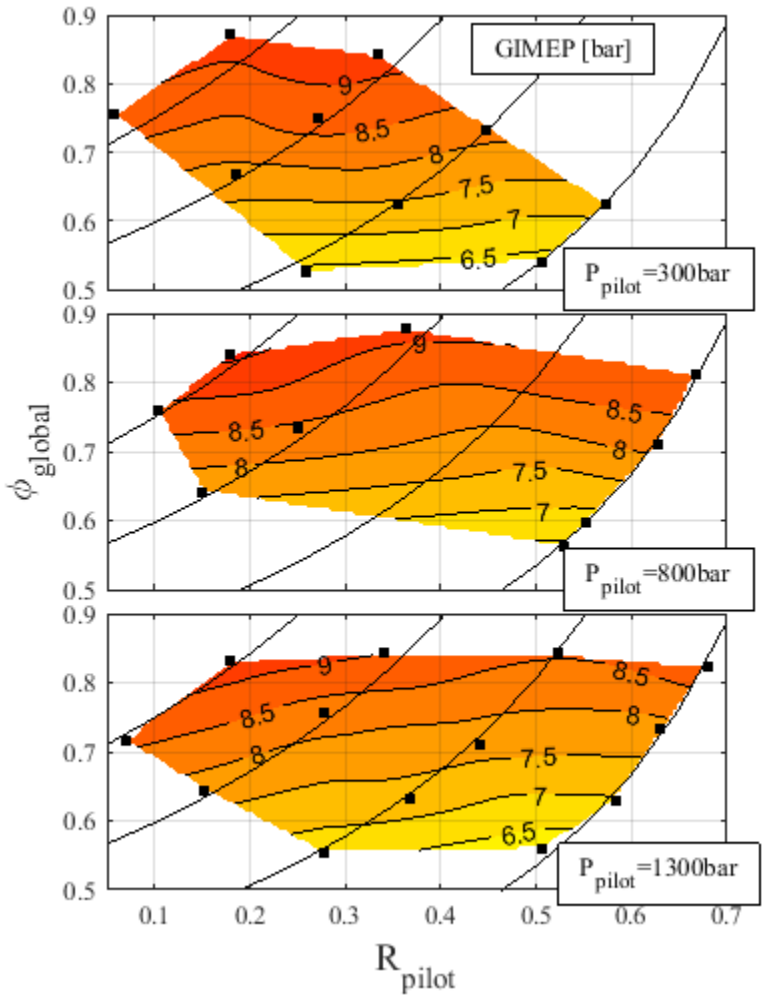

Figure 23: Contour plots of GIMEP across the R_{pilot}-φ_{CH4} operating space for P_{pilot}=300, 800, and 1300bar and best θ_{pilot}.

In Figure 24 and Figure 25, the variation of GISFC and $\eta_{thermal}$, respectively, are shown across the R_{pilot}-φ_{global} operating space for P_{pilot}=300, 800, and 1300bar. For a given φ_{global}, generally

more efficient engine operation is observed for a smaller R_{pilot}. For small R_{pilot}, there is little variation in the engine efficiency across different P_{pilot}. At high R_{pilot}, however, substantially lower efficiencies are observed with increasing P_{pilot}. It is possible that the combination of high P_{pilot} for the long single-pulse pilot injections required to achieve high R_{pilot} operation caused significant liquid diesel impingement on the piston bowl wall, however further investigation is required to confirm this. It is expected that in real-world applications, the use of a split-injection pilot strategy would substantially alter the trends observed in these efficiency maps.

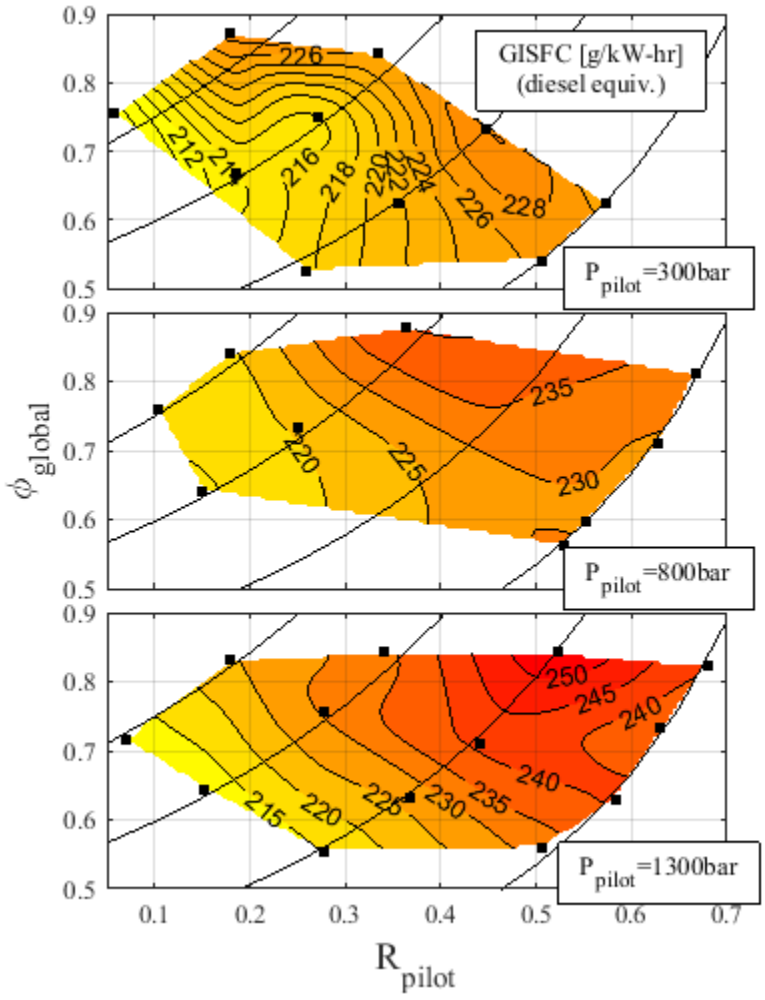

Figure 24: Contour plots of GISFC across the R_{pilot}-φ_{CH4} operating space for P_{pilot}=300, 800, and 1300bar and best θ_{pilot}.

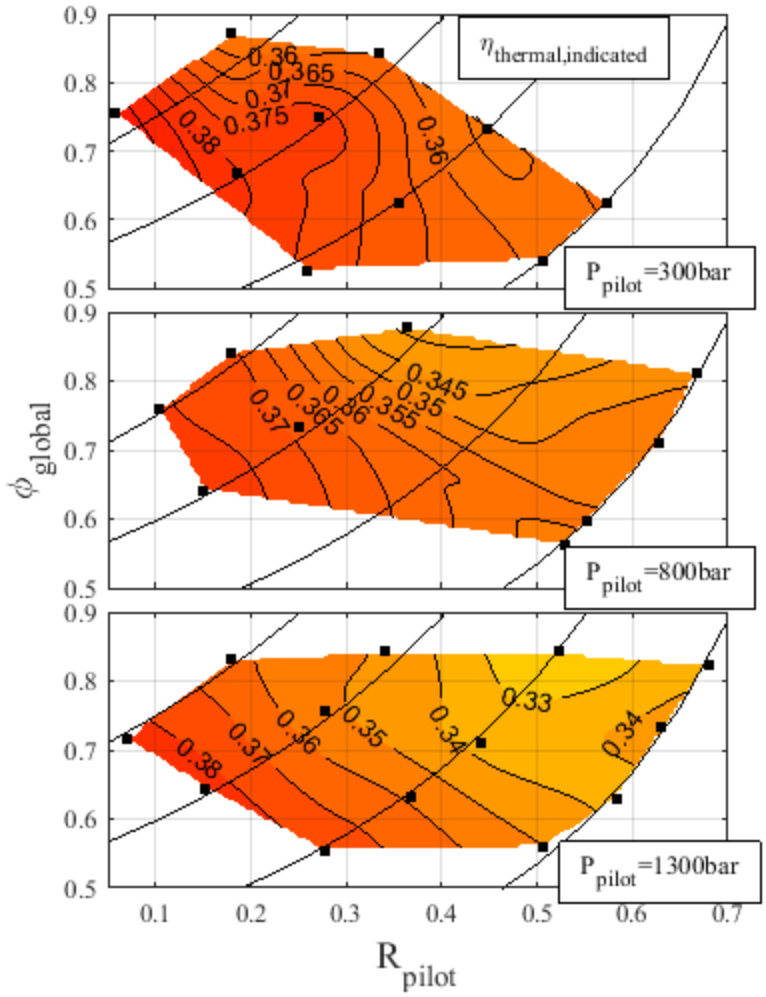

Figure 25: Contour plots of $\eta_{thermal}$ across the R_{pilot}-φ_{CH4} operating space for P_{pilot}=300, 800, and 1300bar and best θ_{pilot}.

Stages of Combustion

In §4.2 the definition and significance of stage 1, 2a, and 2b combustion in DIDF operation was introduced and discussed. Stage 1 and 2 of DIDF combustion (see Figure 17) are qualitatively very different, and in the reviewed literature, are typically associated with diesel-pilot and premixed CH_4 combustion mechanisms, respectively. Based on the literature, it is expected that mechanisms present in the diesel-dominated stage 1 combustion will have a strong influence on

emissions of NO_x [16,17], while the stage 2 combustion mechanisms will influence emissions of CH_4 and CO more substantially [23,29].

To simplify presentation of a large data set, a single, representative scalar metric for each of the identified stages of combustion (1, 2a, 2b) was identified. Here, stage 1, stage 2a, and stage 2b combustion is characterized by $q_{1,max}$, $q_{2a,mean}$, and Q_{2b}/Q_{tot}, respectively. Mathematical definitions of the selected metrics are presented in §4.2. The selection of these metrics attempted to capture characteristic properties of each combustion stage; $q_{1,max}$ is expected to be proportional to the premixed fraction of diesel and entrained CH_4 by the pilot jet, which react rapidly in a premixed auto-ignition mode. $q_{2a,mean}$ gives an indirect measure of the speed and/or intensity of the turbulent flame propagation (discussed in §4.2) expected to occur following stage 1 combustion, and Q_{2b}/Q_{tot} indicates the amount of fuel remaining following the high-intensity reactions occurring in stages 1 and 2a, which must be converted by relatively weak and/or unstable combustion mechanisms in stage 2b.

As shown in Figure 26, $q_{1,max}$ is dependent on both φ_{global} and R_{pilot}, but only a weak function of φ_{CH4} (*i.e.* contours of $q_{1,max}$ are perpendicular to φ_{CH4}). For a given φ_{CH4}, increasing R_{pilot} was generally observed to increase $q_{1,max}$, indicating that the first combustion stage is predominantly influenced by the diesel pilot injection. In the P_{pilot}=1300bar case, a significant region (low R_{pilot} and low φ_{global}) appears to be relatively flat indicating that the mass of the pilot in these cases had a reduced effect on $q_{1,max}$ compared to lower injection pressures, where a levelling off of $q_{1,max}$ trends was only observed for the largest diesel injection masses (high R_{pilot} and high φ_{global}).

It is unexpected that $q_{1,max}$ is fairly independent of φ_{CH4} for the majority of the investigated operating space; a higher premixed mass of fuel entrained by the pilot jet is expected with a higher φ_{CH4}. A marginal increase in the apparent dependence of $q_{1,max}$ on φ_{CH4} is noted for the low R_{pilot} and high P_{pilot} cases. It is possible that the pilot mixing/entrainment rates and CH_4 concentrations for the majority of the investigated operating space are too low to observe the effect of increased CH_4 entrainment by the pilot jet. This conclusion, however, requires further investigation.

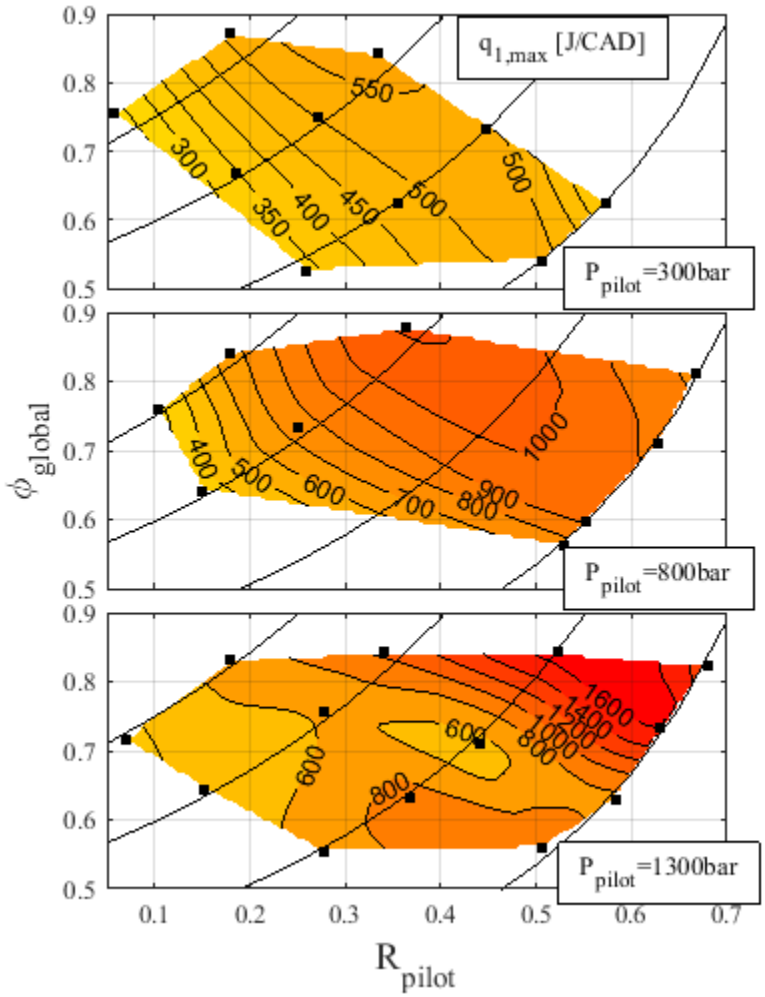

Figure 26: Contour plots of peak AHRR of stage 1 combustion, $q_{1,max}$, across R_{pilot}-φ_{CH4} operating space for P_{pilot}=300, 800, and 1300bar and best θ_{pilot}.

$q_{2a,mean}$ shows a strong dependence on φ_{CH4}, as evidenced by contours being approximately parallel with iso-lines of φ_{CH4} in Figure 27. $q_{2a,mean}$ decreases with decreasing φ_{CH4}, with decreased sensitivity at low φ_{CH4}. Unlike the stage 1 combustion metric ($q_{1,max}$, Figure 26), the second stage combustion characterized by the mean AHRR, is not strongly affected by the pilot injection pressure.

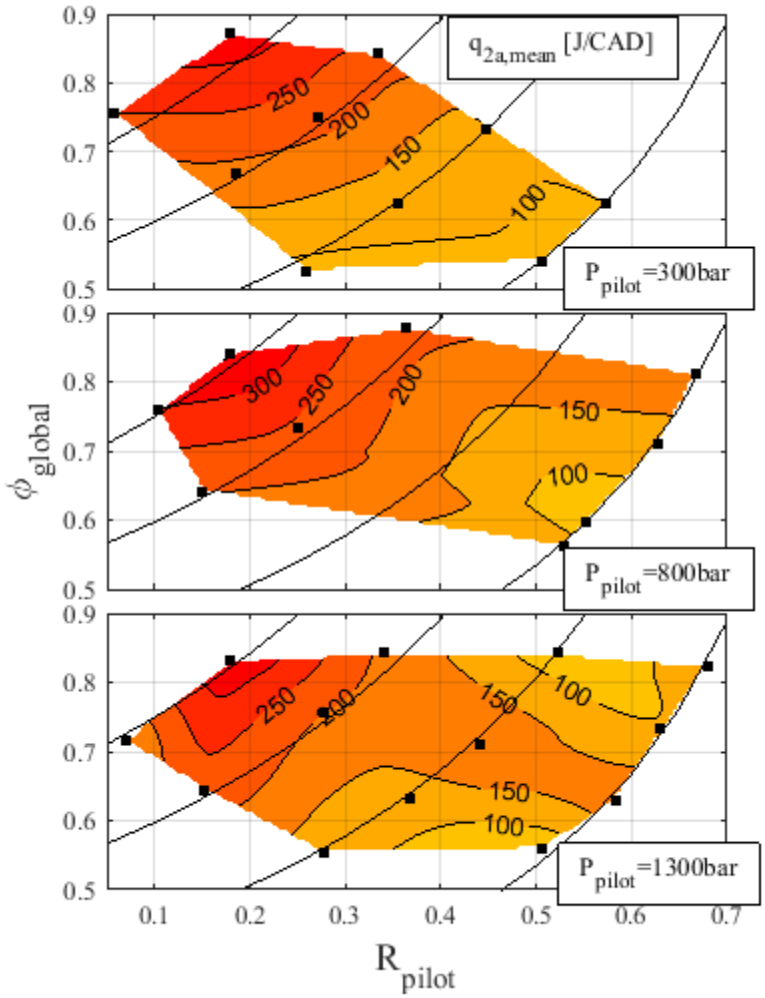

Figure 27: Contour plots of mean AHRR of high-intensity portion of stage 2 combustion, $q_{2a,mean}$, across R_{pilot}-φ_{CH4} operating space for P_{pilot}=300, 800, and 1300bar and best θ_{pilot}.

For the majority of the R_{pilot}- φ_{global} operating space, there appears to be only a weak influence of φ_{global} and R_{pilot} on the fraction of energy released in the low-intensity, stage 2b combustion, as

shown in Figure 28. For operating points having the very highest pilot injection masses (high φ_{global} and R_{pilot}), an increase in the fraction of the total energy released in the late stage combustion is observed. Examination of AHRR traces from the operating points with $R_{pilot}>0.5$ reveals little indication of the 'high-intensity' stage 2a combustion zone observed for all other points, causing a larger range to be labeled 'low-intensity' resulting in increased fractions of energy release. This may be an artefact of the algorithm used to define the transition points between the stages of combustion. A strong dependence of the second stage energy fraction on the injection pressure is noted, in agreement with the trends shown in Figure 19. A similar trend in emissions of CH_4 was also noted (see Figure 30).

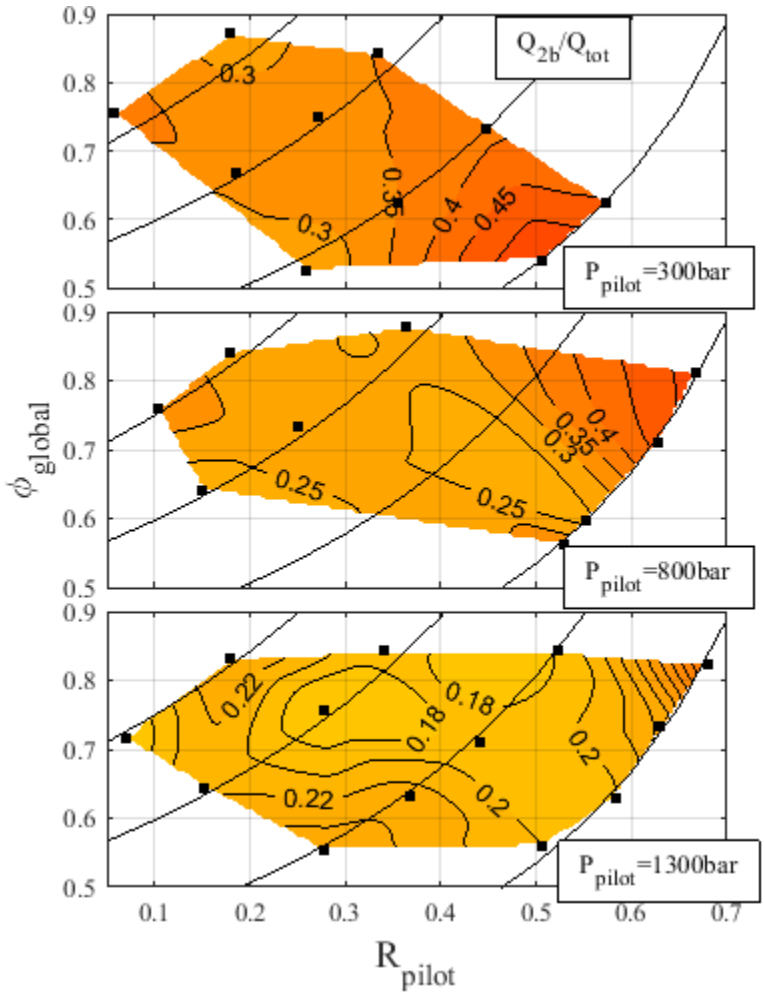

Figure 28: Contour plots of fraction of total cycle energy released during low-intensity portion of stage 2 combustion, Q_{2b}/Q_{tot}, across R_{pilot}-φ_{CH4} operating space for P_{pilot}=300, 800, and 1300bar and best θ_{pilot}.

Impact on Emissions

Figure 30 presents NO_x trends across the investigated operating points. For P_{pilot}=300bar and 800bar, increasing emissions of NO_x correlate strongly with increasing φ_{CH4}, but show little to no relationship to increasing m_{pilot}, which contradicts observations made in some previous investigations [20,23] and requires further study. For P_{pilot}=1300bar, a sharp increase in NO_x

emissions, with increasing m_{pilot} is observed. Generally, emissions of NO_x are observed to increase with increasing P_{pilot}, consistent with the findings of other investigations [18,20,23].

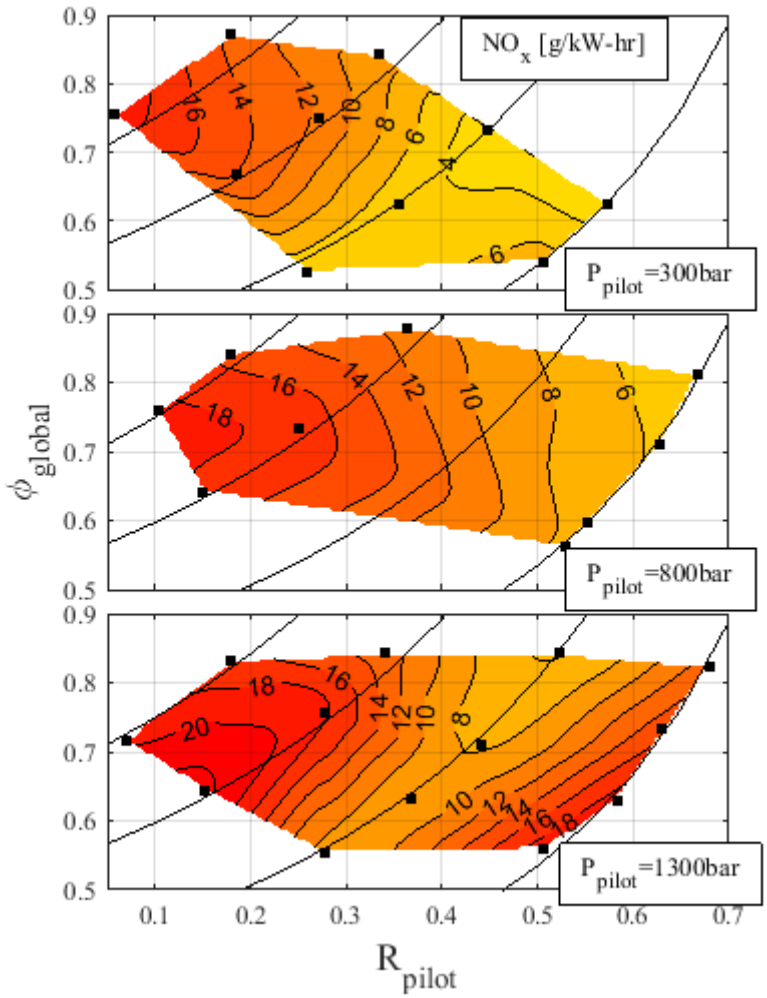

Figure 29: Contour plots of NO_x emissions across R_{pilot}-φ_{CH4} operating space for P_{pilot}=300, 800, and 1300bar and best θ_{pilot}.

In Figure 30, emissions of CH_4 are presented. The primary variable of influence was observed to be φ_{global}, denoted by the horizontal contours of emissions. An apparently weak sensitivity to φ_{CH4} is noted, which does not match the findings of [29] for φ_{CH4} variation with a constant pilot

injection mass. However, in this investigation, measurement points were not performed for constant pilot masses, so it is difficult to compare these findings. A strong sensitivity of CH_4 emissions to P_{pilot} between P_{pilot} = 300—800bar is observed, consistent with previous findings of others, however there exists negligible sensitivity to P_{pilot} for P_{pilot}=800—1300bar.

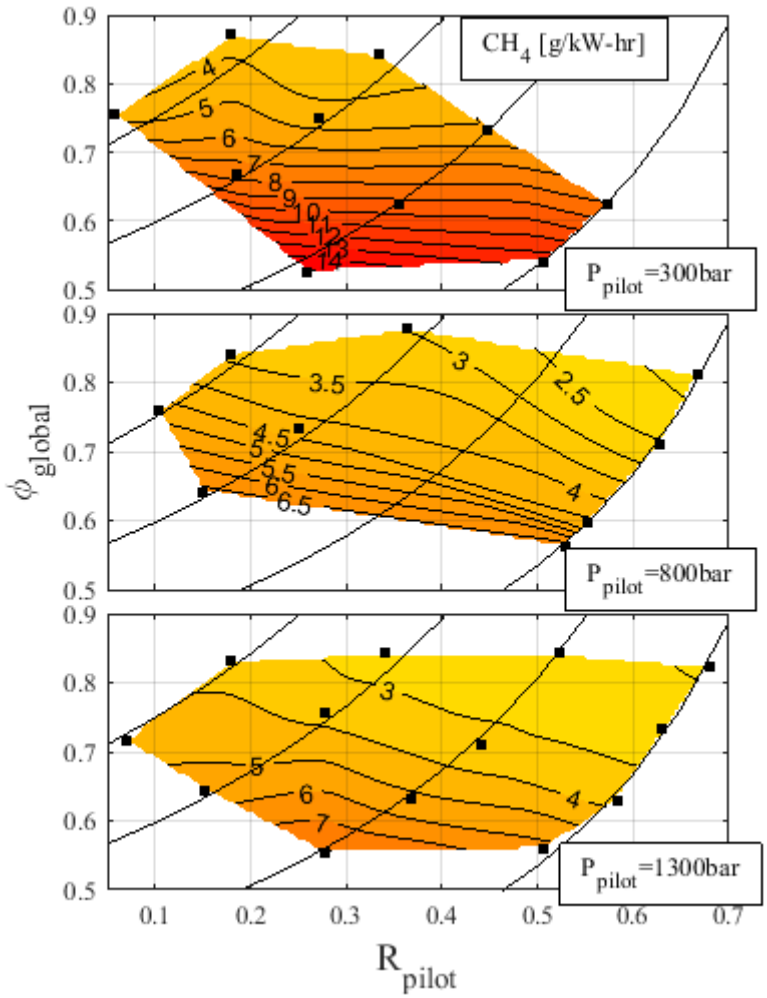

Figure 30: Contour plots of CH_4 emissions across R_{pilot}-φ_{CH4} operating space for P_{pilot}=300, 800, and 1300bar and best θ_{pilot}.

4.4 Discussion

In this section, discussion regarding the characteristics of the three identified stages of combustion (1, 2a, 2b) will be presented and the important combustion mechanisms will be

highlighted. Using the observed characteristics of each combustion stage, distinct regimes of DIDF operation, in terms of the R_{pilot}-φ_{global} operating space, are identified and further explored.

4.4.1 Stages of DIDF Combustion

The objective of this section is to identify likely combustion mechanisms present in each of the combustion stages (1, 2a, 2b) through discussion and exploration of trends in the measured data for each individual stage.

Stage 1 Combustion

The conventional description of the stage 1 combustion, as given by the literature, is rapid combustion of the fully premixed diesel pilot in addition to entrained CH_4 by the pilot jet and CH_4 in the vicinity of the pilot ignition sites [23]. Across wide ranges of P_{pilot} and R_{pilot}, however, it is not immediately clear that only this combustion mechanism is present during stage 1 combustion.

Based on the θ_{pilot}, commanded injection duration, and an estimation of the common rail fuel system response time from injector spray visualizations, a positive injection dwell (the commanded end of injection occurs before the start of combustion) was estimated for all tested operating points. It is therefore expected that a significant fraction of the diesel pilot is premixed to a combustible mixture at the start of combustion (θ_1, see Figure 17). Significant pilot injection premixing is expected because of the application of single-injection pilot strategy and the increased ignition delay typically noted in dual-fuel operation (cooler charge and competition for pre-combustion radicals between CH_4 and diesel [25]). Given longer ignition delays or higher

mixing rates of the pilot fuel jet, larger fractions of the pilot fuel combustion are expected to occur as pre-mixed auto-ignition.

Figure 26 demonstrates that higher P_{pilot} resulted in higher peak AHRRs in the first stage of combustion across the majority of the DIDF operating space. If the stage 1 combustion is considered to be premixed combustion (as in [23]), then higher $q_{1,max}$ indicates that a greater mass of diesel was in vapour phase and available for pre-mixed auto-ignition and/or a greater mass of CH_4 was entrained into the pilot jet. Increasing the diesel pilot mass (m_{pilot} or φ_{diesel}) also increased $q_{1,max}$, consistent with findings of others [20,23].

Figure 31 indicates the effect of m_{diesel} on the amount of energy released in stage 1 combustion, as a fraction of the total energy released, Q_1/Q_{tot}. For each P_{pilot}, a maximum Q_1/Q_{tot} was observed. For smaller m_{diesel} quantities, increasing the injected pilot mass increased the fraction of total cycle energy released during stage 1 combustion. Above a threshold, however, increasing m_{pilot} begins to cause a reduction in the fraction of total cycle energy released in stage 1 combustion, indicating that the additional injected diesel is not contributing to the pre-mixed combustion event heat release to the same extent, and is instead contributing to heat release in later stages of combustion. The combustion mechanism by which the diesel contributes to stage 2 heat release is unclear; it may be through the development of a mixing-controlled flame or as a vapour that is mixed with the surrounding CH_4 and air and is converted during stage 2 flame propagation. The threshold mass of diesel where additional m_{diesel} causes a reduction of Q_1/Q_{tot} is greater for higher P_{pilot}. It is likely that, with higher $P_{pilot,\ a}$ greater maximum m_{diesel} can be premixed sufficiently for stage 1 auto-ignition.

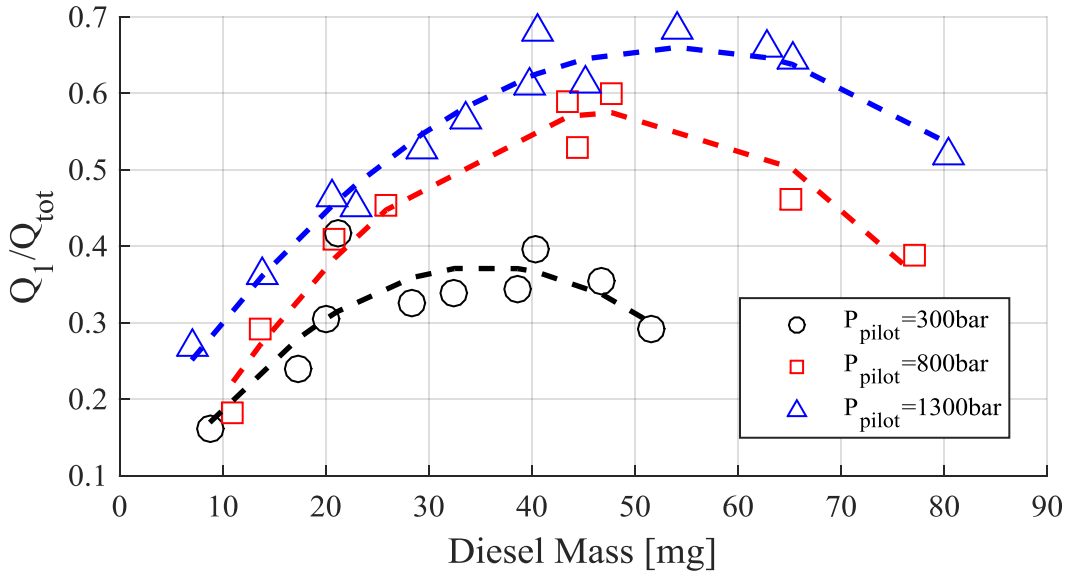

Figure 31: Effect of m_{diesel} on fraction of energy released in stage 1 combustion (Q_1/Q_{tot}).

The authors of [34] proposed a phenomenological model for the combustion of pilot-injections in diesel-only combustion wherein flame propagation through premixed diesel vapour surrounding the ignition sites is a prominent mechanism (occurring coincidentally with auto-ignition though out the premixed diesel vapour – air phase); and may extend into the stage 2 combustion in some cases. This mode of combustion qualitatively matches the bell-shaped single peak combustion observed in the diesel-only measurements made in this investigation.

It is expected that P_{pilot} will have a strong effect on the pilot jet structure, and accordingly the entrainment of air and CH_4 into the diesel pilot jet. It was inferred from Q_1/Q_{tot} in Figure 31, that for sufficiently small pilot injection masses, a maximum 'effective' P_{pilot} existed, above which only a minimal increase in the mass of fuel, that is sufficiently prepared for rapid stage 1 combustion was observed (P_{pilot}=800bar, in this case). When the injected pilot mass exceeds a

threshold value, a limit to the 'useful' injection pressure is no longer observed, coinciding with an observed increase in NO_x for large pilot injections at P_{pilot}=1300bar observed in Figure 29. An assumption in the diesel-vapour flame propagation model proposed in [34] is that the pilot injection mass is sufficiently small for complete evaporation of the entire pilot mass. The observed maxima for each P_{pilot} in Figure 31 may be the point that the validity of this assumption breaks down, for the engine and conditions considered in the current work.

Stage 2a Combustion

As described in §2.1, the combustion of the premixed CH_4 is expected to take place via a turbulent flame propagation event. As a crude approximation of the turbulent flame speed, the mean AHRR of stage 2a combustion, $q_{2a,mean}$ was investigated. The effects of φ_{CH4} on $q_{2a,mean}$ are presented in Figure 32. A strong positive correlation is observed for $\varphi_{CH4} > 0.4$, which is qualitatively similar to the linear relationship between φ_{CH4} and $s_{l,CH4}$ observed in published laminar flame research [55] reinforcing the hypothesis that the stage 2 combustion in these cases can be characterized as flame propagation.

For cases with $\varphi_{CH4} < 0.4$, $q_{2a,mean}$ remains constant with decreasing φ_{CH4}, which is inconsistent with flame propagation theory, suggesting that a mode of combustion other than flame propagation is dominant in these cases. These cases coincide with the operating points in Figure 31, where increasing m_{diesel} was shown to increase the amount of diesel consumed following the stage 1 combustion event. It is possible that these cases correspond to either mixing-controlled diesel combustion, or instances of substantial participation of diesel vapour in the stage 2 flame propagation event.

The correlation between φ_{global} and the mean AHRR of the stage 2 combustion was observed to be positive, but much weaker than the correlation with φ_{CH4}. This indicates that, φ_{CH4} is the more relevant mixture property for describing stage 2 flame propagation.

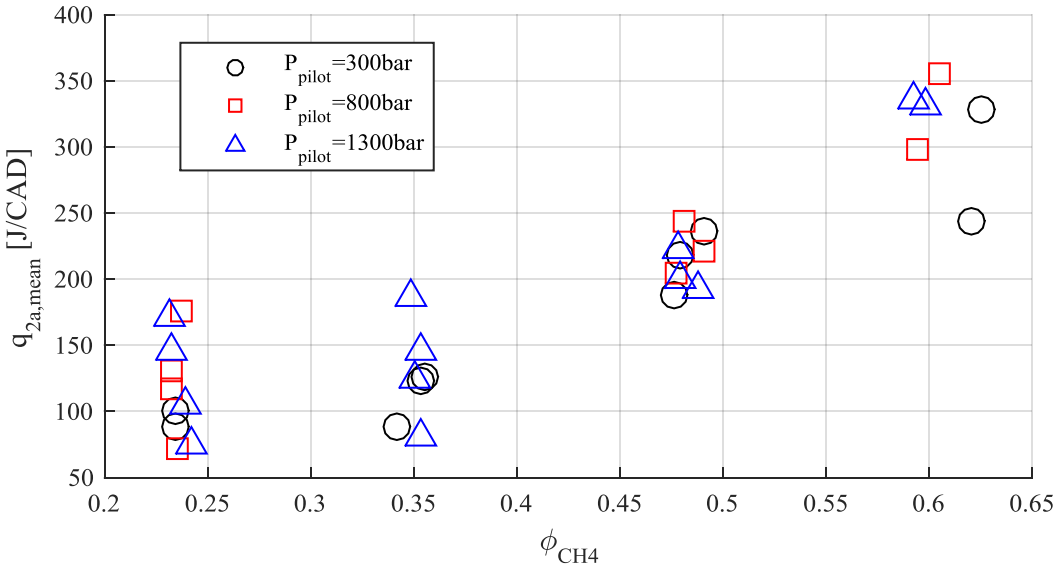

Figure 32: Impact of φ_{CH4} on stage 2 combustion mean AHRR ($q_{2a,mean}$).

Stage 2b Combustion

The low intensity portion of stage 2 combustion is distinguished from the end of the high intensity portion by a decrease in the rate of AHRR decay (*i.e.* dAHRR/dθ has a positive slope, see Figure 17), despite decreasing charge temperatures resulting from cylinder expansion. This stage of combustion is characterized by much lower AHRRs and much longer durations than the previous stages of combustion.

No correlation between φ_{CH4} and $q_{2b,mean}$ is observed, indicating that the combustion processes present should not be considered as flame propagation. The only clearly observed trend in the stage 2b combustion is in relation to P_{pilot} (Figure 19), where the indirect effect of increasing Q_1/Q_{tot} reduces the amount of fuel remaining for later stages of combustion. Description of stage 2b combustion as late burn-out of the remaining fuel in the cylinder seems appropriate, but cannot be rigorously supported by the measurements in this work.

4.4.2 Operating Regimes of DIDF Combustion

For operating points with $\varphi_{CH4} > 0.4$, combustion characteristics consistent with flame propagation, particularly the dependence of combustion intensity (presented as mean AHRR in Figure 32), were observed. For $\varphi_{CH4}<0.4$, no correlation between the intensity of second stage combustion and φ_{CH4} was observed, indicating that a combustion mode not consistent with flame propagation is prevalent in these cases.

Figure 33 illustrates the identified boundaries of the second stage combustion mode across the explored dual-fuel operating space. Note that the precise locations of boundaries presented are calculated based on the locations of the experimental data gathered in this investigation. Different boundary locations are expected if a different engine, fuel combination or baseline operating conditions (*e.g.* engine speed, EGR, *etc*.) were to be considered. Furthermore, the identified boundary represents a transitionary region of the operating map. It is expected that a gradual transition between flame propagation and non-flame propagation in stage 2 combustion would be observed around $\varphi_{CH4}=0.4$ if a high resolution sweep of φ_{CH4} were performed. The following subsections highlight the distinguishing features of each operating mode.

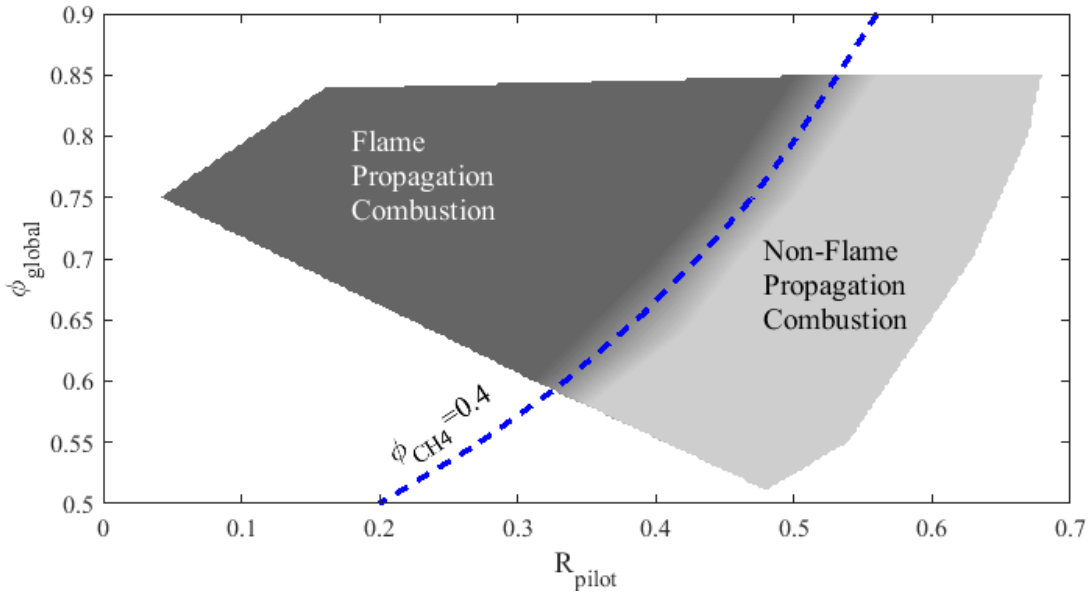

Figure 33: Proposed division of DIDF operating space based on stage 2 combustion mechanisms for all pilot injection pressures.

Non-Flame Propagation Regime

In the non-flame propagation regime, the mixture remaining after the pre-mixed auto-ignition combustion event is unable to sustain a flame propagation event. This behaviour was observed when φ_{CH4} was too low to propagate a stable flame and/or when the R_{pilot} was sufficiently high. Because R_{pilot} is necessarily increased as φ_{CH4} is reduced, it is not evident whether the value of R_{pilot} plays a role in second stage combustion flame propagation in addition to the φ_{CH4} effects previously discussed. It is possible that if a large enough portion of the total fuel (diesel and CH_4) is consumed in the stage 1 combustion, not enough unburned mixture volume or mass remains to propagate a discernable flame front(s), however further investigation is required to support this conclusion.

Practically, the high R_{pilot} and low φ_{CH4} conditions in the non-flame propagation regime correspond to operating modes where low load (approximately proportional to φ_{global}, see Figure 23) is desired, but unburned emissions must be reduced. A conventional solution is to increase the proportion of pilot fuel; the efficacy of this strategy is presented in Figure 34.

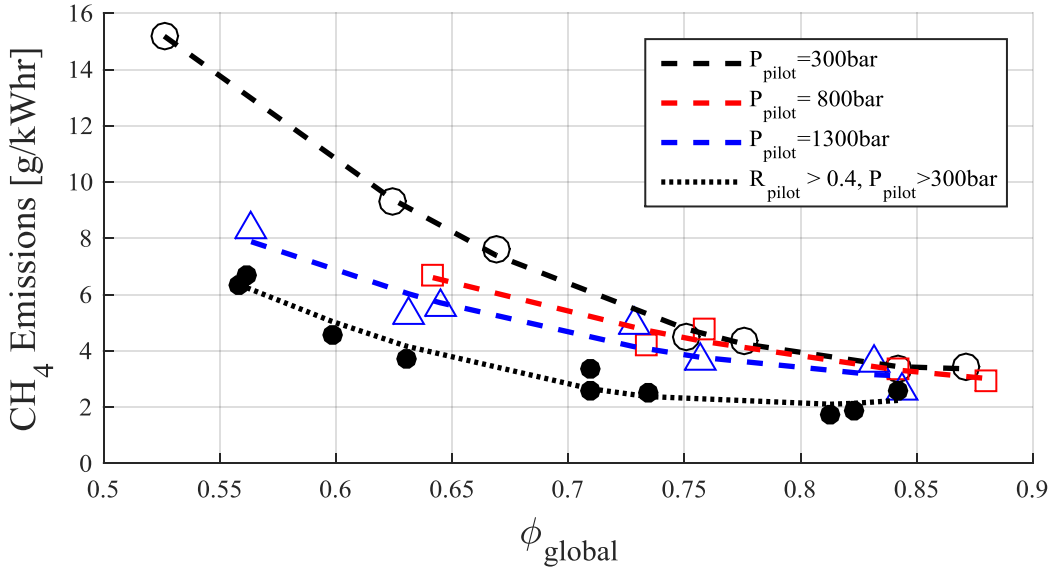

Figure 34: Effect of φ_{global} and pilot injection pressure on CH_4 emissions.

For a given φ_{global}, an increase in R_{pilot} requires the remaining lower equivalence ratio CH_4 to be converted by slow, late stage combustion processes. The slow, late stage combustion is expected to contribute strongly to unburned combustion products. Figure 34 indicates that the application of pilot injections with R_{pilot}>0.4 (indicated by filled-in figures) is a more effective method of controlling CH_4 emissions than increasing φ_{CH4}. In Figure 34, in all cases with P_{pilot} > 300bar, for a given φ_{global}, the pilot-dominated operating mode (R_{pilot}>0.4) yields lower CH_4 emissions than operating modes with a flame propagation combustion mechanism. CH_4 emissions may also be

reduced through an increase of P_{pilot} to 800bar, though there is only a marginal advantage in increasing P_{pilot} beyond 800bar in this application.

A comparison of the relative contribution of the diesel and CH_4 to the dual-fuel AHRR is presented in Figure 35. Comparison of the CH_4-only and diesel-only AHRRs indicates that the pre-mixed auto-ignition of the diesel pilot fuel is the predominant feature of the dual-fuel combustion mode. Some CH_4 is entrained in the large diesel injection, but the majority of the heat release results from the diesel conversion. The calculated duration of stage 2a combustion is very narrow and, as discussed above, not attributed to flame propagation through the premixed CH_4, but rather a transition region from the end of the 1st stage pre-mixed combustion event to the slow conversion processes of the stage 2b combustion. Again it should be noted that the 'CH_4-only' AHRR is the simple arithmetic difference of the DIDF and diesel-only AHRRs (see equation (8)) and is not a direct measurement of the CH_4 conversion rate. The 'CH_4-only' AHRR can be used as a qualitative visualization of the effect of CH_4 addition to the diesel combustion.

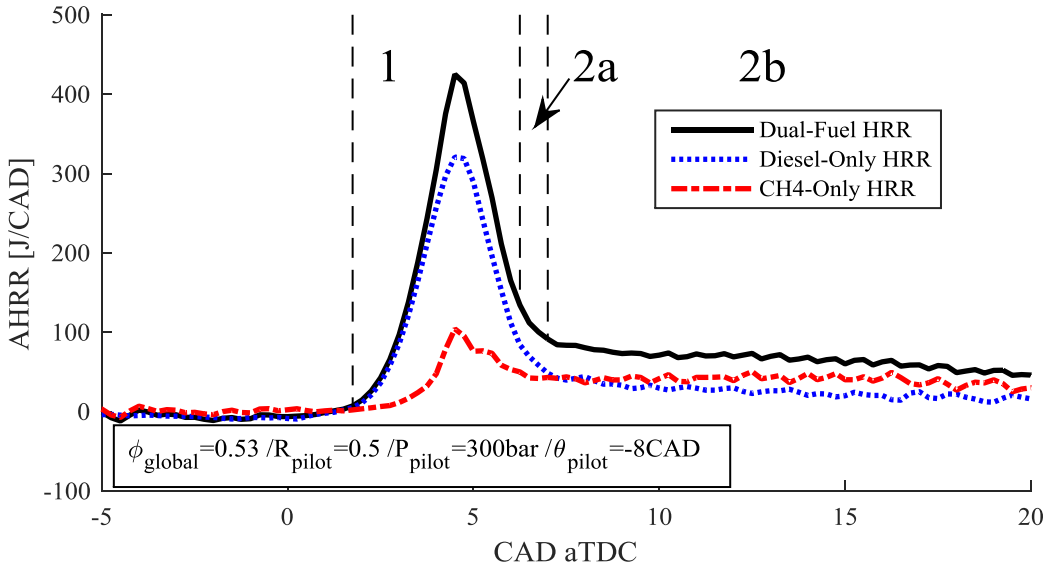

Figure 35: Comparison of DIDF and diesel-only AHRRs for typical operating point found in the 'non flame propagation' regime

A major draw-back of large diesel pilots is expected to be increased emissions of NO_x due to higher expected combustion temperatures. Larger fuel-rich regions, may also form higher PM concentrations, however PM emissions measurements were not taken in this work. In Figure 29, the trade-off between NO_x and pilot mass (represented by R_{pilot} along lines of constant φ_{global} in Figure 29) is only apparent for P_{pilot}=1300bar. In Figure 36, a positive correlation between Q_1/Q_{tot} and emissions of NO_x is clearly observed for operating points classified as not exhibiting flame propagation in stage 2 combustion. In Figure 36, operating points where flame propagation was determined to occur (open markers in Figure 36) produced higher NO_x emissions than operating points classified as not possessing flame propagation mechanisms in stage 2 combustion, for a given Q_1/Q_{tot}. This observation indicates that in cases where second stage combustion is characterized by flame propagation, NOx emissions are less dependent on the pilot combustion (represented by Q_1/Q_{tot}) and more dependent on the flame propagation. These

observations contradict the conventionally observed trend of increased NO_x emissions being most closely linked to the pilot combustion event [16,23] and need to be further investigated.

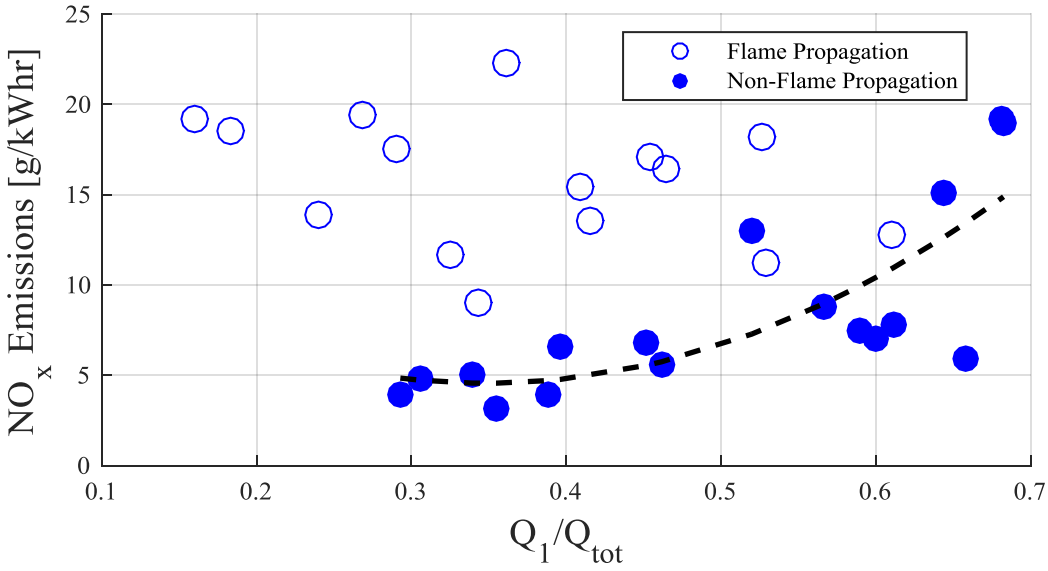

Figure 36: Correlation between the fraction of energy released in stage 1 combustion (Q_1/Q_{tot}) and emissions of NOx (g/kW-hr). Filled figures indicate points categorized as not possessing flame propagation by Figure 33.

Flame Propagation Regime

The flame propagation regime consists of operating modes with stage 2 combustion behaviour that is consistent with turbulent flame propagation. For this, the φ_{CH4} must be high enough to sustain a flame propagation event at the near-TDC pressures and temperatures present during engine operation. In this investigation, the threshold CH_4 concentration for stage 2 turbulent flame propagation was found to be $\varphi_{CH4}\approx 0.4$.

The comparison of the individual AHRR contributions of the diesel and pre-mixed CH_4 to the overall dual fuel AHRR shown in Figure 37, exemplifies a DIDF operating mode from the

'centre' of the explored dual-fuel operating space, where the presence of the two stages of combustion is evident in the AHRR.

In the stage 1 combustion (pre-mixed auto-ignition of diesel pilot and entrained CH_4), an increase in the ignition delay is noted between the diesel-only (dashed line) and dual-fuel (solid line). This is attributed to the pre-mixed CH_4 charge cooling effect and likely competition for radicals between the CH_4 and diesel molecules [25]. This increased ignition delay also results in the artifact of a negative calculated apparent CH_4 AHRR, indicating a limitation in the simple superposition approach used (see equation (8)). The stage 1 combustion is dominated by the pilot fuel, but there is evidence that some CH_4 is also entrained and converted in stage 1. With increasing R_{pilot}, the local equivalence ratio in the vicinity of the ignition sites is expected to be increased, resulting in higher peak AHRRs. This effect can be observed in Figure 26, where a strong positive correlation of $q_{1,max}$ on R_{pilot} is noted.

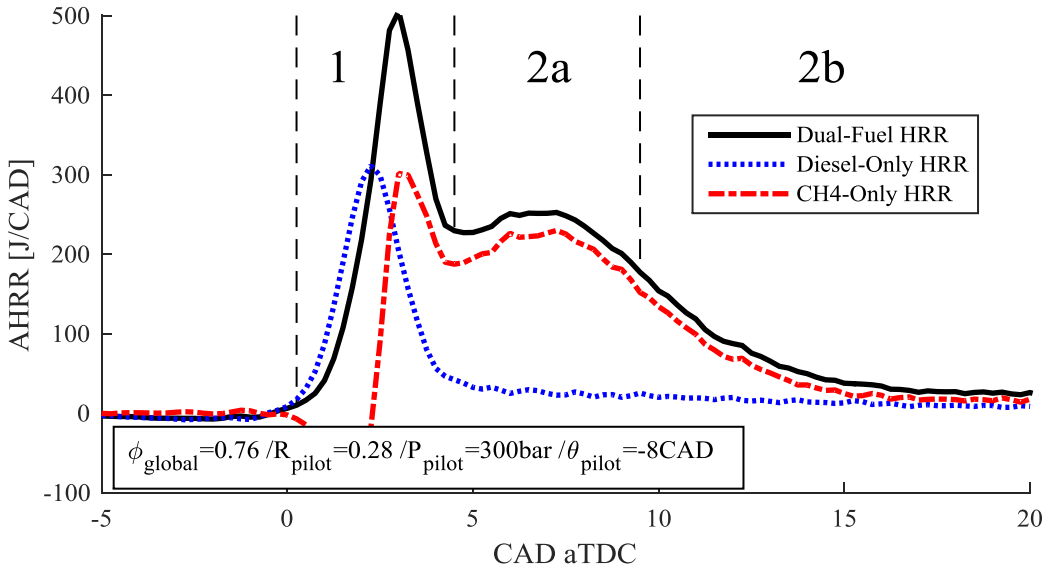

Figure 37: Comparison of dual-fuel and diesel pilot AHRRs for typical operating point within the 'flame propagation' regime.

In this work, stage 2 combustion is assumed to be flame propagation through primarily pre-mixed CH_4, however as φ_{diesel} is increased, increasing amounts of diesel will also participate in the second stage combustion; indicated by the negative trend in Q_1/Q_{tot} with respect to m_{diesel} for large pilot masses in Figure 31. Figure 38 shows a negative correlation between the flame propagation intensity, represented by $q_{2a,max}$ and CH_4 emissions. Above a maximum intensity ($q_{2a,max}$ > ~300J/CAD in this investigation), enhancing the AHRR during the flame propagation event no longer correlates to improvements in CH_4 emissions, indicating emissions are due to a different mechanism. It is possible that enhancement of flame propagation may improve combustion efficiency within the piston bowl, but crevice-volumes remain un-affected, resulting in a 'floor' for emissions improvement through increasing φ_{CH4}.

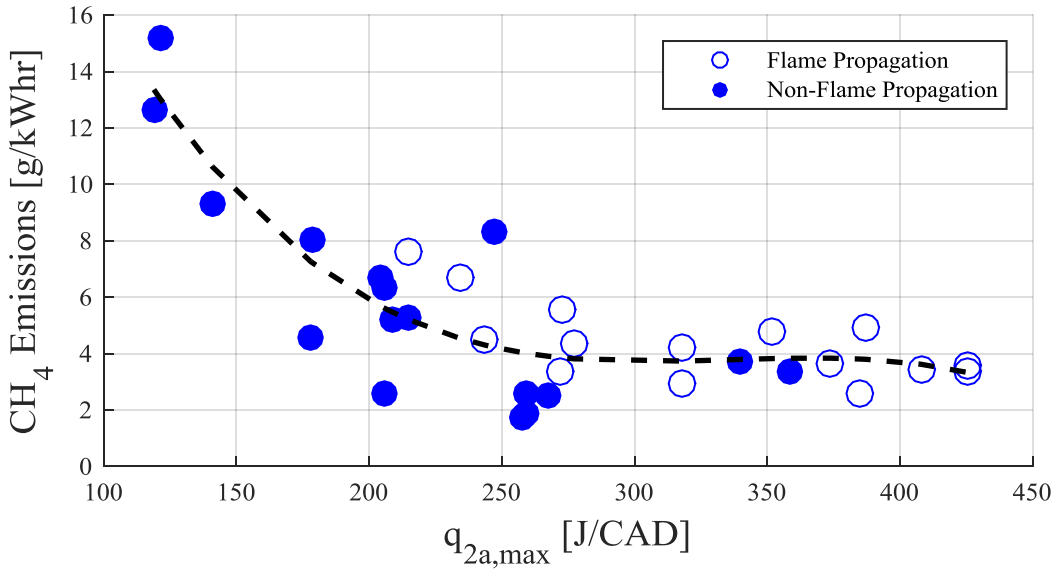

Figure 38: Effect of stage 2 combustion peak intensity ($q_{2a,max}$) on CH_4 emissions. Filled markers represent combustion modes indicated to possess flame propagation mechanisms in Figure 33.

Figure 39 presents the impact of $q_{2a,mean}$ on NO_x emissions, which complements the CH_4 emissions trend in Figure 38. Increasing $q_{2a,mean}$ is associated with increased φ_{CH4}, which will also result in increased combustion temperatures. These higher temperatures result in higher NO_x emissions via the Zeldovich mechanism. For pilot injection pressures of 300bar and 1300bar in Figure 29, the contours of NO_x emissions are parallel to the contours of φ_{CH4}, indicating a high degree of dependence on the pre-mixed fuel concentration.

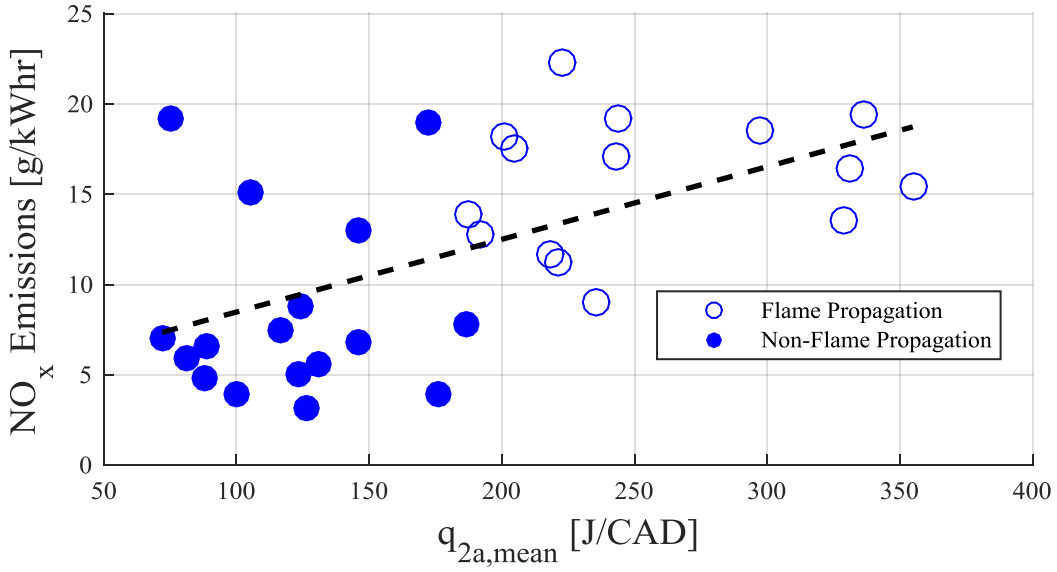

Figure 39: Effect of stage 2 combustion intensity (q2a,mean) on NO_x emissions.

Flame Propagation Regime Special Case: Pilot-Independence

Within the DIDF operating space characterized by the presence of a flame propagation event, a unique subset of measurement points was observed, where emissions and the shape of the AHRR

were not strong functions of P_{pilot} or θ_{pilot}. These measurement points were located in the data set having the highest φ_{CH4} (~0.62) and the lowest R_{pilot} (~0.06).

In Figure 23—Figure 30, the impact of injection pressure on engine performance, emissions of CH_4, NO_x and features of the 2 stages of combustion show minimal variance for this measurement point (denoted as "pilot-independent"). All other regions of the DIDF operating space show a strong dependence on pilot injection pressure. Figure 40 presents the emissions and GIMEP trends for all the measurements taken at the 'pilot-independent' operating point. Emissions of NO_x, CH_4, and CO are constant (within the experimental variability of the measurements) across all θ_{pilot} and all P_{pilot}. The measured GIMEP exhibited some dependence on injection timing; however this trend was substantially weaker than was observed across all other explored operating points. There is also a notable difference in measured GIMEP between the P_{pilot}=1300 and the P_{pilot}=300 and 800bar operating points. This discrepancy is at least partially due to only 2 measurements having been performed for P_{pilot}. It is expected that with additional measurements at P_{pilot}=1300bar, the GIMEP trends across all injection pressures would appear coincident.

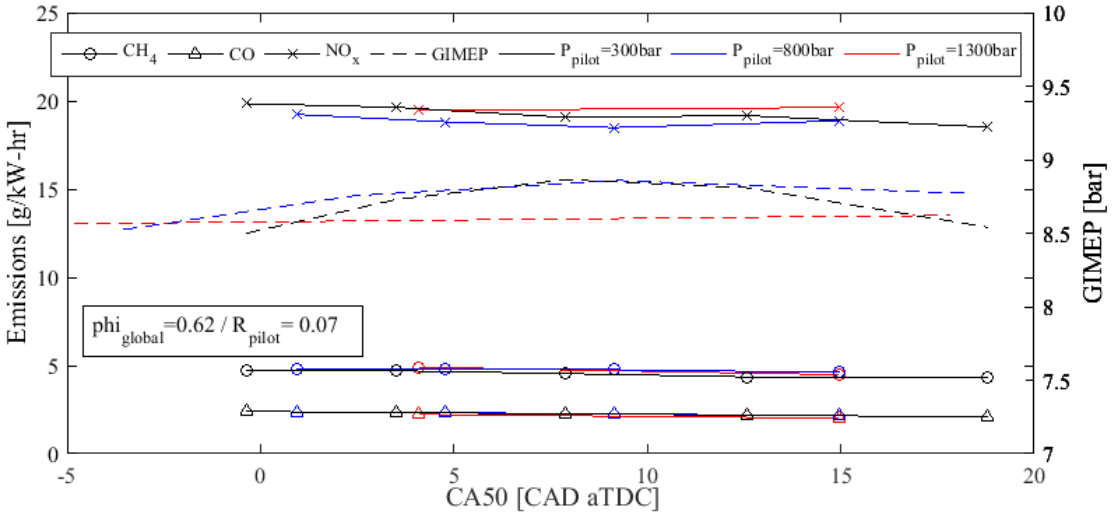

Figure 40: Emissions and GIMEP trends for all θ_{pilot} and P_{pilot} measurements in 'pilot-independent' operating point.

The pilot-independent AHRR in Figure 41 is predominantly composed of flame propagation through premixed CH_4, preceded by a relatively small pre-mixed auto-ignition event resulting from the pilot fuel and entrained CH_4. The diesel-only AHRR is largely completed by the time the stage 2 combustion (flame propagation) event begins in the DIDF AHRR. The AHRR calculated for the stage 1 combustion of the DIDF case is approximately 3 times greater than the diesel-only case, which suggests that the premixed CH_4 contributes more energy to both stage 1 and stage 2 combustion than the diesel pilot; the overall insensitivity of the DIDF combustion performance, in terms of emissions and AHRR shape, to pilot injection parameters logically follows.

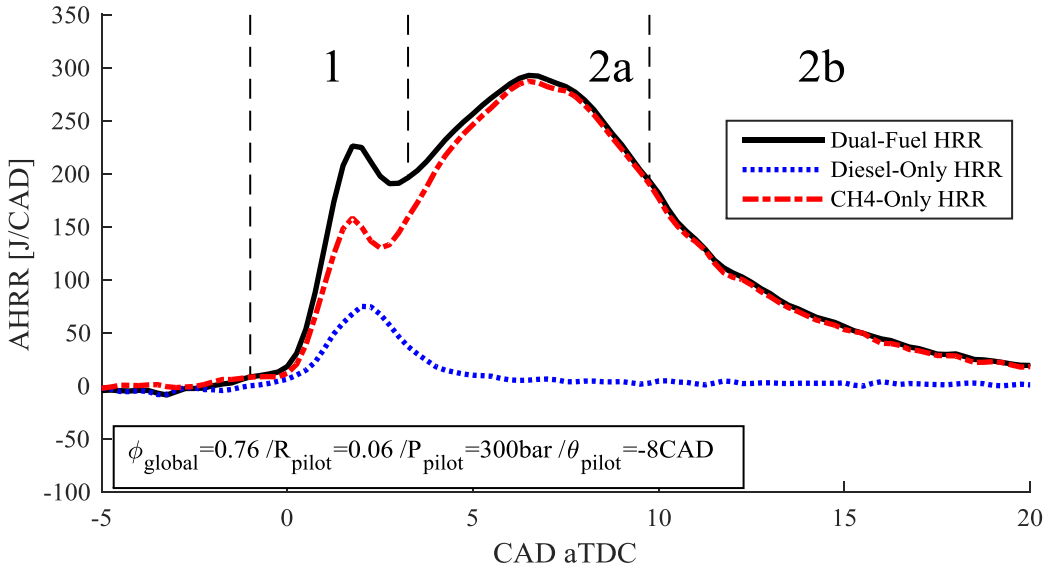

Figure 41: Comparison of DIDF and diesel-only AHRRs for operating point classified as pilot-independent case of flame propagation combustion regime.

4.5 Summary of Thermodynamic DIDF Investigation

The emissions and combustion mechanisms of lean, naturally-aspirated, low-speed DIDF combustion were experimentally investigated across a range of φ_{global} and R_{pilot} operating modes at 4 different values of φ_{CH4}, in a heavy-duty single cylinder research engine. Sweeps of pilot injection pressure and timing at each φ_{global}-R_{pilot} mode produced an experimental data set which bridges some of the observed DIDF combustion and emissions phenomena observed in previous investigations which were focused on either mixture properties or pilot injection properties.

Analysis of DIDF AHRR

For the DIDF combustion modes explored in this investigation, the AHRR can be systematically discretized into sequential stages of combustion, using a novel set of criteria based on AHRR and

dAHRR/dθ (see Figure 17). Physical metrics of the identified stages of combustion, such as peak and mean AHRR, are useful for identifying connections between particular combustion mechanisms, such as premixed auto-ignition or flame propagation, with engine performance parameters, such as emissions of NO_x and CH_4. In this work, discretization of the combustion stages considered the initial rapid apparent heat release to be stage 1 combustion, which was followed by stage 2 combustion. Considering the high-intensity portion of stage 2 combustion separately from the low-intensity portion strengthened correlations between second stage combustion AHRR and φ_{CH4}.

Stage 1 Combustion

The discretization criteria presented in this work, identified stage 1 combustion as beginning with the onset of positive integrated AHRR (at θ_1), and ending at the absolute minimum of dAHRR/dθ following the AHRR peak. Across all operating conditions investigated, stage 1 combustion exhibited heat release behaviour consistent with a pre-mixed auto-ignition event occurring in a diesel-vapour / CH4 / air mixture. Based on diesel pilot literature, this combustion event may also include some flame propagation mechanisms [34].

With the exception of the identified 'pilot-independent' operating points, stage 1 combustion is strongly influenced by m_{pilot} and P_{pilot}. Increasing m_{diesel} increases the proportion of energy released in stage 1 combustion (Q_1/Q_{tot}), indicating that this stage is strongly influenced by the diesel injection. However, as m_{diesel} increases, there is a critical limit above which additional diesel is converted in the second combustion stage and Q_1/Q_{tot} begins to decrease. Increasing P_{pilot} increases the amount of diesel and/or CH_4 consumed during stage 1 combustion; however,

for a sufficiently small m_{pilot}, increasing P_{pilot} above a critical value (800bar in this investigation) does not cause significant additional diesel or CH_4 to be consumed in stage 1 combustion. In all measured points in this investigation, CH_4 was observed to contribute to stage 1 AHRR, consistent with the accepted conceptual understanding of DIDF in the literature [23].

Stage 2 Combustion

As defined by the discretization criteria presented in this work, stage 2 combustion commences immediately following the end of stage 1 combustion and continues to the end of positive AHRR. For the specific operating conditions investigated, stage 2 combustion is composed of a high intensity region (2a) followed by a low intensity region (2b). $\varphi_{CH4} \approx 0.4$ was interpreted as a lean flammability limit, above which the mean AHRR of stage 2a combustion shows a strong, positive correlation with φ_{CH4}, which is consistent with turbulent flame propagation. For $\varphi_{CH4} < 0.4$, the combustion mechanism is no longer consistent with flame propagation and the fuel is converted by some other, slower mechanism. The observed lean flammability limit is affected by m_{pilot} as it is likely that diesel vapour participates in stage 2 turbulent flame propagation. The low intensity, second stage combustion mechanism is not yet classified or well understood and warrants more detailed investigation.

DIDF Operating Regimes

For the naturally-aspirated, low-speed DIDF operating modes investigated, there existed fundamentally different combustion regimes for DIDF operation as different R_{pilot} and φ_{CH4} were used. Figure 42 presents the transition regions between the identified DIDF operating regimes, as

observed in this investigation, which were defined in terms of R_{pilot} and φ_{CH4} alone. The defining characteristics of the DIDF combustion regimes are summarized in Table 8.

In the pilot-independent (A) and flame propagation (B) DIDF regimes, the stage 2a combustion AHRR was observed to increase with increasing φ_{CH4}. The AHRR shape and emissions of NO_x and CH_4 were observed to be strongly dependent on P_{pilot} and θ_{pilot} for operating points in the flame propagation regime (B), however minimal dependence was observed for these properties for points in the pilot-independent regime. In the non-flame propagation regime (C), no correlation between φ_{CH4} and stage 2 combustion AHRR was observed.

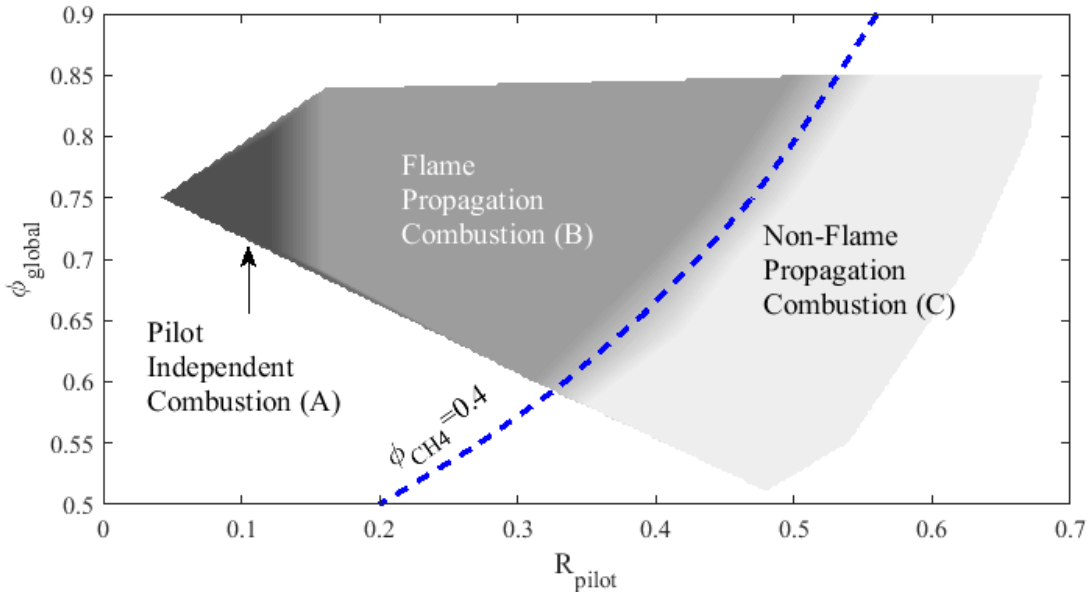

Figure 42: DIDF operating regimes and transitionary boundaries identified for the experimental conditions of this investigation.

Table 8: Summary of DIDF combustion regime characteristics.

Regime of DIDF R_{pilot}-φ_{global} Map	Characteristics
Pilot-Independent Combustion (A)	1. $AHRR_{Stage\ 2a} = f(\varphi_{CH4})$ 2.Emissions, $AHRR \neq f(P_{pilot},\theta_{pilot})$
Flame Propagation Combustion (B)	1. $AHRR_{Stage\ 2a} = f(\varphi_{CH4})$ 2.Emissions, $AHRR = f(P_{pilot},\theta_{pilot})$
Non-Flame Propagation Combustion (C)	1. $AHRR_{Stage\ 2a} \neq f(\varphi_{CH4})$

This chapter has presented selected thermodynamic data from a broad range of DIDF operating modes. A novel organization of the range of DIDF operating modes, the R_{pilot}-φ_{global} map, was introduced and used to discuss three distinct regimes of DIDF operation identified using a proposed set of AHRR analysis criteria. Specific conclusions about each of the three regimes and their characteristic combustion mechanisms will be further analyzed and discussed using spatially-resolved optical measurements in the next chapter.

Chapter 5: Optical Results & Discussion

The objective of this chapter is to support and elaborate on thermodynamic discussion from the previous chapter through analysis and discussion of simultaneous, spatially-resolved measurements of natural broad-band light emissions in the visible spectrum and natural light emissions at 307nm, which correspond to OH*-chemiluminescence.

5.1 Optical Measurement Selection

Optical experiments were designed to replicate the operating conditions of interest observed in the thermodynamic testing as closely as was possible given the significant discrepancies between the optical and thermodynamic engine configurations and operating modes (discussed in § 3.3). Due to the practical limitations of the optical testing method, it was necessary to select a subset of operating points to perform optical measurement and analysis on. Operating points selected from the thermodynamic measurement set for optical measurement are identified by red squares in Figure 43. The selection of operating points for optical measurement was on the basis of operating points with lower peak pressures, to mitigate the risk of damaging the quartz window. During optical testing, an additional operating point was measured, indicated by a blue square. The new operating point used the pilot-injection settings corresponding to the smallest pilot mass used in the thermodynamic testing and φ_{CH4}=0.36.

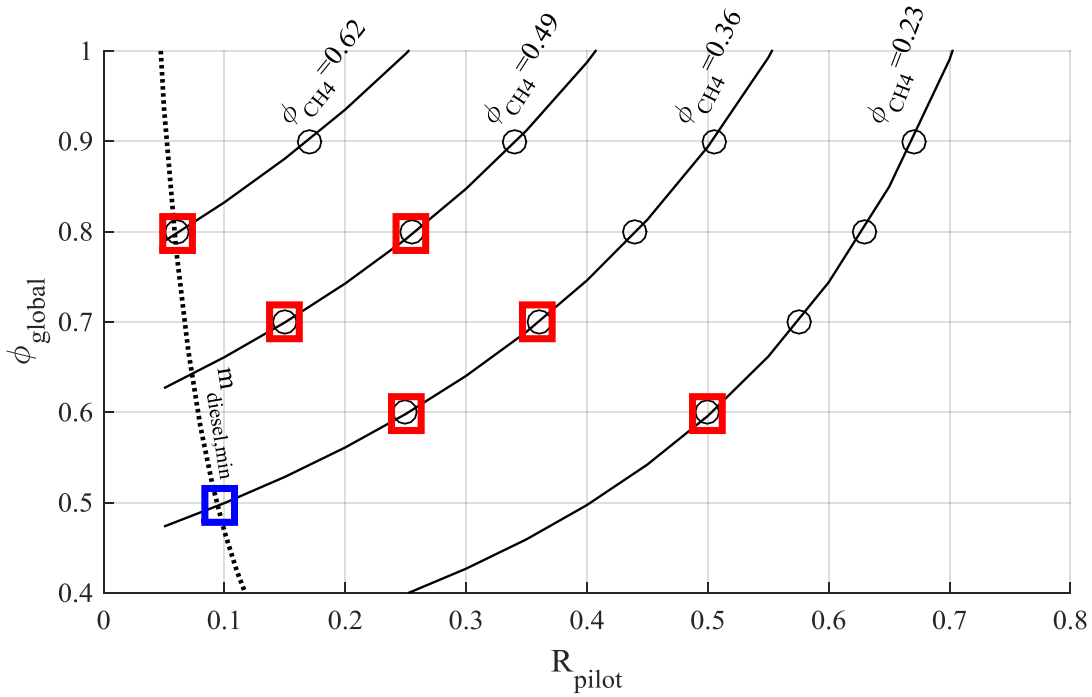

Figure 43: Selected DIDF operating points for optical investigation.

An initial round of optical measurements was performed with very conservative OH*-imaging systems settings; short intensifier gating, low gain settings, and short exposure, in order to protect the intensifier and high-speed CMOS devices. Through successive experiments, nominal OH*-imaging system settings were determined, which were appropriate for all measured points. Substantially more variability in emission intensity was observed for the broadband visible light emissions, however. For every optical measurement point, the visible-imaging system exposure settings were swept within the measurement run; within 15 consecutive sequences of skip-firing, 3—4 different exposure settings were applied. This approach increased the likelihood of recording a set of appropriately exposed images, as it is difficult to determine the best exposure settings for the natural light system *a priori*. However, the range of exposure settings increased the difficulty of comparing images from all 15 imaged cycles.

Thermodynamic analysis in the previous chapter suggested that different regimes of DIDF operation exist, which are characterized by fundamentally different combustion mechanisms. While all optically-measured operating points were reviewed, only one operating point from each of the identified combustion regimes was selected for detailed optical analysis and discussion here. Where possible, a high and low pilot injection pressure was used for the measurement point selected from each operating regime, so that the influence of the injection pressure could be considered.

The following sections discuss the qualitative behaviour observed in the pilot-independent, flame propagation, and non-flame propagation operating regimes, respectively. In each section, the effects of injection pressure are compared, with the exception of the non-flame propagation case (§5.3.3). At the end of this chapter, a summary of the observations made across all measurement points is presented. A summary of the operating points selected for optical analysis and discussion is given in Figure 44.

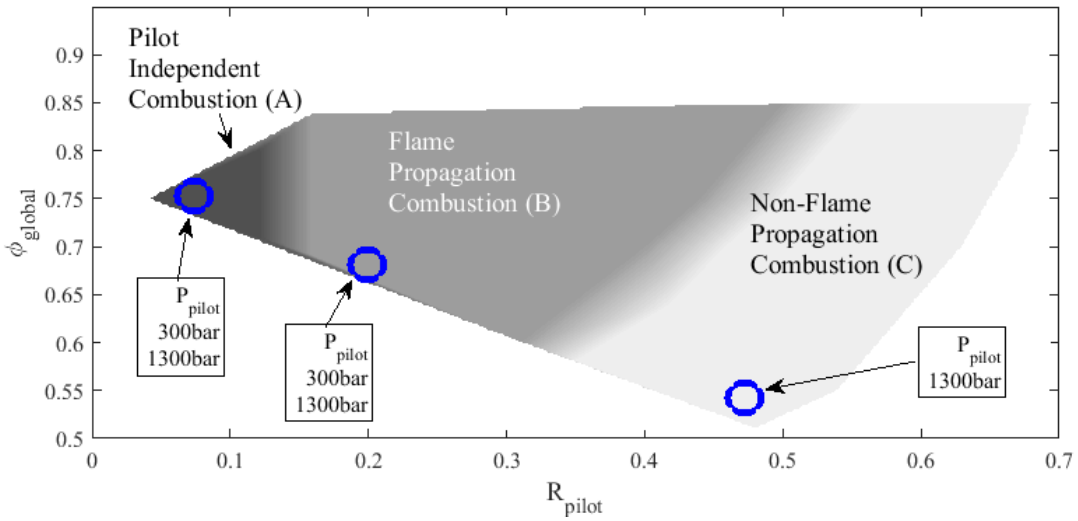

Figure 44: Summary of optical measurement points selected for detailed analysis.

5.2 Optical Measurement Background & Analysis

Analysis of spatially-resolved optical data was performed on representative single-cycles selected from each of the operating points indicated in Figure 44. Interpretation of natural light emission signals must consider that the observed signals represent line-of-sight integrated emissions from each spatial location within the piston bowl volume. No explicit treatment of the three dimensional physics was considered in this investigation; discussion in this chapter is limited to qualitative analysis. This section presents some brief background on the interpretation of images of broadband, natural-luminosity in the visible light spectrum and OH*-chemiluminescence measured at 307nm from combustion sources. A novel optical data presentation is introduced, which illustrates the variation of the spatial distribution of measured light intensity with time.

5.2.1 Visible Light Emissions

Measurement of natural light emission in the visible spectrum is an attractive spatially-resolved technique as standard telephoto lenses can be used. In addition, the emission intensities are sufficiently high, so intensified relay optics (IRO) are not required. The shortcoming of visible-signal analysis arises from the multitude of contributing sources to combustion light emissions in the visible spectrum. Particularly in CI engines with diesel direct injection, incandescent light emission from high temperature PM is the dominant emitter in the visible spectrum [56]. In addition to PM incandescence, natural chemiluminescence from activated C_2, CH, and CH_2O among other radicals is expected to be present, but is much weaker than the PM signal.

Interpretation of broadband visible emissions from the combustion chamber must be considered in a qualitative sense. This signal can be used to visualize regions of the cylinder where locally rich conditions required for PM formation exist. Quantification of local equivalence ratios, however, is not possible beyond a comment on empirically observed PM formation properties, such as local equivalence ratios being typically in the range of 2-4 at the onset of PM formation in diesel jets [30].

5.2.2 OH*-Chemiluminescence

Chemiluminescence occurs due to the relaxation, or quenching, of an electronically-excited molecule back to its quantum ground state, as the result of a chemical reaction. The process of relaxing to the ground state releases a photon [57]. An example of a typical chemiluminescence reaction occurring in a combustion environment is given in equation (18), where OH* is an electronically-excited hydroxyl radical, OH indicates the ground state radical, h is Planck's constant, and ν is the emitted light frequency.

$$OH^* + H_2O \rightarrow OH + H_2O + h\nu \quad \textbf{(18)}$$

Due to the discrete nature of quantum energy levels, molecules release photons at specific wavelengths depending on their molecular structure and energy. It is therefore possible to statistically predict the wavelength at which molecules with simple molecular structures will emit photons when they relax from excited states. OH* in combustion has been observed to have strong chemiluminescent emissions at 308nm, which permits the use of a band-pass filter to selectively observe OH* with minimal interference from other light sources.

OH is an important chemical species for many intermediate reactions in hydrocarbon combustion, such as the oxidation of hydrocarbons, CO, and PM [52] and is present in all engine combustion modes. Strong OH*-chemiluminescence signals require the electronic-excitation of OH, typically due to high temperatures. OH*-chemiluminescence emissions are interpreted as an indicator of the primary reaction zone`s high-intensity reactions [58].

5.2.3 Optical Measurement Analysis

Discussion and interpretation of imaging results is based on unenhanced image sequences from single, representative cycles. The selection of cycles was based on the AHRR shape from each cycle, and similarity to those observed during thermodynamic operation. Due to the optical engine operating mode, a high degree of variability in the combustion phasing and signal noise was observed for all optical measurement points (shown in Appendix C). Selected cycles possessed AHRR features common with the majority of other cycles from the same optical test in addition to the corresponding thermodynamic measurement AHRR.

In addition to the presentation and analysis of individual image frames, a novel method of presenting spatially-resolved combustion light emissions was developed. Figure 45 presents a visual description of how the new presentation method is formulated using a set of visible-signal images from DIDF combustion as an example. A corresponding sequence of image frames is also presented in Figure 45 for clarification.

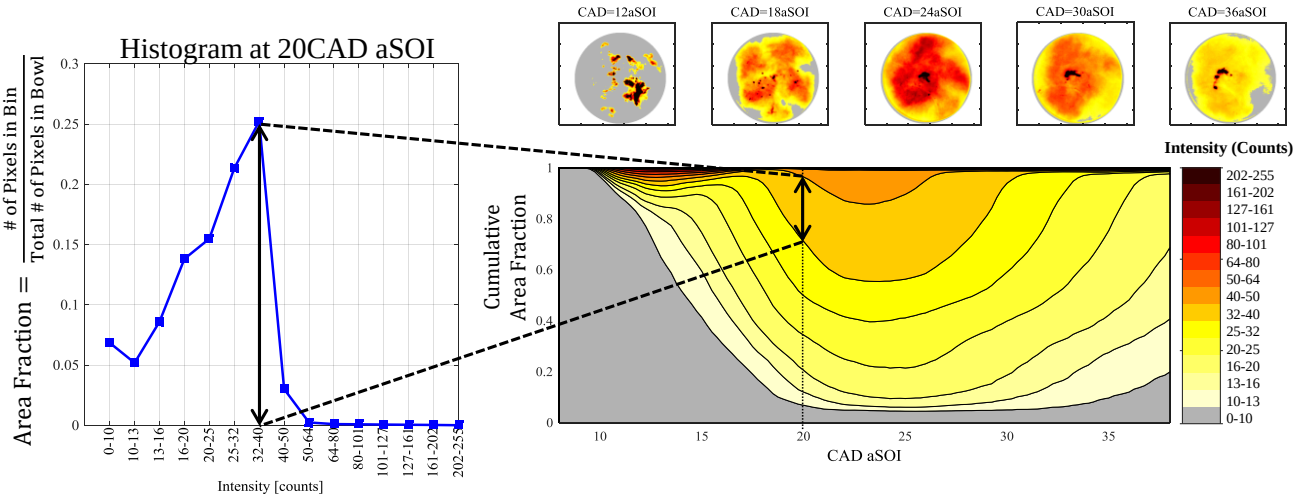

Figure 45: Description of cumulative histogram time series plot formulation.

For every frame in the measured image series (*i.e.* for a given cycle), a histogram with specified bin spacing is calculated, as shown on the left hand side of Figure 45. The bin spacing was set on a logarithmic scale from 10-255 to add resolution to lower intensity ranges. The sequences of image frames use 70 linearly spaced colours, while 15 bins are used for histogram calculation. The bin spacing presented in Figure 45 is used in all subsequent visible- and OH*-signal analyses in this chapter.

The number of pixels in each bin is normalized by the total number of pixels in the piston bowl area in each image, which is calculated by manually fitting a circle to the piston bowl in each image. The normalized pixel count for each bin represents the fraction of the visible bowl area that is emitting light at the intensity given by the bin range. Stacking the area fraction for each intensity bin for every frame (0.25°CA increments), produces a single plot that describes the spatial and intensity information for all collected images in a cumulative histogram time series.

Contours having small y-axis ranges at a given CAD represent intensities that are only present across small areas of the bowl. Conversely, contours with wide y-ranges indicate large areas emitting similar intensity light. For example, in Figure 45 at 12°CA aSOI (first frame), small regions of high intensity are present. These are represented by a small cumulative area fraction with dark red contours in the intensity cumulative area fraction plot. The frame captured at 24°CA aSOI shows emission from almost the entire bowl, which is reflected by the broader contours which extend to cover nearly 100% of the bowl area. Note that due small errors in bowl area calculation and applying a threshold of 0-10 intensity counts, the coloured contours do not completely reach 100% coverage.

5.3 Optical Measurement Results & Discussion

In this section, spatially-resolved broadband single-cycle visible and OH*-chemiluminescence images for P_{pilot}=300bar and 1300bar operating points in the pilot-independent, flame propagation, and non-flame propagation DIDF operating regimes are compared. Additionally, AHRR data from each single-cycle is compared to the spatially-resolved measurements.

5.3.1 Pilot-Independent DIDF Combustion (Regime A)

In the pilot-independent combustion regime (A), variations of the pilot injection pressure and timing produced minimal effect on calculated AHRR and engine-out emissions of CH_4 and NO_x, for the parameter ranges tested. Figure 46 compares the single-cycle OH*-chemiluminescence (cold colour scale) and broad band natural luminosity (hot colour scale) for pilot injection pressures of 300bar and 1300bar. Although the intensities in the two sets of images are not quantified, the camera apertures, exposure times, and intensifier gain are the same for both sets of images at both pilot injection pressures, so images can be directly compared to one another. These fuelling and injection settings produced pilot-independent combustion in thermodynamic testing. Details of specific testing parameters are given in Table 9. A post-processing script developed in MATLAB aligned images of natural luminosity and OH*-chemiluminescence for each test point to the nearest 0.25°CA aSOI. Note that different pilot injection timings were used to approximately match CA50 for the high- and low-pressure pilot injections.

Table 9: Optical test parameters for pilot-independent DIDF operating regime (A) measurements.

Test Parameter	P_{pilot}=300bar	P_{pilot}=1300bar
φ_{global}	0.75	0.72
φ_{CH4}	0.62	0.59
R_{pilot}	0.06	0.07
θ_{pilot} [°CA aTDC]	-8	-4
Selected Cycle	3rd fired cycle of 3rd skip-firing sequence	3rd fired cycle of 3rd skip-firing sequence
Visible Camera Exposure [µs]	4	4
UV IRO gating [ns]	10000	10000

In the 300bar pilot injection pressure case, the initial signal for both the visible emissions and the OH*-chemiluminescence occurs towards the centre of the bowl. In the earliest OH*-chemiluminescence image, the regions through which three of the pilot jets had issued during the pilot injection event are emitting light with noticeably higher intensity than the rest of the combustion chamber. Note that the two residual pilot jet structures that appear to be missing correspond to the pilot jets which are injected closer to the firedeck, an artifact of the non-vertical direct injector (see Figure 7). By 18° CA aSOI, the residual jet structure is visible in both the visible- and OH*-signal series, and remains evident in the OH*-signal series until 30°CA aSOI. With increasing time, increasing visible- and OH*-signal intensity is observed to propagate away from the residual jet structures into the remaining bowl volume, however peak signal intensities never move from the central bowl region. The strong counter-clockwise swirl motion is apparent in both image sets, but the shape of the residual pilot jet structures remain relatively stable.

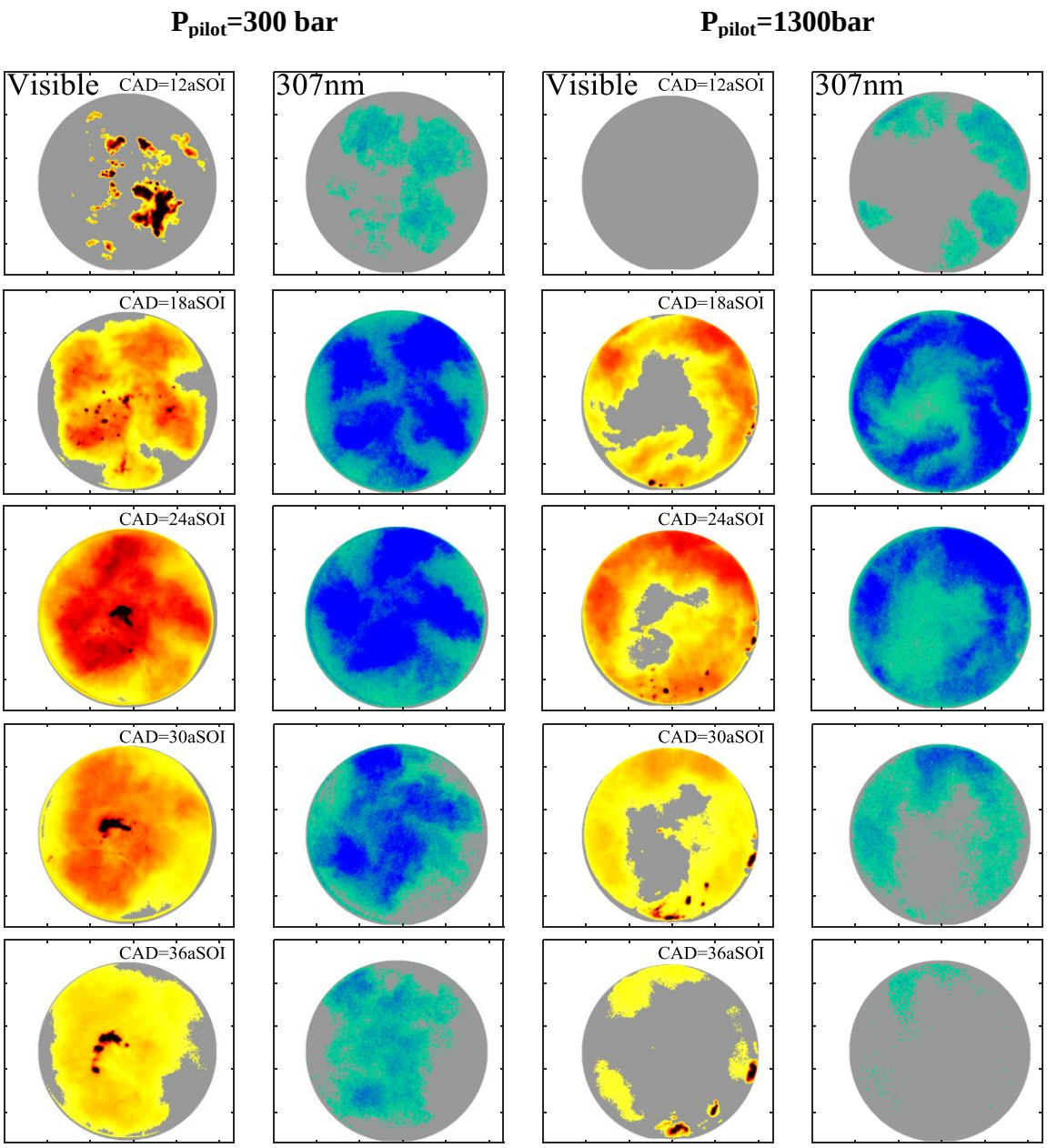

Figure 46: Single-cycle image sequences of pilot-independent regime (A) DIDF combustion using a pilot injection pressure of 300bar (columns 1 and 2) and 1300bar (columns 3 and 4); φ_{global}=0.74, φ_{CH4}=0.61, R_{pilot}=0.07.

In this discussion, the term ‘residual jet structure’ is used to refer to the regions of the combustion chamber where the previous presence of the pilot injection event is evident in the collected images. These regions have higher concentrations of fuel, and therfore higher reactivities, than the surrounding regions of the combustion chamber. In all cases discussed in this chapter, the pilot injection terminates long before any light emission (or heat release) was measured, so there is no jet present, however in cases where the fuel mixing rates are sufficiently low the locations where the pilot jets had previously been are visible.

The persistence of the residual jet structures for a relatively long period of time may indicate either poor mixing of the pilot diesel with the surrounding gases or that regions of the cylinder volume, which are further from the pilot jet axes may not reach equivalence ratios sufficiently high to support combustion for the particular operating conditions of the test. Poor mixing of the diesel pilot is expected for low pilot injection pressures, and has been associated with high emissions of unburned species by other researchers [17,18]. Injector dribble starting at 24°CA aSOI is indicated in the visible images by well-defined, high-intensity forms measured near the injector tip. The injector dribble does not produce any OH*-signal suggesting that this may be a lower temperature region, but with a high PM concentration.

In the 1300bar pilot injection case, the ignition sites are located at the bowl periphery. At 12°CA aSOI, the residual structure from the pilot injection is moderately visible, but for subsequent visible- and OH*- images, the structure is poorly defined. Following ignition at the bowl periphery, increasing visible- and OH*-signal intensity propagates towards the central bowl region with a single, roughly uniform front indicated by the threshold between yellow and grey,

similar to the observations of [28]. As in the 300bar pilot injection pressure case, the peak signal intensity of both the visible- and OH*-signals remains in the same spatial region as the ignition sites. It is expected that with a symmetrical, vertical injector arrangement, a uniform torroid of emitted intensity would have been observed.

It should be noted that from 18°CA aSOI onward, in the visible image series from the 1300bar pilot pressure case, small high-intensity forms are visible near the bowl periphery at the 3—6 o'clock positions. This signal is attributed to the assembly grease used to manualy lubricate the piston rings and cylinder liner between optical tests (see § 3.3), which was found to have impinged on the quartz window during testing. In the visible image series, it can be seen that the emission signals from the grease are unaffected by the strong swirl motion.

From 18—24°CA aSOI, similar peak visible- and OH*-intensities were observed for both pilot injection pressures. The volume of the bowl from which peak visible- and OH*-signal intensity was observed to be emitted from was smaller in the 1300bar pilot injection pressure case compared the 300bar case. In the 1300bar pilot injection case, both the visible- and OH*-signals begin to decrease before the corresponding signals for the 300bar case, indicating a shorter overall combustion event.

The cumulative histogram time series of emitted visible- and OH*-signal intensity measured for P_{pilot}=300bar is presented in Figure 47. Details on interpretation of the intensity cumulative spatial fraction plots are presented in the previous section. Two CAD locations are observed to have local maxima of visible-signal intensity in the cumulative histogram times series of visible

light emissions. The first maxima is a high-intensity (indicated by dark-coloured contours), but spatially-small (indicated by small y-range) signal occuring from approximately 9—16°CA aSOI. Closely spaced contours in the first phase of fuel conversion also indicate a high-degree of heterogeneity of signal intensity emission with respect to spatial dimensions; a high gradient of visible-signal intensity emission. The second mode has a lower peak intensity, but covers a much larger spatial fraction of the piston bowl area and is observed from 16—35°CA aSOI. The start of the measured visible-intensity is approximately coincident with the start of the AHRR rising edge associated with stage 1 combustion.

A single peak is observed in the cumulative histogram time series of the OH*-signal. The onset of the OH*-signal is delayed from the visible-signal by ~2—3°CA, which is roughly coincident with the first peak of the AHRR (location of $q_{1,max}$). The peak OH*-signal intensity occurs earlier than that of the visible signal. Based on the algorithm defined in §4.2, the transition between high-intensity second stage combustion and low-intensity second stage combustion, θ_{2b}, would be approximately coincident with the timing of peak OH*-signal. Note that due to the high level of noise in the single-cycle optical AHRR, the combustion stage definition algorithm could not be reliably applied to AHRR measured for single-cycle optical configuration data without the application of different calculation parameters. In general, the bulk of the measured OH*-emissions appears to occur within the stage 2 combustion range.

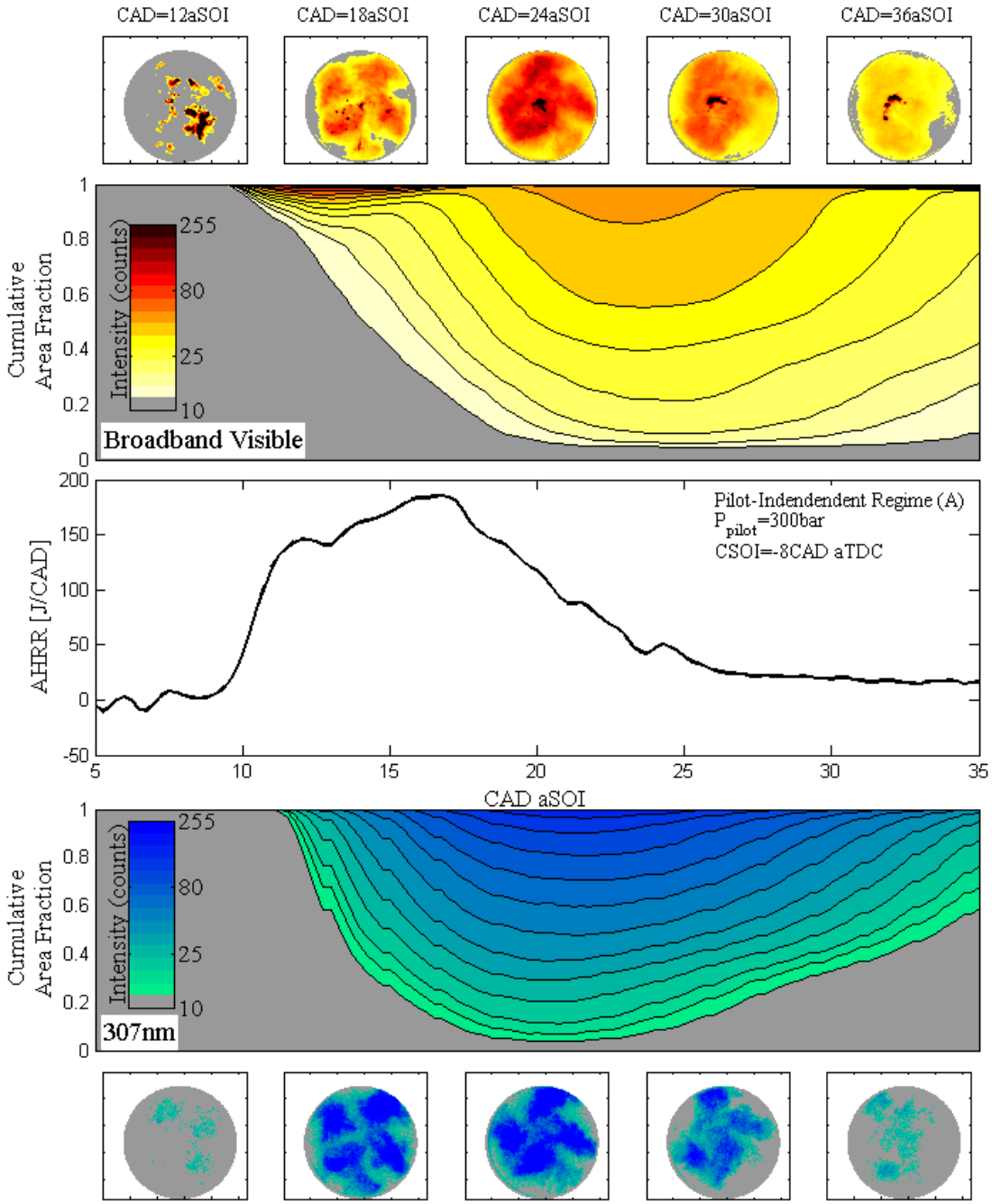

Figure 47: Cumulative histogram time series of visible- and OH*-signal intensities and AHRR for pilot-independent regime (A) DIDF combustion with P_{pilot}=300bar, φ_{global}=0.74, φ_{CH4}=0.61, R_{pilot}=0.07.

The cumulative histogram time series of visible- and OH*-signal intensity and AHRR measured for P_{pilot}=1300bar is presented in Figure 48. Unlike the P_{pilot}=300bar case, the visible signal exhibits a single peak. The change in visible-signal spatial distribution is reflected in the early visible-image frames where the visible signal is observed to be more homogeneously distributed around the bowl periphery as opposed to small regions of high signal intensity near the injector tip as observed in the P_{pilot}=300bar case. The onset of the visible signal is also observed to occur later with respect to the start of stage 1 combustion than in the P_{pilot}=300bar case. The overall duration of measurable light emission is observed to be shorter than the 300bar case.

Overall, the OH*-signal produces a bell-shaped distribution, as observed in the P_{pilot}=300bar case. Unlike the visible-signal, the delay of the OH*-signal relative to θ_{pilot} remained constant between the two pilot injection pressures, and as a result, begins before the visible signal in this case. As with the visible signal, the duration of measurable OH*-signal was shorter for the higher pilot injection pressure. The peak OH*-signal is observed to occur around 20°CA aSOI, which approximately aligns with, θ_{2b} in the measured AHRR.

It is important to note that the AHRR for P_{pilot}=1300bar has a substantially greater magnitude than the AHRR for the P_{pilot}=300bar case, and a much more moderate slope on the rising edge of the stage 1 AHRR. In thermodynamic measurements, no significant difference in AHRR magnitude was observed with changing P_{pilot}, which was the justification for identifying these points as a unique DIDF operating regime (pilot-independent). The observed discrepancies in the optical AHRR are attributed to the differences in optical engine configuration outlined in § 3.3.

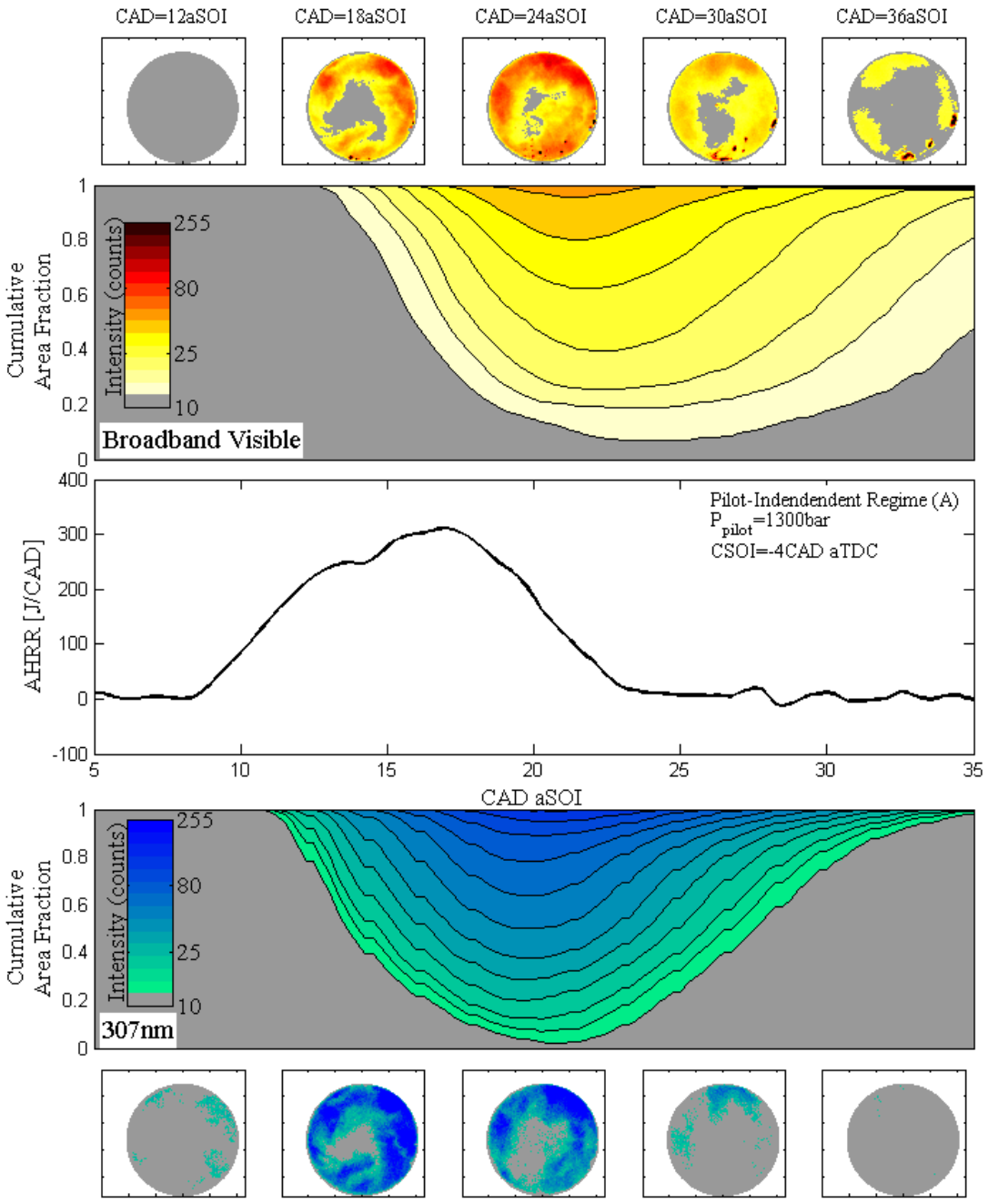

Figure 48: Cumulative histogram time series of visible- and OH*-signal intensities and AHRR for pilot-independent regime (A) DIDF combustion with P_{pilot}=1300bar, φ_{global}=0.74, φ_{CH4}=0.61, R_{pilot}=0.07.

5.3.2 Flame Propagation DIDF Operation Regime (B)

For operating points classified as flame propagation in the thermodynamic measurements of this work, the AHRR of the second stage combustion showed sensitivity to φ_{CH4} consistent with flame propagation, but unlike the pilot-independent operating regime, a strong sensitivity of engine out emissions and AHRR shape to pilot injection pressure and timing was observed. Compared to the pilot-independent regime, the relative amount of diesel, R_{pilot}, is greater and the absolute concentration of CH_4, measured by φ_{CH4} is lower in the flame propagation regime.

In Figure 49, single-cycle image series of visible- and OH*-signals are presented for P_{pilot}=300bar and 1300bar cases on the left and right side of the figure, respectively. Details of the operating parameters used are given in Table 10.

Table 10: Optical test parameters for flame propagation DIDF operating regime (B) measurements.

Test Parameter	P_{pilot}=300bar	P_{pilot}=1300bar
φ_{global}	0.65	0.66
φ_{CH4}	0.48	0.48
R_{pilot}	0.15	0.17
θ_{pilot} [°CA aTDC]	-10	-6
Selected Cycle	3rd fired cycle of 6th skip-firing sequence	3rd fired cycle of 12th skip-firing sequence
Visible Camera Exposure [µs]	8	8
UV IRO Gating [ns]	10000	10000

As observed in the image sequences of pilot-independent DIDF combustion in the previous section, the pilot injection pressure plays a significant role in the flame-propagation DIDF operating regime. For low P_{pilot} operation, both the visible- and OH*-signals initiate towards the centre of the bowl, while at high P_{pilot} the initial reactions are observed in the bowl periphery. For the low P_{pilot} case, the residual jet structures remain visible for a long period of time, as was observed in the pilot-independent images of the previous section. In both the visible- and OH*-image series, more of the residual jet structure features can be resolved than in the pilot-independent images; likely due to the increased mass of injected diesel (~6.5mg for pilot-independent regime test point, ~14.3mg for flame propagation regime test point). In the low P_{pilot} case, higher intensity visible- and OH*-signals in the region of the residual jet structure located near the bowl perimeter were observed for all the pilot jets, with lower intensity emissions leading towards the bowl centre and around the perimeter of each residual jet structure.

At the very centre of the bowl, a region of high-intensity emissions of both visible- and OH*-signals was observed. In the previous section, the very high-intensity visible-signal in the centre of the bowl was attributed to the injector dribbling liquid diesel into low-reactivity regions in the centre of the bowl; this did not produce high enough temperature conditions for any OH*-radicals to produce chemiluminescent signals in the same region of the bowl. However, in the current image sequences, a strong OH*-signal is observed in the central bowl region in the same location as the visible-signal, indicating higher temperature fuel conversion. Based on the image sequence in Figure 49, the visible- and OH*- signals appear to initiate in the region of the residual jet structures closest to the bowl perimeter before they appear in the central bowl region.

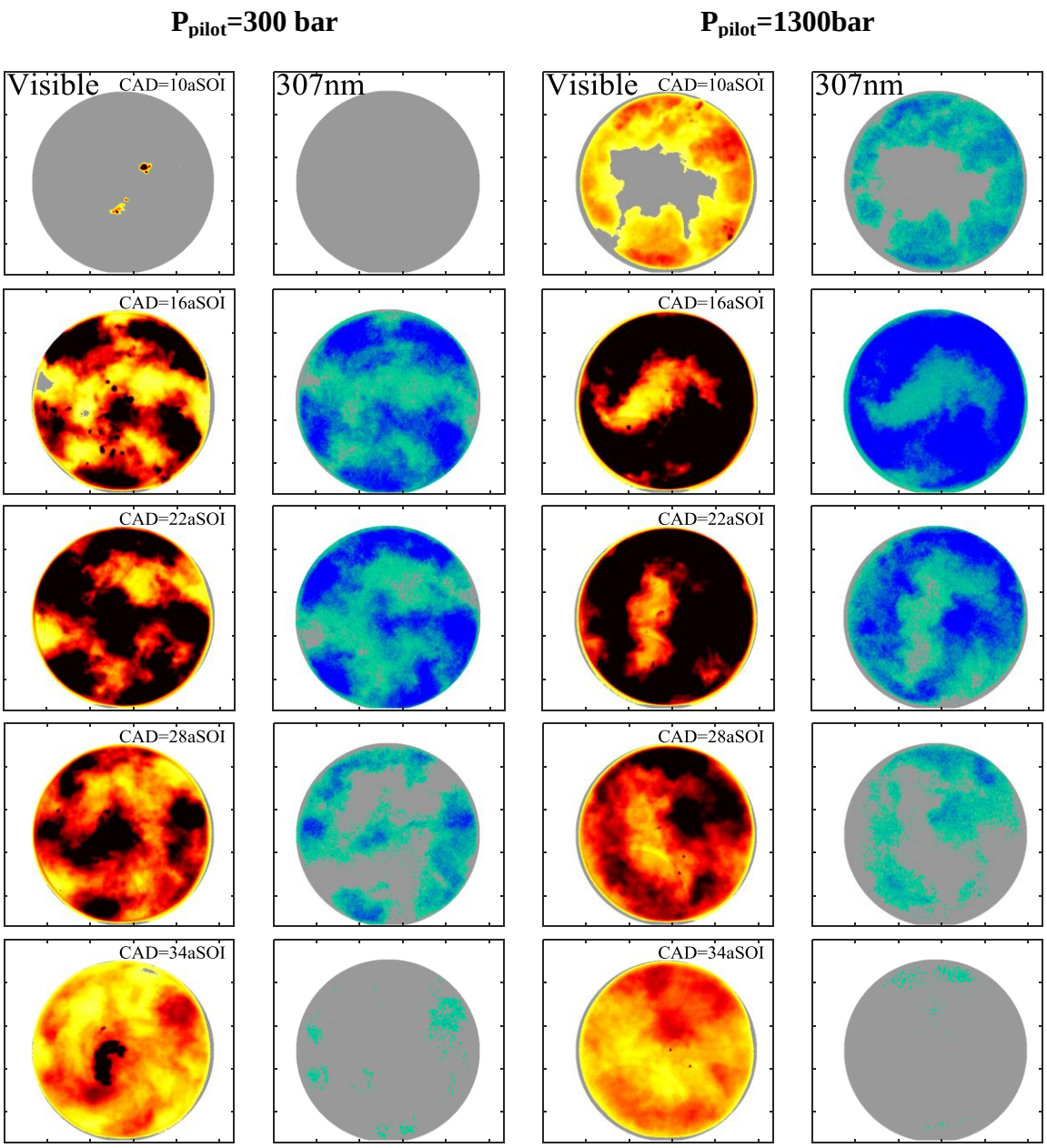

Figure 49: Single-cycle image sequences of flame propagation regime (B) DIDF combustion using a pilot injection pressure of 300bar (columns 1 and 2) and 1300bar (columns 3 and 4); φ_{global}=0.66, φ_{CH4}=0.48, R_{pilot}=0.17.

The φ_{CH4} for this operating point is lower than in the pilot-independent case discussed in the previous section, therefore the increased reactivity at the centre of the bowl is attributed to the

larger mass of injected diesel. If the turbulent mixing rate of the pilot jet is assumed to be constant for a given P_{pilot}, then the concentration of diesel at the centre of the bowl and along the axes of the residual jet structures is predicted to be higher with a larger diesel injection at the same P_{pilot}. The presence of higher fuel concentrations at the bowl centre may explain why significant OH*-signal was measured in the central bowl region for this case, but not for a smaller injected diesel mass.

For the higher P_{pilot} case, the pilot fuel is subject to higher mixing rates due to the increased shear forces resulting from higher initial jet velocities, therefore the residual tail of the injected pilot jet is expected to be more dispersed than in the low P_{pilot} case. Furthermore, the higher pilot jet momentum is expected to transport the fuel further in the radial direction than the low P_{pilot} case. As in the pilot-independent operating regime at high P_{pilot}, the visible- and OH*-signal intensity appears to progress radially-inward from the ignition sites at the bowl periphery. For the high P_{pilot} case, it is possible that the central region of the bowl relies on flame propagation through the more homogeneous lean, premixed CH_4 (and some diesel vapour) for high temperature reactions to proceed, while at low P_{pilot}, a substantial amount of incompletely mixed diesel remains along the residual jet axes for longer durations. Due to higher local equivalence ratios resulting from lower pilot injection pressures, the residual jet axes are more chemically-reactive than the surrounding homogeneous mixture. By either sequential auto-ignition or flame propagation through the diesel vapour / CH_4 / air mixture within the residual jet structure, heat and radicals are transported radially-inward to the centre of the bowl.

In other works [28], it was proposed that for lean DIDF operating conditions, such as the conditions examined in this section, a substantial portion of the CH_4 emissions may be attributed to the incomplete combustion of the central bowl region (see Figure 4). Although the low P_{pilot} case appeared to enhance combustion intensity in the central bowl region, compared to the high P_{pilot} case, the emissions of CH_4 measured using the thermodynamic engine configuration were observed to be significantly lower for the high P_{pilot} case (~5.5g-CH_4/kW-hr) than the low P_{pilot} case (~8g-CH_4/kW-hr). This may indicate that the low P_{pilot} caused a reduction of reaction intensity elsewhere in the cylinder, which more than offset the increased central-bow region chemical reactivity. This conclusion cannot be supported by the current measurements and warrants further investigation. The discrepancies between the thermodynamic and optical engine configurations may also confound this conclusion.

The cumulative histogram time series of emitted visible- and OH*-signal intensity and AHRR measured for P_{pilot}=300bar is presented in Figure 50. As observed for the pilot-independent operating mode, two peaks in the visible-signal are present for the low P_{pilot} case in flame propagation regime DIDF combustion. The first peak is attributed to localized regions of high-intensity emissions, and starts approximately coincidental with the start of stage 1 combustion at 11°CA aSOI. Around the first modal peak at 13°CA aSOI, substantially higher gradients of light intensity contours with respect to the x-axis are observed than in the pilot-independent case, indicating that the formation of regions of higher emission intensity was more rapid in this case.

Throughout the duration of the combustion event, the measured visible intensities are significantly higher for the flame propagation operating mode than the pilot-independent mode.

In the literature, PM production is typically attributed solely to the diesel pilot combustion [16,17], which corroborates the observed increase in visible emission intensity with a larger pilot mass (despite the reduced φ_{global}). It should be noted that, while Figure 50 may appear to indicate saturated (*i.e.* overexposed) pixels, this is an artifact of the colour mapping and bin-range selection. Review of the individual frames data indicated that there were no saturated pixels for this cycle.

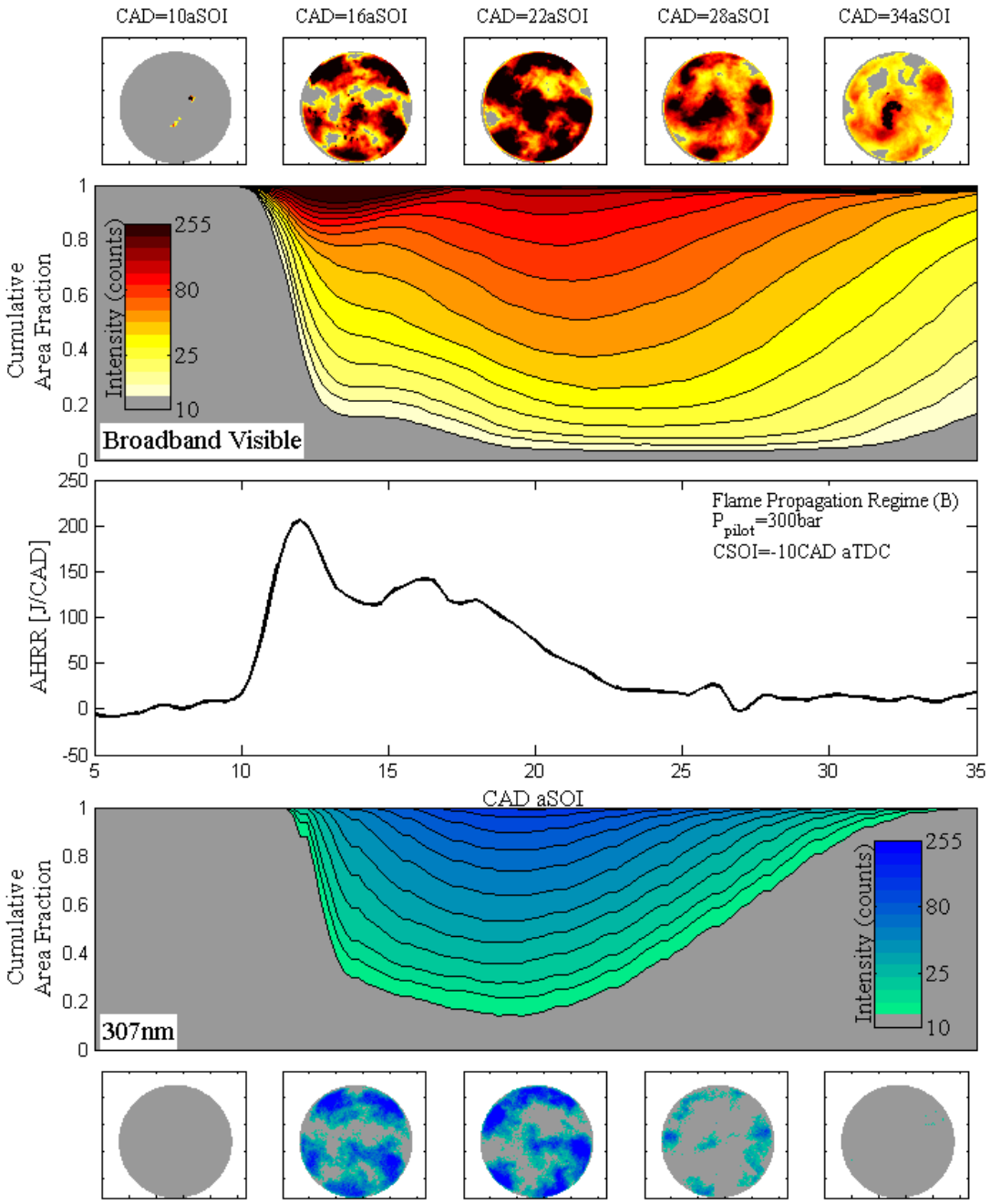

Figure 50: Cumulative histogram time series of visible- and OH*-signal intensities and AHRR for flame propagation regime (B) DIDF combustion with P_{pilot}=300bar, φ_{global}=0.66, φ_{CH4}=0.48, R_{pilot}=0.17.

The OH*-signal cumulative histogram time series is also observed to be similar to the pilot-independent case, with a single peak beginning ~2°CA aSOI later than the measured visible emissions. Overall coverage of the bowl area by measured OH*-signal intensity above the low-threshold is slightly lower than in pilot-independent case, but is otherwise very similar. The location of peak OH*-signal intensity correlates with where the division of high- and low-intensity stage 2 combustion is expected to be calculated. The trailing edge of the OH*-signal also terminates sooner than the corresponding signal in the pilot-independent case.

The cumulative histogram time series of emitted visible- and OH*-signal intensity and AHRR measured for P_{pilot}=1300bar is presented in Figure 51. The AHRR exhibits a higher peak AHRR than the low pressure pilot injection case, as was observed during thermodynamic measurements. The leading edge exhibits a much steeper slope, an effect which was not observed in the thermodynamic data and may be related to differences in the optical and thermodynamic engine configurations.

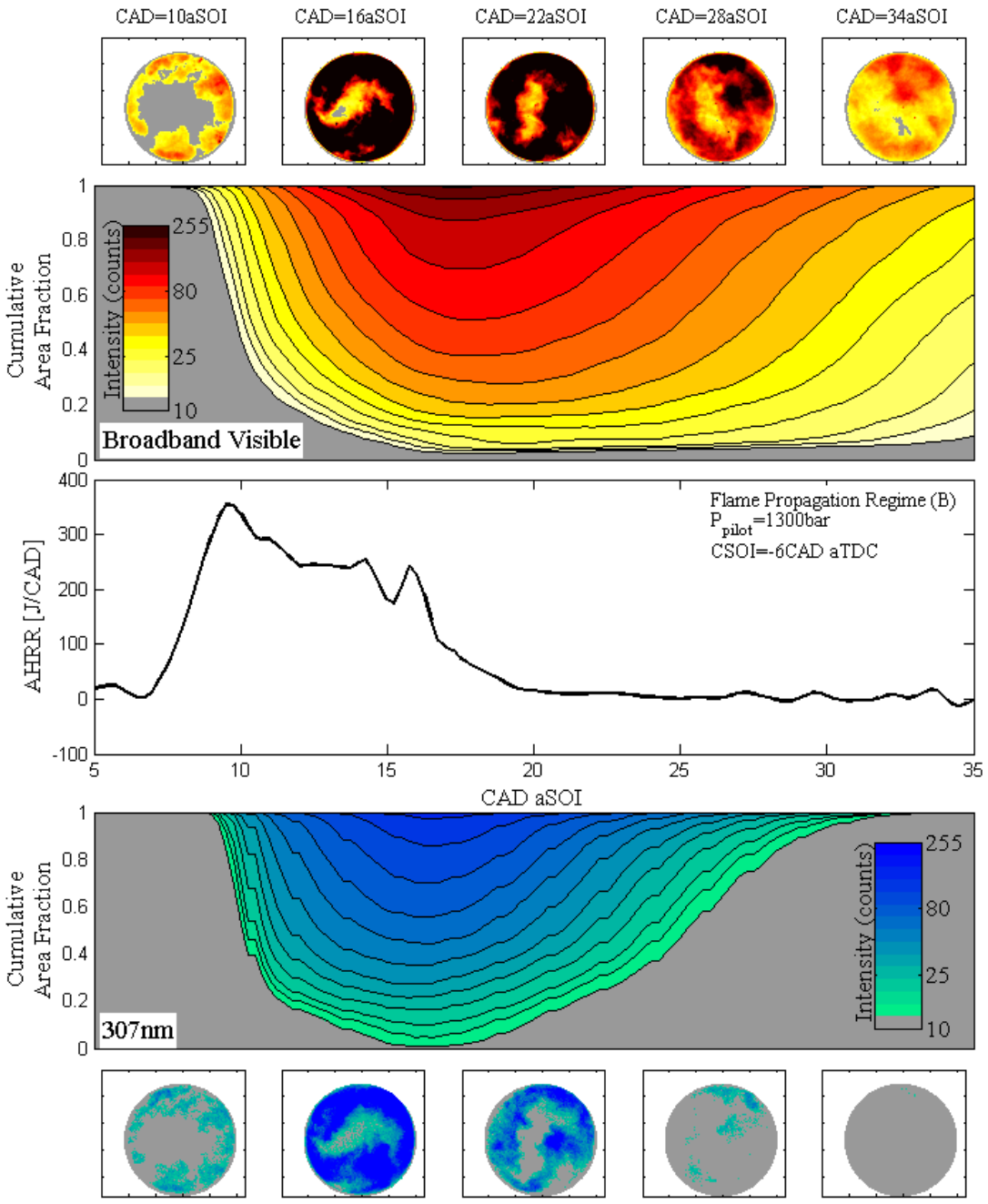

Figure 51: Cumulative histogram time series of visible- and OH*-signal intensities and AHRR for flame propagation regime (B) DIDF combustion with P_{pilot}=1300bar, φ_{global}=0.66, φ_{CH4}=0.48, R_{pilot}=0.17.

Similar trends between the high- and low-pressure pilot injection cases of the flame propagation operating point are observed as the corresponding trends in pilot-independent operating point. For high P_{pilot}, the visible signal has a single peak and begins slightly after the start of stage 1 combustion. The overall intensity levels are also substantially greater than the low pilot injection pressure case. The OH*-signal is observed to have marginally greater maximum area coverage than the low pressure pilot injection case. This is interpreted as an indication of the enhanced transport of diesel throughout the bowl, which increases the reactivity of a greater reaction volume. As in all the previously discussed optical cycles, the onset of the OH*-signal is coincident with the location of peak AHRR in stage 1 combustion, $q_{1,max}$, which may be interpretted as an indication of the timing of rapid temperature rise within the combusiton chamber. The leading edge of the OH*-signal is steeper indicating a more rapid development of the regions emitting higher intensity light than the lower injection pressure case. The trailing edges remain very similar between both sets of OH*-signal data.

5.3.3 Non-Flame Propagation DIDF Combustion

Operating points classified as belonging to the non-flame propagation regime of DIDF combustion showed no clear dependence on φ_{CH4}, and were dominated by the pilot combustion event. For the operating conditions of the thermodynamic testing in this work, the non-flame propagation regime was observed for $\varphi_{CH4}<0.4$.

A representative single-cycle image sequence of non-flame propagation DIDF combustion with P_{pilot}=1300bar is presented in Figure 52, fueling parameters for the selected operating points are given in Table 11. Because of excessive impingement on the piston window, results for

P_{pilot}=300bar are not presented in this section. As for the other operating regimes discussed in the previous two sections, high P_{pilot} produces ignition sites on the bowl periphery. Unlike the more spatially-homogeneous ignition observed in the previous two sections, during non-flame propagation DIDF ignition, the visible- and OH*-signal intensity around the bowl periphery is highly stratified. The stratification of visible- and OH- signal does not follow the spray pattern of the direct-injector, however.

Table 11: Optical test parameters for non-flame propagation DIDF operating regime (C) measurements

Test Parameter	**P_{pilot}=1300bar**
φ_{global}	0.53
φ_{CH4}	0.25
R_{pilot}	0.47
θ_{pilot} [°CA aTDC]	-4
Selected Cycle	3rd fired cycle of 2nd skip-firing sequence
Visible Camera Exposure [µs]	2
UV IRO Gating [ns]	10000

Following the ignition, visible- and OH*- signal intensity is observed to rapidly increase in the central bowl region, however the jet axes are not visible as in the low P_{pilot} case of flame propagation DIDF combustion in the previous section. The high-speed videos of this operating point revealed significant oscillation of the image immediately following ignition accompanied by measured pressure oscillations, attributed to the homogeneous auto-ignition of a large mass of diesel.

In the visible-signal image sequence of Figure 52, several frames exhibit small, localized, high-intensity regions, which are not seen in the corresponding OH* frame. These features are qualitatively similar to the injector dribble seen for the low P_{pilot} cases in the previous two sections. These regions likely correspond to locally rich regions formed from the large single-injections of diesel producing rich regions.

The cumulative histogram time series of emitted visible- and OH*-signal intensity and AHRR measured for P_{pilot}=1300bar is presented in Figure 53. The qualitative shape of both the visible- and OH*- series is significantly less symmetrical and bell-shaped than the corresponding signals measured in the pilot-independent and flame propagation operating points. The AHRR is characterized by a large single peak, rather than the two-stage combustion typical of the flame propagation and pilot-independent operating modes and is similar to the AHRR measured during thermodynamic testing in terms of overall shape and magnitude.

P_{pilot}=1300bar

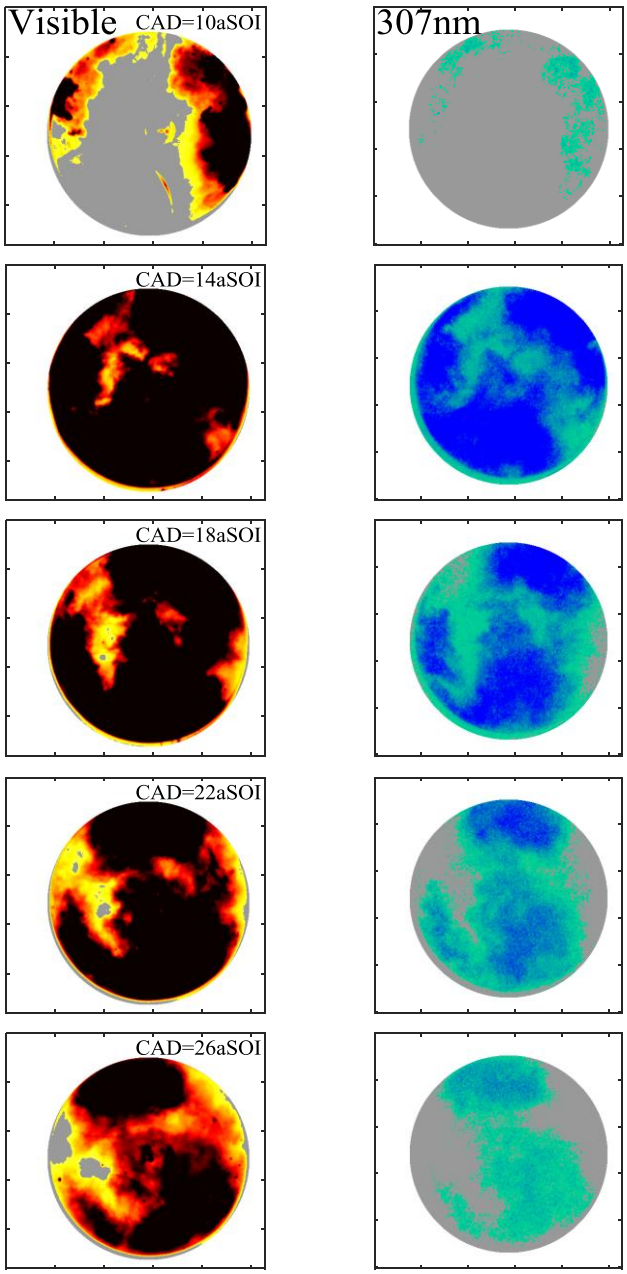

Figure 52: Single-cycle image sequences of non-flame propagation regime (C) DIDF combustion with P_{pilot}=1300bar, φ_{global}=0.53, φ_{CH4}=0.25, R_{pilot}=0.47.

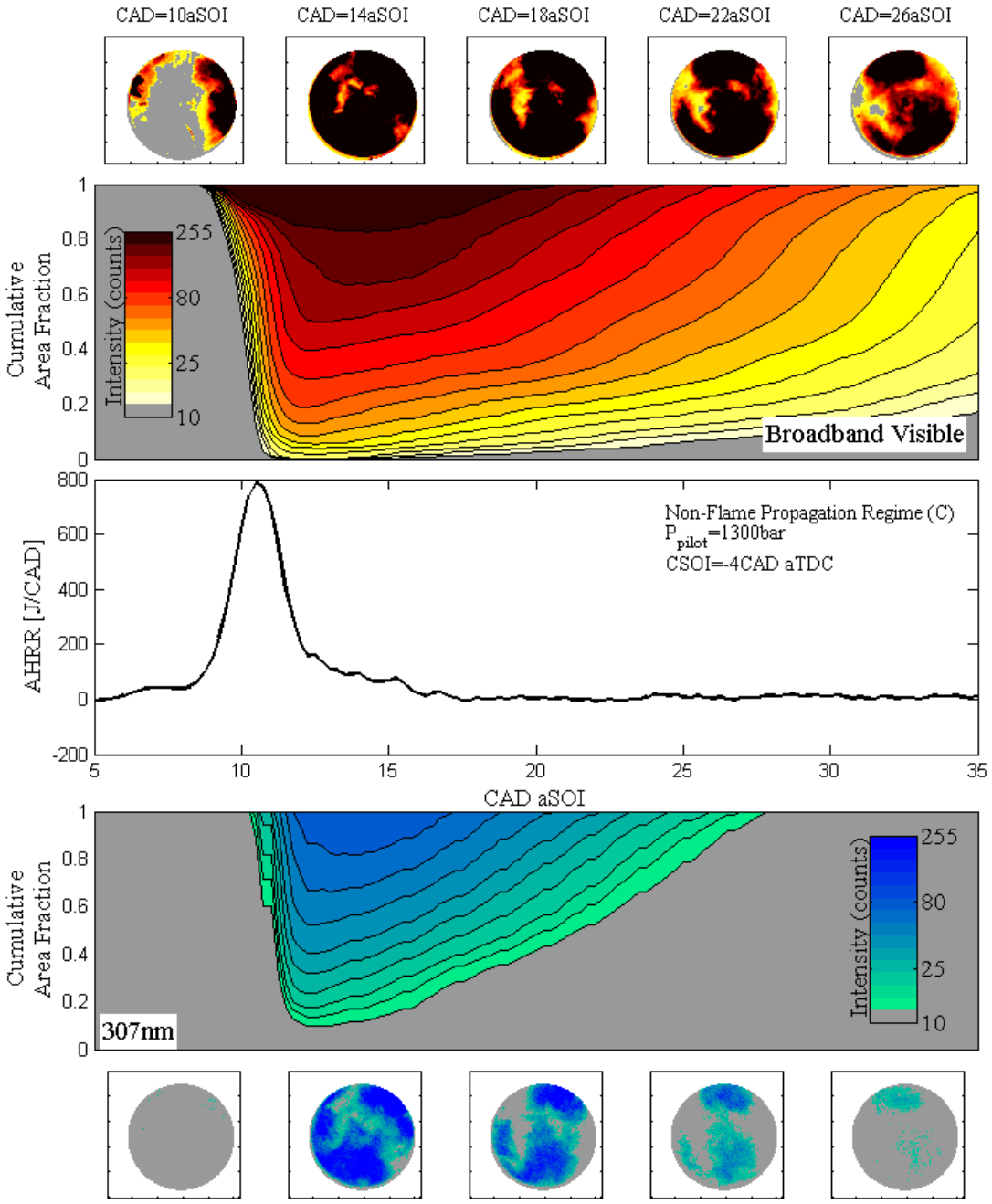

Figure 53: Cumulative histogram time series of visible- and OH*-signal intensities and AHRR for non-flame propagation regime (C) DIDF combustion with P_{pilot}=1300bar, φ_{global}=0.53, φ_{CH4}=0.25, R_{pilot}=0.47.

The visible signal begins at ~9°CA aSOI, which is similar to the signal delay noted in the other P_{pilot}=1300bar measurements. The very rapid growth of large regions emitting high intensity visible light is noted shortly after the first visible signal was measured. Complete spatial coverage of the bowl area by regions emitting high intensity light is also observed to a much greater extent than in any of the previously discussed measurements. Despite the use of the shortest possible visible camera exposure durations (2μs), significant regions of the visible images were saturated, therefore the shape of the highest intensity region contour may be slightly distorted. The total duration of high intensity emissions is also noted to be substantially longer than in previously discussed cases.

As in all other discussed data sets, the onset of the OH*-signal is coincident with the location of $q_{1,max}$, which is approximately 11°CA aSOI. Despite the much higher peak AHRR in the non-flame propagation case compared to the other two operating modes considered, the maximum spatial coverage by measured OH*-signal is less than the other two cases. As observed for the visible-signal, a much more rapid growth in the area of the bowl emitting high intensity OH*-emissions is noted.

5.4 Summary of Optical DIDF Investigation

Crank-angle resolved and simultaneous images of broadband visible and OH*-chemiluminescence emissions were recorded for one representative operating point from each of the DIDF operating regimes identified through thermodynamic analysis:

A) Pilot-independent DIDF combustion

B) Flame propagation DIDF combustion

C) Non-flame propagation DIDF combustion

Comparisons of natural broadband-visible and 307nm-filtered combustion light emissions from representative single cycles from each operating point for P_{pilot}=300bar and 1300bar were analyzed to support the thermodynamic-results based discussion of combustion mechanisms presented in chapter 5.

DIDF Ignition: Despite an asymmetrical pilot injection spray pattern (non-vertical injector), across all three of the DIDF combustion regimes explored, the first emission of visible- and OH*-signal, indicating combustion ignition sites, occurred distributed around the bowl periphery for P_{pilot}=1300bar. P_{pilot}=300bar produced ignition sites within the central bowl region, which appeared to be associated with the previous locations of pilot jets. For P_{pilot}=1300bar, the initial OH*-signal slightly preceded the initial visible-signal emission, indicating more effective premixing of the diesel fuel, thereby reducing the early visible light emission associated with PM. For P_{pilot}=300bar cases, localized high-intensity visible signals in the bowl centre were among the first signals, which preceded both spatially distributed visible-signals and the OH*-

signals indicating that the first reactions occur in very fuel rich regions resulting from poor mixing of the diesel pilot.

Measurement of OH*-Chemiluminescence: Characteristic features of the OH*-chemiluminescence signals, such as phasing of the initial and peak signal intensity, were more consistent with respect to the phasing of measured AHRR features than the corresponding measured broadband emissions in the visible spectrum. This was attributed to the use of a narrow band-pass filter, which ensured a more defined signal source, in contrast to the unfiltered measurement of visible light emissions, which are known to have several contributing sources in internal combustion processes.

For all analyzed pilot-injection pressures and operating points, the onset of measured OH*-chemiluminescence was approximately incident with the location of peak AHRR in stage 1 combustion, $q_{1,max}$. For all analyzed pilot-injection pressures and operating points, the location of maximum spatial coverage by high intensity OH*-emissions occurred in the same region as the transition from high-intensity to low-intensity stage 2 combustion, θ_{2b}, was calculated for corresponding thermodynamic points. It is possible that the inflection point in the AHRR used to define θ_{2b} by the algorithm described in §4.2 corresponds to the point where the high-intensity reaction zones begin to decrease in volume. Some adjustment of the filtering and logic parameters used by the algorithm is required to reliably define the combustion zones for the relatively noisy single-cycle optical measurements, and further investigation of this correlation is recommended.

Sequence of DIDF Combustion Mechanisms: Depending on P_{pilot} and the regime of DIDF combustion considered, three characteristic fuel conversion mechanisms as evidenced by the OH*-signal intensity distribution and rate of change of distribution were observed:

1) Homogeneous-distributed auto-ignition followed by progressive, radially-inward reaction zone growth:

i. Ignition reactions occur homogeneously around the bowl periphery; no clear OH*-signal intensity gradients visible because of high levels of turbulent mixing achieved during pilot injection and a small pilot mass.

ii. Remainder of premixed charge is progressively consumed starting with bowl periphery and ending with central bowl region. OH*-signal magnitude progressively grows and is observed to proceed radially-inward from the ignition zone at the bowl perimeter. This process appears to be flame propagation, but further quantitative measurement and analysis are needed to confirm this conclusion.

This sequence of combustion mechanisms was observed for DIDF regime A and B operating points with P_{pilot}=1300bar.

2) Heterogeneous-distributed auto-ignition followed by progressive reaction zone growth normal to residual pilot jet structures:

i. Ignition reactions occur within the residual structures of the pilot injection jets, where there is a higher local equivalence ratio than the homogeneous surroundings, which produces chemical-reactivity gradients. The reactivity gradients are a result of the low

mixing rates produced by low pressure pilot injection. The first ignition reactions occur within the portion of the residual pilot jet structure closest to the bowl perimeter, likely due to longer residence times.

ii. Following ignition, high-intensity reaction zone growth within the residual pilot structure proceeds radially-inward along the residual jet axes.

iii. Remaining regions of the premixed charge outside of the residual pilot jet structures, which have sufficiently high equivalence ratios, are progressively consumed starting with the boundary of the pilot and proceeding normally outward. Depending on the fuel concentration in regions away from the ignition sites, not all regions of the mixture will be able to support an intense reaction.

This sequence of combustion mechanisms was observed for DIDF operating regime A and B with low pressure pilot injections.

3) Bulk auto-ignition:

i. Bulk auto-ignition of majority of pilot fuel and entrained CH_4 occurs rapidly, with slight spatial bias towards the bowl periphery. The initial rate of change of OH*-signal intensity far exceeds corresponding OH*-signals in regime A and B cases.

This combustion mechanism was observed for DIDF operating regime C with P_{pilot}=1300bar, and was significantly different than the other two sequences of combustion mechanisms, which supports the division of the DIDF operating space into flame propagation and non-flame propagation regimes.

This chapter has supported the selected divisions of the DIDF operating space into operating regimes, which were based on observations made from thermodynamic data. The spatially-resolved data discussed in this chapter has also revealed that for low pilot injection pressures, the flame propagation structure is strongly influenced by the remaining diesel vapour, which is not considered in the existing accepted model of DIDF combustion. In the next chapter, observations from the thermodynamic and optical analyses are re-stated as a unified set of conclusions concerning the fundamental combustion and emissions mechanisms of DIDF operation.

Chapter 6: Conclusions

A combined thermodynamic and optical investigation of lean, naturally-aspirated, low-speed DIDF combustion across a range of operating points was performed in a heavy-duty, single-cylinder research engine. It was found that in the context of fuelling strategies, the operating points were best characterized by φ_{global}, R_{pilot}, and φ_{CH4}. In addition to these fueling metrics, at each operating point the effects of pilot injection pressure and timing were investigated. The operating space defined by φ_{global}, R_{pilot}, and φ_{CH4} was also found to be an effective and novel method to visually categorize the wide range of DIDF operating modes considered and is presented in Figure 54.

The broad combination of operating points and injection parameter sweeps was designed to bridge knowledge gaps regarding the fundamental DIDF combustion mechanisms previously proposed in other investigations, which were focussed primarily on either mixture properties or pilot injection parameters, but which have not previously been considered in a single, combined investigation.

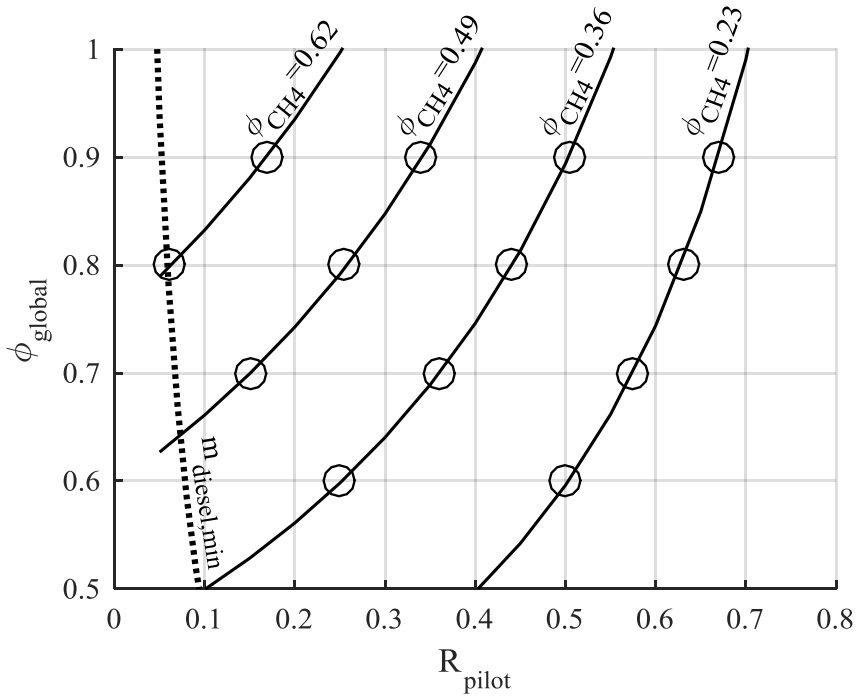

Figure 54: Definition of dual-fuel operating space based on R_{pilot}, φ_{global}, and φ_{CH4} used to design experiments in this investigation.

Analysis Tools for DIDF Combustion

Using a novel set of criteria based on the AHRR measured during thermodynamic experiments, DIDF combustion can be systematically discretized into sequential combustion stages, each with unique characteristics. In this work, the initial rapid apparent heat release was considered as 'stage 1 combustion', and was observed to be strongly dependent on pilot injection parameters in a way that was consistent with the premixed auto-ignition of the pilot diesel, and the widely accepted conceptual description of DIDF combustion presented by [23]. In contrast to observations by [23] and others, no clear correlation between increasing φ_{CH4} and the peak AHRR of stage 1 combustion was observed, which is typically expected due to the entrainment of CH_4 by the pilot jet. It is possible that for the lean conditions considered in this investigation

the effect of the entrained mass of CH_4 was minor compared to pilot fueling parameters. 'Stage 2 combustion' was defined as all processes contributing to the AHRR subsequent to stage 1 combustion.

For φ_{CH4}>0.4, stage 2 combustion was concluded to be characterized by flame propagation through premixed CH_4, diesel vapour, and air followed by a period of low intensity burn out. This description is similar to the accepted conceptual model, but also considers the diesel vapour to significantly influence the flame propagation mechanisms. In [28], the observed lower flame propagation limit was observed at φ_{CH4}=0.6, however in that investigation smaller pilot quantities were employed; it is possible that the lower observed flame propagation limit observed in this investigation was due to residual diesel vapour producing a higher effective φ than just the premixed CH_4. Metrics based on features of the AHRR from each identified stage of combustion are valuable tools to connect particular combustion mechanisms, such as premixed auto-ignition or flame propagation, with engine performance parameters such as NO_x and CH_4. Additional, division of the stage 2 combustion into high- and low-intensity sections strengthened correlations between second stage combustion AHRR and φ_{CH4}.

Using a novel method of presenting the spatial intensity distribution from recorded images in a temporally-resolved plot, broadband visible and OH*-chemiluminescence signals were directly compared to measured AHRR using cumulative histogram time series. Direct, temporally resolved comparison of spatially-resolved optical data and corresponding measured AHRR data is a novel technique, which identified two characteristics of the DIDF combustion stages:

i. Across all operating points and pilot injection pressures, the initial OH*-chemiluminescence signal was found to be coincident with the peak AHRR of stage 1 combustion, indicating the rapid increase of combustion temperatures to be strongly tied to the auto-ignition of the diesel pilot and entrained CH_4.

ii. Across all operating points and pilot injection pressures investigated, the OH*-chemiluminescence signal was also observed to have a single peak value occurring near the AHRR inflection point following stage 2 combustion, which defines the transition from high-intensity to low-intensity stage 2 combustion. The correlation between the peak OH*-chemiluminescence signal and the end of the high-intensity combustion indicates a connection between the decreasing size of high-intensity reaction zones due to the shrinking mass of unburned fuel, and the onset of the slow reaction mechanisms, which were observed in stage 2b AHRR across the thermodynamically investigated DIDF operating space. Further investigation of this connection is required.

An example of the correlation between the OH*-chemiluminescence cumulative histogram time series and the corresponding thermodynamic measurement of AHRR is presented in Figure 55. Dashed lines highlight the correlating features of the two measurements, which have not previously been identified without the application of this optical data presentation method.

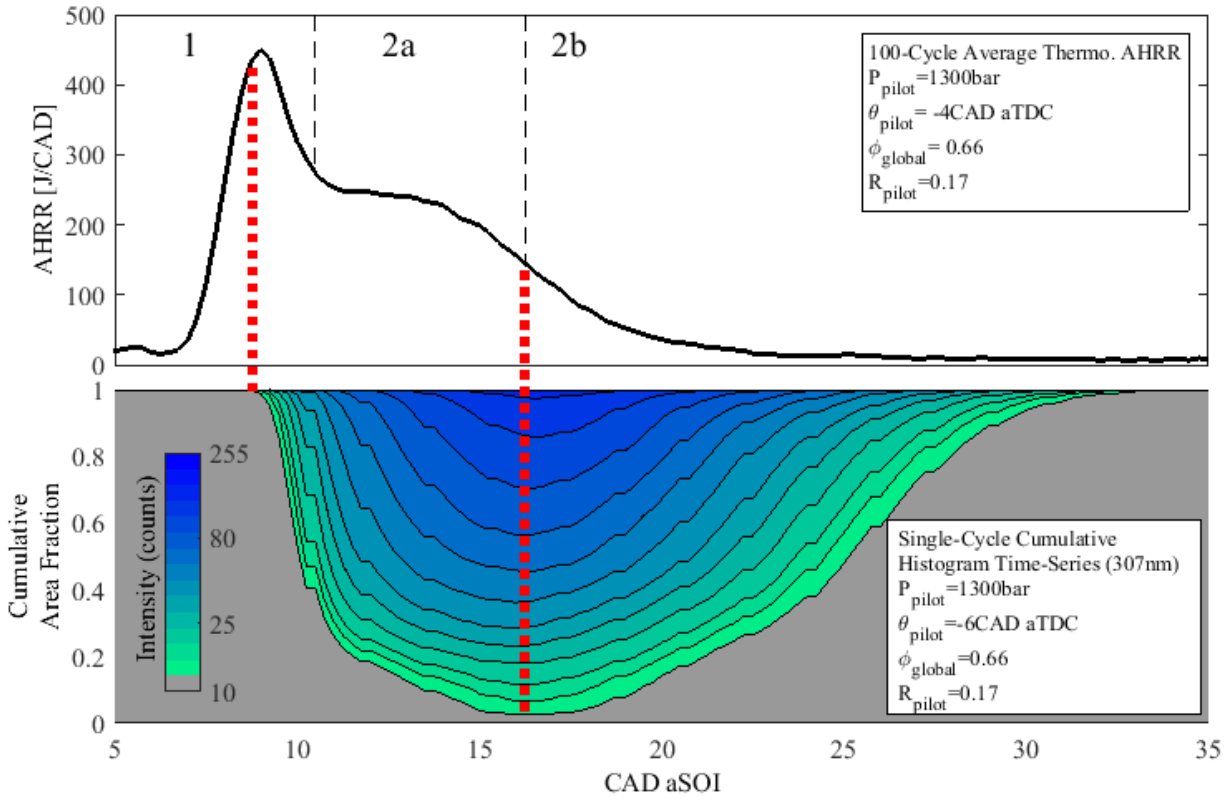

Figure 55: Correlation between cumulative histogram time series of OH*-chemiluminescence measurements and corresponding thermodynamic AHRR.

Regimes of DIDF Operation-Thermodynamic Results

Analysis of AHRR and emissions trends from the DIDF operating points investigated with the thermodynamic configuration of the research engine revealed three fundamentally different combustion regimes for DIDF operation as different R_{pilot} and φ_{CH4} were used. The three identified regimes were 'pilot-independent', 'flame propagation', and 'non-flame propagation' combustion. The observed boundaries of transitions between these combustion regimes are presented across the investigated R_{pilot}-φ_{global} operating space in Figure 56. The locations of the observed transition regions are relevant to the research engine and testing conditions of this

investigation, and are expected to be different for other experimental conditions, and combustion analysis criteria.

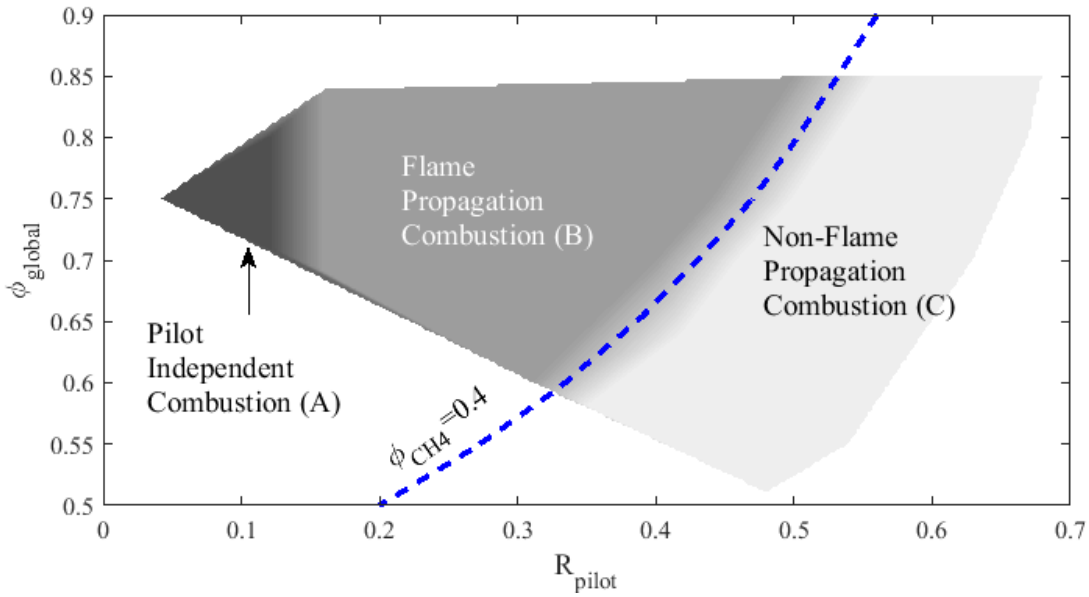

Figure 56: Observed boundaries of transition regions between 'pilot independent', 'flame propagation', and 'non-flame propagation' DIDF combustion regimes across the R_{pilot}-φ_{global} operating space.

For the operating conditions explored, the stage 2 combustion AHRR is linearly proportional to φ_{CH4} for $\varphi_{CH4} > 0.4$, which is consistent with flame propagation behaviour observed in fundamental laminar flame speed measurements [55]. The linear proportionality of stage 2 combustion AHRR to φ_{CH4} distinguished the flame propagation and non-flame propagation regimes, B and C, respectively, from one another. Rapid growth of regions emitting high-intensity OH*-chemiluminescence was observed for DIDF operating regime C, which is consistent with bulk auto-ignition in contrast to the progressive OH*-chemiluminescence reaction zone growth exhibited in regimes A and B. A special case of DIDF regime B operation with sufficiently small R_{pilot}, was observed to have emissions of NO_x and CH_4 and a AHRR

shape, which were insensitive to the pilot injection timing and pressure, which was not observed for any other operating points investigated. Each of the regimes and their characteristic traits during stage 1 and stage 2 combustion are summarized in detail below.

DIDF Operating Regimes A & B: φ_{CH4} >0.4

Stage 1 Combustion: For the specific operating conditions investigated, stage 1 combustion exhibited heat release behaviour consistent with a pre-mixed auto-ignition event occurring in a diesel-vapour / CH_4 / air mixture. Based on diesel pilot literature, this combustion event may also include some flame propagation [34]. As indicated by the initial measurable emissions of OH*-chemiluminescence, the peak of stage 1 AHRR produces a rapid increase in reaction intensity.

Consistent with this description, increasing pilot injection pressure or mass increases the fraction of total energy released in stage 1 combustion. For a given pilot injection mass, increasing P_{pilot} from 300bar to 800bar substantially enhances the turbulent mixing of the diesel pilot with the premixed CH_4 and air. However, this effect is limited when increasing P_{pilot} >800bar, interpreted as approaching the limit for complete, homogeneous pilot mixing. For P_{pilot}=300bar, heterogeneous reaction zones associated with the residual fuel concentration resulting from poor turbulent mixing during the pilot injection were evident in both visible- and OH*-chemiluminescence measurements, but have not been noted previously in the surveyed literature. Within the heterogeneous diesel / CH_4 / air mixtures, the first ignition sites were located near the bowl periphery, which was interpreted as the location of diesel molecules with the longest residence times. For P_{pilot}=1300bar, at two R_{pilot}-φ_{global} operating points, a homogeneous reaction zone located at the bowl periphery was indicated by a relatively uniform OH*-

chemiluminescence signal, as observed by. This OH*-chemiluminescence also preceded the visible-signal measured at the bowl periphery, which is consistent with observations by [28].

Stage 2 Combustion: For all pilot injection pressures and masses, the mean AHRR for the high-intensity portion of stage 2 combustion increased linearly with φ_{CH4}, which is consistent with experimental laminar flame speed measurements in lean, homogeneous mixtures of CH_4 and air [55]. This suggests that for regimes A and B, fuel is converted through a flame propagation mechanism. Spatially-resolved measurements of broadband visible and 307nm light emissions indicated that stage 2 combustion reaction zone structure was strongly dependent on pilot injection pressure.

For P_{pilot}=300bar, low turbulent mixing rates during the pilot injection prevented portions of the diesel vapour from being converted during stage 1 combustion. Consequently, those portions of diesel vapour were converted during stage 2 combustion which was indicated by the persistence of the residual pilot injection structures evident in both the visible-and OH*-measurements. Within the higher reactivity regions of the residual pilot injection structures, reactions were observed to proceed along the pilot injection axes toward the injector. At the same time, relatively slow growth of the reaction zones normal to the pilot jet axes into the leaner surrounding mixture of CH_4, diesel vapour and air was observed. These observations contradict the conventional conceptual model of DIDF combustion, which assumes the complete conversion of pilot fuel in the premixed auto-ignition event, which is labeled stage 1 combustion in this work. For the lean, naturally-aspirated, low pilot injection pressure conditions considered here, a revised conceptual model should be considered.

For P_{pilot}=1300bar, higher turbulent mixing rates during injection caused a greater mass of diesel and entrained CH_4 to be converted in stage 1 combustion and, consequently, less to be converted in stage 2 combustion. Following the homogeneously-distributed ignition reactions in the bowl periphery, a progressive radially-inward growth of the single, toroidal reaction zone was observed in the visible- and OH*-signals, which is consistent with the observations of [28], where it was described as flame propagation. Despite lower reaction intensity in the central bowl region where a portion of CH_4 emissions have previously been proposed to originate during lean DIDF operation, the higher pilot injection pressure produced lower emissions of CH_4, relative to the lower injection pressures considered here.

Following the high-intensity portion of stage 2 combustion was the low-intensity portion. The AHRR of the low-intensity portion of stage 2 combustion was qualitatively similar to late stage burnout in conventional CI combustion. Further investigation is required to more rigorously characterize the combustion mechanisms contributing to the observed release of heat in this combustion stage.

DIDF Operating Regime C: φ_{CH4} <0.4

Stage 1 Combustion: In the non-flame propagation regime of DIDF operation, stage 1 combustion is the dominant feature of the AHRR. As in the flame propagation regime (B), increasing the pilot injection pressure increases the peak AHRR and fraction of energy released in stage 1 combustion. Unlike in the pilot independent and flame propagation regimes (A and B), increasing the mass of injected diesel caused a decrease in the fraction of total energy released in

stage 1 combustion, indicating that the relatively large pilot injection masses (>40mg) cannot be completely prepared for homogeneous auto-ignition, even with high pilot injection pressure and low engine speeds considered here. As observed for high pilot injection pressures in regimes A and B, the initial reaction sites occurred in the bowl periphery. The growth of high-intensity reaction zones, however, was observed to be substantially more rapid than for regime A or B as indicated by the rapid increase OH*-chemiluminescence intensity and spatial coverage. Reaction zone growth rates observed to be much more rapid than the corresponding growth rates of flame propagation was interpreted to indicate bulk auto-ignition of premixed CH_4, and diesel vapour.

Stage 2 Combustion: Relatively slow fuel conversion processes, were observed in thermodynamic measurements of stage 2 combustion AHRR, which was observed to be independent of φ_{CH4}, and therefore unlikely to be flame propagation. Further investigation is required to more rigorously characterize the combustion mechanisms contributing to the observed release of heat in this combustion stage.

Concluding Remark

This investigation presented a primarily qualitative analysis of the fundamental combustion mechanisms present across a broad range of DIDF operating points, and has served to identify many of the physics present during the DIDF combustion process and some novel analysis tools to characterize and discuss them. The commissioned facility and analysis work to date represent the foundation for future investigations to more specifically treat select DIDF combustion phenomena that were observed in this work, but were not quantified. To leverage the outcomes of this work, several major areas for future work are proposed in the following chapter.

Chapter 7: Recommendations

This chapter presents a list of recommendations for future work to be conducted on the obtained data set described in this work, or using the facility that was described. Recommendations for future work are generally categorized as follows:

i. Expansion of the current measurement database.
ii. Addition of models & quantitative analysis tools.
iii. Enhancement of the research engine facility.
iv. Investigation of new aspects of DIDF operation.

Expansion of Current Measurement Database

In light of the combined thermodynamic and optical tools used in this work, only a relatively small range of the conventional engine operating map was considered. Most notably, this work only considered one speed and global equivalence ratios less than ~0.9. In addition, due to the exploratory nature of this work, parameters such as EGR, intake pressure, and intake temperature were not considered. Although broad in scope, the thermodynamic and optical investigations of low-speed, lean, naturally-aspirated DIDF operation with pure CH_4 performed within this work addressed a region of the DIDF operating space, which is of limited practical interest in most applications. To extend observations and conclusions presented in this initial work, the following additions to the measurement campaign are proposed:

- **Increased Engine Speed:** A subset of the R_{pilot}-φ_{global} operating points from the current work should be repeated at additional engine speeds (*e.g.* at 1000-1200rpm). Roughly doubling the engine speed will: consider an engine operating speed typical of heavy-duty applications, increase the crank-angle duration of injection events (possible effect on pilot mixing), and remain within the operating speed limits of the optical engine configuration. Additional, higher speeds can also be considered, but only for thermodynamic investigations.
- **Increased φ_{global} and φ_{CH4}:** Performing measurements using same methods as this work, the examined DIDF operating space should be extended to the maximum φ_{CH4}, which for the current facility at 600rpm is $\varphi_{CH4}\approx0.95$. This will permit further exploration of the pilot-independent regime (A) of DIDF operation, for which there was only a single operating point in this investigation.
- **EGR, Forced Induction, Throttling, and Intake Air Temperature:** Forced induction and EGR are ubiquitous technologies in heavy-duty applications and must be considered in order to connect the current work and methods to commercial applications. Combinations of intake temperature and pressure, and EGR variations have also been shown by other researchers to produce distinct operating modes for DIDF engines through modification of charge reactivity. The existing experimental facility does not have the capability to control EGR, intake pressure, or intake temperature, but these upgrades are recommended.
- **Repeat the Diesel-Only Measurements:** Direct superposition of the diesel-only AHRR and DIDF AHRR for P_{pilot}=800bar, and 1300bar was not possible because θ_{pilot} used in the DIDF and diesel-only experiments were not matched. Repeating the diesel-only

measurements with θ_{pilot} matching the corresponding DIDF measurements is recommended to improve future analysis of the impact of premixed CH_4 on pilot combustion.

Simple Modelling & Quantitative Analyses

The majority of analysis presented in this work was exploratory and qualitative in nature; designed to identify combustion features of interest. More quantitative analyses of the combustion mechanisms noted in this work and the addition of simple models to accompany measurements are needed to: more rigorously define operating regimes and causes for trends in combustion AHRR and emissions, ensure all physics of importance have been captured, and design future experiments. To this end, the following are proposed:

- **Quantitative Analyses (Thermodynamic):** Combustion efficiency, ignition delay periods, and crevice volume calculations are recommended to further support the discussion of stage 1 and stage 2 combustion mechanisms. It is also recommended that quantitative analyses be performed using consistent pilot injection timing, in addition to the 'best timing' used in this investigation.
- **Quantitative Analyses (Optical):** Calculation of flame front speed and flame front area could be performed using the optical data recorded in this investigation. It is recommended that these calculations are performed and correlated with thermodynamic data, such as AHRR.
- **Multi-zone Model for Interpretation of Experimental Results:** Application of observations of flame front area, speed and other optically measured combustion properties incorporated with chemical kinetics models of CH_4 combustion is

recommended to formulate a multi-zone model similar to other investigations, such as [59].

- **Turbulence Modelling:** The turbulent mixing phenomena were highlighted as a crucial parameter for stage 1 combustion, and indirectly affected stage 2 combustion (because of different ignition sites), however only pilot injection pressure was used to characterize the turbulent mixing in this work. The addition of a simple time and length scale based turbulence model would be a valuable addition to identify what, if any, direct effects injection pressure, duration, orifice size may have on stage 2 combustion.
- **Temperature Modelling:** No quantified comments on combustion gas temperature effects were made in this investigation, although this is known to be very important for DIDF ignition delay, flame propagation, and emissions of NO_x and CH_4. A temperature model will also be necessary to implement a multi-zone combustion model.
- **'Puff' Jet Modelling:** The characteristics of the ignition reaction sites, stage 1 combustion, and stage 2 combustion were found to vary significantly with the pilot injection pressure and mass (injection duration also varied with mass). A review of the literature surrounding short injections, such as conventional diesel pilot injections and those employed in DIDF operation, revealed a number of successful empirical models However, these lacked an adequate conceptual description to be more widely applied without 'tuning' for a specific engine or application. The development of a pilot injection model specific to DIDF, which can capture and potentially predict the mixing phenomena would be of great value to future work. This model could be validated by both thermodynamic and optical measurements in the existing facility.

Improvements to the Experimental Facility

This work represents the first major investigation performed using the facility described here, and continued development and upgrading of the facility capabilities is expected. In order to extend the conclusions of this work to more relevant operating conditions, improve the quality and reliability of measurements, and increase the experimental throughput the following upgrades to the facility are recommended:

- **Central & Vertical Mounting of Direct Injector:** Symmetrical mounting of the direct injector is recommended to improve quantification of future optical measurements.
- **Upgrades to the Thermal Management System:** Increasing the heating power is recommended to reduce test set-up times. Increasing the maximum temperature from 65°C to 90°C is recommended to reduce test set-up times and enable more direct comparison of thermodynamic and optical measurements.
- **Re-design of Optical Piston:** Increasing the optical compression ratio to 14:25:1 is recommended to match thermodynamic piston. Re-design of window sealing gaskets is also recommended to improve sealing and reliability during high-load testing. Re-design piston for ring pack as wear-item is recommended to reduce the frequency of optical measurement interruptions.
- **EGR, Intake Pressure & Temperature:** Addition of EGR, intake temperature and pressure control is recommended to achieve combustion conditions relevant to modern applications.
- **Addition of DIDF Metrics to Operator GUI:** Live calculation and display of R_{pilot}, φ_{global}, φ_{CH4} on operator's GUI is recommended to improve measurement quality.

- **Integral Light Measurement:** The addition of band-pass filtered light collection optics and light detectors at a series of wavelengths through the UV and visible spectrums would be a relatively cost effective (compared to spatially-resolved systems) method of identifying which spectra to target with more advanced diagnostics. This method could also be used to reduce the exposure sweeps required for the intensified system when testing a new operating point where emissions are unknown.

New Investigations

Some additional interesting avenues of fundamental DIDF combustion mechanism research have been identified during the literature review, which could be performed at a few selected locations of the current investigation, perhaps from each DIDF operating regime. The following is an incomplete list of potential future investigation topics:

- **Split Injections:** Several investigations have shown substantial benefits to DIDF emissions and combustion performance with the application of split injection techniques.
- **Partially-Premixed Combustion:** Other investigations have previously explored advanced DIDF combustion techniques where very advanced pilot injection timing (>50°CA bTDC) is used to create a more RCCI-like operating mode with a homogeneous diesel-CH_4 mixture accompanied by a small, late pilot injection for combustion phasing control. Addition of a bandpass filter in the near-UV or violet portion of the light spectrum would allow visualization of low temperature pre-reactions involving CH, C_2, CH_2O, CHO, and CN [54].
- **Laminar Flame Speed in Diesel-CH_4 Mixtures at TDC Conditions:** Fundamental flame speed data of DIDF-relevant combustion would be invaluable to supporting

conclusions drawn on observed flame propagation phenomena in this work and many others.

- **Injection Orifice Size:** The size of the direct injector orifices is expected to substantially affect the mixing phenomena related to the pilot injection in DIDF operation. Comparison of the AHRR measured across varying orifice size, pilot pressure and pilot mass may distinguish which effects are due to increased charge reactivity and which are related to turbulent mixing effects.

References

1. Stocker, T.F., D. Qin, G.-K. Plattner, M. Tignor, S.K. Allen, J. Boschung, A. Nauels, Y. Xia, V.B. and P.M.M. (eds. ., "Climate Change 2013: The Physical Science Basis. Contribution of Working Group I to the Fifth Assessment Report of the Intergovernmental Panel on Climate Change," 2013, doi:10.1017/CBO9781107415324.

2. Sims R., R. Schaeffer, F. Creutzig, X. Cruz-Núñez, M. D'Agosto, D. Dimitriu, M.J. Figueroa Meza, L. Fulton, S. Kobayashi, O. and Lah, A. McKinnon, P. Newman, M. Ouyang, J.J. Schauer, D. Sperling, and G.T., "2014: Transport. In: Climate Change 2014: Mitigation of Climate Change. Contribution of Working Group III to the Fifth Assessment Report of the Intergovernmental Panel on Climate Change," 2014.

3. Emission Standards: Europe: Heavy-Duty Truck and Bus Engines, https://www.dieselnet.com/standards/eu/hd.php, Dec. 2015.

4. Emission Standards: USA: Heavy-Duty Onroad Engines, https://www.dieselnet.com/standards/us/hd.php#y2007, Dec. 2015.

5. NGL North America, http://www.bp.com/en_na/gas/north-america/learn-more/ngl.html, 2015.

6. Kokjohn, S.L., Hanson, R.M., Splitter, D. a., and Reitz, R.D., "Experiments and modeling of dual-fuel HCCI and PCCI combustion using in-cylinder fuel blending," *SAE Int. J. Engines J. Engines* 2(2):24–39, 2010, doi:10.4271/2009-01-2647.

7. Harrington, J., Munshi, S., Nedelcu, C., Ouellette, P., Thompson, J., and Whitfield, S., "Direct Injection of Natural Gas in a Heavy-Duty Diesel Engine Reprinted From : Diesel Engine Experiments," *SAE Tech.* (724), 2002.

8. Nieman, D.E., Dempsey, A.B., and Reitz, R.D., "Heavy-Duty RCCI Operation Using Natural Gas and Diesel," *SAE Int.J.Engines* 5(2):270–285, 2012, doi:10.4271/2012-01-0379.

9. Königsson, F., Stålhammar, P., and Ångström, H.-E., "Combustion Modes in a Diesel-CNG Dual Fuel Engine," *SAE Pap.* (2011-01-1962):2387–2398, 2011, doi:10.4271/2011-01-1962.

10. Kahn Ribeiro, S., S. Kobayashi, M. Beuthe, J. Gasca, D. Greene, D. S. Lee, Y. Muromachi, P. J. Newton, S. Plotkin, D. Sperling, R. Wit, P.J.Z., "5 Transport and its infrastructure - AR4 WGIII Technical Summary," 2007.

11. Karim, G.A., "Combustion in Gas Fueled Compression: Ignition Engines of the Dual Fuel Type," *J. Eng. Gas Turbines Power* 125(3):827, 2003, doi:10.1115/1.1581894.

12. Besch, M.C., Israel, J., Thiruvengadam, A., Kappanna, H., and Carder, D., "Emissions Characterization from Different Technology Heavy-Duty Engines Retrofitted for CNG/Diesel Dual-Fuel Operation," *SAE Int. J. Engines* 8(3):2015–01–1085, 2015, doi:10.4271/2015-01-1085.

13. Forster, P., Ramaswamy, V., Artaxo, P., Berntsen, T., Betts, R., Fahey, D.W., Haywood, J., Lean, J., Lowe, D.C., Myhre, G., Nganga, J., Prinn, R., Raga, G., Schulz, M., and Dorland, R. Van, "Changes in Atmospheric Constituents and in Radiative Forcing. Chapter 2," 2007.

14. Liu Z, K.G. a, "The ignition delay period in dual fuel engines," *SAE Tech. Pap. 950466* (41 2):354 a 362, 1995, doi:10.4271/950466.

15. Zhou, L., Liu, Y.-F., Wu, C.-B., Sun, L., Wang, L., Zeng, K., and Huang, Z.-H., "Effect of the diesel injection timing and the pilot quantity on the combustion characteristics and the fine-particle emissions in a micro-diesel pilot-ignited natural-gas engine," *Proc. Inst. Mech. Eng. Part D J. Automob. Eng.* 227(8):1142–1152, 2013, doi:10.1177/0954407013480452.

16. Lin, Z. and Su, W., "A Study On The Determination of the Amount of Pilot Injection and Rich and Lean Boundaries of the Pre-Mixed CNG / Air Mixture For a CNG / Diesel Dual-Fuel Engine," *SAE Tech. Pap. Ser.* 2003-01-07(724), 2003.

17. Ishiyama, T., Kang, J., and Ozawa, Y., "Improvement of Performance and Reduction of Exhaust Emissions by Pilot-Fuel-Injection Control in a Lean-Burning Natural-Gas Dual-Fuel Engine," *SAE Tech. Pap. Ser* 5(1):243–253, 2012, doi:10.4271/2011-01-1963.

18. Ryu, K., "Effects of pilot injection timing on the combustion and emissions characteristics in a diesel engine using biodiesel-CNG dual fuel," *Appl. Energy* 111:721–730, 2013, doi:10.1016/j.apenergy.2013.05.046.

19. Gunea, C., Razavi, M.R.M., and Karim, G. a, "The Effects of Pilot Fuel Quality on Dual Fuel Engine Ignition Delay," *Sae Pap. 982453* (724):1–7, 1998, doi:10.4271/982453.

20. Abd Alla, G.H., Soliman, H.A., Badr, O.A., and Abd Rabbo, M.F., "Effect of pilot fuel quantity on the performance of a dual fuel engine," *Energy Convers. Manag.* 41(6):559–572, 2000, doi:10.1016/S0196-8904(99)00124-7.

21. Sahoo, D., Miles, P.C., Trost, J., and Leipertz, A., "The Impact of Fuel Mass, Injection Pressure, Ambient Temperature, and Swirl Ratio on the Mixture Preparation of a Pilot Injection," *SAE Int. J. Engines* 6(3):2013–24–0061, 2013, doi:10.4271/2013-24-0061.

22. Krishnan, S.R. and inivasan, K.K., "Multi-zone modelling of partially premixed low-temperature combustion in pilot-ignited natural-gas engines," *Proc. Inst. Mech. Eng. Part D J. Automob. Eng.* 224(12):1597–1622, 2010, doi:10.1243/09544070JAUTO1472.

23. Karim, G. a, Z, L., and Jones, W., "Exhaust Emissions from Dual Fuel Engines at Light Load," *Soc. Automot. Eng. Inc, SAE* 932822(412), 1993, doi:10.4271/932822.

24. Sahoo, B.B., Sahoo, N., and Saha, U.K., "Effect of engine parameters and type of gaseous fuel on the performance of dual-fuel gas diesel engines-A critical review," *Renew. Sustain. Energy Rev.* 13(6-7):1151–1184, 2009, doi:10.1016/j.rser.2008.08.003.

25. Karim, G.A., Ito, K., Abraham, M., and Jensen, L., "An Examination of the Role of Formaldehyde in the Ignition Processes of Duel Fuel Engine," *SAE Int. Tech. Pap.*, 1991.

26. Papagiannakis, R., Hountalas, D., and Kotsiopoulos, P., "Experimental and Theoretical Analysis of the Combustion and Pollutants Formation Mechanisms in Dual Fuel DI Diesel Engines," *SAE Tech. Pap. 2005-01-1726* (724), 2005, doi:10.4271/2005-01-1726.

27. Hiroyasu, H., Kadota, T., and Arai, M., "Development and Use of a Spray Combustion Modeling to Predict Diesel Engine Efficiency and Pollutant Emissions," *Jsme* 26(214):569–575, 1983.

28. Dronniou, N., Kashdan, J., Lecointe, B., Sauve, K., and Soleri, D., "Optical Investigation of Dual-fuel CNG/Diesel Combustion Strategies to Reduce CO_2 Emissions," *SAE Int. J. Engines* 7(2):2014–01–1313, 2014, doi:10.4271/2014-01-1313.

29. Badr, O., Karim, G. a., and Liu, B., "Examination of the flame spread limits in a dual fuel

engine," *Appl. Therm. Eng.* 19(10):1071–1080, 1999, doi:10.1016/S1359-4311(98)00108-2.

30. Dec, J.E., "A conceptual model of DI diesel combustion based on laser sheet imaging," *SAE Tech. Pap.* (970873), 1997, doi:10.4271/970873.

31. Chiu, W.S., Shahed, S.M., and Lyn, W.T., "A Transient Spray Mixing Model for Diesel Combustion," *SAE Pap.* 760128, 1976, doi:10.4271/760128.

32. Abramovich, G.N., Krasheninnikov, S.I., Sekundov, A.N., and Smirnova, I.P., "Turbulent mixing of gas jets," *Moscow*, 1974.

33. Stegemann, J., Seebode, J., and Baltes, J., "Influence of throttle effects at the needle seat on the spray characteristics of a multihole injection nozzle," *Zaragoza*, 2002.

34. Barba, C., Burkhardt, C., and Bargende, M., "A Phenomenological Combustion Model for Heat Release Rate Prediction in High-Speed DI Diesel Engines with Common Rail Injection," (724), 2015.

35. Whitehouse, N.D. and Sareen, B.K., "Prediction of Heat Release in a Quiescent Chamber Diesel Engine Allowing for Fuel / Air Mixing," *Sae* 12, 1974, doi:10.4271/740084.

36. Peters, N., "Laminar flamelet concepts in turbulent combustion," *Symp. Combust.* 21(1):1231–1250, 1988, doi:10.1016/S0082-0784(88)80355-2.

37. Stiesch, G., "Modeling Engine Spray and Combustion Processes," Springer Science & Business Media, ISBN 3662087901, 2013.

38. Carlucci, A.P., Laforgia, D., and Saracino, R., "Effects of in-Cylinder Bulk Flow and Methane Supply Strategies on Charge Stratification , Combustion and Emissions of a Dual-Fuel DI Diesel Engine," 2015.

39. Königsson, F., Stalhammar, P., and Angstrom, H.-E., "Characterization and Potential of Dual Fuel Combustion in a Modern Diesel Engine," 2011, doi:10.4271/2011-01-2223.

40. Selim, M.Y.E., "A Study of Some Combustion Characterstics of Dual Fuel Engine Using EGR," *SAE Tech. Pap. Ser. 2003-01-07*, 2003, doi:10.4271/2003-01-0766.

41. Alla, G.H.A., Soliman, H.A., Badr, O.A., and Rabbo, M.F.A., "A Computational Investigation of the Effect of Exhaust Gas Recirculation on the Performance of a Dual Fuel Engine," (724), 2000.

42. Shen, J., Qin, J., and Yao, M., "Turbocharged diesel/CNG Dual-fuel Engines with Intercooler: Combustion, Emissions and Performance," *SAE Tech.* (724), 2003, doi:10.4271/2003-01-3082.

43. Papagiannakis, R.G. and Hountalas, D.T., "Experimental investigation concerning the effect of natural gas percentage on performance and emissions of a DI dual fuel diesel engine," *Appl. Therm. Eng.* 23(3):353–365, 2003, doi:10.1016/S1359-4311(02)00187-4.

44. Kashdan, J.T. and Thirouard, B., "A Comparison of Combustion and Emissions Behaviour in Optical and Metal Single-Cylinder Diesel Engines," *SAE Tech. Pap.* 2(1), 2009, doi:10.4271/2009-01-1963.

45. Kokjohn, S., Reitz, R.D., Splitter, D., and Musculus, M., "Investigation of Fuel Reactivity Stratification for Controlling PCI Heat-Release Rates Using High-Speed Chemiluminescence Imaging and Fuel Tracer Fluorescence," *SAE Int. J. Engines* 5(2):2012–01–0375, 2012, doi:10.4271/2012-01-0375.

46. Schlatter, S. and Schneider, B., "Ignition and Combustion Characteristics of a Diesel Pilot Spray in a Lean Premixed Methane/Air Charge using a Rapid Compression Expansion Machine," *SAE Tech. Pap.* 1–21, 2012, doi:10.4271/2012-01-0825.

47. Hountalas, D.T. and Papagiannakis, R.G., "A Simulation Model for the Combustion Process of Natural Gas Engines with Pilot Diesel Fuel as an Ignition Source," *SAE Pap.* (01-1245), 2001, doi:10.4271/2001-01-1245.

48. Karim, G.A., "An Examination of Some Measures for Improving the Performance of Gas Fuelled Diesel Engines At Light Load," *SAE Int. Tech. Pap.*, 1991.

49. Technology, a R.-I.I. o. and R, R.G.I.I. of T., "Effect of Intake Air Temperature and Pilot Fuel Quantity on the Combustion Characteristics of a LPG Diesel Dual Fuel Engine," *Sae* (724):97–105 ST – Effect of Intake Air Temperature and , 1998, doi:10.4271/982455.

50. Aroonsrisopon, T., Salad, M., Wirojsakunchai, E., Wannatong, K., Siangsanorh, S., and

Akarapanjavit, N., “Injection Strategies for Operational Improvement of Diesel Dual Fuel Engines under Low Load Conditions Tanet Aroonsrisopon , Mongkol Salad and Ekathai Wirojsakunchai,” *SAE Int.* 4970, 2009, doi:10.4271/2009-01-1855.

51. Heywood, J., “Internal combustion fundamentals,” *New York McGraw*, 1988.

52. Turns, S., “An introduction to combustion. 2nd,” *Bost. M cGraw Hill*, 2000.

53. Tomita, E., Kawahara, N., Piao, Z., and Yamaguchi, R., “Effects of EGR and Early Injection of Diesel Fuel on Combustion Characteristics and Exhaust Emissions in a Methane Dual Fuel Engine,” *SAE Tech. Pap. 2002-01-2723* (724), 2002, doi:10.4271/2002-01-2723.

54. Mancaruso, E. and Vaglieco, B.M., “UV-Visible Spectroscopic Measurements of Dual-Fuel PCCI Engine,” *SAE Int. J. Fuels Lubr.* 4(2):2011–24–0061, 2011, doi:10.4271/2011-24-0061.

55. Dong, Y. and Vagelopoulos, C., “Measurement of laminar flame speeds through digital particle image velocimetry: mixtures of methane and ethane with hydrogen, oxygen, nitrogen, and helium,” *Proc. …*, 2002.

56. Taschek, M., Koch, P., Egermann, J., and Leipertz, a., “Simultaneous Optical Diagnostics of HSDI Diesel Combustion Processes,” (724):1–13, 2005, doi:10.4271/2005-01-3845.

57. Nori, V. and Seitzman, J., “Evaluation of Chemiluminescence as a Combustion Diagnostic under Varying Operating Conditions,” *46th AIAA Aerosp. Sci. Meet. Exhib.* (January):1–14, 2008.

58. Kojima, J., Ikeda, Y., and Nakajima, T., “Spatially resolved measurement of OH*, CH *, AND C*\n2 chemiluminescence in the reaction zone of laminar methane/air premixed flames,” *Proc. Combust. Inst.* 28:1757–1764, 2000, doi:10.1016/S0082-0784(00)80577-9.

59. Belaid-Saleh, H., Jay, S., Kashdan, J., Ternel, C., and Mounaïm-Rousselle, C., “Numerical and Experimental Investigation of Combustion Regimes in a Dual Fuel Engine,” 2013, doi:10.4271/2013-24-0015.

Appendices

Appendix A : Experimental Facility P&IDs

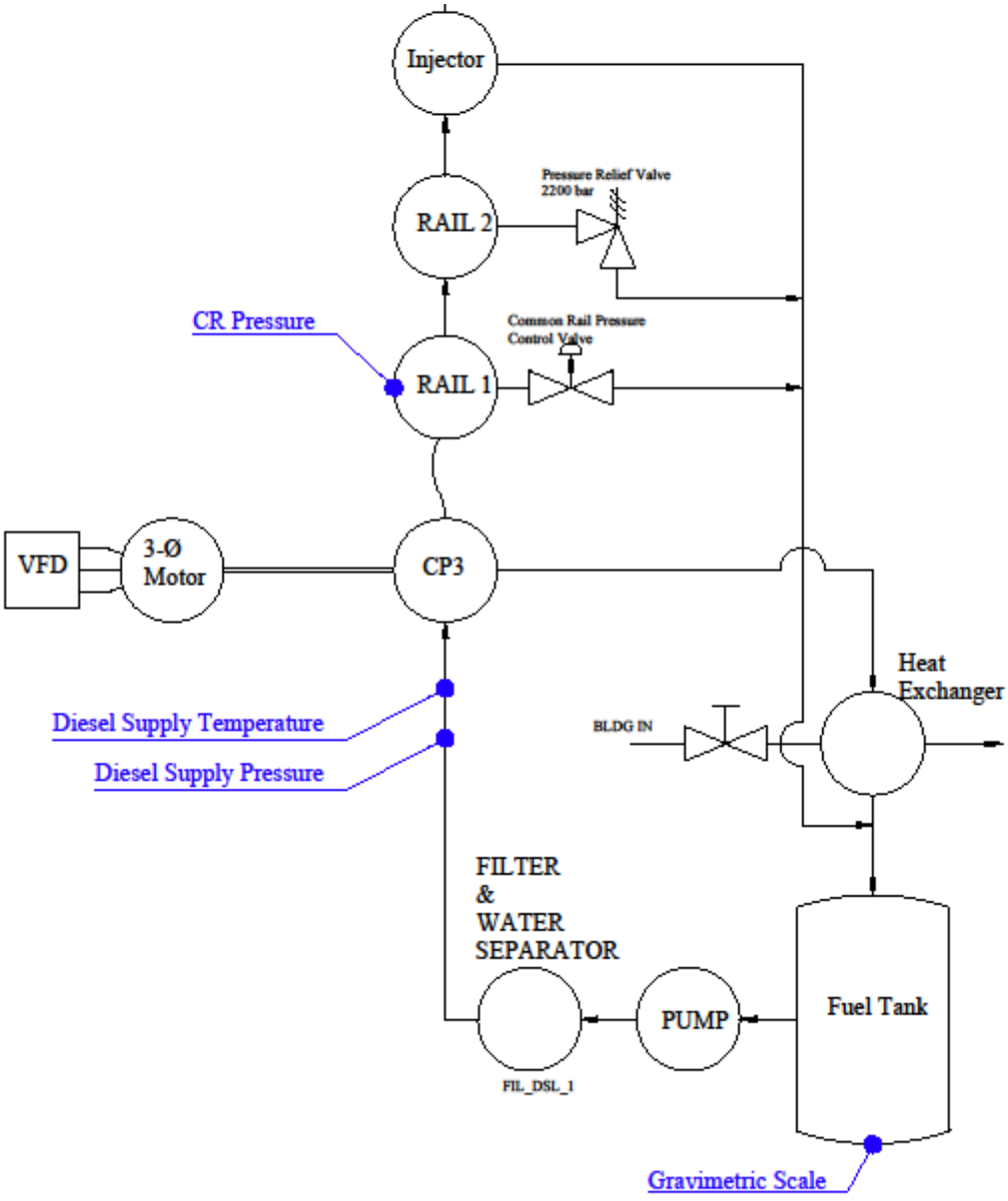

Figure A 1:P&ID of diesel direct injection system.

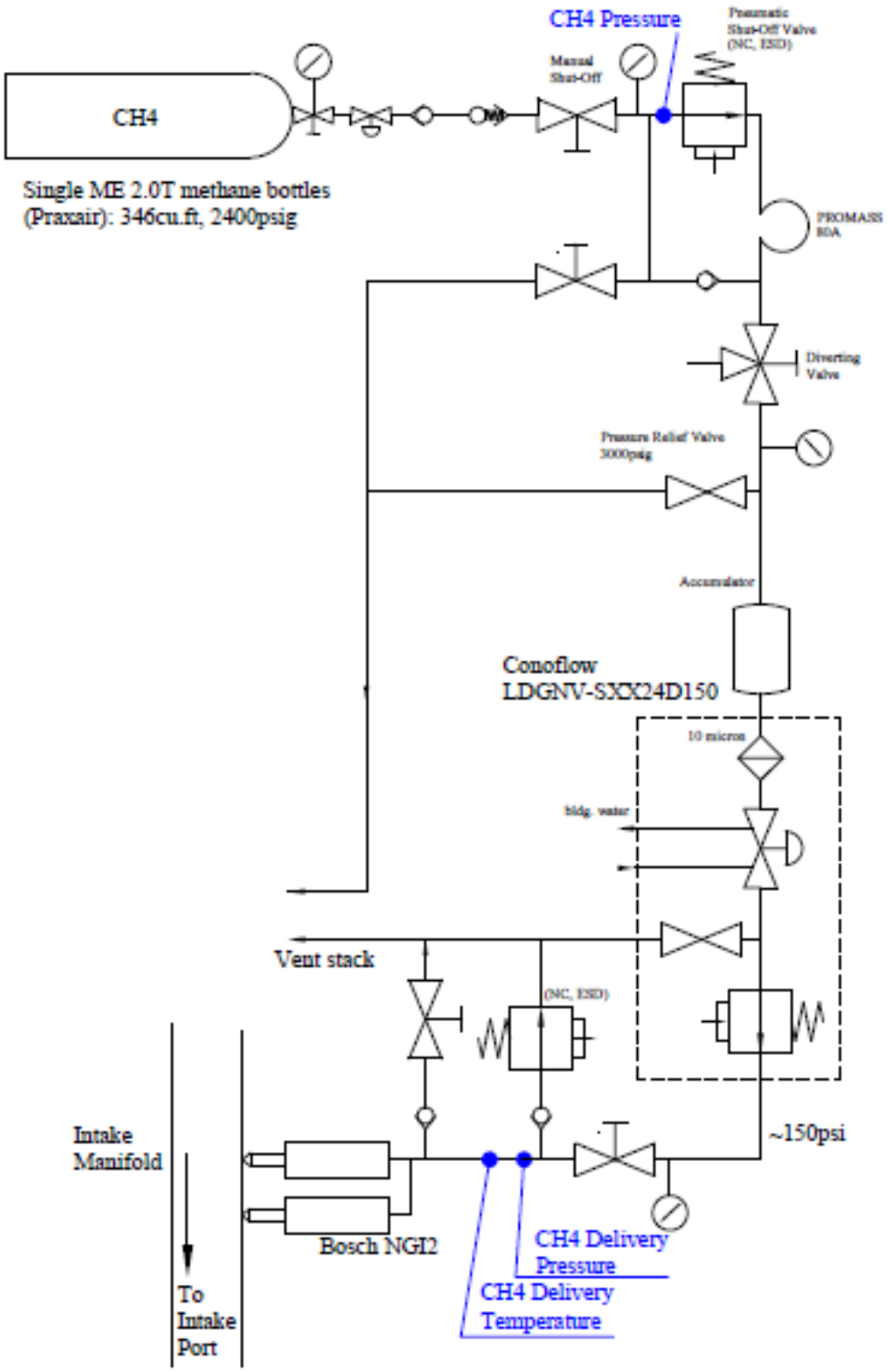

Figure A 2:P&ID of CH_4 port injection system.

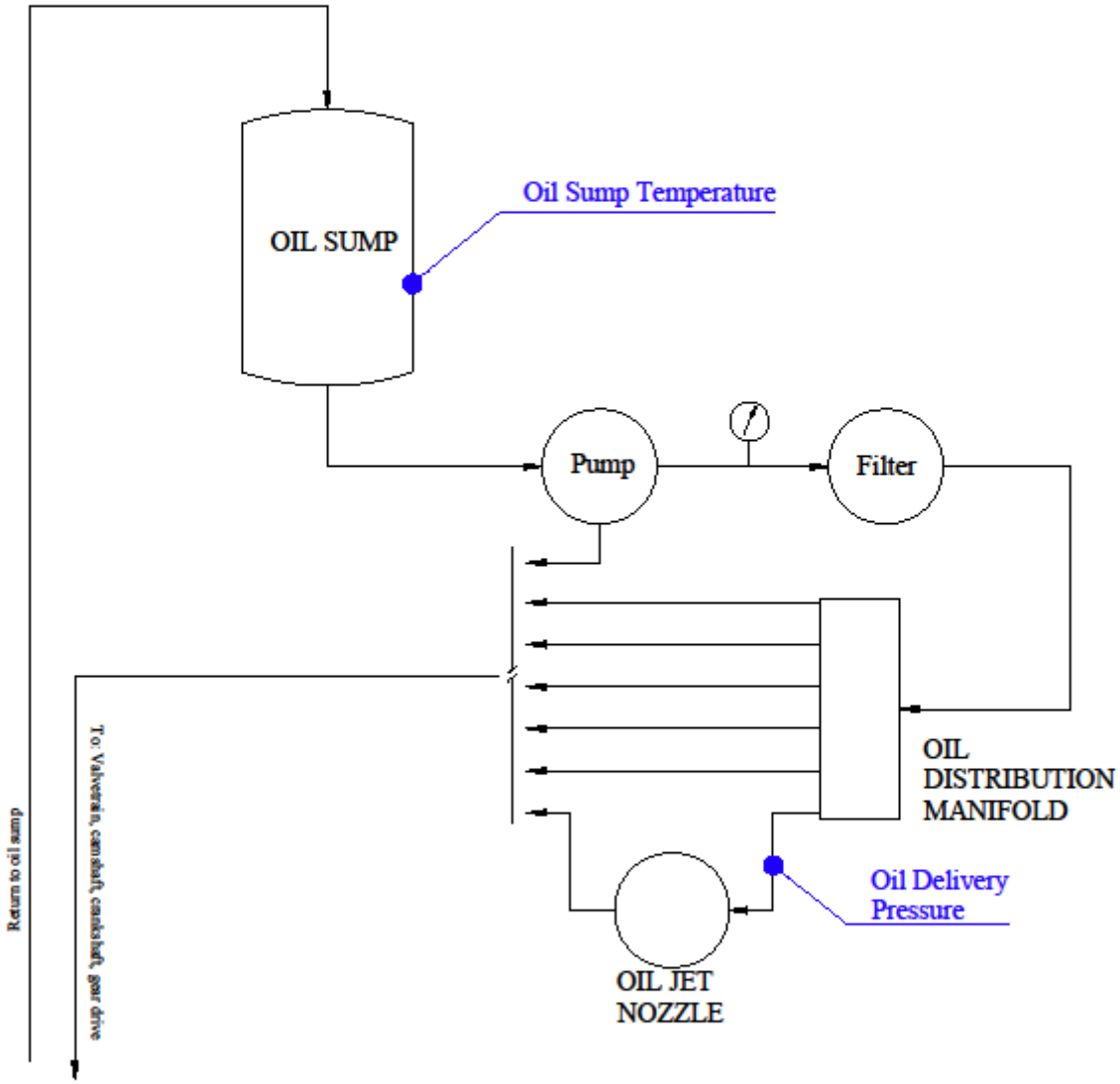

Figure A 3: P&ID of engine lubrication system.

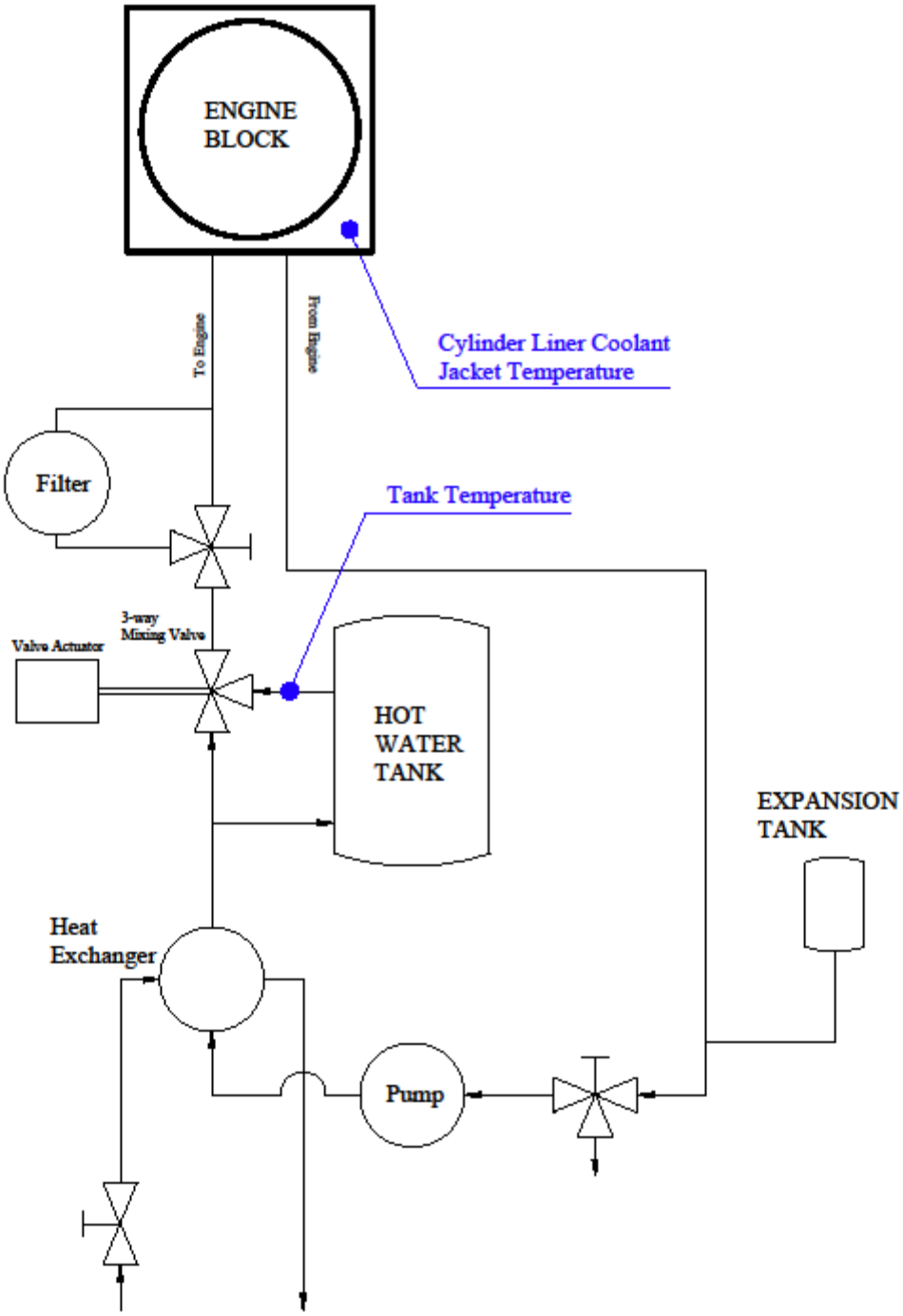

Figure A 4:P&ID of engine thermal management system.

Appendix B : Thermodynamic Test Point Data

The following tables contain thermodynamic measurement data. Bolded rows indicate 'best timing' operating points, which were analyzed in detail throughout this investigation. Operating points labelled 'pX-dXXX' are dual-fuel measurements, operating points labelled 'dX-dXXX' are diesel-only measurements.

B 1: Thermodynamic measurement set-point data

Label	Speed [rpm]	P_{pilot} [bar]	θ_{pilot} [°CA aTDC]	φ_{global} [-]	φ_{CH4} [-]	φ_{diesel} [-]	R_{pilot} [-]
'p2-d300'	600	300	-16	0.72	0.35	0.32	0.44
'p2-d300'	600	300	-12	0.75	0.38	0.31	0.41
'p2-d300'	600	300	-8	0.73	0.36	0.31	0.44
'p2-d300'	**600**	**300**	**-4**	**0.73**	**0.36**	**0.33**	**0.45**
'p2-d300'	600	300	0	0.73	0.36	0.32	0.44
'p3-d300'	600	300	-16	0.65	0.36	0.24	0.37
'p3-d300'	600	300	-12	0.65	0.36	0.24	0.37
'p3-d300'	**600**	**300**	**-8**	**0.62**	**0.35**	**0.22**	**0.35**
'p3-d300'	600	300	-4	0.62	0.35	0.22	0.35
'p3-d300'	600	300	0	0.62	0.35	0.22	0.35
'p4-d300'	600	300	-16	0.55	0.36	0.14	0.26
'p4-d300'	600	300	-12	0.55	0.35	0.15	0.27
'p4-d300'	**600**	**300**	**-8**	**0.53**	**0.34**	**0.13**	**0.26**
'p4-d300'	600	300	-4	0.54	0.34	0.15	0.28
'p4-d300'	600	300	0	0.76	0.55	0.14	0.18
'p7-d300'	600	300	-16	0.64	0.24	0.37	0.57
'p7-d300'	600	300	-12	0.64	0.24	0.37	0.58
'p7-d300'	**600**	**300**	**-8**	**0.63**	**0.23**	**0.36**	**0.57**
'p7-d300'	600	300	-4	0.63	0.23	0.37	0.58
'p7-d300'	600	300	0	0.60	0.23	0.34	0.58
'p8-d300'	600	300	-16	0.53	0.23	0.26	0.50
'p8-d300'	**600**	**300**	**-12**	**0.54**	**0.23**	**0.27**	**0.51**
'p8-d300'	600	300	-8	0.53	0.23	0.26	0.50
'p8-d300'	600	300	-4	0.52	0.23	0.25	0.49
'p8-d300'	600	300	0	0.51	0.23	0.25	0.49
'p9-d300'	600	300	-16	0.84	0.49	0.28	0.33

Label	Speed [rpm]	P_{pilot} [bar]	θ_{pilot} [°CA aTDC]	φ_{global} [-]	φ_{CH4} [-]	φ_{diesel} [-]	R_{pilot} [-]
'p9-d300'	600	300	-12	0.86	0.49	0.29	0.34
'p9-d300'	600	300	-8	0.85	0.50	0.28	0.34
'p9-d300'	**600**	**300**	**-4**	**0.84**	**0.49**	**0.28**	**0.33**
'p9-d300'	600	300	0	0.83	0.49	0.28	0.33
'p10-d300'	600	300	-16	0.76	0.48	0.21	0.28
'p10-d300'	600	300	-12	0.75	0.48	0.20	0.27
'p10-d300'	600	300	-8	0.76	0.48	0.21	0.28
'p10-d300'	**600**	**300**	**-4**	**0.75**	**0.48**	**0.20**	**0.27**
'p10-d300'	600	300	0	0.78	0.48	0.23	0.30
'p11-d300'	600	300	-16	0.65	0.47	0.10	0.16
'p11-d300'	600	300	-12	0.64	0.48	0.10	0.15
'p11-d300'	600	300	-8	0.64	0.48	0.09	0.14
'p11-d300'	**600**	**300**	**-4**	**0.67**	**0.48**	**0.12**	**0.19**
'p11-d300'	600	300	0	0.65	0.48	0.11	0.17
'p12-d300'	600	300	-16	0.87	0.62	0.15	0.18
'p12-d300'	600	300	-12	0.88	0.62	0.17	0.20
'p12-d300'	600	300	-8	0.88	0.62	0.17	0.20
'p12-d300'	600	300	-4	0.87	0.62	0.16	0.19
'p12-d300'	**600**	**300**	**0**	**0.87**	**0.63**	**0.16**	**0.18**
'p13-d300'	600	300	-16	0.77	0.62	0.06	0.08
'p13-d300'	600	300	-12	0.75	0.62	0.04	0.06
'p13-d300'	**600**	**300**	**-8**	**0.76**	**0.62**	**0.04**	**0.06**
'p13-d300'	600	300	-4	0.78	0.62	0.06	0.08
'p13-d300'	600	300	0	0.76	0.62	0.05	0.07
'p5-d800'	600	800	-12	0.85	0.24	0.57	0.68
'p5-d800'	600	800	-8	0.81	0.24	0.54	0.67
'p5-d800'	**600**	**800**	**-4**	**0.81**	**0.24**	**0.54**	**0.67**
'p5-d800'	600	800	0	0.85	0.24	0.58	0.68
'p5-d800'	600	800	4	0.81	0.23	0.54	0.67
'p6-d800'	600	800	-12	0.75	0.24	0.47	0.64
'p6-d800'	600	800	-8	0.71	0.23	0.44	0.63
'p6-d800'	**600**	**800**	**-4**	**0.71**	**0.23**	**0.44**	**0.63**
'p6-d800'	600	800	0	0.71	0.23	0.44	0.63
'p6-d800'	600	800	4	0.71	0.23	0.44	0.63
'p7-d800'	600	800	-12	0.62	0.24	0.35	0.56
'p7-d800'	600	800	-8	0.61	0.24	0.33	0.55
'p7-d800'	600	800	-4	0.63	0.24	0.36	0.57
'p7-d800'	**600**	**800**	**0**	**0.60**	**0.24**	**0.33**	**0.55**

Label	Speed [rpm]	P_{pilot} [bar]	θ_{pilot} [°CA aTDC]	φ_{global} [-]	φ_{CH4} [-]	φ_{diesel} [-]	R_{pilot} [-]
'p8-d800'	600	800	-12	0.53	0.23	0.27	0.51
'p8-d800'	600	800	-8	0.56	0.23	0.29	0.53
'p8-d800'	600	800	-4	0.54	0.23	0.28	0.51
'p8-d800'	**600**	**800**	**0**	**0.56**	**0.23**	**0.30**	**0.53**
'p9-d800'	600	800	-12	0.88	0.51	0.30	0.34
'p9-d800'	600	800	-8	0.88	0.51	0.30	0.34
'p9-d800'	600	800	-4	0.89	0.50	0.32	0.36
'p9-d800'	**600**	**800**	**0**	**0.88**	**0.49**	**0.32**	**0.36**
'p9-d800'	600	800	4	0.86	0.49	0.30	0.35
'p10-d800'	600	800	-12	0.74	0.49	0.18	0.25
'p10-d800'	600	800	-8	0.74	0.49	0.18	0.25
'p10-d800'	600	800	-4	0.73	0.48	0.18	0.24
'p10-d800'	**600**	**800**	**0**	**0.73**	**0.48**	**0.18**	**0.25**
'p11-d800'	600	800	-8	0.64	0.48	0.09	0.14
'p11-d800'	600	800	-4	0.64	0.48	0.10	0.15
'p11-d800'	**600**	**800**	**0**	**0.64**	**0.48**	**0.09**	**0.15**
'p12-d800'	600	800	-8	0.88	0.61	0.18	0.21
'p12-d800'	600	800	-4	0.84	0.61	0.15	0.18
'p12-d800'	**600**	**800**	**0**	**0.84**	**0.60**	**0.15**	**0.18**
'p12-d800'	600	800	4	0.86	0.60	0.17	0.20
'p13-d800'	600	800	-12	0.73	0.60	0.05	0.06
'p13-d800'	600	800	-8	0.73	0.60	0.05	0.07
'p13-d800'	**600**	**800**	**-4**	**0.76**	**0.59**	**0.08**	**0.10**
'p13-d800'	600	800	0	0.73	0.60	0.05	0.06
'p1-d1300'	600	1300	-12	0.81	0.36	0.40	0.49
'p1-d1300'	600	1300	-8	0.82	0.36	0.41	0.51
'p1-d1300'	600	1300	-4	0.81	0.36	0.40	0.50
'p1-d1300'	**600**	**1300**	**0**	**0.84**	**0.35**	**0.44**	**0.52**
'p1-d1300'	600	1300	4	0.80	0.35	0.39	0.50
'p2-d1300'	600	1300	-12	0.72	0.36	0.31	0.43
'p2-d1300'	600	1300	-8	0.72	0.35	0.32	0.44
'p2-d1300'	600	1300	-4	0.71	0.36	0.31	0.43
'p2-d1300'	600	1300	0	0.71	0.35	0.31	0.44
'p2-d1300'	**600**	**1300**	**4**	**0.71**	**0.35**	**0.31**	**0.44**
'p3-d1300'	600	1300	-12	0.64	0.37	0.22	0.35
'p3-d1300'	600	1300	-8	0.63	0.35	0.22	0.35
'p3-d1300'	600	1300	-4	0.66	0.35	0.25	0.39
'p3-d1300'	**600**	**1300**	**0**	**0.63**	**0.35**	**0.23**	**0.37**

Label	Speed [rpm]	P_{pilot} [bar]	θ_{pilot} [°CA aTDC]	φ_{global} [-]	φ_{CH4} [-]	φ_{diesel} [-]	R_{pilot} [-]
'p3-d1300'	600	1300	4	0.61	0.35	0.21	0.35
'p4-d1300'	600	1300	-12	0.55	0.35	0.15	0.27
'p4-d1300'	600	1300	-8	0.55	0.35	0.15	0.27
'p4-d1300'	**600**	**1300**	**-4**	**0.55**	**0.35**	**0.15**	**0.28**
'p4-d1300'	600	1300	0	0.56	0.35	0.16	0.28
'p5-d1300'	600	1300	-12	0.81	0.24	0.54	0.67
'p5-d1300'	600	1300	-8	0.80	0.23	0.53	0.67
'p5-d1300'	**600**	**1300**	**-4**	**0.82**	**0.23**	**0.56**	**0.68**
'p5-d1300'	600	1300	4	0.81	0.23	0.54	0.67
'p6-d1300'	600	1300	-12	0.75	0.24	0.47	0.63
'p6-d1300'	600	1300	-8	0.74	0.24	0.46	0.63
'p6-d1300'	600	1300	-4	0.74	0.24	0.46	0.63
'p6-d1300'	**600**	**1300**	**0**	**0.73**	**0.24**	**0.46**	**0.63**
'p6-d1300'	600	1300	4	0.74	0.23	0.47	0.64
'p7-d1300'	600	1300	-12	0.62	0.24	0.34	0.56
'p7-d1300'	600	1300	-8	0.62	0.24	0.35	0.57
'p7-d1300'	600	1300	-4	0.61	0.24	0.34	0.56
'p7-d1300'	**600**	**1300**	**4**	**0.63**	**0.23**	**0.37**	**0.58**
'p8-d1300'	600	1300	-12	0.56	0.25	0.28	0.50
'p8-d1300'	600	1300	-8	0.53	0.25	0.25	0.47
'p8-d1300'	600	1300	-4	0.53	0.24	0.25	0.48
'p8-d1300'	**600**	**1300**	**0**	**0.56**	**0.24**	**0.28**	**0.51**
'p9-d1300'	600	1300	-8	0.82	0.51	0.24	0.30
'p9-d1300'	600	1300	-4	0.85	0.50	0.28	0.33
'p9-d1300'	600	1300	0	0.85	0.49	0.29	0.34
'p9-d1300'	**600**	**1300**	**4**	**0.84**	**0.49**	**0.28**	**0.34**
'p10-d1300'	600	1300	-12	0.74	0.49	0.18	0.24
'p10-d1300'	600	1300	-8	0.74	0.49	0.19	0.25
'p10-d1300'	600	1300	-4	0.73	0.48	0.18	0.25
'p10-d1300'	600	1300	0	0.75	0.48	0.20	0.26
'p10-d1300'	**600**	**1300**	**4**	**0.76**	**0.48**	**0.21**	**0.28**
'p11-d1300'	600	1300	-12	0.66	0.48	0.11	0.17
'p11-d1300'	600	1300	-4	0.66	0.48	0.11	0.17
'p11-d1300'	**600**	**1300**	**0**	**0.64**	**0.48**	**0.10**	**0.15**
'p12-d1300'	600	1300	-12	0.88	0.63	0.16	0.18
'p12-d1300'	600	1300	-8	0.84	0.61	0.14	0.17
'p12-d1300'	600	1300	-4	0.83	0.60	0.14	0.17
'p12-d1300'	**600**	**1300**	**0**	**0.83**	**0.60**	**0.15**	**0.18**

Label	Speed [rpm]	P_{pilot} [bar]	θ_{pilot} [°CA aTDC]	φ_{global} [-]	φ_{CH4} [-]	φ_{diesel} [-]	R_{pilot} [-]
'p13-d1300'	600	1300	-8	0.73	0.59	0.05	0.07
'p13-d1300'	**600**	**1300**	**0**	**0.72**	**0.58**	**0.05**	**0.07**
'd2-d300'	600	300	-8	0.31	0.00	0.31	1.00
'd3-d300'	600	300	-8	0.20	0.00	0.21	1.00
'd4-d300'	600	300	-8	0.14	0.00	0.14	1.00
'd7-d300'	600	300	-8	0.33	0.00	0.33	1.00
'd8-d300'	600	300	-8	0.24	0.00	0.25	1.00
'd9-d300'	600	300	-8	0.07	0.00	0.08	1.00
'd10-d300'	600	300	-8	0.17	0.00	0.18	1.00
'd11-d300'	600	300	-8	0.26	0.00	0.27	1.00
'd12-d300'	600	300	-8	0.13	0.00	0.14	1.00
'd13-d300'	600	300	-8	0.03	0.00	0.04	1.00
'd5-d800'	600	800	-6	0.52	0.00	0.52	1.00
'd6-d800'	600	800	-6	0.43	0.00	0.44	1.00
'd7-d800'	600	800	-6	0.33	0.00	0.34	1.00
'd8-d800'	600	800	-6	0.25	0.00	0.26	1.00
'd9-d800'	600	800	-6	0.27	0.00	0.28	1.00
'd10-d800'	600	800	-6	0.20	0.00	0.20	1.00
'd11-d800'	600	800	-6	0.09	0.00	0.10	1.00
'd12-d800'	600	800	-6	0.14	0.00	0.15	1.00
'd1-d1300'	600	1300	-2	0.38	0.00	0.39	1.00
'd2-d1300'	600	1300	-2	0.27	0.00	0.28	1.00
'd3-d1300'	600	1300	-2	0.20	0.00	0.21	1.00
'd4-d1300'	600	1300	-2	0.11	0.00	0.12	1.00
'd5-d1300'	600	1300	-2	0.51	0.00	0.52	1.00
'd6-d1300'	600	1300	-2	0.42	0.00	0.43	1.00
'd7-d1300'	600	1300	-2	0.34	0.00	0.34	1.00
'd8-d1300'	600	1300	-2	0.27	0.00	0.27	1.00
'd9-d1300'	600	1300	-2	0.27	0.00	0.27	1.00
'd10-d1300'	600	1300	-2	0.16	0.00	0.17	1.00
'd11-d1300'	600	1300	-2	0.08	0.00	0.09	1.00
'd12-d1300'	600	1300	-2	0.13	0.00	0.13	1.00
'd13-d1300'	600	1300	-2	0.04	0.00	0.04	1.00

B 2: Performance and flowrate data from thermodynamic measurements

	Flowrates			Emissions				Performance		
	Air	CH_4	Diesel	CH_4	NO_X	CO	CO_2	GIMEP	$\eta_{thermal}$	GISFC
Label	[kg/hr]	[kg/hr]	[kg/hr]	[g/kW-hr]	[g/kW-hr]	[g/kW-hr]	[g/kW-hr]	[bar]	[-]	[g(diesel)/kW-hr]
'p2-d300'	38.37	0.90	0.81	5.63	6.47	8.65	589.38	8.15	0.36	224.97
'p2-d300'	38.63	0.99	0.79	5.52	4.73	8.24	580.51	8.28	0.35	230.23
'p2-d300'	**38.77**	**0.93**	**0.81**	**5.47**	**3.59**	**8.31**	**580.40**	**8.31**	**0.36**	**224.25**
'p2-d300'	38.77	0.92	0.84	5.22	3.17	7.76	588.57	8.18	0.35	229.97
'p2-d300'	40.01	0.95	0.85	5.17	3.91	7.26	634.95	7.79	0.33	247.44
'p3-d300'	39.75	0.95	0.64	9.90	8.84	7.00	600.99	7.21	0.34	236.63
'p3-d300'	39.72	0.94	0.63	9.58	6.57	6.60	584.47	7.41	0.35	229.45
'p3-d300'	**40.02**	**0.94**	**0.58**	**9.30**	**4.98**	**6.32**	**582.33**	**7.45**	**0.37**	**221.67**
'p3-d300'	40.16	0.94	0.58	9.18	4.47	6.53	593.17	7.32	0.36	224.72
'p3-d300'	40.20	0.94	0.58	9.49	4.80	6.75	624.87	6.94	0.34	236.46
'p4-d300'	39.99	0.95	0.37	16.28	8.99	7.30	568.74	6.45	0.36	224.60
'p4-d300'	40.18	0.93	0.39	17.06	6.30	7.48	563.59	6.51	0.37	221.98
'p4-d300'	**40.16**	**0.91**	**0.36**	**15.17**	**4.81**	**8.54**	**563.25**	**6.41**	**0.37**	**217.48**
'p4-d300'	40.58	0.91	0.41	16.11	4.18	10.46	584.85	6.12	0.34	236.00
'p4-d300'	40.67	1.48	0.37	18.87	2.65	11.67	628.14	5.42	0.22	377.88
'p7-d300'	39.02	0.62	0.95	6.78	7.68	6.09	609.59	7.32	0.36	225.91
'p7-d300'	39.16	0.61	0.96	7.61	5.57	5.92	603.63	7.36	0.36	224.59
'p7-d300'	**39.13**	**0.61**	**0.93**	**8.05**	**3.91**	**6.40**	**608.85**	**7.22**	**0.36**	**224.47**
'p7-d300'	39.48	0.61	0.97	8.54	3.10	7.61	633.39	6.97	0.34	237.45
'p7-d300'	40.60	0.61	0.93	8.38	3.66	8.31	672.66	6.75	0.34	240.08
'p8-d300'	39.79	0.62	0.70	12.39	9.63	6.20	618.49	6.20	0.36	225.81
'p8-d300'	**40.18**	**0.63**	**0.73**	**12.63**	**6.56**	**6.40**	**612.79**	**6.34**	**0.36**	**226.47**
'p8-d300'	40.28	0.62	0.71	13.10	4.82	8.11	615.91	6.26	0.36	226.03
'p8-d300'	40.29	0.62	0.67	14.42	4.26	9.57	624.94	6.08	0.36	226.32
'p8-d300'	40.26	0.62	0.67	15.43	4.34	10.64	651.53	5.76	0.34	238.01
'p9-d300'	37.63	1.23	0.70	3.74	16.45	7.30	564.13	8.91	0.35	234.77
'p9-d300'	37.44	1.23	0.72	3.86	13.53	7.14	547.21	9.09	0.35	232.98
'p9-d300'	37.22	1.23	0.70	3.69	10.81	7.02	537.78	9.19	0.36	227.89
'p9-d300'	**37.40**	**1.22**	**0.70**	**3.39**	**9.06**	**7.04**	**539.24**	**9.21**	**0.36**	**225.97**
'p9-d300'	37.57	1.22	0.69	3.15	8.79	7.23	554.33	9.00	0.35	230.13
'p10-d300'	38.33	1.22	0.54	4.98	20.10	5.84	564.56	8.39	0.36	228.65
'p10-d300'	38.39	1.22	0.52	5.05	18.39	5.44	552.33	8.58	0.37	220.92
'p10-d300'	38.29	1.22	0.55	4.81	14.16	5.34	541.03	8.73	0.37	220.65

	Flowrates			Emissions				Performance		
	Air	CH_4	Diesel	CH_4	NO_X	CO	CO_2	GIMEP	$\eta_{thermal}$	GISFC
Label	[kg/hr]	[kg/hr]	[kg/hr]	[g/kW-hr]	[g/kW-hr]	[g/kW-hr]	[g/kW-hr]	[bar]	[-]	[g(diesel)/kW-hr]
'p10-d300'	**38.02**	**1.21**	**0.51**	**4.53**	**11.66**	**5.14**	**537.65**	**8.72**	**0.38**	**216.05**
'p10-d300'	37.74	1.21	0.58	4.23	10.86	4.84	544.88	8.55	0.36	228.03
'p11-d300'	38.30	1.21	0.26	7.97	24.87	4.94	530.57	7.59	0.38	215.33
'p11-d300'	37.97	1.21	0.24	7.87	22.19	4.84	513.22	7.76	0.39	207.87
'p11-d300'	38.05	1.21	0.22	7.84	17.40	4.69	507.23	7.87	0.40	202.46
'p11-d300'	**38.15**	**1.21**	**0.31**	**7.62**	**13.93**	**4.39**	**509.76**	**7.86**	**0.38**	**214.02**
'p11-d300'	38.05	1.21	0.27	6.98	12.51	4.01	522.51	7.67	0.38	213.69
'p12-d300'	37.25	1.55	0.38	3.77	17.26	7.07	551.20	8.92	0.34	238.66
'p12-d300'	37.29	1.54	0.43	3.74	16.60	6.85	533.09	9.23	0.35	235.75
'p12-d300'	37.50	1.54	0.43	3.77	16.48	6.77	527.28	9.39	0.35	231.33
'p12-d300'	37.22	1.54	0.41	3.71	16.02	6.71	522.49	9.41	0.36	227.85
'p12-d300'	**36.83**	**1.53**	**0.38**	**3.42**	**13.54**	**1.25**	**528.35**	**9.24**	**0.36**	**228.95**
'p13-d300'	37.29	1.53	0.15	4.74	19.84	2.40	521.18	8.50	0.37	221.61
'p13-d300'	37.31	1.53	0.10	4.70	19.63	2.33	507.19	8.73	0.39	209.72
'p13-d300'	**36.88**	**1.53**	**0.11**	**4.54**	**19.06**	**2.27**	**493.89**	**8.86**	**0.39**	**206.90**
'p13-d300'	36.97	1.53	0.16	4.35	19.16	2.19	497.22	8.81	0.38	214.21
'p13-d300'	37.02	1.53	0.12	4.31	18.52	2.09	513.03	8.54	0.38	216.76
'p5-d800'	38.26	0.61	1.46	1.81	6.15	5.81	640.73	8.89	0.33	242.84
'p5-d800'	38.25	0.61	1.37	1.77	4.87	6.13	633.04	8.98	0.35	230.10
'p5-d800'	**38.54**	**0.61**	**1.39**	**1.76**	**3.95**	**7.57**	**637.39**	**8.92**	**0.35**	**233.05**
'p5-d800'	38.69	0.61	1.48	1.72	3.34	9.77	651.77	8.71	0.33	249.41
'p5-d800'	38.76	0.61	1.40	1.65	4.64	7.07	673.70	8.40	0.33	248.77
'p6-d800'	38.58	0.62	1.22	2.95	8.54	3.42	651.05	7.93	0.34	241.52
'p6-d800'	39.62	0.61	1.17	2.51	7.17	3.46	655.99	8.07	0.35	230.88
'p6-d800'	**39.69**	**0.61**	**1.17**	**2.57**	**5.63**	**3.03**	**651.88**	**8.14**	**0.35**	**229.44**
'p6-d800'	39.89	0.61	1.18	2.65	5.12	3.32	666.28	7.99	0.35	234.67
'p6-d800'	40.03	0.61	1.18	2.58	6.10	4.40	690.64	7.65	0.33	245.42
'p7-d800'	38.65	0.62	0.90	5.00	12.21	4.57	660.78	6.73	0.34	237.45
'p7-d800'	38.80	0.62	0.86	4.51	9.46	4.18	646.67	6.90	0.36	226.10
'p7-d800'	38.71	0.62	0.92	4.44	7.57	4.10	639.75	6.93	0.35	232.75
'p7-d800'	**39.28**	**0.62**	**0.86**	**4.59**	**6.98**	**4.46**	**655.42**	**6.82**	**0.36**	**228.32**
'p8-d800'	39.84	0.62	0.71	7.62	14.81	4.63	666.64	6.25	0.36	225.32

	Flowrates			Emissions				Performance		
	Air	CH_4	Diesel	CH_4	NO_X	CO	CO_2	GIMEP	$\eta_{thermal}$	GISFC
Label	[kg/hr]	[kg/hr]	[kg/hr]	[g/kW-hr]	[g/kW-hr]	[g/kW-hr]	[g/kW-hr]	[bar]	[-]	[g(diesel)/kW-hr]
'p8-d800'	39.91	0.62	0.78	7.06	10.92	4.47	650.69	6.39	0.35	230.85
'p8-d800'	40.05	0.61	0.73	6.67	8.84	4.61	645.45	6.45	0.37	221.66
'p8-d800'	**39.70**	**0.61**	**0.78**	**6.72**	**7.49**	**5.45**	**640.23**	**6.38**	**0.35**	**231.52**
'p9-d800'	36.50	1.24	0.73	3.19	16.85	7.02	579.70	8.81	0.34	241.95
'p9-d800'	36.75	1.24	0.73	3.07	14.96	4.69	561.05	9.11	0.35	234.49
'p9-d800'	36.88	1.24	0.77	3.00	12.56	9.22	554.26	9.23	0.35	235.69
'p9-d800'	**37.88**	**1.24**	**0.80**	**2.95**	**11.26**	**9.39**	**573.03**	**9.17**	**0.34**	**240.04**
'p9-d800'	38.13	1.24	0.77	2.59	10.84	9.46	590.43	8.95	0.34	241.90
'p10-d800'	37.78	1.23	0.45	4.85	21.16	3.32	578.79	8.09	0.36	228.67
'p10-d800'	38.05	1.24	0.46	4.84	20.86	3.25	565.55	8.31	0.36	223.70
'p10-d800'	38.28	1.23	0.45	4.44	19.82	3.12	562.94	8.43	0.37	219.39
'p10-d800'	**38.45**	**1.23**	**0.47**	**4.25**	**17.06**	**2.62**	**561.95**	**8.43**	**0.37**	**220.76**
'p11-d800'	38.51	1.23	0.22	7.31	25.58	4.25	537.03	7.57	0.38	213.54
'p11-d800'	38.75	1.23	0.25	7.34	21.56	4.29	528.85	7.70	0.38	213.58
'p11-d800'	**38.82**	**1.23**	**0.25**	**6.67**	**17.49**	**3.84**	**533.25**	**7.66**	**0.38**	**214.17**
'p12-d800'	37.89	1.54	0.45	3.80	15.05	6.95	530.80	9.54	0.35	229.72
'p12-d800'	38.04	1.54	0.38	3.51	15.23	5.90	526.52	9.64	0.37	219.69
'p12-d800'	**38.01**	**1.53**	**0.38**	**3.38**	**15.39**	**4.62**	**524.63**	**9.61**	**0.37**	**219.33**
'p12-d800'	37.88	1.52	0.43	3.06	13.60	4.69	546.02	9.25	0.35	232.61
'p13-d800'	38.30	1.52	0.12	4.82	19.23	2.31	522.60	8.52	0.38	215.63
'p13-d800'	38.28	1.52	0.12	4.81	18.81	2.32	507.06	8.76	0.39	210.15
'p13-d800'	**38.39**	**1.52**	**0.20**	**4.77**	**18.48**	**2.27**	**501.56**	**8.86**	**0.38**	**216.37**
'p13-d800'	38.25	1.52	0.12	4.61	18.87	2.14	504.04	8.77	0.39	209.29
'p1-d1300'	38.42	0.92	1.01	2.63	8.92	5.37	646.02	8.52	0.34	241.68
'p1-d1300'	38.84	0.92	1.07	2.70	7.48	4.61	642.60	8.59	0.33	245.49
'p1-d1300'	38.81	0.92	1.03	2.60	6.45	4.65	640.17	8.62	0.34	240.04
'p1-d1300'	**38.87**	**0.91**	**1.13**	**2.58**	**5.87**	**4.98**	**642.66**	**8.56**	**0.32**	**253.16**
'p1-d1300'	39.03	0.91	1.02	2.38	6.38	4.51	643.37	8.56	0.34	240.15
'p2-d1300'	38.62	0.92	0.79	4.19	12.88	4.06	653.40	7.48	0.33	245.49
'p2-d1300'	38.92	0.92	0.82	4.19	10.67	3.70	644.24	7.60	0.33	245.02

	Flowrates			Emissions				Performance		
	Air	CH_4	Diesel	CH_4	NO_X	CO	CO_2	GIMEP	$\eta_{thermal}$	GISFC
Label	[kg/hr]	[kg/hr]	[kg/hr]	[g/kW-hr]	[g/kW-hr]	[g/kW-hr]	[g/kW-hr]	[bar]	[-]	[g(diesel)/kW-hr]
'p2-d1300'	38.87	0.92	0.79	4.11	8.96	3.33	636.74	7.66	0.34	239.44
'p2-d1300'	39.23	0.92	0.81	3.82	8.12	3.06	637.64	7.71	0.34	240.57
'p2-d1300'	**39.44**	**0.91**	**0.81**	**3.35**	**7.78**	**2.78**	**638.58**	**7.69**	**0.34**	**240.71**
'p3-d1300'	37.69	0.92	0.55	6.68	15.02	5.02	620.83	6.78	0.35	235.08
'p3-d1300'	38.98	0.92	0.57	6.75	12.65	4.49	626.14	6.96	0.35	232.01
'p3-d1300'	39.25	0.92	0.66	6.12	10.42	3.90	616.38	7.10	0.34	239.34
'p3-d1300'	**39.41**	**0.92**	**0.60**	**5.26**	**8.81**	**3.70**	**604.33**	**7.25**	**0.36**	**226.80**
'p3-d1300'	39.80	0.92	0.57	6.24	6.03	4.04	635.44	6.85	0.35	234.94
'p4-d1300'	39.05	0.92	0.38	9.60	14.91	5.79	612.15	6.41	0.37	221.56
'p4-d1300'	39.43	0.92	0.39	9.19	12.18	5.55	607.21	6.50	0.37	219.78
'p4-d1300'	**39.50**	**0.92**	**0.40**	**8.15**	**9.44**	**5.13**	**587.21**	**6.71**	**0.38**	**215.01**
'p4-d1300'	39.13	0.92	0.41	8.29	6.82	5.45	579.21	6.63	0.37	219.36
'p5-d1300'	38.70	0.61	1.40	1.87	5.74	4.89	661.12	8.69	0.34	240.69
'p5-d1300'	39.08	0.61	1.39	1.79	16.05	4.04	656.56	8.83	0.35	235.25
'p5-d1300'	**39.01**	**0.60**	**1.45**	**1.85**	**12.98**	**3.39**	**651.62**	**8.86**	**0.34**	**240.53**
'p5-d1300'	39.06	0.61	1.41	1.76	12.06	6.12	678.66	8.47	0.33	247.20
'p6-d1300'	38.07	0.61	1.20	2.72	21.76	3.43	667.66	7.74	0.33	244.61
'p6-d1300'	38.10	0.61	1.17	2.64	20.72	3.11	648.62	7.89	0.35	235.43
'p6-d1300'	38.22	0.61	1.17	2.61	16.92	2.83	644.94	7.95	0.35	234.22
'p6-d1300'	**38.33**	**0.61**	**1.17**	**2.53**	**15.05**	**2.86**	**655.00**	**7.86**	**0.34**	**237.29**
'p6-d1300'	39.42	0.61	1.24	2.54	16.92	3.27	683.11	7.74	0.33	248.72
'p7-d1300'	39.30	0.62	0.90	4.66	28.00	4.50	708.38	6.61	0.33	243.39
'p7-d1300'	39.26	0.62	0.92	4.52	27.19	4.16	690.88	6.76	0.34	239.82
'p7-d1300'	39.28	0.62	0.88	4.17	22.73	3.82	685.91	6.81	0.35	233.10
'p7-d1300'	**40.04**	**0.62**	**0.97**	**3.72**	**18.92**	**4.28**	**671.35**	**6.95**	**0.34**	**240.59**
'p8-d1300'	38.24	0.63	0.71	7.43	32.80	5.42	685.98	5.84	0.33	243.40
'p8-d1300'	38.43	0.63	0.63	7.04	27.80	5.00	684.15	5.90	0.36	228.39
'p8-d1300'	38.58	0.63	0.65	6.58	22.83	4.56	671.07	6.02	0.36	226.01

	Flowrates			Emissions				Performance		
	Air	CH_4	Diesel	CH_4	NO_X	CO	CO_2	GIMEP	$\eta_{thermal}$	GISFC
Label	[kg/hr]	[kg/hr]	[kg/hr]	[g/kW-hr]	[g/kW-hr]	[g/kW-hr]	[g/kW-hr]	[bar]	[-]	[g(diesel)/kW-hr]
'p8-d1300'	**38.96**	**0.63**	**0.73**	**6.34**	**19.14**	**5.34**	**645.82**	**6.21**	**0.35**	**232.06**
'p9-d1300'	36.43	1.23	0.59	3.06	16.90	5.62	579.10	8.78	0.36	225.81
'p9-d1300'	36.76	1.23	0.68	3.06	15.69	5.45	570.92	8.93	0.35	231.90
'p9-d1300'	37.71	1.23	0.73	2.99	14.00	5.31	581.63	9.00	0.35	235.27
'p9-d1300'	**37.82**	**1.23**	**0.72**	**2.60**	**12.76**	**5.54**	**584.64**	**9.02**	**0.35**	**233.74**
'p10-d1300'	37.53	1.23	0.45	4.76	21.31	3.12	591.85	7.93	0.35	231.47
'p10-d1300'	37.86	1.22	0.47	4.75	21.24	2.99	583.09	8.08	0.35	229.78
'p10-d1300'	37.97	1.22	0.46	4.48	21.24	2.74	576.44	8.17	0.36	225.43
'p10-d1300'	38.04	1.22	0.50	4.07	20.17	2.29	568.35	8.32	0.36	225.61
'p10-d1300'	**38.26**	**1.22**	**0.53**	**3.67**	**18.22**	**1.99**	**570.66**	**8.29**	**0.35**	**230.47**
'p11-d1300'	38.30	1.23	0.28	6.36	25.54	3.63	571.50	7.40	0.36	225.80
'p11-d1300'	38.55	1.23	0.28	6.19	25.10	3.63	546.47	7.67	0.37	217.89
'p11-d1300'	**38.62**	**1.23**	**0.25**	**5.54**	**22.32**	**3.19**	**542.47**	**7.76**	**0.38**	**211.45**
'p12-d1300'	36.34	1.53	0.38	3.39	15.65	6.16	547.58	8.97	0.35	234.90
'p12-d1300'	37.68	1.53	0.36	3.81	16.44	3.81	548.56	9.10	0.36	228.86
'p12-d1300'	37.88	1.52	0.36	3.72	16.36	3.50	539.81	9.26	0.36	224.41
'p12-d1300'	**38.07**	**1.52**	**0.37**	**3.55**	**16.47**	**3.00**	**538.78**	**9.31**	**0.36**	**224.19**
'p13-d1300'	38.38	1.51	0.13	4.91	19.46	2.23	524.22	8.56	0.38	214.73
'p13-d1300'	**38.62**	**1.50**	**0.13**	**4.48**	**19.63**	**2.01**	**522.56**	**8.62**	**0.39**	**211.27**
'd2-d300'	40.26	0.00	0.84	-	-	-	-	3.73	0.37	220.56
'd3-d300'	41.31	0.00	0.58	-	-	-	-	2.54	0.37	221.04
'd4-d300'	41.69	0.00	0.39	-	-	-	-	1.58	0.34	241.24
'd7-d300'	41.29	0.00	0.91	-	-	-	-	4.31	0.39	207.78
'd8-d300'	41.21	0.00	0.69	-	-	-	-	3.10	0.38	216.26
'd9-d300'	41.39	0.00	0.21	-	-	-	-	0.93	0.38	211.60
'd10-d300'	40.60	0.00	0.48	-	-	-	-	2.37	0.41	197.05
'd11-d300'	39.70	0.00	0.71	-	-	-	-	3.27	0.38	213.10
'd12-d300'	40.71	0.00	0.38	-	-	-	-	1.66	0.38	212.96
'd13-d300'	42.04	0.00	0.10	-	-	-	-	0.19	0.19	430.88
'd5-d800'	41.14	0.00	1.44	-	-	-	-	6.36	0.37	222.43

	Flowrates			Emissions				Performance		
	Air	CH_4	Diesel	CH_4	NO_X	CO	CO_2	GIMEP	$\eta_{thermal}$	GISFC
Label	[kg/hr]	[kg/hr]	[kg/hr]	[g/kW-hr]	[g/kW-hr]	[g/kW-hr]	[g/kW-hr]	[bar]	[-]	[g(diesel)/kW-hr]
'd6-d800'	40.99	0.00	1.19	-	-	-	-	5.32	0.37	220.71
'd7-d800'	39.74	0.00	0.89	-	-	-	-	3.91	0.36	223.25
'd8-d800'	41.05	0.00	0.70	-	-	-	-	3.23	0.38	212.54
'd9-d800'	41.05	0.00	0.77	-	-	-	-	3.31	0.36	224.65
'd10-d800'	40.17	0.00	0.54	-	-	-	-	1.97	0.31	264.96
'd11-d800'	40.20	0.00	0.27	-	-	-	-	0.78	0.26	316.36
'd12-d800'	40.32	0.00	0.40	-	-	-	-	1.63	0.34	238.01
'd1-d1300'	40.62	0.00	1.05	-	-	-	-	4.31	0.34	238.36
'd2-d1300'	40.83	0.00	0.75	-	-	-	-	3.24	0.36	224.50
'd3-d1300'	41.06	0.00	0.57	-	-	-	-	2.40	0.36	228.37
'd4-d1300'	41.83	0.00	0.33	-	-	-	-	1.23	0.33	247.87
'd5-d1300'	40.30	0.00	1.39	-	-	-	-	6.12	0.36	223.81
'd6-d1300'	40.69	0.00	1.17	-	-	-	-	5.02	0.36	228.20
'd7-d1300'	39.37	0.00	0.90	-	-	-	-	3.88	0.36	227.66
'd8-d1300'	40.57	0.00	0.74	-	-	-	-	3.16	0.35	229.88
'd9-d1300'	40.57	0.00	0.74	-	-	-	-	3.16	0.35	229.88
'd10-d1300'	40.70	0.00	0.47	-	-	-	-	2.03	0.37	219.97
'd11-d1300'	41.20	0.00	0.25	-	-	-	-	0.54	0.19	422.27
'd12-d1300'	40.86	0.00	0.36	-	-	-	-	1.56	0.37	218.78
'd13-d1300'	41.64	0.00	0.12	-	-	-	-	-0.24	-0.18	-453.75

Appendix C : Optical Heat Release Rates

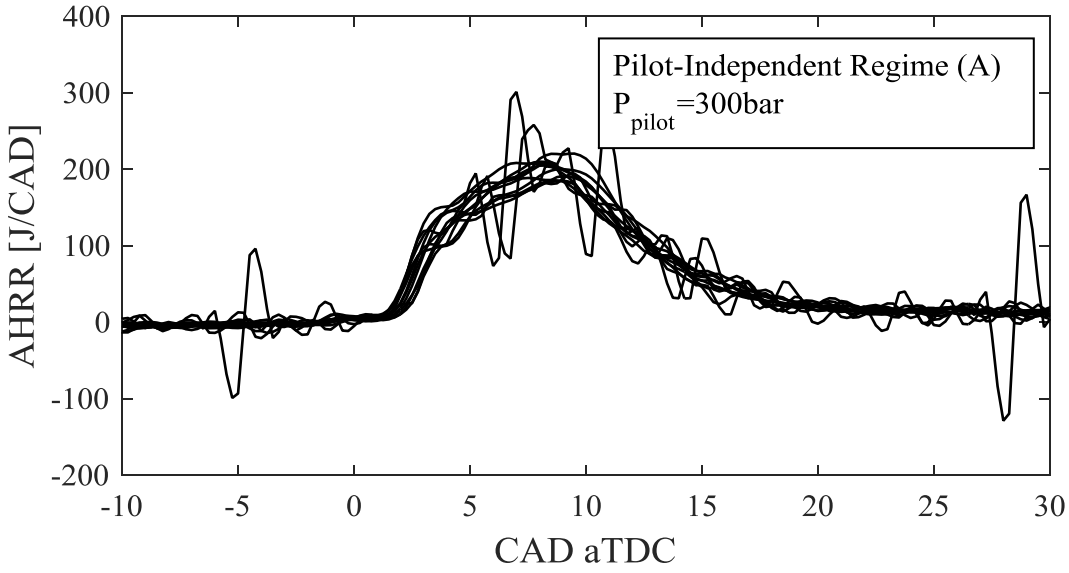

Figure C 1:All (15), unfiltered single-cycle AHRR measured during optical testing of pilot-independent DIDF combustion with P_{pilot}=300bar.

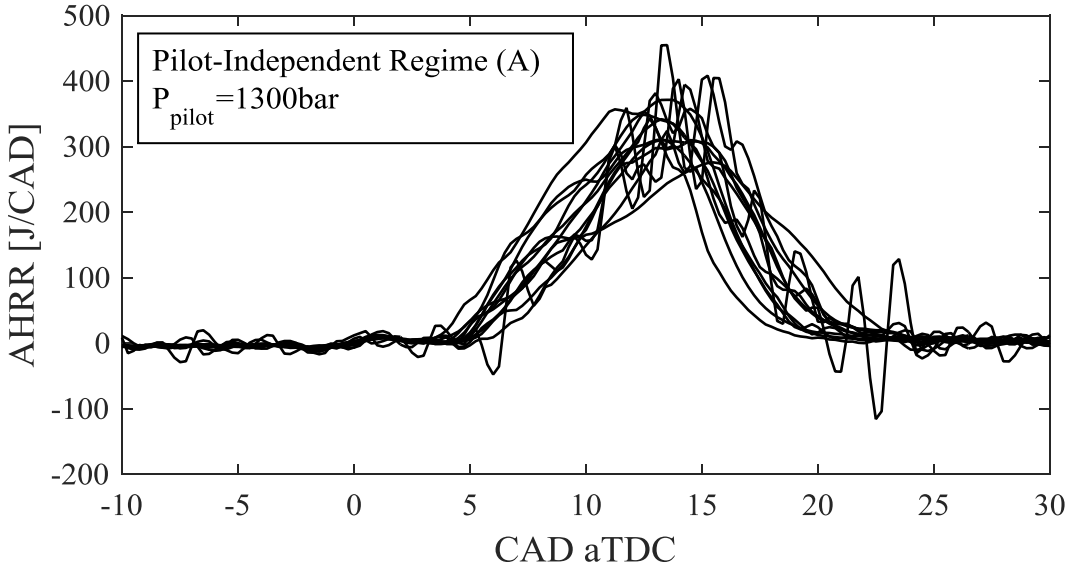

Figure C 2: All (15), unfiltered single-cycle AHRR measured during optical testing of pilot-independent DIDF combustion with P_{pilot}=1300bar.

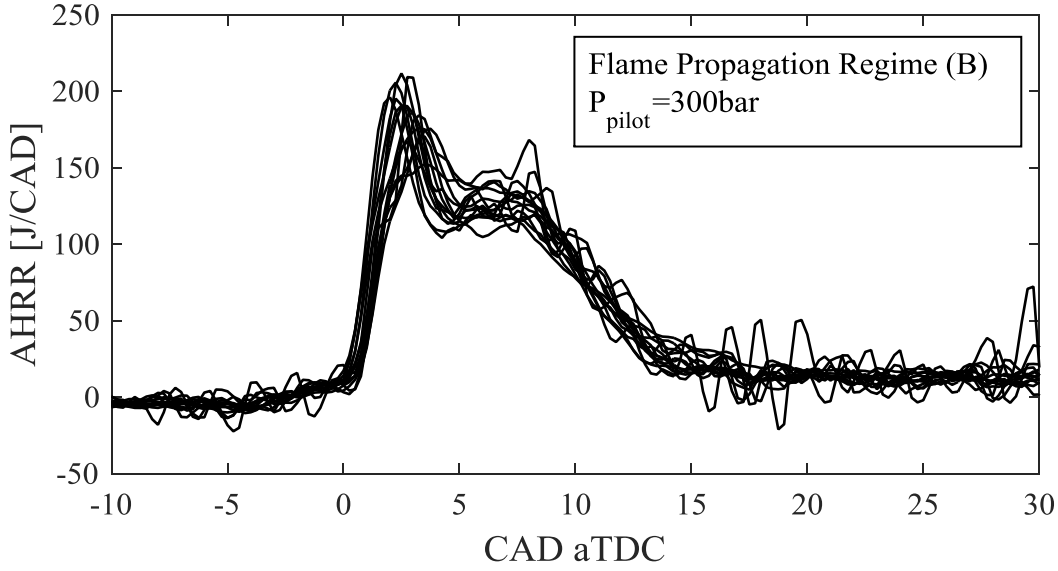

Figure C 3: All (15), unfiltered single-cycle AHRR measured during optical testing of flame propagation DIDF combustion with P_{pilot}=300bar.

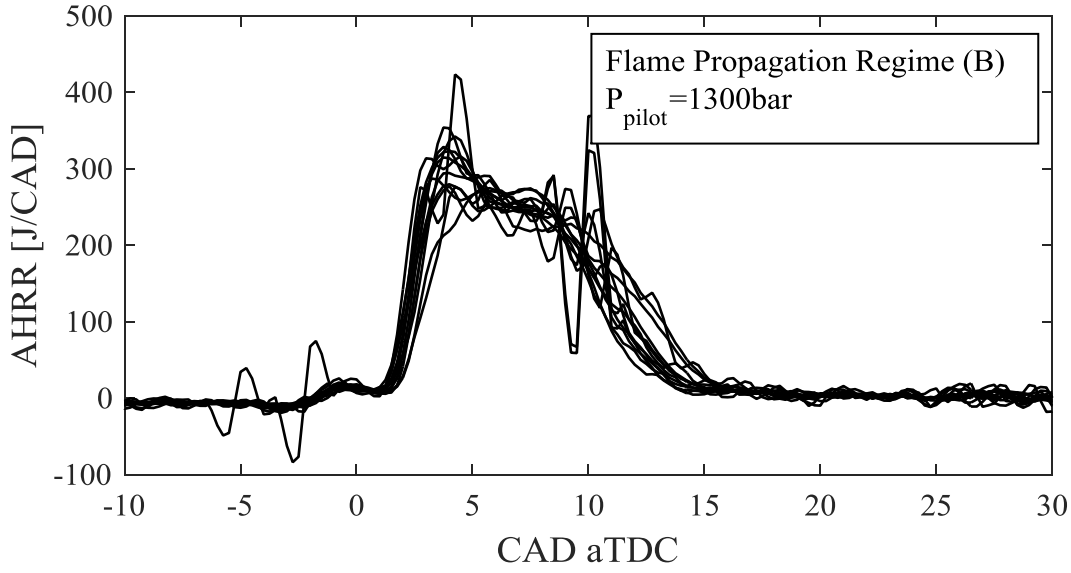

Figure C 4: All (15), unfiltered single-cycle AHRR measured during optical testing of flame propagation DIDF combustion with P_{pilot}=1300bar.

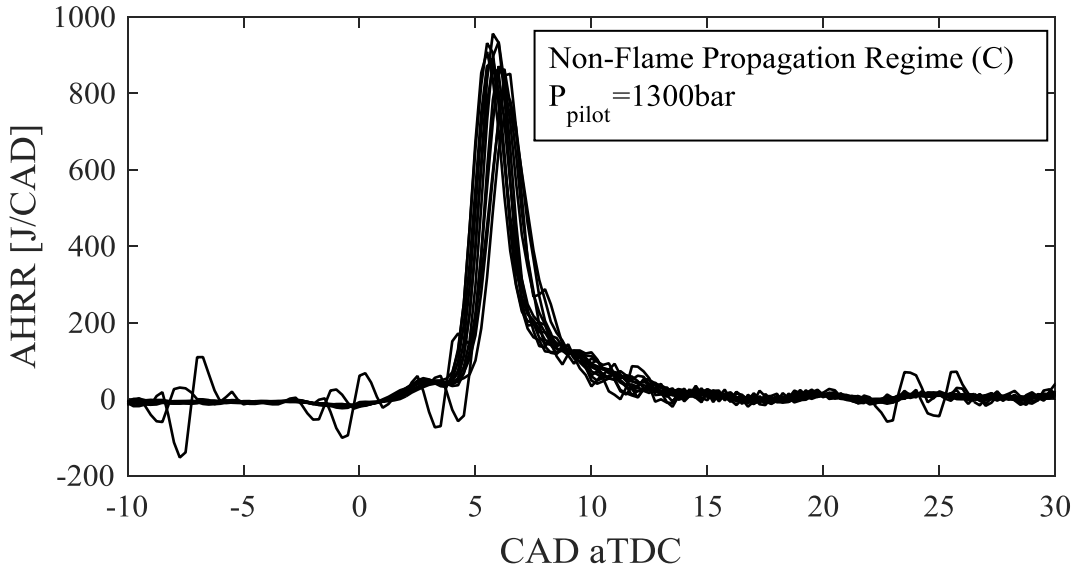

Figure C 5: All (14), unfiltered single-cycle AHRR measured during optical testing of non-flame propagation DIDF combustion with P_{pilot}=1300bar.